NUREG/CR-6920
SAND2006-3772P

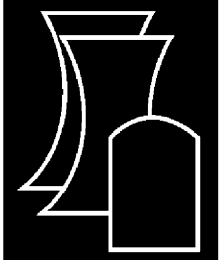

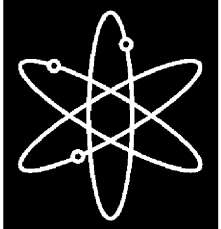

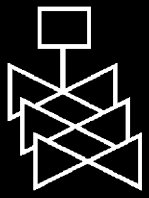

Risk-Informed Assessment of Degraded Containment Vessels

Sandia National Laboratories

U.S. Nuclear Regulatory Commission
Office of Nuclear Regulatory Research
Washington, DC 20555-0001

NUREG/CR-6920
SAND2006-3772P

Risk-Informed Assessment of Degraded Containment Vessels

Manuscript Completed: June 2006
Date Published: November 2006

Prepared by
B.W. Spencer, J.P. Petti, D.M. Kunsman

Sandia National Laboratories
Operated by Sandia Corporation for the
U.S. Department of Energy
P.O. Box 5800
Albuquerque, NM 87185-0744

H.L. Graves, III, NRC Project Manager

Prepared for
Division of Fuel, Engineering and Radiological Research
Office of Nuclear Regulatory Research
U.S. Nuclear Regulatory Commission
Washington, DC 20555-0001
Job Code Y6164

INTENTIONALLY LEFT BLANK

Abstract

Various forms of degradation have been observed in the containment vessels of a number of operating nuclear power plants in the United States. Examples of degradation include corrosion of the steel shell or liner, corrosion of reinforcing bars and prestressing tendons, loss of prestressing, and corrosion of bellows. The containment serves as the ultimate barrier against the release of radioactive material into the environment. Because of this role, compromising the containment could increase the risk of a large release in the unlikely event of an accident.

It is possible to assess the effect that degradation has on the pressure retaining capacity of the containment vessel by performing structural analysis using a model that takes into account the effects of the degradation. While such an analysis provides useful information about the effects of the degradation on the structural capacity of the containment, it does not necessarily provide a perspective on the effect that the degradation could have on the risk associated with operating a nuclear power plant. To understand the risk, one must take into account both the structural capacity of the containment and the probabilities of occurrence of a variety of loading scenarios.

In this study, structural analysis results are integrated with risk models to gain a risk-informed perspective on the issue of containment degradation. Risk models require a probabilistic description of the capacity of the containment to resist a number of different failure modes. Latin hypercube sampling is used to develop sets of inputs for detailed finite element models of the containment in both its original and degraded condition. Probabilistic descriptions of the containment capacity are obtained from the results of the structural analysis models, and used as input for the risk model. By using this approach, both the risk and the change in risk associated with the degradation can be measured.

The approach described above has been applied to case studies of containment degradation at four "typical" U.S. nuclear power plants. These include a Pressurized Water Reactor (PWR) with a large, dry reinforced concrete containment, a Boiling Water Reactor (BWR) with a Mark I steel containment, a PWR with a steel ice condenser containment, and a PWR with a large, dry prestressed concrete containment. In this study, each of these containments is subjected to a number of hypothetical degradation scenarios. While this degradation is typical of that which has been observed in actual plants, it is not implied that such degradation was actually observed in the plants studied here.

The risk analysis results reflect the effects of degradation and are evaluated with respect to the guidelines given in the U.S. Nuclear Regulatory Commission (NRC) Regulatory Guide 1.174. Recommendations are made on the appropriateness and limitations of this approach. Integrating structural analysis with risk analysis can give plant operators and regulators improved information to make the best decisions on how to deal with containment degradation.

INTENTIONALLY LEFT BLANK

FOREWORD

Through the years, the containment vessels of operating nuclear power plants in the United States have exhibited various forms of degradation, including corrosion of the steel shell or liner, reinforcing bars, and prestressing tendons; loss of prestressing; and corrosion of bellows. Because the containment serves as the ultimate barrier against the release of radioactive material into the environment, compromising the containment could increase the risk of a large release in the unlikely event of an accident.

It is possible to assess the effect of degradation on the pressure-retaining capacity of the containment vessel by performing a structural analysis using a model that considers the effects of degradation. While such an analysis provides useful information about the effects of degradation on the structural capacity of the containment, it does not necessarily provide a perspective on the potential effect of degradation on the risk associated with operating a nuclear power plant. To understand that risk, one must consider both the structural capacity of the containment and the probabilities of occurrence of a variety of loading scenarios.

This study integrates structural analysis results with risk models to gain a risk-informed perspective on the issue of containment degradation. Risk models require a probabilistic description of the capacity of the containment to resist a variety of failure modes. Latin hypercube sampling is used to develop sets of inputs for detailed finite element models of the containment in both its original and degraded conditions. Probabilistic descriptions of the containment capacity are obtained from the results of the structural analysis models, and used as input for the risk model. Using this approach, one can measure both the risk and the change in risk associated with the degradation. Moreover, integrating structural and risk analyses can give plant operators and regulators improved information to make the best decisions on how to deal with containment degradation.

This study applied the approach described above to case studies of containment degradation at four "typical" U.S. nuclear power plants, including a pressurized-water reactor (PWR) with a large, dry reinforced concrete containment; a boiling-water reactor (BWR) with a Mark I steel containment; a PWR with a steel ice condenser containment; and a PWR with a large, dry prestressed concrete containment. In this study, each of these containments was subjected to a number of hypothetical degradation scenarios. While this degradation is typical of that observed in actual plants, the reader should not infer that such degradation was actually observed in the plants studied here.

The risk analysis results of the effects of degradation were evaluated with respect to the guidelines in U.S. Nuclear Regulatory Commission (NRC) Regulatory Guide 1.174, "An Approach for Using Probabilistic Risk Assessment in Risk-informed Decisions on Plant-Specific Changes to the Licensing Basis," Rev. 1, dated November 2002. Recommendations are made on the appropriateness and limitations of this approach. With magnitudes depending on the depth and location, liner/shell corrosion significantly reduces the capacity of a given containment. Nonetheless, only the case involving 50% corrosion at the basemat of the steel PWR ice condenser containment shows low probabilities of leakage near the design pressure. Other degradation cases throughout these containment studies show shifts in the fragility curves, but not approaching the design pressure even at low probabilities.

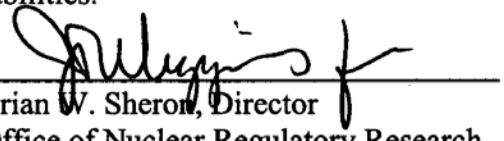

Brian W. Sheron, Director
Office of Nuclear Regulatory Research
U.S. Nuclear Regulatory Commission

INTENTIONALLY LEFT BLANK

Table of Contents

Figures

Tables

INTENTIONALLY LEFT BLANK

Executive Summary

Various forms of degradation have been observed in the containment vessels of a number of operating nuclear power plants in the United States. Examples of degradation include corrosion of the steel shell or liner, corrosion of reinforcing bars and prestressing tendons, loss of prestressing, and corrosion of bellows. The containment serves as the ultimate barrier against the release of radioactive material into the environment. Because of this role, compromising the containment could increase the risk of a large release in the unlikely event of an accident.

It is possible to assess the effect that degradation has on the pressure retaining capacity of the containment vessel by performing structural analysis using a model that takes into account the effects of the degradation. While such an analysis provides useful information about the effects of the degradation on the structural capacity of the containment, it does not necessarily provide a perspective on the effect that the degradation could have on the risk associated with operating a nuclear power plant. To understand the risk, one must take into account both the structural capacity of the containment and the probabilities of occurrence of a variety of loading scenarios.

Structural analysis results are integrated with risk models in this study to gain a risk-informed perspective on the issue of containment degradation. Risk models require a probabilistic description of the capacity of the containment to resist a number of different failure modes. Probabilistic effects are introduced into the analyses using Latin hypercube sampling to develop sets of inputs for detailed finite element models of the containment in both its original and degraded condition. The results of the structural analysis models are used to obtain the probabilistic descriptions of the containment capacity and used as input for the risk model. By using this approach, both the risk and the change in risk associated with the degradation can be measured.

The approach described above has been applied to case studies of containment degradation at four "typical" U.S. nuclear power plants. These include a Pressurized Water Reactor (PWR) with a large, dry reinforced concrete containment, a Boiling Water Reactor (BWR) with a Mark I steel containment, a PWR with a steel ice condenser containment, and a PWR with a large, dry prestressed concrete containment. In this study, each of these containments is subjected to a number of hypothetical degradation scenarios. While this degradation is typical of that which has been observed in actual plants, it is not implied that such degradation was actually observed in the plants studied here.

The results of the risk analysis of the effects of degradation are evaluated with respect to the guidelines given in the U.S. Nuclear Regulatory Commission (NRC) Regulatory Guide 1.174. Recommendations are made on the appropriateness and limitations of this approach. Integrating structural analysis with risk analysis can give plant operators and regulators improved information to make the best decisions on how to deal with containment degradation.

The results of the fragility and PRA models for each plant with various forms of degradation can be summarized easily due to the observed consistent trends. With magnitudes depending on the depth and location, liner/shell corrosion significantly reduces the capacity of a given containment. Only the 50% corrosion at the basemat case for the steel PWR ice condenser containment shows that leaks are possible near the design pressure. Other degradation cases throughout the containments studies here show shifts in the fragility curves, but not approaching the design pressure even at low probabilities.

PRA models suggest that liner/shell degradation causes a small increase in Large Early Release Frequency (LERF) in cases where catastrophic rupture dominates the failure mode. In such cases,

containment failure proceeds directly from leak to catastrophic rupture with little or no gap between the failure modes. This is observed in the steel shell containments where sufficient energy exists within the pressurized containment to propagate a crack after the initiation of a leak. Of the catastrophic rupture dominated cases examined here with corrosion in the steel shell of a steel containment, all remain within Region III of Figure 2.2.

Concrete containments also show increases in LERF with degradation when the overall capacity is affected by the degradation. The two cases of tendon degradation of the prestressed concrete containment show increases in LERF. The largest increase occurs when 50% of the area is reduced for the midheight hoop tendons. The degradation of the tendons leads to a significant probability of catastrophic rupture at low pressures. Here, LERF increases enough to enter Region II of Figure 2.2. Based on Regulatory Guide 1.174, the increase in risk is still considered small and may still be permitted.

Other cases actually show LERF remaining constant or even experiencing a reduction with degradation. These cases were encountered when leak was the dominant failure mode at low pressures. Specifically, these cases occurred in the basemat and bellows corrosion cases for the steel PWR ice condenser and the two concrete containments with liner corrosion. The large bending field at the base of the ice condenser containment causes leaks at low pressures prior to catastrophic rupture. The concrete containment liners tear at relatively low pressures compared to the overall capacity of the concrete vessel.

Since LERF was found to decrease in some cases where leaks dominates and would cause a release, the Small Early Release Frequency (SERF) was included in the PRA results for each containment. When leak dominates the failure, SERF increases and leads to the observed decrease in LERF. In these cases, the leak site acts as a "vent" at low pressures, slowly releasing material with the possibility of preventing or delaying a catastrophic rupture.

Since SERF decreases for the cases where catastrophic rupture dominates, the Total Early Release Frequency (TERF = LERF + SERF) was computed for each containment at each degradation case. TERF was included to illustrate that the total frequency increases or remains constant when introducing degradation regardless of the dominant failure mode.

If limits were placed on the increase in SERF or TERF that where analogous to those for LERF in Figure 2.2, Region II would be reached for several additional degradation cases in this study. In addition, the PRA models used here do not directly compute LERF or SERF. The binning process is performed during the post-processing of the PRA results. It is at this point where the results from the event tree analysis are placed into LERF, SERF, and other "bins" depending on the failure mode (e.g. leak, rupture, etc). This study places leak failures into the SERF bin, and ruptures and catastrophic ruptures into the LERF bin. This was done assuming that a leak would not depressurize the containment in less than two hours (NUREG-1150 definition).

This study has examined several representative examples of containment degradation. The specific results presented here should not be applied to any existing plant since actual degradation may be considerable more severe or widespread than examined here. The purpose of this study was to demonstrate a methodology of applying a risk-informed assessment to structural degradation. This methodology could be applied to specific degradation found in an existing plant. Although, many of the assumptions and techniques adopted in this study are still the subject of open research. In addition, the definitions for leak, rupture, and catastrophic rupture and associated failure criteria were used here to remain consistent with the existing NUREG-1150 PRA models. In reality, containments leak as a continuous function of pressure. These items should be considered when examining the findings illustrated in this report.

INTENTIONALLY LEFT BLANK

Acknowledgements

The project team acknowledges the continuous guidance, support, and encouragement from Herman L. Graves III, Engineering Research Applications Branch, Division of Engineering Technology, Nuclear Regulatory Commission.

Special thanks are extended to everyone involved for their support and contribution to this project. The project team would also like to thank Sandia colleagues Jason V. Zuffranieri, Michael F. Hessheimer, Eric W. Klamerus, Jeffrey A. Smith, Jeffrey L. Cherry, Matthew C. Turgeon, David G. Robinson, Gregory D. Wyss, Sharon L. Daniel, and Mark T. Leonard for valuable discussions and help in all phases of this project.

Sandia is a multiprogram laboratory operated by Sandia Corporation, a Lockheed Martin Company, for the United States Department of Energy's National Nuclear Security Administration under Contract DE-AC04-94AL85000.

Acronyms

APB	accident progression bin
APET	accident progression event tree
BWR	boiling water reactor
CDF	core damage frequency
CDWR	catastrophic drywell rupture
COV	coefficient of variation
CWWR	catastrophic wetwell rupture
DWHL	drywell head leak
DWHR	drywell head rupture
DWL	drywell leak
DWR	drywell rupture
EPFM	elastic-plastic fracture mechanics
IPE	individual plant evaluation
LEFM	linear-elastic fracture mechanics
LERF	large early release frequency
LHS	Latin hypercube simulation
LOCA	loss of coolant accident
PCCV	prestressed concrete containment vessel
PRA	probabilistic risk assessment
PWR	pressurized water reactor
RC	reinforce concrete
SERF	small early release frequency
TERF	total early release frequency
WWLaW	wetwell leak above waterline
WWLbW	wetwell leak below waterline
WWRaW	wetwell rupture above waterline
WWRbW	wetwell rupture below waterline

1. Introduction

Containment structures in nuclear power plants fill the critical role of providing the final barrier against the release of radioactive materials in the event of a severe accident. The ability of the containment structure to resist internal pressures without leaking can have a significant effect on the risk that operation of a plant could result in a release of radionuclides to the surrounding environment.

In the United States, degradation of the containment vessel has been observed at a large number of nuclear power plants. Corrosion has been observed in a number of steel containments, as well as in the steel liners of reinforced concrete containments. Loss of prestressing in the tendons of prestressed concrete containment vessels has also been observed. Degradation of bellows, which are another critical part of the pressure boundary, is also of concern.

Any of these modes of degradation can have an adverse effect on the ability of a containment vessel to perform its intended function. Previous studies have investigated the ability of containments to resist leakage under overpressurization. Cherry and Smith (2001) investigated how corrosion of the steel shell or liner affects the capacities of steel, reinforced concrete, and prestressed concrete containments under internal pressurization. The effect of the loss of prestressing force on the pressure capacity of prestressed concrete containment vessels was investigated by Smith (2001). Ellingwood and Cherry (1999) developed fragility curves for a steel containment with corrosion damage under overpressurization.

Although the aforementioned studies provide valuable information on the pressure capacity of a degraded containment, they provide little insight into the effect that the degradation has on the risk of a radiation release. In the studies mentioned above, the pressure capacities of containments were generally found to be well in excess of their design pressures, even with significant degradation. However, under severe accident conditions, pressures far above the design pressure can potentially be encountered.

The goal of this study is to take the previous studies on degraded containments one step further and determine the significance of containment degradation on the risk of a radiation release. This can give valuable insight into the performance of the containment under beyond-design-basis loading events. A better understanding of the significance of the various factors that contribute to the risk can lead to improved decisions on how to allocate resources to best ensure the safety of a nuclear power plant.

2. Approach for Risk-Informed Assessment of Containment Degradation

2.1 Guidelines for Probabilistic Risk Assessment of Plant Modifications

The judicious application of probabilistic risk assessment (PRA) techniques to engineering problems can lead to improved safety and better allocation of limited resources. The United States Nuclear Regulatory Commission (NRC) recognizes the value of these techniques for nuclear applications, and has released a policy statement (USNRC, 1995) encouraging greater use of PRA in all areas of regulatory decision-making. As part of its effort to increase the use of PRA in the regulatory process, the NRC developed guidelines for using PRA to make risk-informed decisions regarding changes to a nuclear power plant's licensing basis. These are outlined in Regulatory Guide 1.174 (USNRC, 2001).

In Regulatory Guide 1.174, five principles to guide a risk-informed licensing basis change are outlined:

- "The proposed change meets the current regulations unless it is explicitly related to a requested exemption or rule change, i.e., a "specific exemption" under 10 CFR 50.12 or a "petition for rulemaking" under 10 CFR 2.802."
- "The proposed change is consistent with the defense-in-depth philosophy."
- "The proposed change maintains sufficient safety margins."
- "When proposed changes result in an increase in core damage frequency (CDF) or risk, the increases should be small and consistent with the intent of the Commission's Safety Goal Policy Statement. " (USNRC, 1986)
- "The impact of the proposed change should be monitored using performance measurement strategies."

As mentioned in the fourth principle above, if a change results in an increase in risk, the increase in risk must be small and fall within certain acceptance guidelines. In Regulatory Guide 1.174, core damage frequency and large early release frequency (LERF) have been designated as criteria for determining the acceptance of a proposed change. If a proposed change in the licensing basis results in an increase in either the CDF or LERF, the change is only deemed acceptable if the baseline values of CDF and LERF, as well as the change in those values due to the proposed change, fall within certain bounds. The changes in CDF and LERF due to the licensing basis change are denoted as ΔCDF and ΔLERF, respectively.

The acceptance criteria for a proposed licensing basis change are shown graphically in terms of CDF and LERF in Figure 2.1 and Figure 2.2, respectively. In both cases, the change in the risk metric is plotted versus the baseline metric. This space is divided into three regions. In the area denoted as Region I, the risk of the proposed change is deemed too high to be acceptable, and the change is not permitted. In Region II, the risk increase is considered small, and the change is permitted. In Region III, the risk increase is considered very small, and the change is permitted. In this case, however, the risk increase is deemed small enough that there is no longer a need to compute the value of the baseline risk metric. A proposed change must meet the acceptance guidelines for both CDF and LERF to be deemed acceptable. If a change is deemed acceptable, the cumulative impact of other plant changes on the risk over time must be monitored.

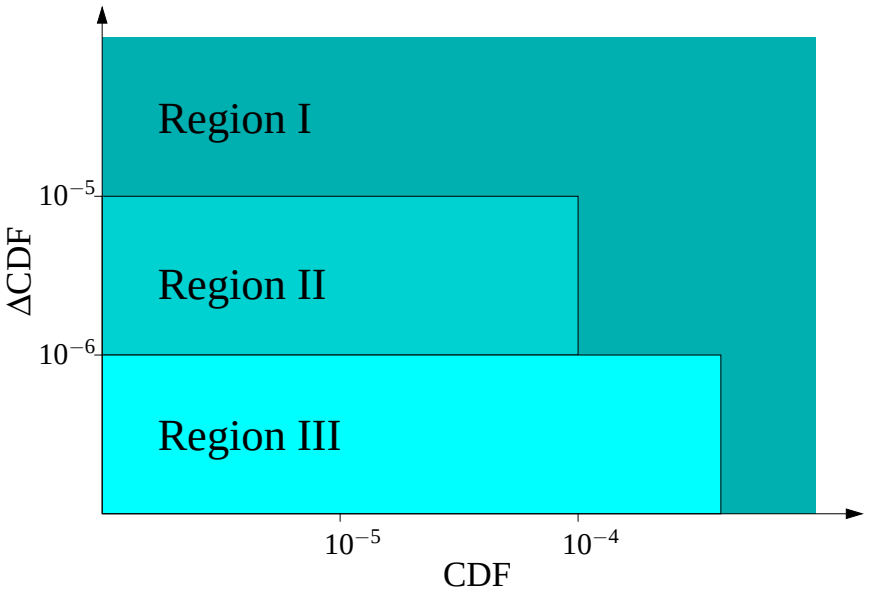

Figure 2.1: Acceptance Guidelines for Core Damage Frequency

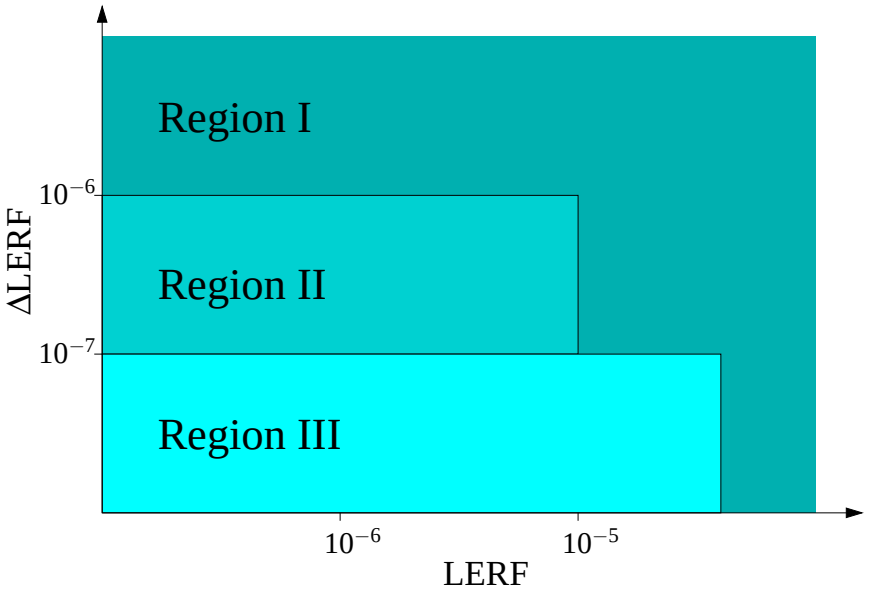

Figure 2.2: Acceptance Guidelines for Large Early Release Frequency

When proposing risk-informed changes to a plant's licensing basis, licensees are expected to clearly define the proposed change, and perform an appropriate engineering analysis of the change to ensure that it meets the aforementioned principles. They also must define an implementation and monitoring strategy before submitting the proposed change.

The approach defined in Regulatory Guide 1.174 for risk-informed decision-making is not intended to relieve the duty of licensees to do things that they view as undesirable simply because

those things can be demonstrated to have a minimal impact on the risk. If a proposal results in a risk increase, there must be clearly demonstrated benefits that outweigh the risk.

2.2 Application of Risk Assessment Guidelines to Degraded Containments

Degradation of various types has been observed in the containments of many U.S. commercial nuclear power plants during routine inspections. Any degradation of a containment vessel could potentially decrease the capacity of the containment to resist internal pressure without leaking. This could lead to a release of radiation to the outside of the containment earlier than would have been the case had the containment been in its original, un-degraded state.

It is useful to study the problem of containment degradation with a risk-informed perspective to determine its relative significance. In this study, the guidelines of Regulatory Guide 1.174 are applied to assess the risk associated with various types of postulated degradation of containment vessels and bellows. The degradation is considered to be a temporary change in the plant's licensing basis, and recommendations for action are made based on the outcome of the PRA and Regulatory Guide 1.174.

While actual plants are being used as examples in this study, it should be emphasized that the analyses in this report are not intended to represent the actual condition of the plants. The information concerning the plant systems and structures used in the analyses is not current, and current operating conditions likely differ considerably from those assumed in the analyses. Most important, degradation is assumed only to demonstrate an analytical methodology, and does not represent actual degradation that has been observed at any of the plants. Any similarity between the degradation assumed in this study and that observed in the plants used for these demonstrations is purely coincidental.

2.3 Containment Performance Characterization

A number of different criteria can be used to characterize the performance of a structure. In design codes, structures are typically required to satisfy a number of different criteria to be deemed acceptable. The most obvious of these is that the structure must have adequate strength to resist the loads that it is designed for, with appropriate safety factors. For acceptable performance, the structure also must meet deflection criteria under those loads. Design codes also impose a number of other requirements that ensure that if a structural failure occurs, it will fail in a manner that will present the least possible danger to the public.

When studying the pressure capacity of containment vessels, it is important to have an understanding of how these structures behave under pressure loading, and of how the performance under this load can be measured. One of the most difficult and important tasks when performing a structural analysis of a containment structure is to determine how performance is to be measured and how the structural analysis results can be interpreted in terms of the chosen performance criterion. By their nature, the behavior and performance characteristics of containment vessels are somewhat different than that of typical civil structures.

Arguably, the most important performance metric of a containment vessel undergoing pressurization is its leak rate at a given pressure. For every type of containment vessel, there exists a limiting pressure beyond which the structure can no longer be pressurized. This structural capacity limit pressure is also an important performance characteristic, although it can be of secondary importance simply because it is often far in excess of the pressure at which the

containment first begins to leak, especially for reinforced and prestressed concrete containment vessels. As with all structures, deflections can also be an important characteristic of containment performance. Deflections are important in containments because they may adversely affect the performance of components attached to the containment walls.

Over the past 20 years, Sandia National Laboratories has conducted overpressurization tests of a number of scale models of different types of containment vessels for the NRC and Japan's Nuclear Power Engineering Corporation (NUPEC). These have included tests on models of different types of steel containments, a reinforced concrete containment, and most recently, a prestressed concrete containment. These tests have provided valuable insights into the behavior of these different types of containment vessels under internal pressurization loads, and efforts have been made to incorporate the insights of those tests in the present work.

In the NUREG-1150 risk analyses, containment performance was characterized by three categories of failures: "Leak", "Rupture", and "Catastrophic Rupture". While the leak rate is in reality a continuous function of the internal pressure, these categories are used for computational convenience in the binning process used in these risk analyses. A leak is defined as "… an opening that would arrest a gradual containment pressure buildup but would not result in containment depressurization within 2 h." "… A rupture is an opening that would result in rapid (<2 h) containment depressurization." A catastrophic rupture "… would eliminate major portions of the containment structures". Based on these definitions, specific sizes of holes corresponding to the threshold leak rates for leak and rupture were given.

Figure 2.3 shows a hypothetical plot of the leak rate vs. pressure for a containment vessel. The solid line shows the leak rate for a containment in its original condition, and is based roughly on observations from the 1:4 scale prestressed concrete containment vessel (PCCV) model test conducted at Sandia (Hessheimer et. al., 2003). At the design pressure, the leak rate is equal to the design leak rate, and the leak rate steadily increases as the pressure is increased. Horizontal lines are shown to approximately show the leak rates corresponding to the "leak" and "rupture" criteria used in the NUREG-1150 analyses, and solid vertical lines show corresponding pressures for the containment in its original state. At a certain pressure, denoted by the solid vertical line with the label "Original Catastrophic Rupture", the structural capacity of the containment is reached. This is the limit state of the containment, and it should be emphasized that this is not related to a leak rate, unlike the "leak" and "rupture" pressures. The pressure shown here is what was observed in the "structural failure mode test" phase of the 1:4 scale PCCV model test.

In addition to the performance of the containment in its original state, Figure 2.3 also illustrates with dashed lines how degradation of the containment might affect its performance. Depending on the type of degradation, any or all of the three performance criteria used in the risk model may be altered. The performance of the degraded containment in this plot is purely hypothetical, and is simply used for illustrative purposes.

In the NUREG-1150 risk models, as well as in the current work, the pressures corresponding to the three failure modes mentioned above summarize containment performance. Random sampling is used to generate probability distributions of these failure pressures, as described in the previous section.

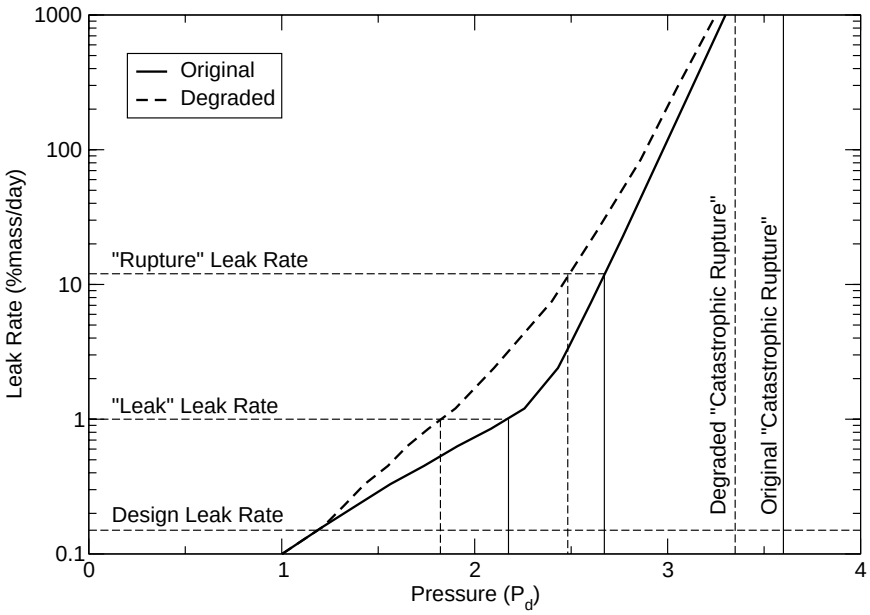

Figure 2.3: Hypothesized Effect of Degradation on Containment Performance

While the method for performance characterization presented here is relatively straightforward, devising appropriate criteria to evaluate structural analysis results and translate them into leak rates is quite complex. When a containment is designed, the allowable stresses prescribed by the design codes assure that the leakage will be less than the prescribed design leak rate during integrated leak rate tests. In severe accident scenarios when the containment is subjected to pressures significantly higher than the design pressure, translating structural response metrics such as strain and displacement in to leak rates can be quite difficult, and dependent on the containment design.

2.4 Containment Modeling

To determine the change in risk due to containment degradation, one of the most critical tasks is to develop structural models that will accurately predict the pressures at which the various performance limits required by the risk analysis model are met when the containment is in its original and degraded states. For most of the containments studied here, the performance limits are the “leak”, “rupture”, and “catastrophic rupture” failure modes mentioned in the previous section. For one of the plants studied here, a BWR with a Mark I steel containment, there are actually ten different performance limits of interest because the performance limits are defined not only in terms of the failure size, but also in terms of the location of the failure.

Tears in containment liners and shells initiate in regions of stress concentration, which can be caused by welds, local geometric details, or corrosion. Because the dimensions of these stress risers are generally orders of magnitude smaller than the overall dimensions of the containment, the structural modeling approach taken here is to use global finite element models of the containment structure to compute displacements and strains, which are used as boundary conditions for refined finite element models of local details in regions where stress concentrations are expected to occur.

All of the finite element models used in this study are run using the ABAQUS (HKS, 2002) general-purpose nonlinear finite element analysis program. Nonlinear constitutive models for

steel and concrete are used in an effort to model structural response into the nonlinear regime as realistically as possible using current commercially available technology.

Because steel and concrete containments exhibit fundamentally different behavior, the approaches used to model them differ somewhat. The basic principles used in this study for determining when the performance limits have been reached for steel and concrete (reinforced and prestressed) containments are outlined below. These basic guidelines are sometimes modified for analyses of specific containments. Such modifications will be outlined in the descriptions of the containment analyses for those plants in later chapters.

2.4.1 Steel Containments

2.4.1.1 Leak Criterion

For the steel containments considered in this study, it is assumed that the "leak" criterion is met when a tear initiates in the steel shell. At internal pressures below the level at which a tear first initiates, there is a small amount of leakage, but it is assumed to be below the level of the "leak" threshold as defined in the risk analysis.

Determining where the first tear is likely to occur is a difficult because of the large number of local details that can potentially have a stress rising effect. The approach taken here is to analyze submodels of a representative group of local details distributed throughout the containment. Engineering judgment is used to select details that appear to have the highest potential for early failure. It is of course possible that a detail more critical than those selected for analysis could exist in the containment. Because of the large number of details present in a containment, one has to accept the fact that resources are limited and that not every detail can be analyzed. The level of detail used in this study is believed to offer a reasonable balance between computational effort and desired accuracy given the available resources.

After the local models are run, their results are post-processed to determine the point at which tearing occurs. Tearing is assumed to occur when the effective plastic strain, $\varepsilon_{p,eff}$, reaches a limiting value. The baseline limiting value of $\varepsilon_{p,eff}$ is the plastic strain found from a uniaxial tension test, denoted as $\varepsilon_{f,uniaxial}$. Various conditions may be present that can cause a tear to initiate when $\varepsilon_{p,eff}$ is less than $\varepsilon_{f,uniaxial}$. An approach similar to that of Cherry and Smith (2001) is used to account for these conditions. The effective plastic strains from the analysis are multiplied by factors to account for the multiaxial stress state, the effect of corrosion on the failure strain, and the model sophistication, or gauge length:

$$\bar{\varepsilon}_p = f_m \, f_c \, f_{c-u} \, f_g \, f_{FEM-u} \, \varepsilon_{p,eff} \tag{2.1}$$

In this equation,

- f_m accounts for the effects of multiaxial stress state,
- f_c accounts for the presence of corrosion,
- f_{c-u} accounts for the uncertainty in f_c,
- f_g is a gauge length factor,
- f_{FEM-u} denotes a finite element modeling uncertainty factor,
- $\bar{\varepsilon}_p$ denotes the factored plastic strain, and
- $\varepsilon_{f,uniaxial}$ denotes the uniaxial tensile strength.

The factored plastic strain, $\bar{\varepsilon}_p$ accounts for all of these effects. Failure occurs when $\bar{\varepsilon}_p$ is greater than $\varepsilon_{f,uniaxial}$.

Whereas Cherry and Smith multiplied $\varepsilon_{f,uniaxial}$ by factors to reduce the failure strain due to these effects, the approach taken here is to multiply $\varepsilon_{p,eff}$ by equivalent factors to increase the plastic strain. This difference has no effect on the results. This slightly different approach was chosen for compatibility with strain magnification factors used to represent details in concrete containments, which are described in the next section.

The multiaxial stress state factor used in this study, denoted as f_m is that developed by Hancock and Mackenzie (1976):

$$f_m = \frac{1.0}{1.648\, e^{-(\sigma_1+\sigma_2+\sigma_3)/2\sigma_{vm}}} \tag{2.2}$$

Where σ_i are the principal stresses and σ_{vm} is the von Mises stress.

Cherry and Smith found from experiments that if a steel plate is thinned by corrosion, the corrosion can be reasonably represented in an analytical model by appropriately reducing the thickness of the plate. However, in the experiments, the failure strain in the corroded areas was about 50% of the failure strain of steel without corrosion. This is due to the fact that the corroded surface is uneven, and pits in the surface serve as local strain risers. Based on these observations, corrosion in the steel shell or liner is modeled by thinning an appropriate area and applying a corrosion factor, f_c of 2.0 to account for the effects of pitting. In order to further account for the uncertainty in the effect of corrosion on failure, f_{c-u} is introduced as a random parameter which is varied with the LHS method. The value of f_{c-u} follows a lognormal distribution with 1.0 as the median and 0.2 as the β factor. In all other areas of the model, f_c and f_{c-u} are set equal to 1.0.

The final adjustment factor is the analysis sophistication, or gauge length factor, denoted as f_g. The purpose of this factor is to account for the fact that strains tend to localize in areas of minor imperfections in the material. These localized strains can be much higher than the strains in the rest of the material a short distance from the localization area. Tang et al. (1995) used a gauge length factor of 4.0 in the derivation of strain magnification factors used to represent typical details in reinforced and prestressed concrete containments. As described in the next section, these magnification factors are used in the current work to simplify the analysis of the concrete containments studied here. Since gauge factor of 4.0 may be overly conservative for steel containments, a constant gauge length factor of 2.0 is used in this study for all detailed models of steel shells. In addition, f_{FEM-u} is included to reflect the uncertainty in the local strains produced by the finite element model. The value of f_{FEM-u} follows a lognormal distribution with 1.0 as the median and 0.30 and 0.35 as the β factors for 3D models and shell models, respectively.

A post-processing program was developed to automatically cycle through the integration points of all elements in a model and compute the value of $\bar{\varepsilon}_p$ based on the local stress and strain states. When $\bar{\varepsilon}_p$ exceeds $\varepsilon_{f,uniaxial}$, tearing occurs and thus, the "leak" performance limit has been reached.

2.4.1.2 Rupture and Catastrophic Rupture Criteria

While the criteria for initiation of tearing are fairly well accepted, determining when a tear reaches sufficient size to be considered a "rupture" or a "catastrophic rupture" is a more difficult problem. Once a tear has initiated, it will continue to grow if the stress state at the tip of the crack is sufficiently high. Otherwise, it will remain stationary. Determining whether the crack will grow or arrest itself is considerably complicated by the fact that crack growth is a function not only of the stress state at the crack tip, but also of the crack length.

In the current work, it is assumed that all cracks form in the regions of elevated stress that occur in discontinuity or corrosion regions. It is also assumed that if the stress is high enough to cause crack initiation in that region, it is also high enough to force the crack to propagate across the full length of the region of elevated stress. This length is conservatively taken to be equal to the dimension of the discontinuity feature.

As mentioned already, in the NUREG-1150 risk analyses, a "rupture" is defined as a hole large enough to depressurize the containment in less than about 2 hours. In that work, early analyses estimated the hole area corresponding to that depressurization rate to be about 0.167 m^2 (1.8 ft^2). In later analyses, the hole area was estimated to be from 0.028 m^2 (0.3 ft^2) to 0.046 m^2 (0.5 ft^2).

In developing a rupture criterion, it is important to have a basic understanding of the length of crack that will result in a leak area equal to the "rupture" hole area mentioned above. If a crack the length of a sufficiently large stress rising feature were to be under elevated tensile stress, but not sufficiently high to result in unstable crack growth, the resulting leak area could potentially be large enough for that crack to cross the "rupture" threshold, even though the crack does not experience unstable growth.

To address this issue, quarter symmetry finite element models were developed of plates containing stationary cracks of lengths varying from 1.02 m (40 in) to 5.08 m (200 in). Figure 2.4(a) shows a view of the un-deformed mesh of a plate with a 5.08 m (200 in) crack. The crack is actually 2.54 m (100 in) long, but by symmetry, it is equivalent to a crack twice its length. The overall length and width of the quarter symmetry panel are 25.4 m (1000 in). The panel is modeled using plane stress 2D elements with a thickness of 19.1 mm (0.75 in) and the material properties for A516 Gr. 70 steel, which is typical of that used in steel containments. The panel thickness actually has no effect on the computed opening area because of the 2D plane stress assumption.

The panels with shorter cracks use very similar meshes. The only difference is that the crack is shorter and the refined area around the crack is proportional to the crack length. Tensile stresses were applied in the far field in the direction perpendicular to the crack, and the analysis results were post-processed to compute the crack opening area at a given far-field stress for each of the crack lengths. Figure 2.4(b) shows a zoomed-in view of the deformed mesh at the point when the applied far-field stress is equal to the yield strength of the material.

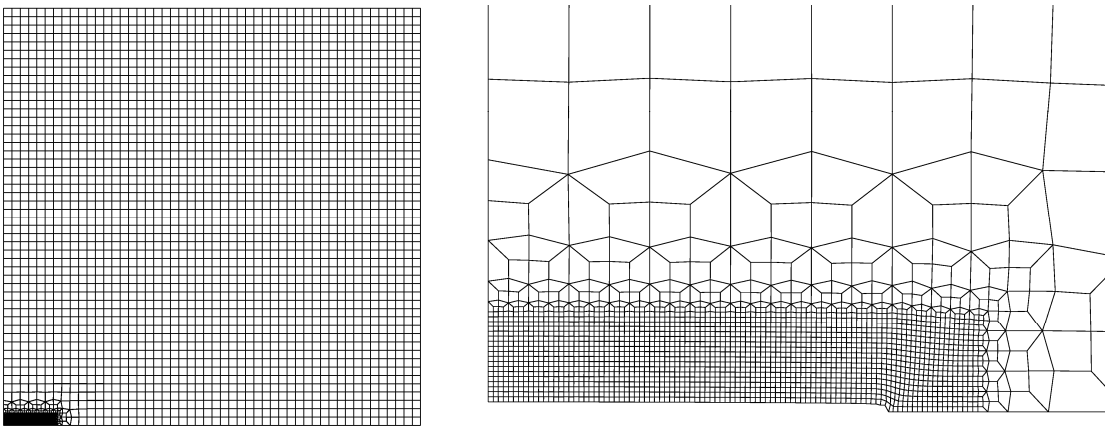

(a) Full view of original mesh

(b) Zoomed-in view of deformed mesh at yield (3x deformation magnification)

Figure 2.4: Finite Element Mesh of Plate with 5.08 m (200 in) Crack

Figure 2.5 shows a series of plots of the computed hole area vs. the applied far field tensile stress (given as the ratio of the applied stress, $\sigma_{applied}$ to the yield strength, σ_y). From these plots, it can be seen that the crack has to be quite long, and subjected to fairly significant stress to create a hole large enough to satisfy the "rupture" criterion. As mentioned previously, the hole size required to meet this criterion is not clearly defined, but even using the lowest estimate of 0.028 m^2 (0.3 ft^2), a 3.05 m (120 in) crack would be large enough to be considered a "rupture" only when the far-field stresses reach the yield stress. As will be demonstrated later, a crack of that size would go unstable at a stress level well below the yield stress. Therefore, in this study, a crack is considered to be a "rupture" only at the point when the applied far field stress is high enough to cause unstable growth.

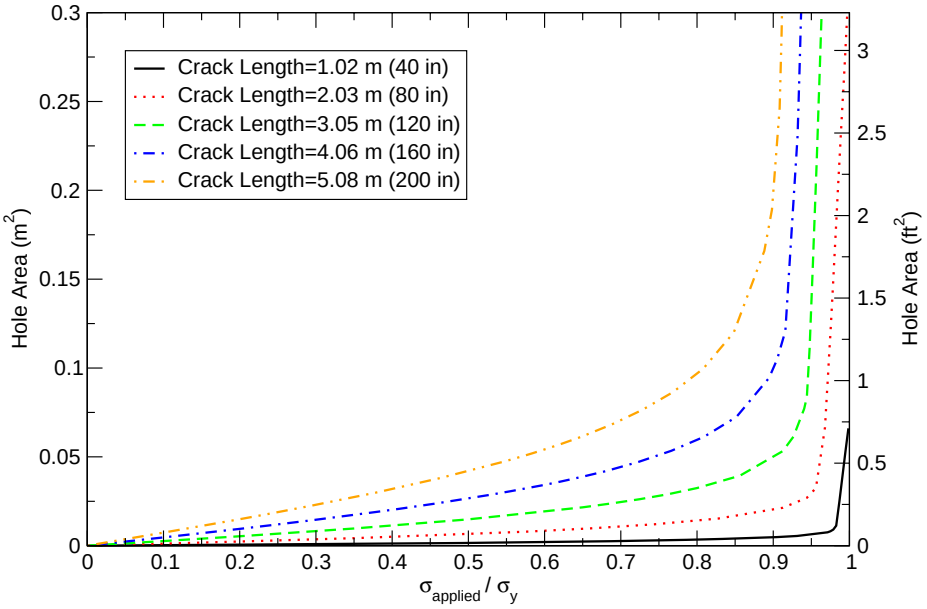

Figure 2.5: Hole Area vs. Applied Stress for Various Crack Lengths

As mentioned previously, cracks are conservatively assumed to propagate along the full length of the stress rising feature at which they formed. Principles of fracture mechanics are used to

determine the applied internal pressure at which the crack experiences unstable growth, and hence, makes the transition from "leak" to "rupture".

Because of the ductile nature of the steel used in containment vessels, the yielding zone ahead of a propagating crack is significant. Thus, it is more appropriate to use elastic-plastic fracture mechanics (EPFM) than linear elastic fracture mechanics (LEFM). The text of Anderson (1995) gives a good overview of this topic. In materials with high toughness, the traditional stress intensity factors used in LEFM fail to properly characterize the onset of unstable crack growth. The *J* integral has been found to be a useful indicator of stress intensity that can be used to predict unstable crack growth when significant yielding exists ahead of the crack tip. *J* is a measure of the energy release rate, and is computed by taking a line integral around an arbitrary contour around a crack tip. The value obtained by computing the *J* integral is independent of the contour line chosen for integration.

To apply EPFM to an engineering problem, it is necessary to obtain a family of plots of the *J* integral vs. the crack length. This can be done by performing a number of detailed finite elements analyses of specimens having cracks of various lengths. There are also a number of analytical equations in the literature. For the present work, it is reasonable to model the crack as a crack in an infinite plate. Shih and Hutchinson (1976) developed simple equations for *J* for a number of different geometries of cracks, including a crack in an infinitely wide plate for an arbitrary material whose stress-strain relationship can be described by the following Ramberg-Osgood power law:

$$\frac{\varepsilon}{\varepsilon_0} = \frac{\sigma}{\sigma_0} + \alpha\left(\frac{\sigma}{\sigma_0}\right)^n \tag{2.3}$$

In this equation, α and n are dimensionless parameters fitted to describe a particular material, and σ_0 and ε_0 are reference values of the stress and strain (typically chosen as the yield stress and strain). For the A516 Gr. 70 steel investigated in this study, values of α and n were fit to the stress-strain curves at a given temperature.

The equation given by Shih and Hutchinson for the plastic component of the *J* integral for a crack in an infinite sheet is given below:

$$J_{pl} = \alpha\sigma_0\varepsilon_0 a\left[3.85\sqrt{n}(1-1/n)+\pi/n\right]\left(\sigma^\infty/\sigma_0\right)^{n+1} \tag{2.4}$$

where a is half of the crack length, and σ^∞ is the far-field applied stress.

The elastic component is given by the common equation:

$$J_{el} = \left(\sigma^\infty\right)^2 \pi\ a_{eff}/E \tag{2.5}$$

where *E* is the elastic modulus and

$$a_{eff} = a + \frac{a}{1+\left(\frac{\sigma^\infty}{\sigma_0}\right)}\frac{1}{2}\left(\frac{n-1}{n+1}\right)\left(\frac{\sigma^\infty}{\sigma_0}\right) \tag{2.6}$$

for $a << W$ (*W* denotes half of the specimen or structure width).

The total *J* integral is simply:

$$J = J_{el} + J_{pl}\,. \tag{2.7}$$

In addition to the driving *J* caused by the load, it is also necessary to characterize the resistance of the material, denoted here as J_R. By performing a series of laboratory tests, it is possible to generate a plot of J_R vs. the crack length for a material. Figure 2.6 shows such a plot for A516 Gr. 70 steel based on data for quasi-static tests given by Papaspyropoulos et al. (1986). The specimen tested is relatively large, a 10T (25.4 cm (10 in) remaining ligament and initial crack length) compact tension specimen (C(T)) with a 2.54 cm thickness (1 in). This test was performed at 288 ^{o}C (550 ^{o}F). The 2.54 cm thickness is similar to the containment thicknesses examined here. While, the inplane dimension of 25.4 cm remains significantly smaller than the inplane dimensions. The resistance curve will obviously be affected by temperature, constraint conditions, local features, biaxial loading, etc.

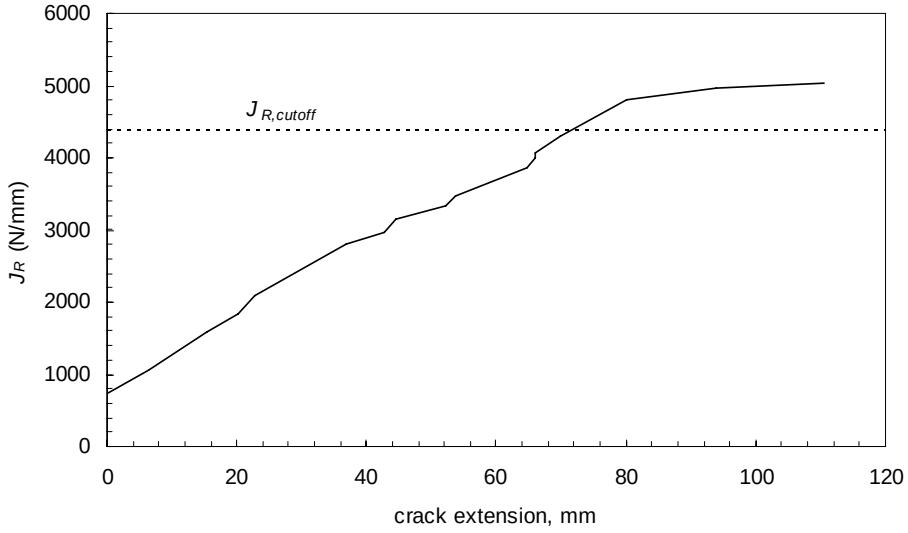

Figure 2.6: J_R Curve for A516 Gr. 70 Steel with Cutoff Used in Current Work

Unstable crack propagation occurs when the *J* curve is tangent to the J_R curve. The tearing modulus, proportional to the slope of the *J* curve, is useful in determining when this occurs. The tearing modulus is defined by:

$$T = \frac{E}{\sigma_0^2}\left(\frac{\mathrm{d}J}{\mathrm{d}a}\right) \tag{2.8}$$

where E is the elastic modulus of the material. The applied tearing modulus, associated with the to the applied *J*, is denoted here as T, while the modulus of tearing resistance is denoted as T_R, to correspond with J_R. Unstable crack growth occurs when $J \geq J_R$ and $T > T_R$. The procedure for determining the length at which a crack will grow unstably is shown graphically in Figure 2.7, as described in Sindelar et al. (2000) and Lam and Sindelar (2000). Instability will occur at the point when the plot of J vs. T intersects the plot of J_R vs. T_R. The critical crack length under a given far field stress is found from the *J* vs. crack length curve using the value of *J* at the instability point found from the intersection of the two curves.

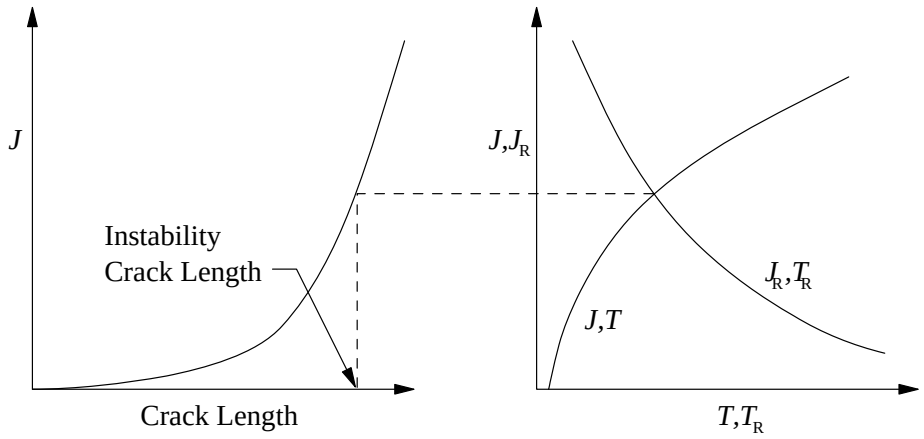

Figure 2.7: Methodology for Computing Critical Crack Length (Lam and Sindelar, 2000). Permission to use this copyrighted material is granted by the American Society of Mechanical Engineers.

One challenge encountered in applying this method is that the J_R curve is only available for relatively short crack lengths due to the size of the laboratory specimens. This curve would have to be extrapolated significantly to obtain values of J_R for crack lengths of interest in the present application. The approach taken here is that used by Lam and Sindelar (2000). A cutoff value of J_R is selected at the upper bounds of the experimentally observed values. The slope of the J_R curve remains nearly linear below 5000 N/mm and then decreases with further crack extension. For the current work, a slightly lower cutoff value of 4375 N/mm is used, as illustrated graphically in Figure 2.6. As mentioned previously, the resistance curve and applied *J* (Equation 2.7) will be strongly affected by the conditions specific to a given containment. The method presented above is used as a simple estimate for catastrophic rupture. For cracks assumed to have lengths within the range of the experiment (<25.4 cm), the Lam and Sindelar method is employed. For longer cracks, instability is conservatively assumed to occur when *J* (applied) exceeds $J_{R,cutoff}$. The applied *J* is calculated with interpolated values of α, *n*, σ_0, and ε_0 at a given temperature (the elastic modulus, *E*, is assumed to remain constant with temperature). A value for the crack length, *a*, is also assumed for specific locations of concern within the discussion for each analyzed containment.

The stress raising features, and hence, the assumed crack lengths are all larger than the crack lengths tested experimentally. Therefore, this study always computes unstable fracture based on $J_{R,cutoff}$. Figure 2.8 shows an example plot of the far field tensile stress at the stability limit vs. crack length ($2a$) for A516 Gr. 70 steel. The material properties, and therefore the curve in Figure 2.8, vary with temperature. This example uses constant values of $\alpha = 5.1$, $n = 5.2$, $\sigma_0 = 402.3$ MPa, and $E = 200$ GPa. Once a tear, and hence, a "leak" is found to occur using the procedures outlined in the previous section, this curve is used to check for unstable crack growth.

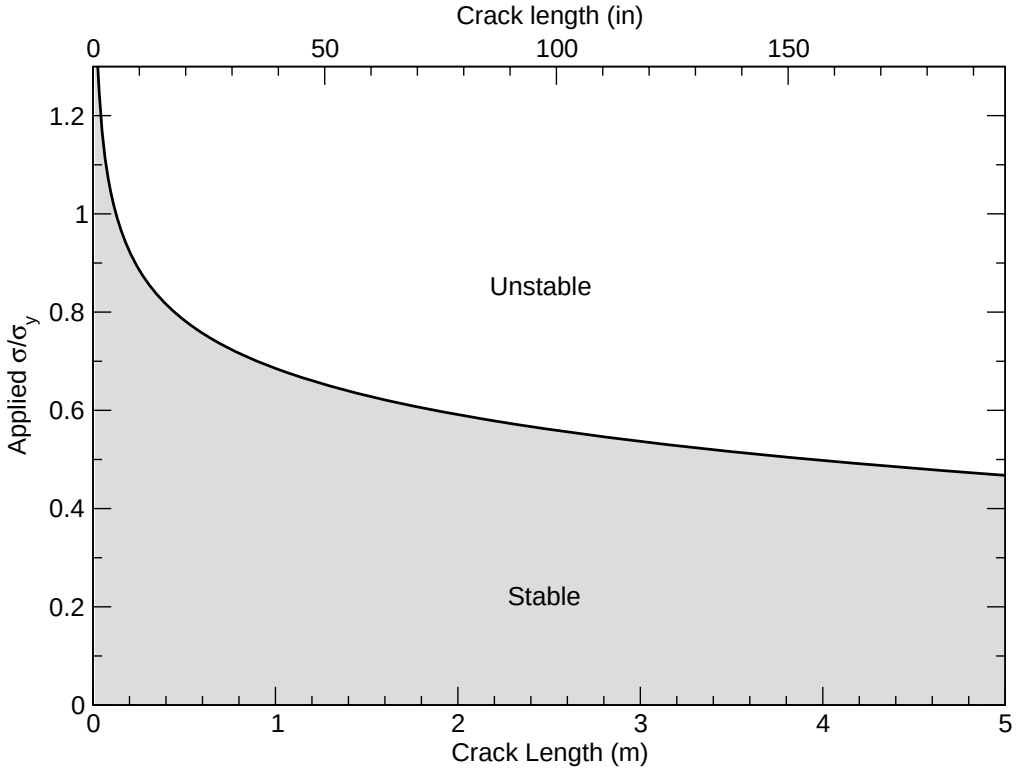

Figure 2.8: Stability Limit for Applied Far-Field Stress vs. Crack Length for A516 Gr. 70 Steel

In most cases, it is assumed that if unstable crack growth occurs in a steel containment, the crack quickly grows large enough that it can be considered a "catastrophic rupture", completely skipping the "rupture" mode. The exception to this is that when the containment would come in contact with a shield building, the presence of that building is assumed to prevent the crack from causing a failure that could be considered "catastrophic rupture". This is consistent with the observations made in the 1:6 scale test of a steel containment vessel model conducted at Sandia (Luk et al., 2000).

2.4.2 Reinforced and Prestressed Concrete Containments

2.4.2.1 Leak Criterion

In reinforced and prestressed concrete containments, it is assumed that the "leak" criterion is met when tearing occurs in the steel liner, just as was assumed for steel containment shells. The same tearing criterion used for the steel containments is applied to these liners. The modeling process is complicated somewhat by the presence of studs and anchors, but the theory is the same.

One could construct detailed models of typical discontinuities in concrete containments to check for tearing at stress risers just as is done for steel containments in this study. This step was not necessary, however, because the results of analytical models and experiments on such details have been applied in a study reported by Tang et al. (1995). In this study, which is reported in more detail in Castro et al. (1993), strain magnification factors were developed to approximate the effects of discontinuities typical of those found in the liners of reinforced and prestressed concrete containments.

Four locations have been identified as being critical for tearing: at large steam penetrations, at the junction of the wall and the basemat, at personnel or equipment hatches, and at the springline. Detailed finite element models, and in some cases, experimental models, were developed to find the level of strain concentration at those locations. From these models, a set of strain magnification factors were developed to compute the plastic strain in a discontinuity region from the global strain, which is found from an axisymmetric model of the whole containment. For the steam penetration and hatch locations, the global strain quantity is the hoop strain, whereas for the wall-basemat junction and springline, the meridional strain in the wall is used as the global strain quantity. For the reinforced and prestressed containments, Figure 2.9 and Figure 2.10 show plots of these four magnification factors as functions of the normalized global strain. The normalized global strain is simply the appropriate global strain quantity divided by the yield strain of the liner material.

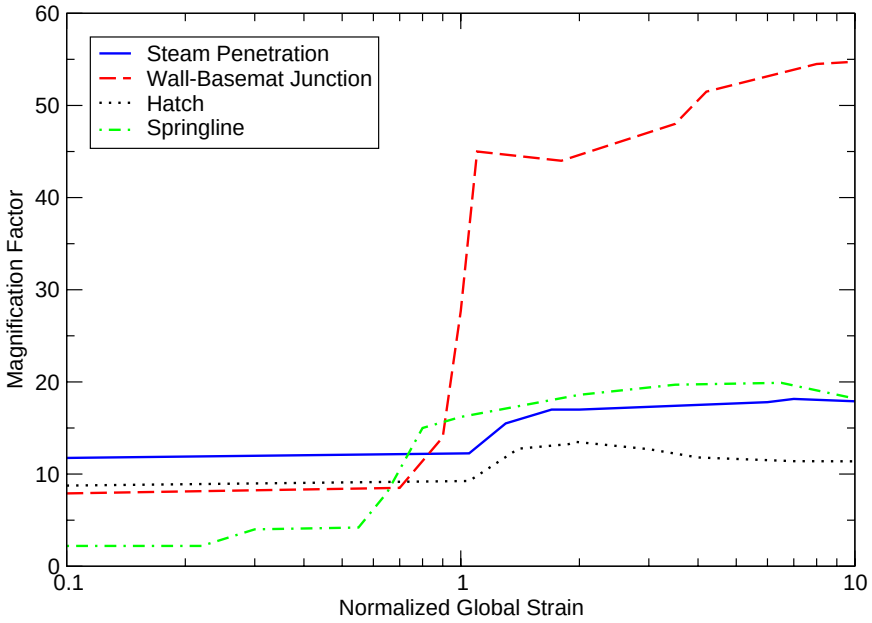

Figure 2.9: Strain Magnification Factors for Typical Discontinuities in RC Containments (Tang et al., 1995). Permission to use this copyrighted material is granted by Elsevier.

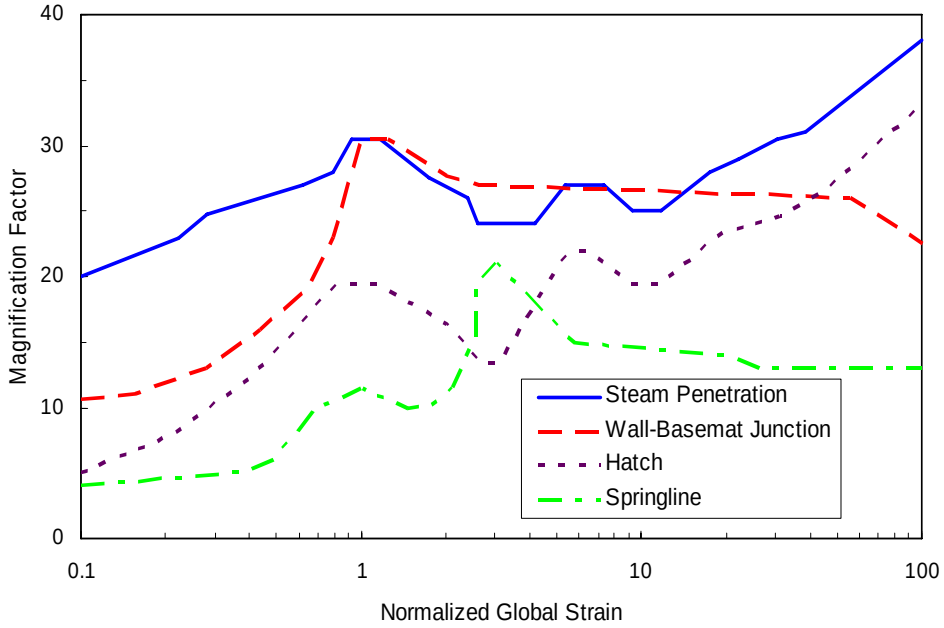

Figure 2.10: Strain Magnification Factors for Typical Discontinuities in Prestressed Containments (Tang et al., 1995). Permission to use this copyrighted material is granted by Elsevier.

These strain magnification factors account for the effects of multiaxial stress states, and also include a "gauge length" factor of 4.0 to account for the fact that when strains begin to localize, the actual strains at the tear location are much higher than those observed in strain gauges in experiments or in finite element models. This is analogous to the "analysis sophistication" factor used by Cherry and Smith (2000), although the factor is considerably higher.

To use the strain magnification factors to check for failure, one first computes the global strain, ε_g, at the specific discontinuity location within an axisymmetric model. This is normalized, and the magnification factor, *M*, is found from the appropriate curve in Figure 2.9. The localized plastic strain, $\bar{\varepsilon}_p$, is then simply computed as:

$$\bar{\varepsilon}_p = M \quad f_{FEM-u} \quad \varepsilon_g \tag{2.9}$$

where f_{FEM-u} denotes a finite element modeling uncertainty factor. If $\bar{\varepsilon}_p$ is greater than the uniaxial plastic failure strain of the liner material, ε_{fail}, a tear has initiated and a leak has formed. Equation 2.9 assumes no corrosion exists at these locations. Corrosion is introduced in analyses of detailed liner submodels which adopt the same leakage criterion (Equation 2.1) as for the steel containments.

2.4.2.2 Rupture Criterion

As mentioned previously, the hole size in the steel liner required to meet the rupture criterion is not clearly defined, often estimated between 0.028 m^2 (0.3 ft^2) and 0.093 m^2 (1.0 ft^2). Here we define rupture using the more conservative value of 0.028 m^2 (0.3 ft^2). Since the analyses performed here do not explicitly model the actual crack (leak) initiation and growth, an

approximate method must be employed to estimate the hole size. The method developed by Dameron et al. (1995) is used here for that purpose. Given a location and orientation (meridional or hoop) of an assumed crack within a model, a crack width is calculated by

$$w = \varepsilon_g \; s \tag{2.10}$$

where ε_g denotes the global strain and *s* equals the span or spacing between anchorages or stud layers perpendicular to the liner crack. The area of the opening can be estimated by multiplying the crack width by an assumed crack length, *a*.

$$A = w \; a \tag{2.11}$$

The length of the crack can be estimated as the region of uniform peak strains or stresses, the size of local features, or the spacing of anchorages of studs in the direction of the crack. Equation 2.11 leads to a conservative estimate of the opening area since the opening is assumed square. Alternate estimates of the crack area can be constructed, but Equation 2.11 is assumed sufficient due to the large number of approximations employed here.

Since Equation 2.11 estimates the area for only one crack, the total open area at a given load step (or pressure) is computed by

$$A_{total} = f_{rupt-u}\left(A_1\delta_1 n_1 + A_2\delta_2 n_2 + ...\right) \tag{2.12}$$

where the subscripts 1 and 2 are associated with different locations within the model where cracks are assumed to have a possibility of initiating.

- A_i denotes the crack area for one crack at location *i*,
- δ_i equals 1 if the leakage criterion has been obtained at location *i* and equals 0 if no leak has initiated,
- n_i denotes the number of cracks assumed to exist and initiate at location *i*, and
- f_{rupt-u} accounts for the uncertainty in the total area.

The variable, δ_i, enforces the requirement that a leak must initiate prior to a specific location contributing to the total open area. The crack number variable, n_i, enables the inclusion of the effects of multiple cracks initiating near the same location. Based on Equation 2.12, rupture occurs at a given pressure when the total area, A_{total}, equals 0.028 m^2 (0.3 ft^2). If at a given pressure the rupture criterion is not reached, the pressure at the next load step is examined. Due to the increase in global strain, the area will increase in size for locations which previously contributed to the total rupture area. The leak criterion may also be obtained at additional locations, which would then also contribute to the total area.

2.4.2.3 Catastrophic Rupture Criterion

A simple method is used to estimate the onset of catastrophic rupture. By assuming a cylinder with contributions only from the rebar, liner, and tendons for the prestressed containment, the pressure to cause catastrophic rupture is computed with

$$P_{cat-rupt} = f_{cat-u}(0.9)\left(\frac{\sigma_{rebar-ult}\; A_{rebar}}{R\; s_{rebar}} + \frac{\sigma_{liner-ult}\; t_{liner}}{R} + \frac{\sigma_{tendon-ult}\; A_{tendon}}{R\; s_{tendon}}\right) \tag{2.13}$$

where

- $\sigma_{rebar-ult}$, $\sigma_{liner-ult}$, and $\sigma_{tendon-ult}$ denote the ultimate strength for the rebar, liner, and tendons,
- A_{rebar} and A_{tendon} are the area of the rebars and tendons

- s_{rebar} and s_{tendon} denote the spacing of the rebars and tendons,
- t_{liner} is the thickness of the liner,
- R equals the radius of the containment, and
- f_{cat-u} accounts for the uncertainty in the catastrophic rupture pressure.

In addition, Equation 2.13 includes a reduction factor of 0.9. This factor reflects overestimation of the simple method observed in the analysis and testing of a 1:4-scale prestressed containment. The 1:4-scale prestressed containment tested at Sandia National Laboratories (Hessheimer et al., 2003) failed at 1.42 MPa, while the simple ultimate strength estimated failure at 1.54 MPa (Dameron et al., 2000). The ratio of 1.42 MPa to 1.54 MPa is reduced slightly to 0.9.

2.5 Procedure for Risk-Informed Containment Analysis

In this study, risk models that have been developed for previous analyses are being adapted to study the effect of containment degradation on the risk. During an accident scenario, there are many potential modes in which the integrity of the containment vessel can be breached. The containment may be subject to excessive pressures and temperatures, direct contact with core material, and debris generated from internal explosions. The containment system may also fail to perform its function in a bypass mode due to a hatch being left open during an accident. This listing is not inclusive of all of the potential modes in which a containment can fail to perform its primary function. For the purposes of this study, it is assumed that the degradation only affects the capacity of the containment under over-pressurization. The probabilities associated with all of the other containment failure modes investigated in the previous studies are assumed to remain the same.

The structural fragility serves as the interface between the structural analysis model and the risk model of the systems. Traditionally, a structural analysis results in a deterministic estimate of a structure's capacity under a given loading. In a risk-informed analysis, a probabilistic distribution of the structural capacity is required in place of the traditional deterministic estimate of that capacity. A fragility curve is a cumulative probability distribution of a structure's capacity to resist a given load.

Contributors to the uncertainty of the structural capacity can be grouped into two main categories: inherent randomness in the components that make up the system, and uncertainty in the analyst's ability to characterize the behavior of the system. These are often referred to as aleatory uncertainty and epistemic uncertainty, respectively (Ellingwood and Cherry, 1999).

There are several ways that an analyst can approximate the probability distribution function for the strength of a structure. A basic method is to estimate the mean capacity of the structure using traditional analysis methods, and then make assumptions about the overall aleatory and epistemic uncertainty inherent in the system. An appropriate probability distribution function (typically log-normal for structures) is chosen and used in conjunction with the analytical mean strength and assumed uncertainty to describe the uncertainty in the system. While fairly simplistic, this is a reasonable method, and has been used to describe the containment fragility in many of the risk assessments of nuclear power plants submitted as part of the Individual Plant Evaluation (IPE) program.

A more rigorous method to determine the structural fragility is to consider the probability distributions of the individual components that make up the structure. Structural analysis models are typically far too complex to incorporate the probability distributions of the components in a

closed form manner. Instead a large number of samples of the individual random variables that describe the components of the system can be generated. The structural analysis is performed for each set of samples, and a fragility curve can be developed from the distribution of the outcomes of all of the structural analyses. This method is known as Monte Carlo simulation.

For complicated structural systems, the time required to analyze the system with a single set of parameters can be significant. Classical Monte Carlo simulation requires a large number of samples to give reasonable results. The Latin Hypercube Simulation (LHS) technique (McKay et al, 1979) reduces the number of samples required to a much more reasonable number by dividing the sample space of each variable into a limited number of equiprobable strata. Instead of generating a purely random variable for each sample, in this technique, the stratum for each variable is randomly selected, and a value for that variable that falls within the selected stratum is used for the analysis.

The LHS technique is used in this study to generate the structural fragility curves because it offers the ability to explicitly account for the probabilities of the individual components in a structural system with a reasonable amount of computational effort. The DAKOTA (Eldred et al, 2001) uncertainty analysis software was used to generate the LHS samples for the structural analyses in this study.

The risk analyses of the plants are essentially sensitivity studies of the effect of structural degradation on the overall risk. With the exception of the fragilities for containment overpressurization, the risk models are the same as those used for the NUREG-1150 study (USNRC, 1990). To ensure that the fragilities of the containments in their original and degraded states are consistent with each other, new fragilities of the containments in their original state have been developed and replace the containment fragilities used in the NUREG-1150 analyses.

2.5.1 Computation of Overall and Conditional Probabilities from Analysis Results

The NUREG-1150 risk analysis models require two inputs to describe the performance of the containment vessel. The first of these is an overall fragility curve, which describes the cumulative probability of failure as a function of the internal pressure. In addition to this, probabilities of failure in the various possible modes given that failure has occurred must be provided. These are also functions of the failure pressure. The determination of which modes are needed from the containment analysis is based on the effects that various modes of failure may have on the outcome of an accident progression. In the simplest plant risk models, the number of failure modes can be quite small. In some cases, the risk model only requires that the conditional probabilities of leak, rupture, and catastrophic rupture be provided. In the more complex models, the conditional probabilities must be specialized to provide probabilities of leak, rupture, and catastrophic rupture at a number of different locations. The procedure used to develop overall and conditional probability distributions for the failure modes needed by the risk model will be described in this section.

The LHS procedure mentioned above is used to generate 30 sets of random parameters to be used as input into the analytical models of the containment. For each containment, a number of different locations where failure could potentially occur are modeled. The results of these models of local details are compared against failure criteria to determine the pressure at which failure would occur at a given detail. Ideally, for each of the sample sets, the analysis procedure would

produce a failure pressure for each detail. However, in some cases, the local details under consideration are not very likely to fail at low pressure, and as a result, the failure criterion is not met before the analysis is completed. At high pressures, the containment models typically experience very large deformations in some areas, making it very difficult to advance the solution to higher pressures. Because of this, it is often simply not practical to advance the solution to reach a pressure at which every monitored detail would fail.

A fragility curve describing the cumulative probability of failure vs. pressure for a given failure location can be produced by sorting the analytical failure pressures in ascending order. If there are n LHS sample sets, the lowest failure pressure is assigned a cumulative probability of $1/(n+2)$, the next highest is assigned a probability of $1/(n+2)+1/n$, and so forth. Due to the large amount of time required to run one set of analyses, it is impractical to run a large number of samples. The lowest probability for which a failure pressure is available is $1/(n+2)$. Lognormal distributions are fitted to the results to provide extrapolated information in the tail regions that would otherwise be unavailable.

If failure pressures are obtained at a location for all of the sample sets, the parameters of the lognormal distribution to fit the data are found in the standard manner based on the mean and variance of the data. If failure does not occur at a given location because of an early termination of the analysis, which might occur for the reason described above, an alternative procedure is used. First, an attempt is made to obtain more failure pressure data points by linearly extrapolating the results from the last two time steps of the analysis. If a location is already relatively close to the point of failure at the end of the analysis, this can be reasonably accurate. Extrapolated pressures are only used if they are less than 15% higher than the pressure in the last analysis step. Due to the nonlinear nature of the structural behavior, it is not reasonable to extrapolate beyond that amount.

If the set of results is still incomplete after extrapolation, the available data is sorted and a probability is assigned to each available failure pressure starting with the lowest pressure as described previously. It is assumed that all cases that did not fail have failure pressures above the highest actual recorded pressure. A nonlinear least squares procedure is used to fit a lognormal cumulative distribution function to the available data.

After the parameters of fitted distributions are estimated from the raw data for all of the failure locations, the process of developing an overall fragility curve from these is fairly straightforward. Using de Morgan's rule (Ang and Tang, 1975), the probability of occurrence of any one of a number of statistically independent events E_n can be computed as:

$$P(E_1 \cup E_2 \cup ... \cup E_n) = 1-(1-P(E_1))(1-P(E_2))...(1-P(E_n)) \tag{2.1}$$

Failure in containments typically occurs at stress concentrations around penetrations, and the various penetrations in a containment can reasonably be assumed to be statistically independent. The penetrations modeled are just a sample of what may be a large number of very similar penetrations. For an arbitrary number of penetrations similar to the ones being modeled, at a given pressure, the overall probability of failure $P(F)$ can be computed from the cumulative failure probabilities of the locations investigated by

$$P(F) = 1-(1-P(F_1))^{m_1}(1-P(E_2))^{m_2}...(1-P(E_n))^{m_n} \tag{2.2}$$

where $P(F_i)$ is the cumulative probability of failure at location i at a given pressure, and m_i is the number of penetrations having similar characteristics and loading as that at location i. Because the overall fragility is the cumulative distribution of the probability of a failure of any size, and a larger size of failure at a location can only occur after the smallest size of failure at that location

can occur, the distribution function for the smallest failure mode at every location is used in this calculation.

Computing the conditional probabilities of failure for the modes used in the risk analysis is less straightforward. Because the various locations where failure could occur are statistically independent, there is a potential that failure could occur at more than one location simultaneously. In the event trees used in the risk model, it is assumed that failure cannot occur in more than one mode simultaneously. The failure modes needed by the risk model are defined in terms of failure sizes and locations. The locations generally cover a large area of a containment, and failure may occur at any number of locations within the location grouping defined by the risk model.

The first step is to compute the conditional probabilities of failure of the three sizes (leak, rupture, and catastrophic rupture) at each of the location groupings and at each pressure increment for which output will be given. This is done using Equation 2.2 for the leak, rupture, and catastrophic rupture distribution functions for every considered detail located within the grouping. This provides distributions for the pressures at which a leak, rupture, or catastrophic rupture will occur at each grouping.

A leak is a breach that is smaller than the rupture size. A rupture is bigger than the rupture size, but smaller than the catastrophic rupture size. The conditional probability of leak is obtained by subtracting the rupture probability from the leak probability and dividing by the leak probability. Likewise, the rupture conditional probability is obtained by subtracting the catastrophic rupture probability from the rupture probability and dividing by the leak probability. The catastrophic rupture conditional probability is computed by dividing the catastrophic rupture probability by the leak probability.

Once the overall probability distributions for each of the location groupings and the conditional probabilities for the various sizes of failure in each of those groupings are formed, a Monte Carlo sampling method is used to determine conditional probabilities of failure for all of the groupings and sizes of failure within those groupings. A large number of sets of random numbers are generated. For each grouping, two random numbers are generated: one conforms to the overall failure probability distribution for that location, and the second is a uniformly distributed random number in the range from 0 to 1. The second number is used in conjunction with the conditional distributions of failure size at that location to determine the failure size at a given pressure.

For each set of randomly generated samples, an algorithm is used to determine at every output pressure interval whether the containment fails, and the grouping and size of failure if failure does occur. The algorithm starts at a low pressure and incrementally increases the pressure. Once the pressure is higher than at least one of the randomly sampled overall failure pressures for the various groupings, the containment is assumed to have failed at the grouping with the lowest sampled pressure. That location grouping is assumed to be controlling unless another grouping has a failure of a larger size than the failure at that grouping. In this manner, a dominant failure location and size is determined for every pressure interval for each of the samples. The sum of the number of failures at each pressure interval is taken over every sample and divided by the total number of samples to determine the conditional probability of failure of each of the modes. The assumption that the first location to experience a failure of a given size overrides all others of that size allows for conditional probabilities that conform to the requirement that failure can only occur in one mode at a time.

2.5.2 Risk Assessment of Plant with Degraded Containment

For the examination of potential risk increases caused by containment corrosion, the risk assessment models developed for actual steel and concrete containments in the NUREG-1150 (USNRC, 1990) study are used. The models are documented in both NUREG-1150 and in detail in NUREG/CR-4551. It is very important to emphasize that the analysis performed here, although based on an actual plants, is intended to be generic and not representative of actual conditions at that plants. The models used date from the late 1980s, and the plants have changed since then. Also, as mentioned previously, the corrosion assumed to exist in the containment is purely hypothetical, and does not represent corrosion actually observed in any particular containment. The analyses presented here are a "proof of concept." That is, it is an example of how such an analysis could be done and, if corrosion existed, how the risk of a plant that had containment corrosion might be affected.

For the NUREG-1150 study, the containments at the plants under investigation had no corrosion, and experts from the government, academia, and industry estimated their failure pressure. Several different failure types were believed possible, from bypasses to small leaks to larger containment ruptures. As discussed previously, a rupture is differentiated from a leak by the fact that it is large enough to depressurize the containment atmosphere after failure. Anything smaller is simply referred to as a leak.

The risk measures used for this analysis are the frequency of large early releases of radioactive material and the probability of a large early containment failure, given core damage.

2.5.3 Approach

As noted, the NUREG-1150 risk analysis models are used as a starting point. A brief discussion of the treatment of the uncertainties in those models is warranted. The risk analysis done for this plant in NUREG-1150 addressed uncertainties throughout the risk calculations. It used a stratified Latin Hypercube sampling (LHS) routine for efficient representation of the uncertainties. These uncertainties existed in all the individual portions of the risk analysis—the Level I core damage frequency estimation, the Level II accident progression and source term evolution calculations, and the Level III public consequence determination.

A total of around 100 parameters (the actual number varies by the plant) were included as having uncertain values in the analysis, and their distributions were sampled in a sample size of 200 using LHS. These parameters represent more than the containment failure pressure. They include component failure data, in-vessel phenomena, and containment loading physics. For each sample member, each parameter value is a discrete number, and for each set of such discrete numbers (with the thousands, or tens of thousands, of other discrete numbers in the models, those that were not varied for the uncertainty analysis), the entire risk analysis was run, including all core damage sequences, all possible paths through the accident progression event tree (there are millions), and, if the particular analysis required it, all source term releases and health consequences (the latter two are not needed for this application). Hence, each of the two hundred runs can be viewed as a separate, complete, defensible answer of the risk of the plant, including LERF.

The approach in this study is to perform calculations with the PRA model developed in the NUREG-1150 study but to substitute the containment fragilities developed in the current study for those used in the original study. These calculations are carried through the Level 2 portion of the overall risk assessment. As discussed in detail in following sections, a model of an un-degraded containment is developed for this study, and that model is then modified to reflect

various possible corrosion conditions. The results of each of these containment models are analyzed using the Level 2 NUREG-1150 PRA models. Furthermore, as the fragility analysis described above is performed using *two* different uncertainty parameters, representing the "best estimate" and the "lower bound" cases.

Since the un-degraded models developed here might produce results not exactly equivalent to those of the NUREG-1150 experts, a new fragility model for the containment in its original condition is needed so that the model can be modified directly to represent possible corrosion. If the risk analysis results from the NUREG-1150 were to be used for the un-degraded case and compared to a model incorporating corrosion, it would not be clear whether the differences were due to the effects of corrosion, or due to differences in structural models.

Because CDF, LERF and containment failure probability conditional on core damage are the risk metrics desired in this study, there is no need to carry forward the calculations past the Level 2 risk assessment into radioactive dose estimates. Furthermore, the issue of containment corrosion and its effect on containment failure pressure does not impact the evolution of core damage accident sequences at these plants. Thus, the analysis of the core damage sequences and their frequencies was not changed in this study.

The ARRAMIS suite of computer codes was used to address the problem in the current study. This is simply a driver code that allows one to work with a suite of PRA codes interactively on personal computers. Except for changes noted below, the accident progression event tree (APET), post-event processing, and Latin hypercube sampling were all the same for this analysis as they were for NUREG-1150. While the codes and models were readily accessible, getting them to run properly took some effort as computer operating systems have significantly changed since the last time the codes and models were exercised.

For example, a thorough summary of the risk analysis process can be found in Breeding et. al. (1990) for the Surry containment. As a very brief introduction to the PRA process, specifically concerning an APET, p. S.2 and S.4 of that document are quoted:

> The accident progression analysis uses large, complex event trees to determine the possible ways in which an accident might evolve from each PDS [plant damage state—groups of core damage sequences]. The definition of each PDS provides enough information to define the initial conditions for the accident progression event tree (APET) analysis. Past observations, experimental data, mechanistic code calculations, and expert judgment were used in the development of the model for accident progression that is embodied in the APET and in the selection of the branch probabilities and parameter values used in the APET. Due to the large number of questions in the Surry APET and the fact that many of these questions have more than two outcomes, there are far too many paths through the APET to permit their individual consideration in subsequent source term and consequence analysis. Therefore, the paths through the trees are grouped into accident progression bins (APBs), where each bin is a group of paths through the event tree that define a similar set of conditions for source term analysis.

For this application, the APET APB output was re-grouped into different bins. The primary interest in the current study is large early containment failures. Hence, the output was re-binned so that all APBs with the characteristic of large early containment failures would be grouped together.

For both the best estimate and lower bound sets of fragility curves, the entire analysis was run for the original (no corrosion) model and various corrosion cases. For all of these cases, the datum representing the containment failure pressure was replaced with a failure pressure derived from the new fragility model for each of the 200 sample members. These new failure pressures were computed so that they would have the same failure probability as the original sample member. That is, if the *nth* sample member of the 200 sample members drawn for the NUREG-1150 analysis called for the 63^{rd} percentile failure pressure, the 63^{rd} percentile from the new curve was used in the *nth* sample member. In this way, a new sample did not have to be drawn, which would have necessitated re-running the entire analysis. Instead, most of the old computations could be used without introducing spurious correlations.

2.5.4 Un-Damaged Case Analysis

For all of the analyses, the event tree question needing changing is, "What is the containment failure pressure?" As stated above, this was changed for each analysis by taking the appropriate percentile response from the fragility curve of the case being examined. The results then needed to be re-binned to automate the computation of the risk measures.

Except for the change to the fragility curve, everything in the original case analysis was the same as that for the NUREG-1150 analysis. The only reason that a new fragility curve was computed was so that, when it was perturbed to represent different corrosion possibilities, comparisons between it and the perturbations would be straightforward and not potentially confused with differences in models.

2.5.5 Corroded Case Analysis

Each corroded case was analyzed separately to determine their effects on the risk. From the containment fragility curves generated for these situations, failure pressures were identified for each of the percentiles needed for the sample members. For each corrosion case, these pressures were substituted for the original pressures in the LHS input files. Then, the entire ARRAMIS analysis was re-run to ascertain the risk from the revised input.

As mentioned above, the uncertainty in the fragility curves was treated in two different ways, the best estimate and the lower bound. Therefore, the analysis of "original case and several sensitivity cases" was each actually run twice, once for each uncertainty output set of fragility curves.

Because the issue of corrosion, and more broadly, the issue of containment failure pressure, does not affect the core damage frequency for the plants examined here, there was no need to re-visit, revise, and then re-run the Level 1 PRA results. *For applications to other types of plants, this likely will not be the situation*. Hence, for other applications, more plant analysis and analysis changes will be necessary to examine the corrosion issue.

2.5.6 Risk Analysis Summary

In this study, the process of performing an integrated risk-informed analysis will be demonstrated for several containment types. The effect of different hypothetical areas of corrosion on the risk of operating the plant will be investigated. Corrosion is introduced into the model by thinning an area of the steel shell or liner plate. In addition to thinning the plate, corrosion is assumed to have reduced the strain at which tearing would occur.

Latin hypercube sampling is used to generate a series of 30 sets of input parameters for the structural analysis models for each containment. The analyses are run for each of these 30 cases, and the failure pressures obtained from these analyses were sorted to obtain fragility curves.

Fragility curves are generated for the containment in its un-degraded state, and for each case of corrosion. These fragility curves were used as input to a risk model of the plant, and estimates of the core damage frequency and large early release frequency are found.

3. Risk Analysis of PWR Plant with Reinforced Concrete Containment

A typical pressurized water reactor (PWR) nuclear power plant was chosen as the subject for a risk-informed investigation of liner corrosion in a reinforced concrete (RC) containment vessel. The effects of corrosion in the liner wall was investigated near the wall-basemat juncture and at the mid-height of the containment. Figure 3.1 shows these two corrosion locations on a schematic diagram of the containment building, along with potential paths for leakage from the interior to the exterior.

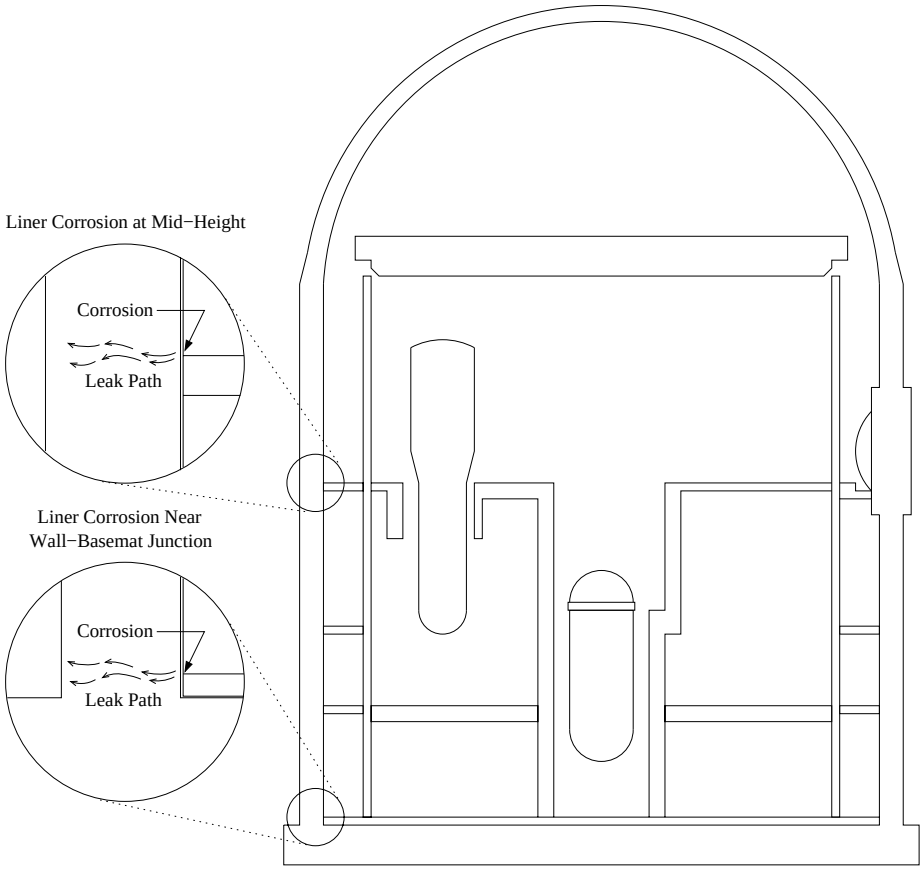

Figure 3.1: Postulated Corrosion in Liner of RC Containment

These locations were chosen both because they are regions of potentially high liner strains and because water could potentially accumulate at those points, accelerating corrosion. There is a 61 cm (2 ft) thick non-structural concrete slab cast on top of the containment liner at the basemat. Water could potentially leak through the seal between the side of that slab and the wall liner, causing corrosion. At the containment mid-height, moisture could also accumulate on the liner where a floor abuts the wall. It should be re-emphasized that although the dimensions and other

properties of the containment vessel were taken from the drawings of an actual plant, the corrosion assumed for this study is not representative of actual corrosion observed at that plant.

3.1 Structural Model of Reinforced Concrete Containment

Experimental evidence from a pressurization test of a 1:6 scale RC containment vessel with a steel liner (Horschel, 1988) indicates that this type of containment tends to fail by leakage due to tearing in the liner at geometric discontinuities. In the 1:6 scale test, the containment exhibited essentially elastic behavior and very little leakage up to an internal pressure of around 827 KPa (120 psi). At that point, the containment began to experience global yielding of the reinforcing, especially in the hoop direction in the mid-height region. As the pressure was increased to a final level of 1.0 MPa (145 psi), the strains in the reinforcement, especially in the hoop direction at the mid-height, increased dramatically as the reinforcing steel began to yield. The final hoop strains at the mid-height were between 1% and 2.5%

The leakage rate remained very low through most of the test as the internal pressure increased, but began to increase rapidly at about 965 KPa (140 psi). The test had to be terminated at 1.0 MPa (145 psi) because the leak rate was too high to allow further pressurization. After the test, several tears were found near discontinuities in the liner thickness around penetrations. The concrete in the regions of those tears was essentially intact, but was fractured enough to allow the gas to penetrate it.

Based on this experimental evidence, in this study it is assumed that a linear tear results in failure of the containment. Because the liner serves primarily as a pressure-resisting boundary, and acts relatively independently of the RC shell, which provides the structural strength, the liner can have a significant tear without leading to a large rupture of the containment. This agrees with the general consensus of the panel of experts who performed the structural analyses of an RC containment for the NUREG-1150 study.

The procedure used in this study to analyze the RC containment is very similar to that used by Cherry and Smith (2000). In that study, an axisymmetric model of the containment structure was developed to find the global strains. This model included the effects of the liner, the concrete, and the reinforcing steel. The global strains were then used as boundary conditions for refined 2-D models of local areas that had experienced corrosion damage. An area of the liner with a reduced thickness modeled corrosion damage. A strain criterion was used to determine the point when tearing occurred. Factors were introduced in the failure criterion to account for the multi-axial stress state, the level of model refinement, and the level of refinement in the analytical model.

The approach of this study closely follows the work done by Cherry and Smith, with a few notable exceptions. The global axisymmetric model of the containment has essentially remained unchanged. Local 2-D models are also used to model the corroded regions in the liner. However, the finite element meshes of the corroded areas have been modified to more realistically model the shape of a corroded region. In the meshes used by Cherry and Smith, the corroded regions were rectangular in shape, which resulted in stress concentrations at the corners of those regions. The edges of the corroded regions have been rounded, and the transition between the corroded and non-corroded areas has been made more gradual.

The work of Cherry and Smith was primarily focused on finding the failure pressure of degraded containments. For the purposes of this study, it is important to not only characterize the strength of degraded containments, but to find the difference between the containment in its original and

degraded conditions for the purposes of computing the change in risk. For this reason, an effort has been made to model the un-degraded containment in more detail. In addition, we include distinctions between leak, rupture, and catastrophic rupture, where Cherry and Smith only considered leak in their failure estimates.

3.1.1 Axisymmetric Global Model

As mentioned previously, the global behavior of the containment is modeled with essentially the same axisymmetric finite element model used by Cherry and Smith. The axisymmetric finite element mesh of the containment is shown in Figure 3.2(a).

The concrete is modeled using the ANACAP-U (ANATECH, 1997) constitutive model, which is linked with the ABAQUS program. Nonlinear behavior of the concrete is modeled with a stress-strain law evaluated at element integration points, so the effects of cracking and crushing are "smeared out" over an element. When a tensile strain criterion, which takes multi-axial stress states into account, is met at an integration point, a fixed smeared crack is initiated and softening occurs. A hardening-softening model accounts for the nonlinear behavior of concrete in compression.

Reinforcing bars are modeled by embedding them within the concrete elements with the ABAQUS `*REBAR` command. A uniaxial model accounts for hardening in the reinforcing steel. The liner is modeled with axisymmetric shell elements directly attached to the concrete elements on the inside face of the containment. Nonlinear behavior of the steel in the shell is modeled using a steel plasticity model. Nonlinear spring elements are used to approximate the contact conditions between the containment and the soil below. The spring elements have a high elastic stiffness in compression, and have no strength in tension.

The containment model is subjected to a monotonically increasing internal pressure loading. An increasing temperature is applied to the containment in conjunction with the pressure loading. Initially, the internal surface of the containment has a temperature of 21^o Celsius (70^o Fahrenheit). This increases to a maximum of 176^o Celsius (349^o Fahrenheit) at a pressure of 1.38 MPa (200 psi). Though possible during a severe accident, pressure and temperature spikes were not included in these structural analyses. These spikes will affect the potential failures in the containment, but they are assumed to be minimal (see International Standard Problem No. 48). Because the analysis is performed using load control, it reaches a point where small increases in the pressure result in very large deformations. At this point, the analysis cannot continue because obtaining a converged solution becomes too difficult. This point is generally in the range of 1.1 MPa (160 psi) for this model, but varies depending on the input parameters.

Figure 3.2(b) shows the deformed shape of the axisymmetric model for a typical case near the end of the analysis. Deformations have been magnified by a factor of 10 in this figure. It is evident from the figure that hoop strains are very large near the mid-height of the containment. There are also large bending deformations in the basemat. From this analysis, it appears that shearing in the wall near the junction with the basemat is not critical. However, smeared crack models of concrete have a well-documented tendency to over-predict the capacity of structures subjected to shear loading (Rots and Blaauwendraad, 1989). This over-prediction of shear capacity isn't likely to be as severe in a shell as it would be in a typical structural member because in this case, the strength in the hoop direction provides considerable resistance to shearing at the base. Nevertheless, these results should still be treated with some caution, and further research in this area would be helpful.

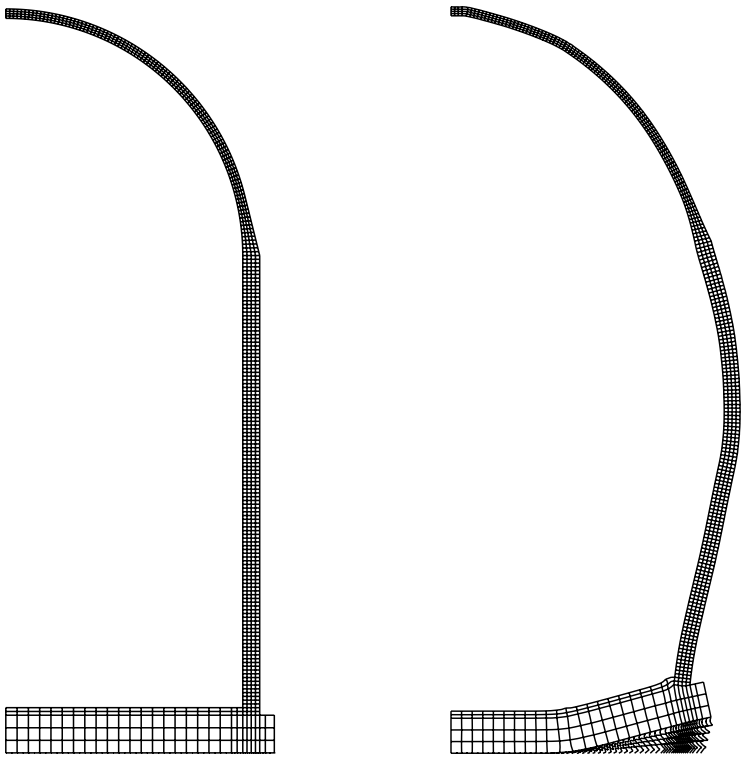

(a) Original Mesh (b) Deformed at 1.05 MPa (152 psi) (magnified 10x)

Figure 3.2: Axisymmetric Finite Element Model of RC Containment

3.1.2 Local Detail and Corrosion Modeling

In the analysis of this containment, the strain magnification factors described in Section 2.4.2.1 are used to approximate strain concentrations in the liner at discontinuities, while detailed 2-D finite element models are used to model regions of hypothetical corrosion. To determine the relative significance of corrosion in different locations, two cases of liner corrosion are assumed: at the mid-height of the containment, and in the wall just above the junction with the basemat.

In both cases, corrosion is assumed to have penetrated at two levels, 50% and 65%, of the liner thickness. In the case of the mid-height model, corrosion was assumed to have occurred over a region 8 cm (3 in) wide and 13 cm (5 in) high. The finite element mesh of this region is shown in Figure 3.3. The mesh covers a 91 cm (36 in) wide square area. At the boundaries of the mesh, the average length of an element edge is 25 mm (1 in), while in the corroded area, the mesh is refined considerably and the average element length is approximately 8 mm (0.3 in).

A larger area of corrosion, also at 50% and 65% through the wall thickness, is assumed near the wall-basemat junction. Figure 3.4 shows the finite element mesh of that region. The corroded region is 25 cm (10 in) wide and 18 cm (7 in) high. The corrosion is positioned so that the top of the corroded coincides with the top of the non-structural floor. The shape of the area is intended to represent what may occur if water leaks below the seal at the floor level. The same level of mesh refinement used in the mid-height model is used in this model.

In both of these cases, a single layer of elements surrounding the fully corroded region is used to make a more gradual transition from the un-damaged area to the corrosion zone. In that layer of elements, the corrosion is assumed to penetrate 25% and 32.5% of the wall thickness for the 50% and 65% corrosion cases, respectively. In these models, the steel is modeled using a plasticity model. Nonlinear spring elements are used to approximate the behavior of the shear studs that attach the liner to the concrete wall. The stud locations are illustrated in the finite element meshes, and are typical of details that would be seen in an actual RC containment. Many variations of the size of the corroded area and its location relative to the studs were studied. The ones chosen for these analyses are those that yielded the highest plastic strains. However, it was found that the size of the corroded area and its location relative to the studs had a fairly minor impact on the maximum strains.

The results from the local models are post-processed to determine the point at which tearing (leak), rupture, and catastrophic rupture occurs. For a leak, the effective plastic strains are multiplied by factors to account for the effects of the multiaxial stress state, corrosion, gauge length, and modeling uncertainty, as described in Section 2.4.1.1.

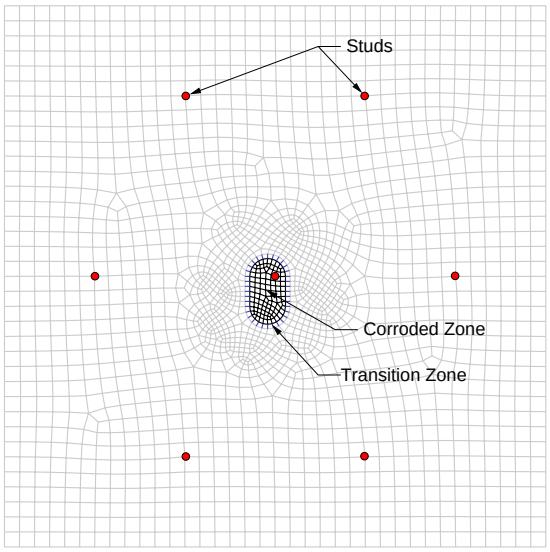

Figure 3.3: Finite Element Mesh of Corrosion at Midheight

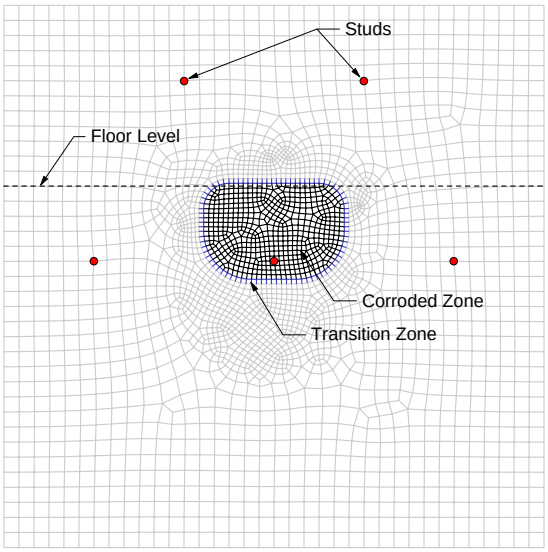

Figure 3.4: Finite Element Mesh of Corrosion in Wall Near Basemat

3.1.3 Structural Analysis with Best Estimate Properties

The primary focus of the structural analysis in this study is to develop fragility curves to interface with the risk model. However, it is instructive to study the results of a baseline analysis that uses the median values of the input parameters that are randomly generated for the LHS analyses.

Six potential liner failure modes are considered: failure at the four locations of geometric discontinuities for which magnification factors are used (see Section 2.4.2.1), failure at a corroded region at the wall midheight, and failure at a corroded region on the wall near the basemat. To investigate the potential for failure (leak) at all of these locations, the global axisymmetric model is analyzed, and results are extracted for use as displacement boundary conditions for the two local corrosion models. The two local corrosion models are run with 50% and 65% corrosion and post-processed to find the most critical value of $\bar{\varepsilon}_p$ at every loading step using the steel leak criterion (see Section 2.4.1.1). A separate post-processing tool is applied to the results of the axisymmetric model to apply appropriate magnification factors to find $\bar{\varepsilon}_p$ for the four selected discontinuity locations at every loading increment. The uniaxial plastic failure strain, ε_{fail}, was assumed to be 25% for these analyses. The gauge length factor was assumed to be 4.0 for the local corrosion models in this baseline analysis.

Figure 3.5 shows the plot of the ratio of $\bar{\varepsilon}_p$ for the 6 failure modes to ε_{fail} (0.25) as a function of internal pressure for the baseline analysis. A horizontal line has been drawn at 1.0 to show the failure criterion. It is evident that the failure condition is met first at the corroded area at the midheight, and that the corroded area near the basemat appears to be the least critical location. Of the geometric discontinuities, the steam penetration is the most critical. From this analysis, it appears that a containment without any degradation would fail at 0.896 MPa (129.9 psi) at the steam penetration. If the postulated corrosion were present at the mid-height, it would fail at that location at an internal pressure of 0.829 MPa (120.3 psi) and 0.812 MPa (117.8 psi) for 50% and 65% corrosion, respectively. Leak near the corroded basemat does not occur until 0.947 MPa

(137.4 psi) and 0.939 MPa (136.2 psi) for 50% and 65% corrosion, respectively. Leakage occurs at the steam penetration prior to leak in the corroded basemat location. Table 3.1 summarizes the leak pressures for each location.

Although Cherry and Smith (2001) assumed somewhat different corrosion patterns, it is useful to compare their failure pressures with those obtained in this study. For their best estimate model of the containment, they found that the un-damaged containment failed at 1.03 MPa (150 psi). With corrosion 50% through the wall, they found that the containment failed at 0.880 MPa (127 psi) when the corrosion was at the mid-height and 0.970 MPa (141 psi) with corrosion at the basemat. The failure pressures for the un-damaged model and mid-height corrosion obtained in the current study are somewhat lower than those found by Cherry and Smith. This is due to the fact that a higher gauge length factor was used in this study. Cherry and Smith assumed corrosion to be uniform around the entire circumference of the containment vessel at the basemat. In this study, the corrosion at the basemat was only assumed to occur in a local area. This is a possible reason for the higher capacity of the corroded area found in the current study.

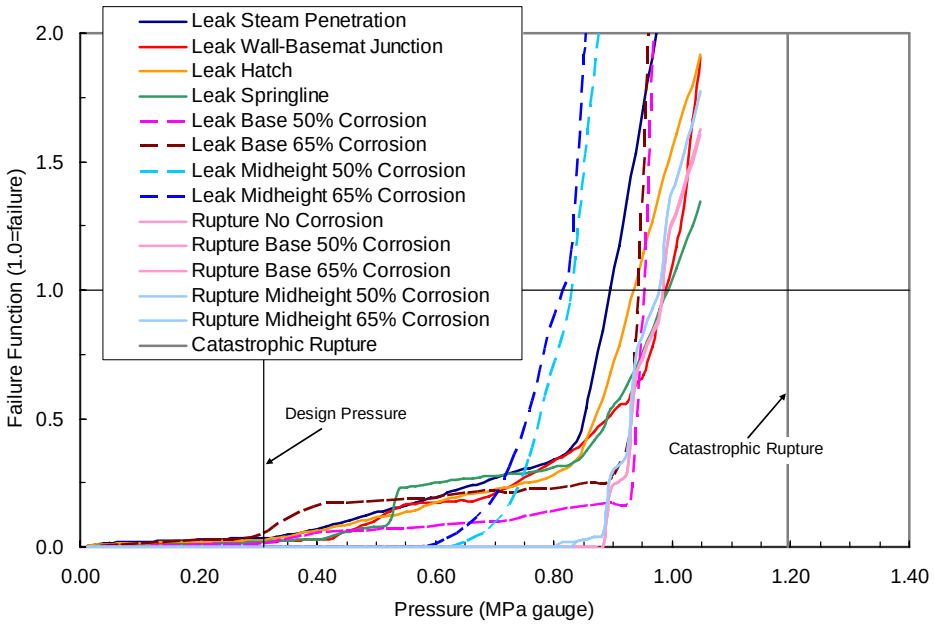

Figure 3.5: Failure Potential at Corrosion and Discontinuity Locations

Figure 3.5 and Table 3.1 also include failure curves and pressures for five rupture cases: the original containment with no corrosion, 50% corrosion at the basemat, 65% corrosion at the basemat, 50% corrosion at the midheight, and 65% corrosion at the midheight. The procedure in Section 2.4.2.2 is used to compute the ratio of the total rupture area, A_{total}, to the rupture area limit of 0.028 m2 (0.3 ft2), as a function of pressure. The four features, steam penetration, wall-basemat junction, hatch, and springline, are each assumed to contain four cracks (n_i) each after the leak criterion has been reached. The choice of four cracks at each location is based on the upper limit of the number of tears observed in the 1:6 scale reinforced concrete containment testing at Sandia National Laboratories (Horschel, 1992). The number of cracks at each location could have been introduced as a random variable, but due to the severely approximate nature of the rupture estimate employed here, a random variable with a large uncertainty is imposed on the

total rupture area. One crack is assumed at the basemat and midheight locations for cases considering corrosion.

For the two basemat corroded case, leak does initiate prior to the overall rupture failure. This has only a negligible effect on the total rupture area, since only one crack is assumed to initiate at the corroded location. Therefore, the rupture curves for the original case with no corrosion and the two basemat corrosion cases share the same curve. A small increase in the rupture area is caused by corrosion at the midheight. Since the global strains do not differ between the 50% and 65% corrosion cases, the rupture curves are the nearly identical. Obviously, assuming more than one corroded location for each case will increase the rupture area and lower the rupture pressure. This is especially true or corrosion at the midheight, where leak initiates at the corroded location well before initiation at the steam penetration. The effect of multiple basemat corroded locations will be minimal since leak at the corroded basemat initiates just prior to the current rupture thresholds. Variation in the total area assumed to cause rupture (0.028 m^2 or 0.3 ft^2) will also affect the rupture pressure. As mentioned previously, a large uncertainty is imposed on the total rupture area to account for the approximate nature of the rupture criterion. Finally, Figure 3.5 and Table 3.1 include the simple estimate for catastrophic rupture described in Section 2.4.2.3.

Table 3.1: Summary of Locations and Failure Pressures

Location	Failure Pressure MPa (psig)
Leak Steam Penetration	0.896 (129.9)
Leak Wall-Basemat Junction	0.988 (143.3)
Leak Hatch	0.935 (135.6)
Leak Springline	0.992 (143.9)
Leak Base 50% Corrosion	0.947 (137.4)
Leak Base 65% Corrosion	0.939 (136.2)
Leak Midheight 50% Corrosion	0.829 (120.3)
Leak Midheight 65% Corrosion	0.812 (117.8)
Rupture No Corrosion	0.983 (142.6)
Rupture Base 50% Corrosion	0.983 (142.6)
Rupture Base 65% Corrosion	0.983 (142.6)
Rupture Midheight 50% Corrosion	0.976 (141.6)
Rupture Midheight 65% Corrosion	0.976 (141.6)
Catastrophic Rupture	1.195 (173.3)

3.2 Fragility Analysis of Degraded Containment

The principal goal of the current study is to integrate structural analyses of degraded containments with risk analysis models to understand the significance of the degradation from a risk-informed perspective. Fragility curves of containments under pressurization with and without degradation serve as the interface between the structural and risk analyses. As explained in Section 2.5, Latin Hypercube Sampling is used in this study to generate sets of random variables to be used as input to the structural finite element analyses. In the current work, 19 input parameters were selected as random variables, and 30 samples of those parameters were taken for analysis.

Of the 19 input parameters, 14 describe the inherent randomness, or aleatory uncertainty, in the basic properties of concrete, reinforcing bars, and liner steel. The remaining 5 parameters describe epistemic uncertainty, or uncertainty in the ability to characterize the failure pressure. Several of the random input parameters are correlated with others. For concrete, the tensile strength, f'_t, and modulus of elasticity, E_c, are correlated with the cylinder compressive strength, f'_c. Likewise, there is correlation between the yield strength and ultimate strength of steel.

Whenever possible, statistical test data was used as the basis for the probability distributions in this study. When such data was unavailable, engineering judgment was used to provide reasonable estimates of uncertainty. A thorough statistical analysis of concrete strength was performed by Mirza et. al. (1979). Based on recommendations from that analysis, the elastic modulus of concrete is computed as:

$$E_c = c_1 60400\sqrt{f'_c} \tag{3.3}$$

where c_1 is a random variable with a median of 1.0 and a coefficient of variation of 0.077. Likewise, f'_t is computed as:

$$f'_t = c_2 8.3\sqrt{f'_c} \tag{3.4}$$

where c_2 has a median of 1.0 and a coefficient of variation of 0.196. Units of psi are used in both of these equations. Under average control conditions, Mirza et al. suggest that a coefficient of variation (COV) of 0.15 can be assumed for f'_c.

The RC containment investigated in this study has reinforcing bars of both Grade 40 and Grade 50 steel. Unfortunately, less information was available on the correlation between yield strength and ultimate strength, and between the elastic modulus and strength for steel. The elastic modulus, E_s is assumed to be independent of the yield strength, f_y, and the ultimate strength, f_u. Correlation is induced between f_y and f_u in a manner similar to that for concrete:

$$f_y = s_1 r\, f_u \tag{3.5}$$

where s is a random variable with a median of 1.0. The variable r is the ratio of the yield stress to the ultimate stress, and differs depending on the type of steel. For Grade 40 reinforcement, a value of 0.6 was assumed for r. For Grade 50 reinforcing, this value was set at 0.62, and for the liner steel, a value of 0.535 was used.

Five separate variables are used to describe the epistemic uncertainty. Variable describes the uncertainty inherent in predicting the global strains, the local strains from the 2-D submodels with

corrosion, the strain magnification in the presence of corrosion, the calculation of the rupture area, and the simple estimate for catastrophic rupture.

Each of these variables has a median value of 1.0. A COV of 0.3 was assumed for the global strain prediction variable, f_{FEM-u}. This agrees well with the scatter in the analytical predictions submitted by several analysts for the behavior of the 1:6 scale RC containment test conducted at Sandia National Laboratories (Clauss, 1987). The magnification factors for the liner discontinuities are simply multiplied by this uncertainty factor in Equation 2.9.

The COV of the local model uncertainty factor, f_{FEM-u}, was set to 0.35 because it was felt that there is more uncertainty in the local models than in the global models. For the local detailed models, Equation 2.1 is used to compute the magnified strains. Since the local models contain corrosion, the corrosion factor, f_c, equals 2 and is multiplied by an uncertainty factor, f_{c-u}, with a COV of 0.20.

The final two epistemic factors account for the uncertainty in the rupture area, f_{rupt-u}, and catastrophic rupture pressure, f_{cat-u}. Since the calculation of the rupture area in Equation 2.12 contains several approximations, a large COV is employed, equal to 0.40. The simple method used here to compute the catastrophic rupture pressure (Equation 2.13) should provide a reasonable estimate, enabling the use of a low COV of 0.10. This uncertainty is in addition to the variation in the ultimate strengths random variables used in Equation 2.13.

Table 3.2 shows all of the random input parameters. This table shows the median values of the parameters, a measure of the variation assumed for the parameter, and the type of distribution. For variables with normal distributions, the COV is used as the measure of variation, while β is used for variables represented with a lognormal distribution.

A total of 30 sets of these input parameters were generated based on analyses using the specified distribution functions. Once the analyses were run, the 30 leak pressures were used to develop fragility curves for each of the four locations of linear discontinuity. Figure 3.6 shows the fragility curves based on the sorted analyses values and associated lognormal curve fits. The fragility curves represent the leak pressure for the four discontinuity locations. Figure 3.7 shows the fragility curves for leak at the two corroded locations, basemat and midheight, at the two levels of corrosion, 50% and 65%. These plots indicate that increasing the level of corrosion from 50% to 65% of the liner thickness has only a minimal effect. Due to the shape of the distributions, the lognormal curve fits for each of the corroded cases requires one curve fit for high probabilities and one curve fit for low probabilities.

Table 3.2: Random Input Parameters

Property	Median	COV/β	Distribution
Concrete			
Compressive Strength (f'_c)	27.3 MPa (3.956 ksi)	0.15	Lognormal
Elastic Modulus factor (c_1)	1.0	0.077	Normal
Tensile Strength factor (c_2)	1.0	0.196	Normal
Grade 40 Reinforcing Steel			
Ultimate Strength (f_u)	508.3 MPa (73.72 ksi)	0.09	Lognormal
Yield Strength Factor (s_1)	1.0	0.07	Normal
Elastic Modulus (E_s)	200 Gpa (29000 ksi)	0.06	Normal
Grade 50 Reinforcing Steel			
Ultimate Strength (f_u)	590.5 MPa (85.65 ksi)	0.09	Lognormal
Yield Strength Factor (s_1)	1.0	0.07	Normal
Elastic Modulus (E_s)	200 Gpa (29000 ksi)	0.06	Normal
Liner Steel			
Ultimate Strength (f_u)	577.1 MPa (83.70 ksi)	0.09	Lognormal
Yield Strength Factor (s_1)	1.0	0.07	Normal
Elastic Modulus (E_s)	200 GPa (29000 ksi)	0.06	Normal
Uniaxial Failure Strain (ε_{fail})	0.25	0.12	Normal
Corrosion Depth Uncertainty	1.0	0.10	Normal
Epistemic Uncertainty			
Axisymmetric Model Strain Factor Uncertainty (f_{FEM-u})	1.0	0.30	Lognormal
Submodel Model Strain Factor Uncertainty (f_{FEM-u})	1.0	0.35	Lognormal
Corrosion Factor Uncertainty (f_{c-u})	1.0	0.20	Lognormal
Leak Area for Rupture Uncertainty	1.0	0.40	Lognormal
Catastrophic Rupture Uncertainty	1.0	0.10	Lognormal

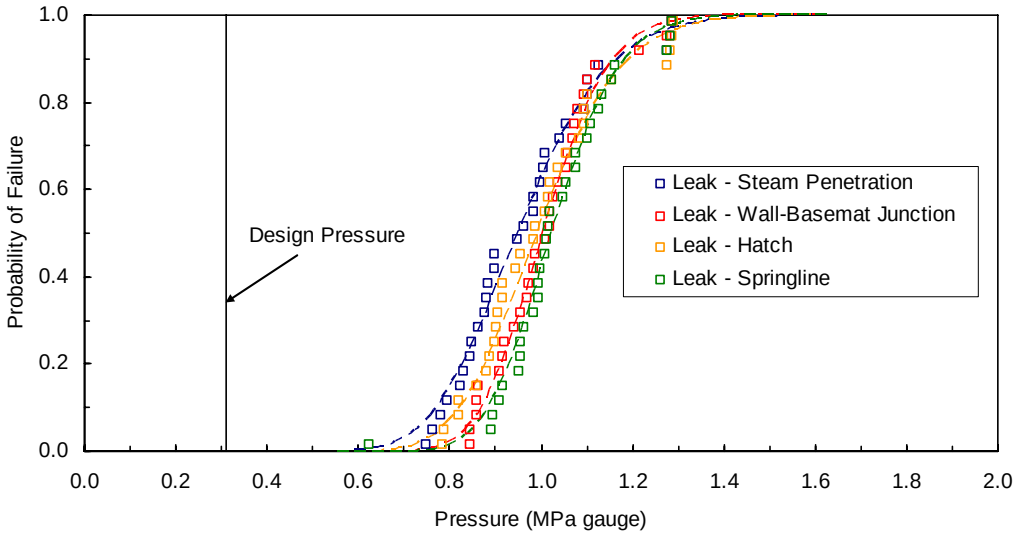

Figure 3.6: Fragility Curves for Leak at Discontinuity Locations

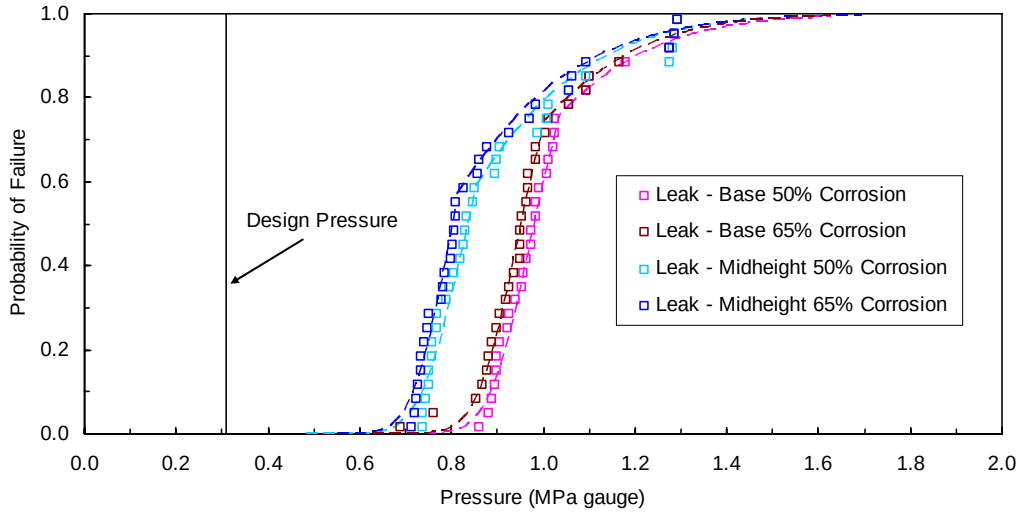

Figure 3.7: Fragility Curves for Leak at Corroded Locations

As discussed previously, the rupture threshold is assumed to be reached when the total crack opening caused by initiated leaks, exceeds 0.028 m^2 (0.3 ft^2). Figure 3.8 shows the rupture fragility curves for the five cases examined in this study. Since no significant change in pressure occurs for the corroded basemat cases, the curves for these cases remain identical. The crack opening near the midheight corroded locations are large enough to cause a slight decrease in rupture pressure. Since the global strains are employed to estimate the rupture pressure, the 50% and 65% corroded cases are the same. Figure 3.8 also illustrates the fragility curve for catastrophic rupture. Since the criteria for catastrophic rupture is not affected my the corrosion in the liner, the catastrophic rupture fragility remains the same for all five cases.

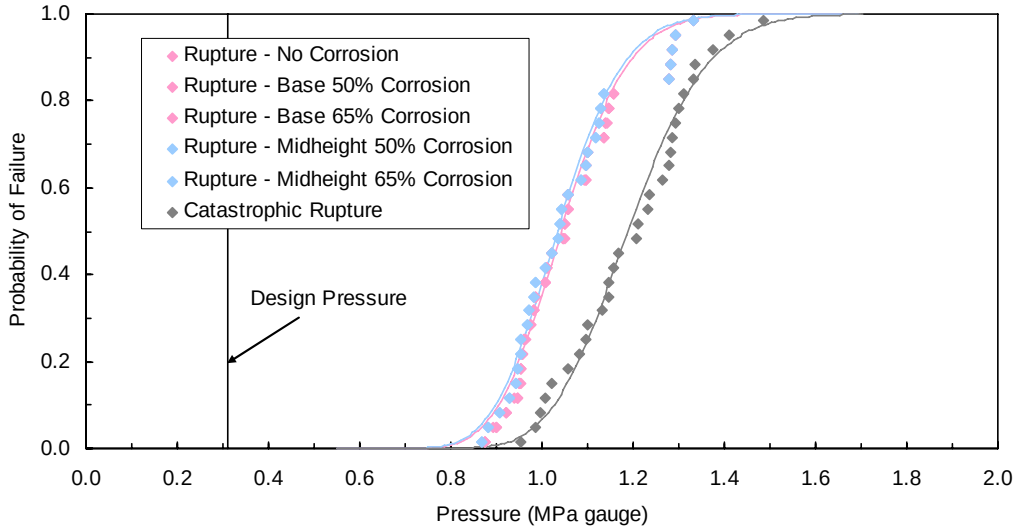

Figure 3.8: Fragility Curves for Rupture and Catastrophic Rupture

The leak fragilites for the four discontinuity locations were used to develop a cumulative probability of failure curve for the original, non-corroded, containment. The fragility curve for the same containment, compiled from several experts' analyses for the NUREG-1150 study, is also shown in Figure 3.9 for comparison. The correspondence between these two curves is fairly close. The median values of the two curves are fairly close, but the variance from the current work is somewhat lower.

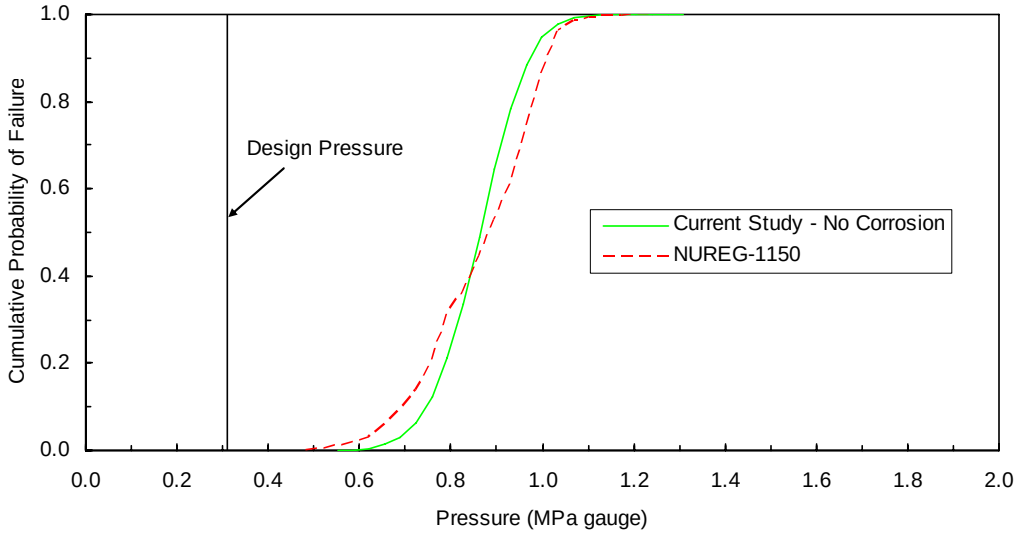

Figure 3.9: Comparison of the Undamaged Containment Fragilities from the Current Study and NUREG-1150

Figure 3.10 shows the cumulative probability of failure (leak) curves obtained in the current study for the containment with corrosion degradation at the midheight and at the base, along with the fragility of the containment in its original condition. As would be expected from the baseline analysis, the drop in capacity due to corrosion at the mid-height is much greater than that due to corrosion at the basemat.

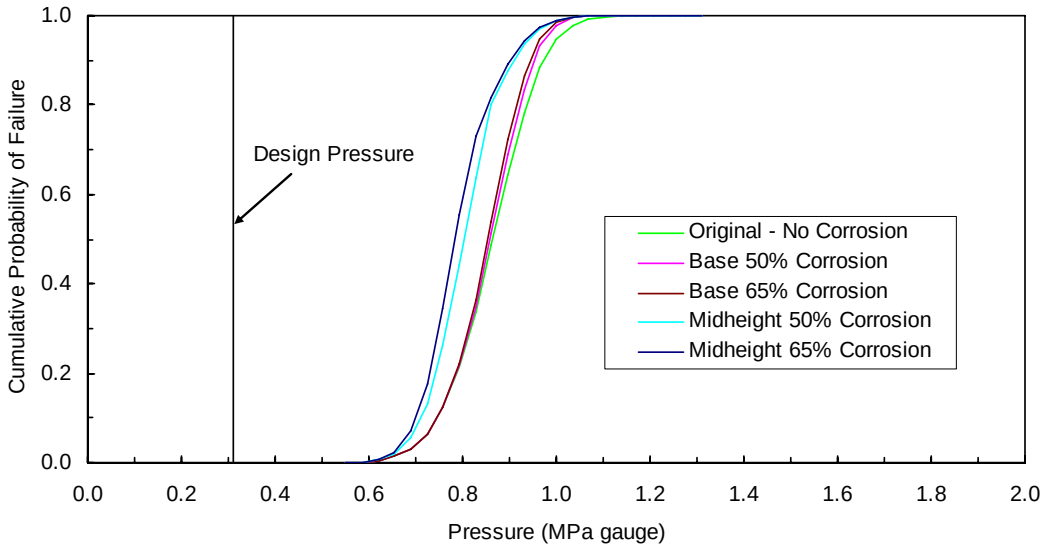

Figure 3.10: Cumulative Probability of Failure Curves for Original and Degraded RC Containment

The conditional probability of failure curves were computed for each of the five cases and shown in Figure 3.11Figure 3.15. Since the rupture and catastrophic curves are relatively constant throughout the five cases, the conditional probability distributions are extremely similar. At low pressures ($P < 0.65$ MPa), the probability of leak is equal to 1 with the rupture and catastrophic rupture probabilities at 0. Increases in pressure cause the rupture and eventually the catastrophic rupture conditional probabilities to increase. The leak probability decreases quickly as the rupture probabilities increase. The rupture curve peaks at approximately 1.1 MPa. At this point, both the leak and rupture curves decrease gradually to probabilities of 0 and the catastrophic curve increase to a probability of 1 at approximately 1.7 MPa.

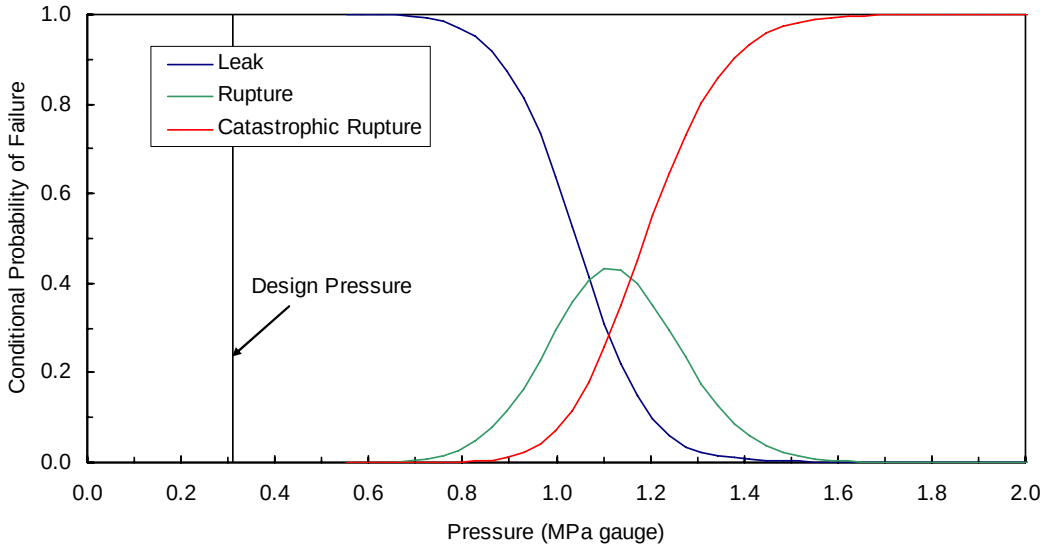

Figure 3.11: Conditional Probability of Failure for Original Containment (No Corrosion)

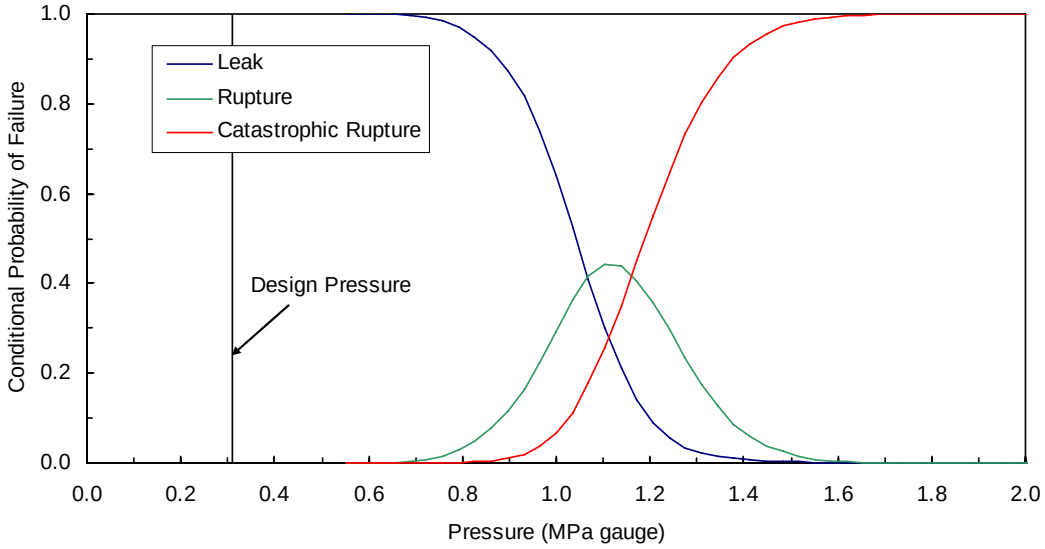

Figure 3.12: Conditional Probability of Failure for 50% Corrosion at Basemat

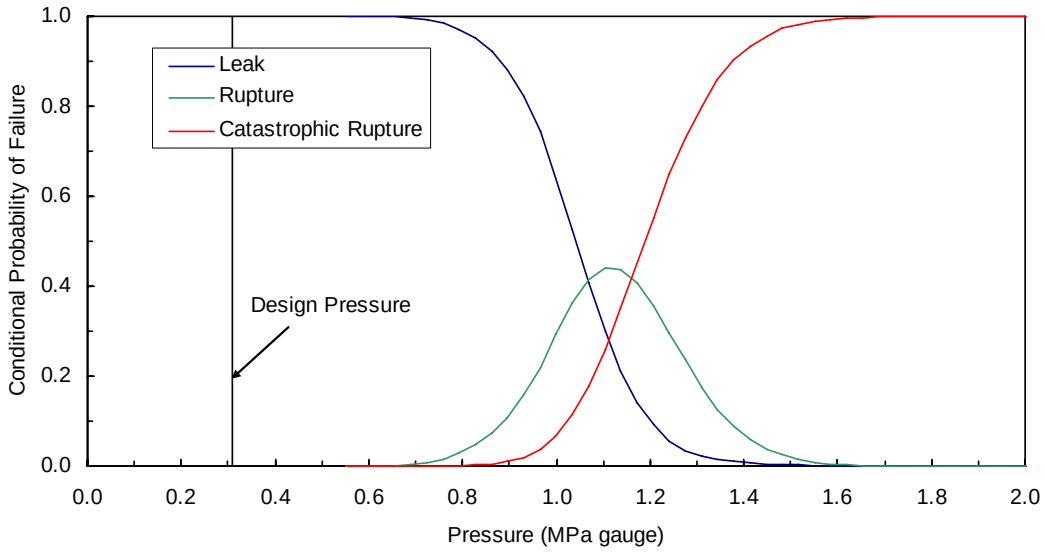

Figure 3.13: Conditional Probability of Failure for 65% Corrosion at Basemat

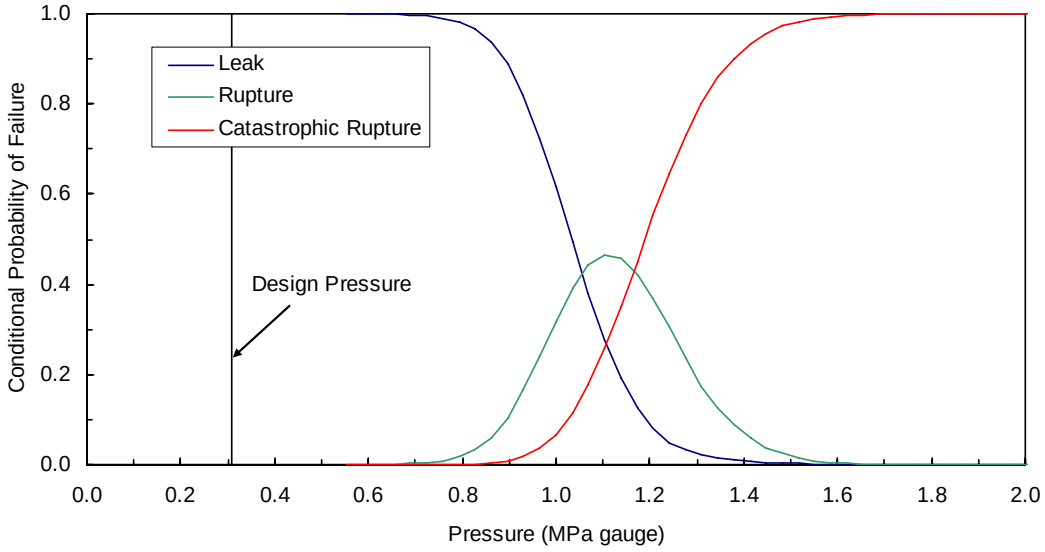

Figure 3.14: Conditional Probability of Failure for 50% Corrosion at Midheight

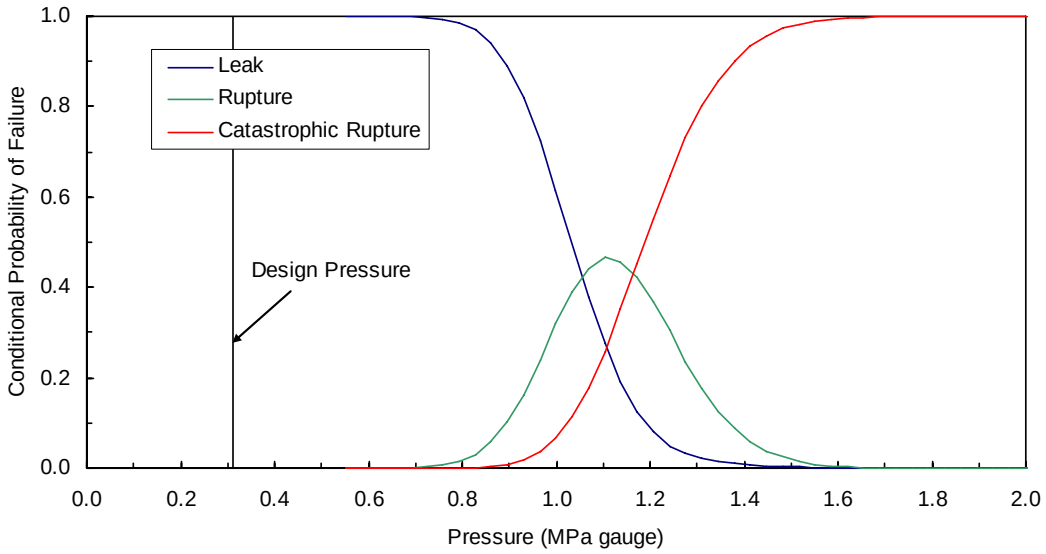

Figure 3.15: Conditional Probability of Failure for 65% Corrosion at Midheight

3.3 Risk Analysis Results

Table 3.3 shows the CDF values from NUREG 1150. Because the containment response does not affect the CDF for this plant, the results are the same for all of the cases studied.

Table 3.3: Core Damage Frequency (yr^{-1})

Case	Mean	5%	50%	95%
All	4.1E-5	6.8E-6	2.3E-5	1.3E-4

Table 3.4 shows the LERF results, and Table 3.5 shows the probability of large early containment failure conditional on core damage. LERF is the product of the CDF and the probability of large early containment failure conditional on core damage.

Table 3.4: Large Early Release Frequency (yr^{-1})

Case	Mean	5%	50%	95%
Un-damaged (Reference)	1.10E-7	0	3.61E-10	1.54E-6
Un-damaged (Current Study)	1.01E-7	0	3.16E-10	1.12E-6
50% Corrosion near basemat	1.01E-7	0	3.16E-10	1.12E-6
50% Corrosion at midheight	1.01E-7	0	3.16E-10	1.12E-6
65% Corrosion near basemat	1.01E-7	0	3.16E-10	1.12E-6
65% Corrosion at midheight	1.01E-7	0	3.16E-10	1.12E-6

Table 3.5: Probability of Large Early Containment Failure Conditional on Core Damage

Case	Mean	5%	50%	95%
Un-damaged (Reference)	0.0027	0	1.57E-5	0.019
Un-damaged (Current Study)	0.0025	0	1.38E-5	0.0086
50% Corrosion near basemat	0.0025	0	1.38E-5	0.0086
50% Corrosion at midheight	0.0025	0	1.38E-5	0.0086
65% Corrosion near basemat	0.0025	0	1.38E-5	0.0086
65% Corrosion at midheight	0.0025	0	1.38E-5	0.0086

Table 3.6: Change in the Large Early Release Frequency (yr^{-1}) due to Degradation

Case	Mean	5%	50%	95%
50% Corrosion near basemat	0	0	0	0
50% Corrosion at midheight	0	0	0	0
65% Corrosion near basemat	0	0	0	0
65% Corrosion at midheight	0	0	0	0

The key risk criteria for acceptance of a proposed plant change in Regulatory Guide 1.174 (USNRC, 2001) are the baseline values of CDF and LERF, and the changes in those values due to the proposed modification, denoted as ΔCDF and ΔLERF. The acceptance criteria must be met for both the pairs of ΔCDF and CDF and of ΔLERF and LERF. Because CDF is unaffected by the containment properties in this particular plant, ΔCDF is 0, so the effects of the change clearly fall within Region III for the CDF acceptance criteria, which can be seen in Figure 2.1. In Region III, it is not actually necessary to compute the baseline CDF, although for these analyses, the mean CDF was computed, and has a value of 4.1E-5, which is clearly acceptable.

For both the lower bound and best estimate fragility curves, there is no change in LERF relative to the un-damaged containment in the case where corrosion exists near the basemat or the midheight. Because LERF is unaffected by the increases in leak introduced by the liner corrosion in this particular plant, ΔLEFF is 0 (Table 3.6), so the effects of the change clearly fall within Region III for the LERF acceptance criteria, which can be seen in Figure 2.2. Therefore, the corrosion cases investigated in this study would be permissible modifications from a risk standpoint by Regulatory Guide 1.174, there are other criteria for acceptance that also must be met. A change proposed under that risk-informed methodology must also satisfy other design goals. It must still maintain defense in depth and acceptable safety margins.

The results presented above can potentially be somewhat misleading. One would intuitively expect that at least a small increase in the risk measure would be observed in the cases with containment degradation. This lack of increase in the risk measures presented in

Table 3.4 and Table 3.5 can be traced to the definition of LERF used in the process of binning the risk analysis results. LERF is, by definition, the frequency of large, early containment failures resulting from accidents stemming from a certain set of initiating events. The question of whether the failure is large is determined by the mode of failure, which is computed based on the combination of the overall fragility curve and the conditional probabilities of leak, rupture, and catastrophic rupture. Failure occurrences are grouped into LERF only if the containment fails in a rupture or catastrophic rupture mode.

Because the types of degradation considered here only affect the containment liner, and not the main load-bearing structural system, they only contribute to leakage failures. The increase in probability of rupture failure due to such corrosion is very minor. To gain a more complete perspective on the risk associated with these types of degradation, it is instructive to introduce an additional risk metric: the small early release frequency (SERF). This is the frequency of small, early containment failures that stem from the same set of initiating events used in computing LERF. The values computed for SERF for the various degradation cases are shown in Table 3.7 for comparison. The probability of small early containment failure conditional of core damage is also shown in Table 3.8. This quantity is analogous to the probability of large early containment failure conditional on core damage reported previously, except that it accounts for only the cases in which the containment fails by leaking. The change in SERF is shown in Table 3.9.

Table 3.7: Small Early Release Frequency (yr^{-1})

Case	Mean	5%	50%	95%
Un-damaged (Reference)	4.65E-8	2.89E-10	1.36E-9	1.27E-8
Un-damaged (Current Study)	4.45E-8	2.89E-10	1.37E-9	2.23E-8
50% Corrosion near basemat	4.70E-8	2.89E-10	1.37E-9	2.23E-8
50% Corrosion at midheight	1.15E-7	2.89E-10	1.37E-9	4.94E-7
65% Corrosion near basemat	4.70E-8	2.89E-10	1.37E-9	2.23E-8
65% Corrosion at midheight	1.46E-7	2.89E-10	1.37E-9	3.23E-6

Table 3.8: Probability of Small Early Containment Failure Conditional on Core Damage

Case	Mean	5%	50%	95%
Un-damaged (Reference)	0.00113	4.24E-5	5.91E-5	9.74E-5
Un-damaged (Current Study)	0.00108	4.24E-5	5.96E-5	1.71E-4
50% Corrosion near basemat	0.00115	4.24E-5	5.96E-5	1.71E-4
50% Corrosion at midheight	0.00280	4.24E-5	6.00E-5	3.80E-3
65% Corrosion near basemat	0.00115	4.24E-5	5.96E-5	1.71E-4
65% Corrosion at midheight	0.00357	4.24E-5	6.01E-5	2.49E-2

Table 3.9: Change in the Small Early Release Frequency (yr^{-1}) due to Degradation

Case	Mean	5%	50%	95%
50% Corrosion near basemat	2.58E-9	0	0	0
50% Corrosion at midheight	7.03E-8	0	0	4.72E-7
65% Corrosion near basemat	2.58E-9	0	0	0
65% Corrosion at midheight	1.02E-7	0	0	3.21E-6

It is also instructive to evaluate another metric, designated here as the total early release frequencies (TERF). This is simply the summation of LERF and SERF. TERF, the total probability of early containment failure conditional on core damage, and the change in the total early release frequencies are shown in Table 3.10 through Table 3.12.

Table 3.10: Total Early Release Frequency (yr^{-1})

Case	Mean	5%	50%	95%
Un-damaged (Reference)	1.56E-7	2.89E-10	1.72E-9	1.56E-6
Un-damaged (Current Study)	1.45E-7	2.89E-10	1.69E-9	1.15E-6
50% Corrosion near basemat	1.48E-7	2.89E-10	1.69E-9	1.15E-6
50% Corrosion at midheight	2.16E-7	2.89E-10	1.70E-9	1.62E-6
65% Corrosion near basemat	1.48E-7	2.89E-10	1.69E-9	1.15E-6
65% Corrosion at midheight	2.47E-7	2.89E-10	1.70E-9	4.36E-6

Table 3.11: Probability of Total Early Containment Failure Conditional on Core Damage

Case	Mean	5%	50%	95%
Un-damaged (Reference)	0.00381	4.24E-5	7.49E-5	0.0120
Un-damaged (Current Study)	0.00354	4.24E-5	7.33E-5	0.0088
50% Corrosion near basemat	0.00360	4.24E-5	7.33E-5	0.0088
50% Corrosion at midheight	0.00526	4.24E-5	7.38E-5	0.0124
65% Corrosion near basemat	0.00360	4.24E-5	7.33E-5	0.0088
65% Corrosion at midheight	0.00603	4.24E-5	7.39E-5	0.0335

Table 3.12: Change in the Total Early Release Frequency (yr^{-1}) due to Degradation

Case	Mean	5%	50%	95%
50% Corrosion near basemat	2.58E-9	0	0	0
50% Corrosion at midheight	7.03E-8	0	0	4.72E-7
65% Corrosion near basemat	2.58E-9	0	0	0
65% Corrosion at midheight	1.02E-7	0	0	3.21E-6

When these additional risk metrics are evaluated, the effect of the degradation on the risk becomes much clearer. In all of these cases, the risk measured in terms of SERF or TERF increases as a result of liner corrosion. Because the liner corrosion only increases the risk of small releases, ΔSERF and ΔTERF are equal. The risk of both small and large early releases is still quite small, and the risk criteria of Regulatory Guide 1.174 would be easily satisfied, even if TERF and ΔTERF were used in place of LERF and ΔLERF.

The example plants examined here serve as good case studies indicating that one should be very cautious about simply applying the ΔLERF criterion to evaluate the significance of containment degradation. It is important to closely examine how degradation can increase the likelihood of one failure mode while decreasing the likelihood of another, and evaluate the consequences of these different modes. It cannot be stressed enough that the cases of degradation examined here are extremely limited in scope. There are currently no means of predicting degradation prior to its discovery. Since the location and specific nature of any degradation could dramatically affect the containment capacity and risk, a detailed analysis of that scenario would be required. There are also a number of assumptions that would require additional consideration when performing a site specific analysis. The specific results reported in this study should in no way be applied to making regulatory decisions on existing plants.

4. Risk Analysis of BWR Plant with Mark I Steel Containment

To investigate the effects of corrosion in a steel containment vessel, a typical boiling water reactor (BWR) plant with a Mark I steel containment was chosen for study. Figure 4.1 shows a schematic diagram of the containment at this plant, with the areas where the effects of corrosion are investigated in this study. As was done for the RC containment, corrosion is assumed to occur in areas where moisture is likely to collect, and where the presence of corrosion is likely to weaken the containment. This is the same containment studied by Cherry and Smith (2000), and the locations for postulated corrosion in the steel shell coincide with those assumed in that study. Corrosion is assumed to occur at the knuckle between the spherical and cylindrical portions of the drywell, which has the shape of an inverted light bulb. Corrosion is also considered in the region of the sand pocket at the concrete floor inside the drywell, and in the wetwell at the waterline. In addition, corrosion in one of the large bellows in the vent lines that connect the drywell and wetwell is also considered. The effect of bellows corrosion was not considered by Cherry and Smith.

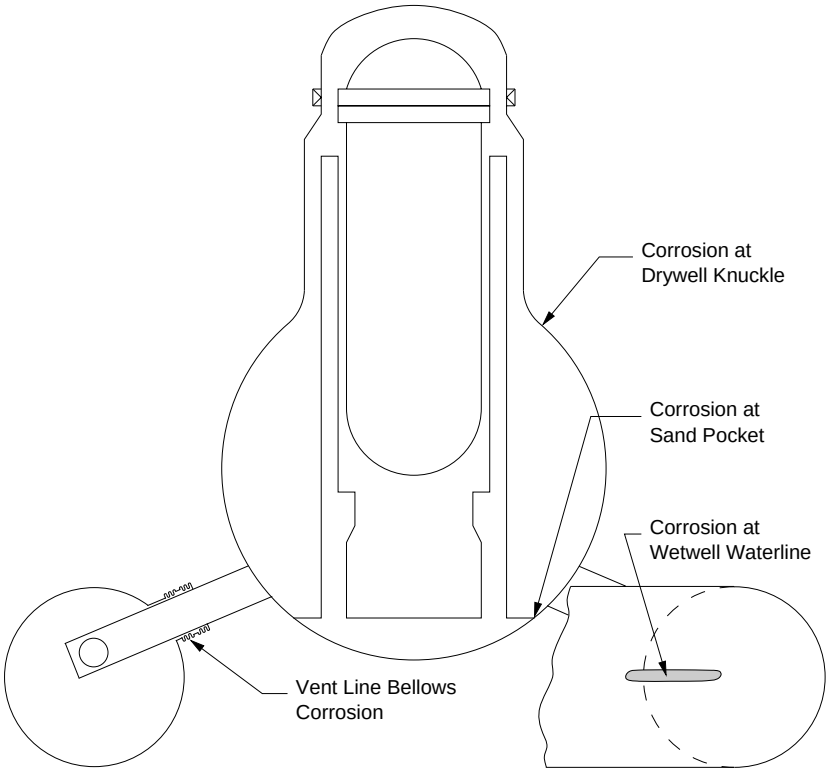

Figure 4.1: Postulated Corrosion in Liner of Steel Mark I Containment

4.1 Structural Model of Steel Mark I Containment

A combination of several different finite element models was used to model the steel Mark I containment in its original state and with the presence of corrosion in the locations mentioned previously. To model the global behavior of the containment, 3D models of a 22.5 degree slice of the containment were created using shell elements. Four such models were created and analyzed in this study. The first one contained the basic features of the containment. The second model of

the whole containment was used to model the effects of some of the larger penetrations, including the equipment hatch and a wetwell access hatch. The third and fourth models of the whole containment included the effects of corrosion. In addition to the global models of the containment, a series of 3D models of the local regions around representative penetrations was also created. In these models, the steel is modeled by continuum elements, rather than by shell elements, as is the case in the coarser, global models.

The models of the steel Mark I containment use the same baseline material properties and temperature/pressure relationship used by Cherry and Smith. The material properties are varied in the parametric analyses that use the parameters generated by LHS.

4.1.1 Global Baseline Containment Model

As mentioned above, all of the global models of the containment model a 22.5 degree slice using shell elements. The drywell, wetwell, and vent line are all included in a single model, as shown in Figure 4.2. As can be seen in the detailed view of the vent line shown in Figure 4.3, the bellows convolutions are explicitly modeled. This model differs somewhat from the model used by Cherry and Smith for this containment. In that model, the drywell and wetwell were modeled separately, and the forces transmitted through the vent line were estimated and applied as boundary conditions to the two models. Because of increased computational power available at the time of the current work, it seemed more practical to explicitly model the coupling between the drywell and wetwell in a single model. This helped simplify the process of analyzing the effects of corrosion in the vent line bellows.

The baseline model of the containment incorporates relatively few local features. The flanges in the region of the head gasket, as well as the vent line details and the ring stiffeners in the region of the wetwell supports. Any details such as penetrations that are not repetitive in nature are not included. The thickness of the shell varies throughout the containment, and these changes are incorporated into the model.

Along the edges of the slice, the containment model uses boundary conditions appropriate for the symmetry assumptions made. The base of the drywell, which lies below the concrete floor, is not included in the model. The drywell model begins at the edge of the concrete floor, which is in roughly the same location as the sand pocket. The nodes along this bottom edge of the model are fixed against displacement. As was the case in the analyses of Cherry and Smith, contact between the drywell shell and the concrete shield building, which are separated by a 5.1 cm (2 in) wide air gap, is neglected. This is a conservative assumption, because the shield building limits further deformation of the steel shell once contact occurs.

Figure 4.2: Finite Element Mesh of Drywell, Vent Line, and Wetwell

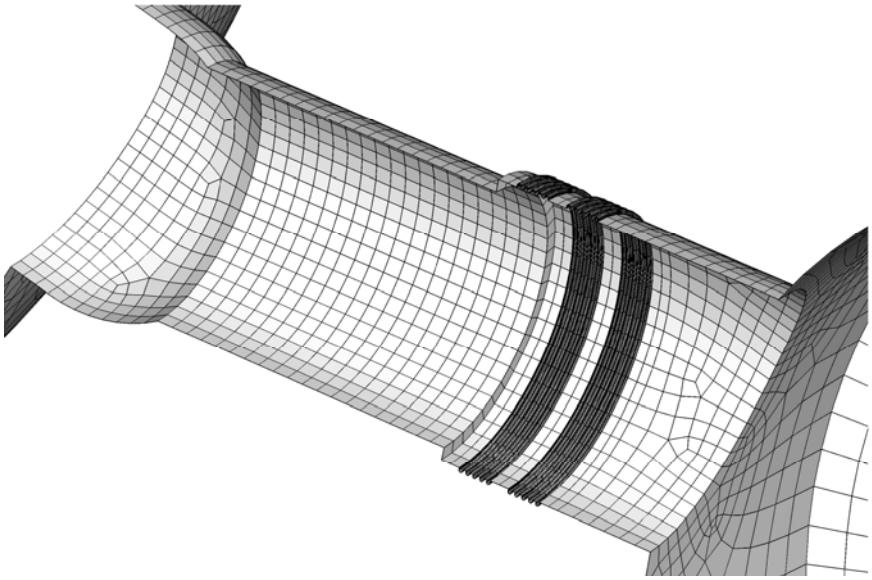

Figure 4.3: Detailed View of Mesh in Vent Line Region

4.1.2 Containment Penetration Models

Figure 4.4 shows the approximate locations of the local details modeled in this study. These details include relatively large features, such as the equipment hatch and wetwell access hatch, as well as smaller pipe penetrations. In addition to these, the vent line bellows are modeled with a reasonable level of detail in all of the global models. Finally, the behavior of the drywell head gasket is modeled using a separate computer program. While the details selected here are not all-inclusive, it is believed that they provide a representative sample of the details present in all parts of the containment. The models used to analyze these local details are described below.

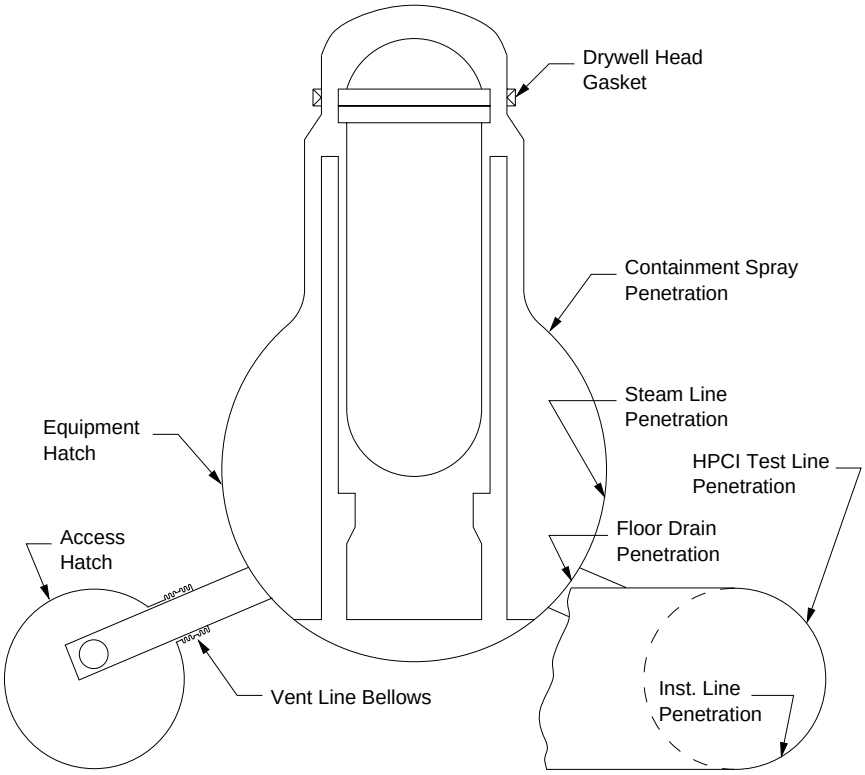

Figure 4.4: Approximate Locations of Local Details Analyzed in Steel Mark I Containment

4.1.2.1 Global Model with Large Penetrations

The basic global model of the containment that was shown in Figure 4.2 was modified to include two large features: an equipment hatch and a wetwell access hatch. These were not included in the basic model because they are large enough that they could have a significant effect on the response in the areas surrounding them, and would have unduly complicated the basic model. Because of the large size of these penetrations, it is not reasonable to simply transfer boundary conditions from the basic model to submodels of these features. Figure 4.5 shows a view of the entire mesh of the model with these large penetrations.

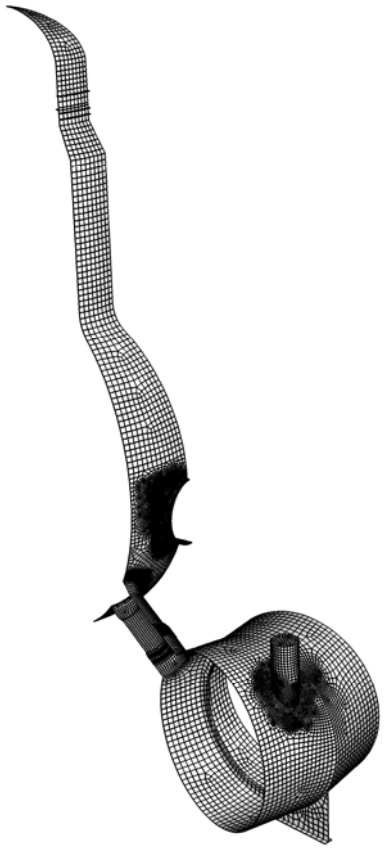

Figure 4.5: Finite Element Mesh of Containment with Large Penetrations

Figure 4.6 shows a detailed view of the region around the equipment hatch, and Figure 4.7 shows a similar detailed view of the wetwell access hatch. The shaded regions in these figures represent areas where the plate is thickened around the penetrations. Like the base model, the penetration regions are modeled entirely with shell elements.

In the case of the equipment hatch, the thickened plate around the hatch is 4.45 cm (1.75 in) thick, while the surrounding containment shell makes a transition from 1.91 cm (0.75 in) thick in the upper area to 3.18 cm (1.25 in) thick in the lower area around the equipment hatch. While the lower part of the stiffening plate is curved to ease the transition to the rest of the shell, there are fairly sharp corners on the upper portion. This causes a stress concentration, and the mesh is refined to a relatively high degree in that region to capture that. The stiffening plate around the wetwell access hatch is 4.45 cm (1.75 in) thick, while the wetwell shell surrounding that area is 2.86 cm (1.125 in) thick.

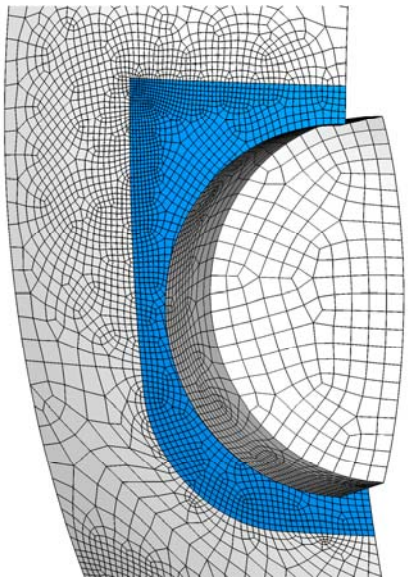

Figure 4.6: Mesh Detail of Equipment Hatch Area

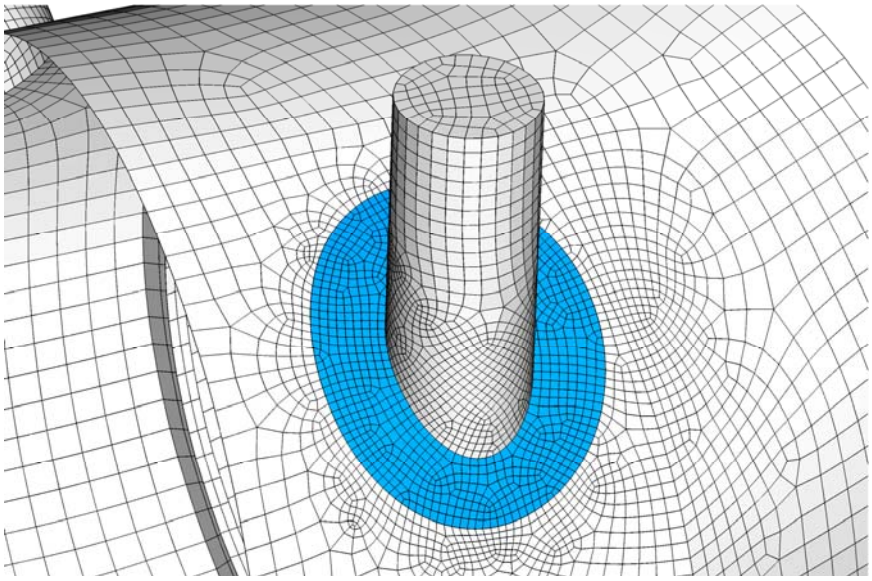

Figure 4.7: Mesh Detail of Wetwell Access Hatch Area

4.1.2.2 Detailed Models of Smaller Penetrations

The rest of the penetrations selected for study were modeled with detailed 3D finite element models. These models, which use 3D continuum elements, represent the pipe, the stiffener surrounding the penetration, the transition to the surrounding containment shell, and a section of the surrounding containment large enough to reasonably contain the local effects. These models are either half-symmetry or quarter-symmetry, depending on the geometric details. Strains were taken from the global model at points corresponding to the locations of the penetrations, and used to compute appropriate displacement boundary conditions. Temperatures were also applied to coincide with those applied to the global model.

Figure 4.8 shows the mesh used to analyze the region around a steam line penetration, the approximate location of which is shown in Figure 4.4, as are all of the penetrations studied here. In this location, two identical pipes 1.66 m (65.4 in) apart at their centers penetrate the drywell shell side by side. The pipes are 3.81 cm (1.5 in) thick, and do not penetrate the containment normal to the shell. The penetration angle is approximately 11 degrees from the vertical and 20 degrees from the horizontal. The finite element model uses half symmetry to include only one of the pipes. While the orientations of the pipes are such that the penetrations are not exactly symmetric, this simplification does not affect the results significantly. The thickened area around the two pipes is 4.45 cm (1.75 in) thick, and the surrounding drywell shell is 1.91 cm (0.75 in) thick. The transition from the thickened plate to the surrounding plate is made on a 1:4 slope on either side. This is true of all of the penetrations modeled here. The thickened plate is 1.17 m (46 in) high by 2.83 m (111.4 in) wide, measured from points before the transition begins to the thinner material.

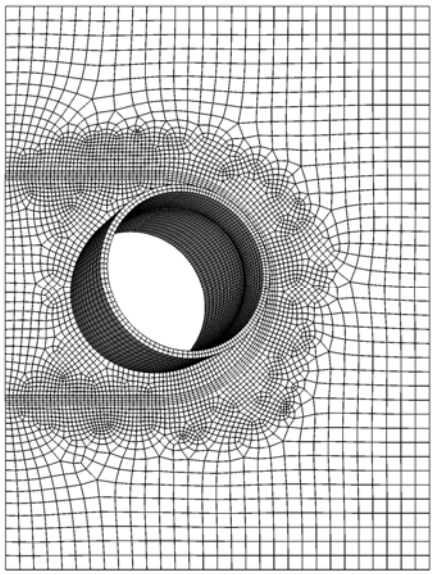

Figure 4.8: Steam Line Penetration Submodel

The next penetration studied, a floor drain line penetration, is similar to the steam line penetration in that there is again a pair of pipes penetrating the drywell shell side by side. These pipes penetrate the drywell at a point lower than the steam lines, where the drywell shell is 3.18 cm (1.25 in) thick. The pipes are much smaller than the steam lines, with outside diameters of 8.89 cm (3.5 in) and wall thicknesses of 0.76 cm (0.3 in). The thickening plate is 33.0 cm (13 in) high and 94.0 cm (37 in) wide, and the pipes are spaced 61.0 cm (24 in) apart from center to center. The pipes are horizontal, but because of the angle of the containment at that point, they penetrate at about 29 degrees from normal. Similarly to the steam line penetration, half symmetry was assumed to reduce the model size. Figure 4.9 shows the mesh used to model this penetration.

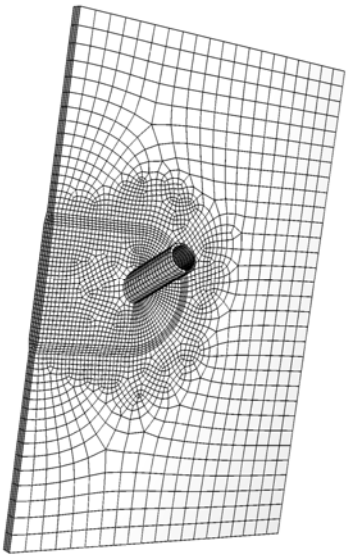

Figure 4.9: Floor Drain Penetration Submodel

The third drywell penetration chosen for study by a detailed finite element model is a containment spray line penetration located just below the transition from a cylinder to a sphere. This penetration is of particular interest because initial analyses indicated that under pressure loads, this area experiences higher strain than other areas in the shell. The shell in this region is 1.91 cm (0.75 in) thick, and the thickened plate is 4.45 cm (1.75 in) thick. In this case, a single pipe with outside diameter of 35.6 cm (14.0 in) and thickness of 1.91 cm (0.75 in) penetrates the containment, at an angle of 34 degrees from normal. The stiffener plate is 68.6 cm (27 in) in diameter. Figure 4.10 shows the half symmetry mesh generated for this penetration.

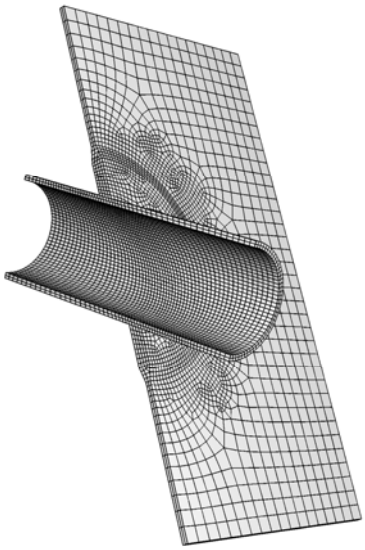

Figure 4.10: Containment Spray Line Penetration Submodel

To model a representative sampling of details located throughout the containment, two local models of penetrations in the wetwell were also developed. One of these, a wetwell instrumentation line penetration, is located in the lower portion of the wetwell, and the other, a

high pressure coolant injection (HPCI) test line penetration, is located in the upper portion. In both cases, a single pipe surrounded by a circular thickening plate is oriented normal to the wetwell shell, making it possible to use quarter symmetry models. Figure 4.11 and Figure 4.12 show the models of these two penetrations.

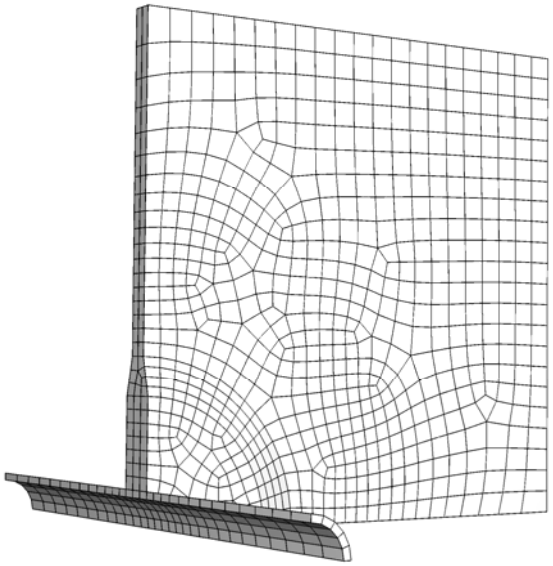

Figure 4.11: Wetwell Instrumentation Line Penetration Submodel

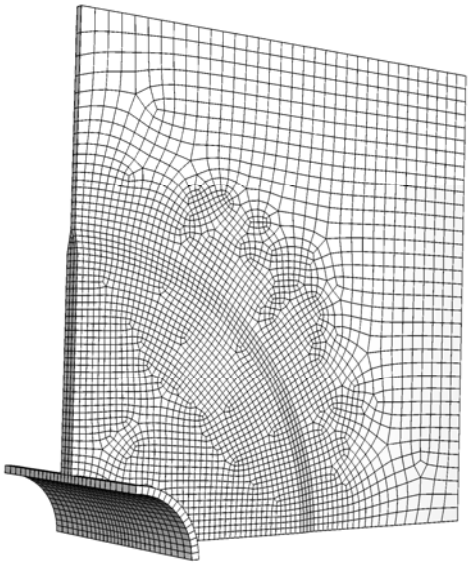

Figure 4.12: Wetwell HPCI Test Line Penetration Submodel

The wetwell instrumentation line has an outside diameter of 6.03 cm (2.38 in) and a wall thickness of 0.55 cm (0.22 in). The thickened plate around the penetration is 3.18 cm (1.25 in) thick and 19.6 cm (7.7 in) in diameter, and the wetwell shell surrounding the penetration is 1.71 cm (0.675 in) thick.

The HPCI test line has an outside diameter of 27.31 cm (10.75 in), and the pipe wall is 1.51 cm (0.59 in) thick. The circular thickened plate around this penetration is 3.81 cm (1.5 in) thick and has a diameter of 109.6 cm (43.2 in). The wetwell shell surrounding this penetration is 1.53 cm (0.604 in) thick.

4.1.3 Analysis of Drywell Head Gasket

In addition to considering tearing and rupture at local details, it is also important to consider the possibility of leakage of seals. The drywell head gasket was analyzed for leakage in this study because it is an important potential location for early leakage, and the drywell head is one of the leakage locations specifically considered in the risk analysis of this plant.

Rather than use a detailed analytical model, the approach used here is to perform a basic engineering calculation of the leakage area that results from opening of the head gasket due to internal pressurization. In the process of obtaining expert judgment of the failure pressures for this containment in the NUREG-1150 study, expert C used a relatively simple FORTRAN program to obtain probability distributions of the leakage and rupture pressures for the drywell head gasket. The source code for this program appears in page 5.3-38 of NUREG/CR-4551 Vol. 2, Rev. 1, Part 3 (Breeding et al., 1992). This code accounts for the amount of preload in the drywell head bolts, the deformation of the head bolts and drywell shell in that region, the temperature difference between the head bolts and the drywell shell, and the ability of the head gasket to spring back to fill an opening.

The code was modified slightly to input and output the computed data in a different format, but the intent was to leave the core parts associated with the leak area computation unchanged because the underlying principles seemed reasonable. In the process of adapting this code, however, two critical errors were discovered in the original code. In a part of the code that interpolates over a table of temperature-dependent material properties, the interpolation is not done properly. Also, in computing the leak area, the preload force for just one bolt is considered, when that force should have been multiplied by the number of bolts. These two errors actually tended to cancel each other out, resulting in fairly plausible results. The code used in the current work corrects both of these errors.

The end result of running the head gasket code is an opening area vs. pressure curve. When the opening reaches a size of 64.5 cm^2 (10 in^2), it is considered a “leak”, and when it reaches a size of 1672 cm^2 (259 in^2), it is considered a “rupture”.

4.1.4 Corroded Region Models

In the current work, corrosion is postulated in two locations in the drywell and one location in the wetwell. The locations and sizes of these corroded zones are similar to those assumed by Cherry and Smith. In addition to those regions, the current work also considers corrosion in one of the plies of the vent line bellows. The corroded areas are modeled using modified versions of the global shell model of the entire containment. The mesh is refined in the areas where corrosion is postulated, and the shell elements are thinned to account for the corrosion. New models were developed for the current work, and one difference between the models used in the current work and those used by Cherry and Smith is that the boundaries of the corroded areas are made of smooth curves and contain no sharp corners, which tend to increase the stresses and could cause failure at a lower pressure. In the present work, corrosion is assessed with penetration depths of 25% and 50% through the containment shell in all areas investigated. In addition, corrosion is investigated in the drywell vent bellows. In the plant under consideration, the drywell vent

bellows have two-ply construction. One of the bellows plies is assumed to have experienced corrosion.

The original intent in the current work was to simply create a single model of the entire containment that incorporated all of these corroded regions. The corroded regions are far enough apart that negligible coupling is expected between them, meaning that a single model where all of these regions are corroded would produce essentially the same results as separate models for each of these cases would produce. When performing the parametric studies to generate probability distributions of the failure pressures, it was found that because of the level of mesh refinement in all of the corroded areas, the single model that incorporated all of the corroded areas required an unreasonable amount of analysis time. Therefore, two models of the containment with corrosion were developed. The first one only modeled the corrosion assumed in the drywell sand pocket region, while the other model contained the corrosion in the drywell knuckle region, the wetwell, and the bellows. This change resulted in more reasonable run times with very similar results.

4.1.4.1 Corroded Shell Models

Figure 4.13 shows a detail of the mesh in the region where corrosion is postulated in the drywell knuckle region just below the point where the transition is made to a sphere from a cylinder. This area was selected because it is a region of elevated strains under pressure because it is close to a discontinuity. Water dripping down the outside of the drywell could also accumulate here, and the outside of the shell at this location is inaccessible for visual inspection because of the shield building. The elements in the corroded area are shaded. The shell in this area has a thickness of 1.91 cm (0.75 in), and with the assumption of corrosion 25% through the depth, the corroded elements have a thickness of 1.429 cm (0.563 in). In the model with corrosion 50% through the depth, the corroded elements have a thickness of 0.953 cm (0.375 in). The assumed corrosion region is about 38 cm (15 in) high and its 1.27 m (50 in) width spans half of the 22.5 degree slice of the containment. Accounting for the symmetry of the model, the actual width of the corroded zone would be 2.54 m (100 in).

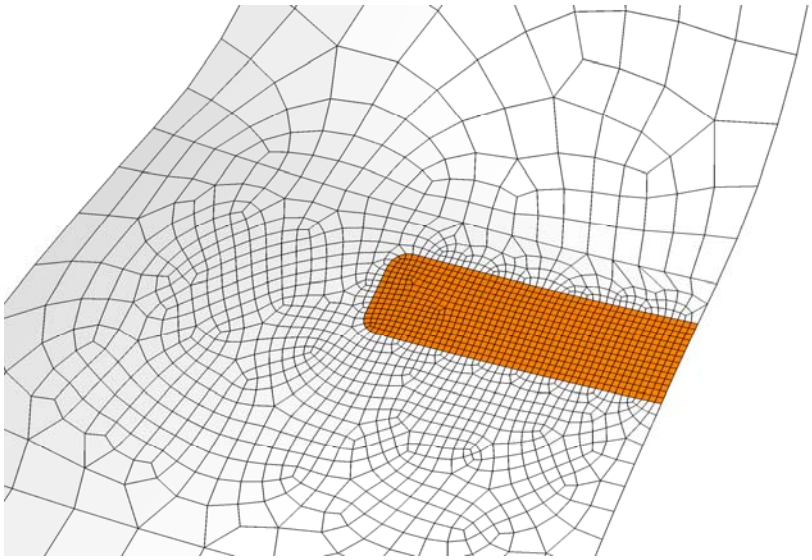

Figure 4.13: Mesh Detail of Drywell Knuckle Corrosion Area

The other region in the drywell where corrosion is studied is just above the sand pocket region. This is also a difficult to inspect area where moisture could potentially accumulate. As for the sand pocket area, a region extending half way across the slice was assessed with corrosion 25% and 50% through the shell. The corroded region in the model (shown in Figure 4.14) is about 32 cm (13 in) high, and 1.07 m (42 in) wide, meaning that with symmetry conditions, the region is actually 2.14 m (84 in) wide. The shell in this region is 3.18 cm (1.25 in) thick. In the model of corrosion 25% through the depth, the corroded area is 2.38 cm (0.938 in) thick, while in the 50% corrosion model, it is 1.59 cm (.63 in) thick.

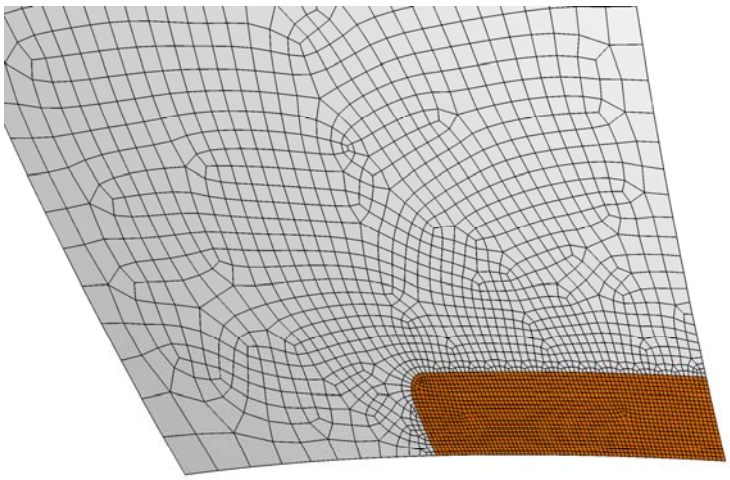

Figure 4.14: Mesh Detail of Corroded Area at Sand Pocket

The final corroded region (Figure 4.15) in the containment shell was assumed to occur at the water line in the wetwell. In the segments of the wetwell without vent line penetrations, which is where this corrosion is assumed to occur, the shell is 1.53 cm (0.604 in) thick in the upper half, and 1.71 cm (0.675 in) thick in the lower half. During normal operation, the water level in the wetwell is very close to the transition point between these two thicknesses. A region of corrosion 25.4 cm (10 in) high is assumed to straddle this transition point. The corroded region assumed here is centered on the outside of the torus between two ring stiffeners, and extends half of that distance. The corroded zone in the model is 2.16 m (85 in) wide, meaning that by symmetry, it is actually modeling a zone 4.32 m (170 in) wide. It is assumed that a uniform corrosion depth occurs over the full corrosion region. The corrosion depth is expressed as a percentage of the upper, thinner shell. Thus, with 25% corrosion, the upper shell is 1.15 cm (0.453 in) thick and the lower shell is 1.33 cm (0.524 in) thick. In the case where 50% corrosion is evaluated, the upper shell is 0.767 cm (0.302 in) thick, and the lower shell is 0.947 cm (0.373 in) thick.

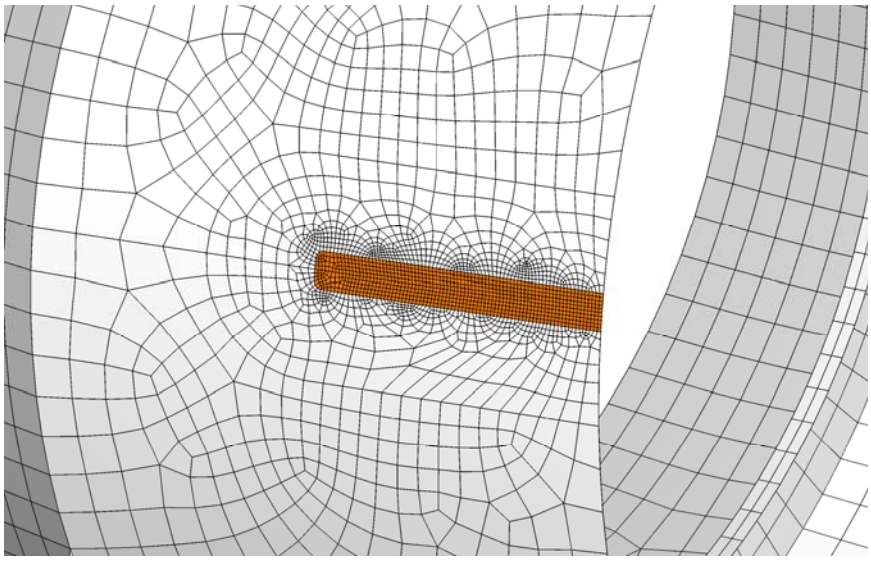

Figure 4.15: Mesh Detail of Corroded Area at Wetwell Waterline

4.1.4.2 Corroded Bellows Model

One of the objectives of the current study is to investigate the effects of bellows corrosion in a risk-informed framework. Bellows can be found in both steel and concrete containments, but are found more often in steel containments. Most bellows that form a part of the containment pressure boundary are used in process piping penetrations to allow for relative movement between the pipe and the containment. These process piping bellows are typically located on the outside of the containment, so that as the containment expands due to internal pressurization, as could potentially occur in an accident, the bellows would be compressed. The bellows may be subjected to a combination of lateral and axial movements, depending on the orientation of the pipe relative to the containment.

In addition to the process piping bellows, the second major use of bellows in nuclear power plant containment vessels is in the vent lines that connect the drywell and wetwell in steel Mark I containments, such as the one investigated here. These bellows typically have a larger diameter than process piping bellows, and would not be subjected to relative movements as large as those observed in process piping bellows.

Both process piping bellows and vent line bellows can have either a single ply or two plies. Two-ply bellows are separated by a wire mesh, which allows for the region between the two plies to be pressurized to check for leaks. The vent line bellows in the containment studied here have two plies, but it is actually quite common for these bellows to only have a single ply.

Corrosion in bellows, which are made of stainless steel, is of a much different nature than corrosion in the carbon steel that makes up the rest of the containment pressure boundary. Because of the large residual stresses retained in the bellows during the forming process, they are susceptible to transgranular stress corrosion cracking (TGSCC). Unlike corrosion in the liner shell, which penetrates the steel to a certain depth, leaving the uncorroded material untouched, TGSCC results in microscopic cracks that are difficult to detect and typically extend through the depth of the material. Very little residual strength remains in the region of the bellows where this has occurred. TGSCC is usually detected by leak rate tests rather than visual observation (Cherry et al., 2001).

An experimental study conducted at Sandia National Laboratories (Lambert and Parks, 1995) subjected a number of bellows to extreme conditions of pressure and displacement, and found that before they have experienced any age-related degradation, bellows are generally very resistant to leakage under these conditions. Leakage was only observed when the bellows were subjected to displacements close to the point of full compression.

In addition to testing bellows in their original state, Lambert and Parks also attempted to induce corrosion in bellows and determine how their capacity is reduced. Their goal was to induce corrosion sufficient to potentially degrade the bellows performance in severe accident conditions, but not so much that the bellows would fail a leak rate test prior to being subjected to those extreme conditions. In attempting to do this, they found that because of the nature of stress corrosion cracking, it is very difficult to control the amount of corrosion. Of the six corroded bellows tested, three had no detectible leakage prior to being loaded, two had minor leakage, and one had a significant amount of leakage.

Five of the corroded bellows tested were two-ply, and intended to be representative of process piping bellows. The sixth bellows specimen had a single ply, and was typical of a vent line bellows. All of the bellows were corroded from the outside, meaning that for the two-ply bellows, the inner ply was not corroded. Great care was taken to not excessively corrode the single ply bellows because breaking the pressure boundary would have made testing very difficult.

In general, the findings of these tests were that for the two-ply bellows, large deformations of the bellows caused the existing corrosion cracks to expand. When the bellows were highly compressed, the leak rate tended to decrease due to the pressing together of the convolutions, but when they were returned to their un-displaced configuration, the leak paths were allowed to open up. The containments that exhibited minor leakage prior to the test had large leak rates, while those that were initially leak-tight had small leak rates after the tests. The single ply bellows had fairly minor corrosion, and did not leak after the test, although cracks had grown and it appeared that it was on the verge of leaking.

The level of deformation required to initiate leaking in a corroded bellows is a very uncertain quantity due to the nature of stress corrosion cracking. It appears that little would be gained by performing detailed structural analyses of a degraded process piping bellows because of the difficulty in developing a criterion for the initiation of leakage. In the Mark I containment studied here, process piping bellows are not likely to experience very large deformation during severe accident conditions because the drywell displacement is limited to about 5.1 cm (2 in) because of contact with the shield building.

The vent line bellows in the Mark I containment seemed to be a better candidate for study. As has been mentioned previously, the baseline shell model of the containment explicitly incorporates the bellows with a reasonable level of detail. The two-ply bellows are approximated as a single ply with twice the thickness of a single ply in the model. In the finite element model, each 180-degree turn in the bellows convolutions is traversed by 6 elements, with an edge length of about 0.8 cm (0.3 in), and the edge length of those elements in the other direction is about 14.5 cm (5.7 in). In the baseline analyses, the differential movement in the vent line bellows in the late stages of the analysis is a small fraction of the original bellows length. Thus, it appears that the ability of the vent line bellows to withstand high internal pressures is more important than their ability to withstand large deformations.

The degraded vent line bellows are assumed to have corrosion in one of the plies. To model this, it is assumed that the corroded region of the ply has lost all of its strength. Much like the other corroded zones in the containment shell, the elements in the corroded zone of the ply are assigned half of the thickness of the surrounding bellows elements to simulate the loss of strength of one of the plies. Shell elements are used throughout all parts of the bellows plies.

The vent line bellows are universal bellows, with two 26.4 cm (10.4 in) long sections of bellows convolutions separated by a 15.3 cm (6 in) long center spool. The inside diameter of the bellows is 226 cm (89 in), the convolution depth is 4.8 cm (1.9 in), and the convolution pitch is 5.9 cm (2.3 in). The bellows are constructed of two 0.20 cm (0.08 in) thick plies of A240 Type 304 stainless steel.

Figure 4.16 shows a detailed view of the degraded portion of the bellows. The degraded area covers an approximately 25 x 100 cm (10 x 40 in) elliptical area that spans the length of one of the sets of convolutions at the lower part of the bellows. In the view of the mesh, the corroded zone is shaded. The other set of convolutions shown in the figure illustrates the meshing scheme used in the un-corroded bellows.

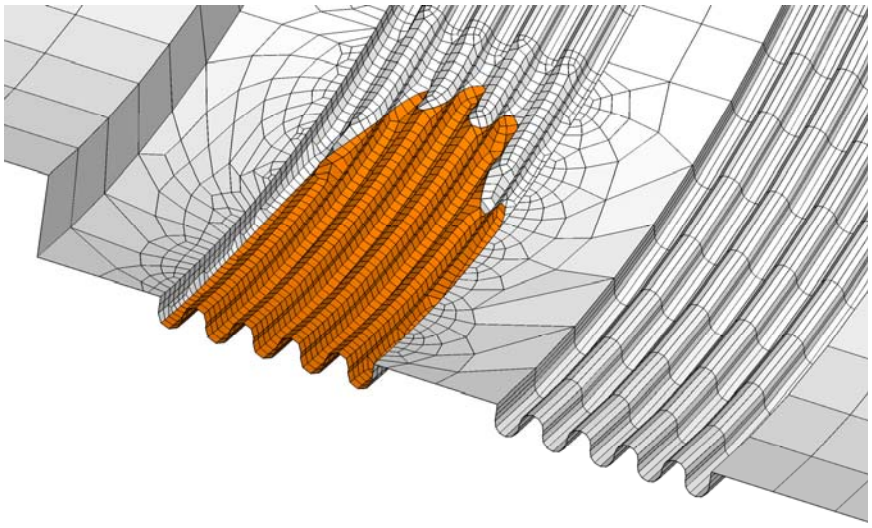

Figure 4.16: Mesh Detail of Corroded Bellows Area

The same methodology for checking for tearing in the containment shell is used in the bellows. The report of Lambert and Parks provides a series of stress-strain curves taken from 40 specimens at temperatures ranging from room temperature to 371 °C (700 °F). This data is used to develop the statistical parameters describing the bellows material in this work. Bellows material is extremely ductile at room temperature, with ultimate strains of around 0.7. At elevated temperatures, the ductility is significantly decreased. At 218 °C (415 °F), the ultimate strain drops to about 0.4.

One important consideration in the investigation of the bellows is whether a tear is likely to develop into a hole large enough to be considered a “rupture”. A series of experiments on cracked bellows subjected to severe loading conditions is reported in Takenaka et al. (1989). In these experiments, circumferential through-wall cracks of varying lengths were imposed on the

bellows with a machining process. The longest of these cracks extended 120° around the bellows. A rubber sealing material was used to prevent leakage to allow for the bellows to be pressurized. Even in the bellows with the longest crack, no unstable crack growth was observed when the bellows was subjected to high pressure and displacement conditions. In the specimen with the longest crack, unstable squirm of the bellows occurred under the loading conditions, but no crack propagation was observed. These experiments confirm that bellows steel is extremely tough and resistant to unstable crack propagation. Based on this, it is assumed in the current work that a bellows tear results only in a "leak", and that "rupture" will not occur in the bellows.

4.1.5 Structural Analysis with Best Estimate Properties

In addition to the parametric analyses performed with the input parameters generated by LHS, a baseline analysis of the BWR Mark I containment was performed using mean values of those parameters. The results of this analysis will be presented first because they help in the understanding of the fragility analysis results. The containment analysis consists of a combined study of the global and local models described in previous sections.

Figure 4.17 shows a plot of the potential for failure vs. pressure for all of the potential failure locations considered in the current work for the un-degraded containment, as well as for the locations with assumed 25% corrosion depth. The local details in the un-degraded containment are shown in solid lines, the corroded areas are shown in dashed lines, and the head gasket is shown in a dotted line. In this plot, the failure function is simply the quantity used to determine when leakage occurs, divided by its limiting value. In the locations where tearing would cause leakage, the magnified plastic strain is used to determine when leakage occurs. The limiting value of the magnified plastic strain is the uniaxial failure strain. For the head gasket leak, the failure function is obtained by dividing the opening area by the "leak" threshold area.

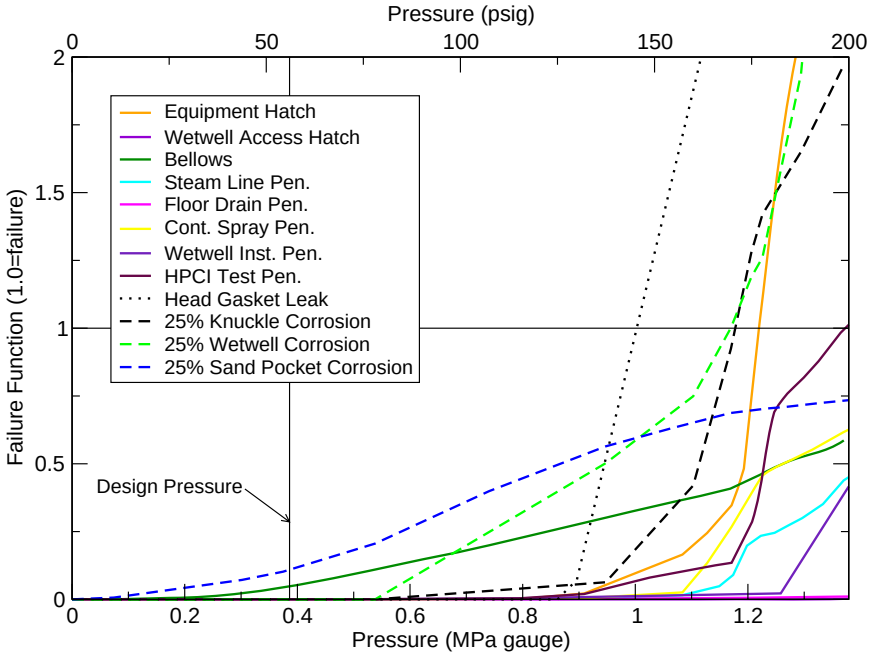

Figure 4.17: Leakage Potential for All Penetration Details and 25% Corrosion Locations

From this plot, it is clear that for the un-degraded containment, the head gasket is the dominant cause of leakage. The bellows and several of the penetrations all appear to fail at about the same point. The floor drain penetration is not likely to result in a failure, as the magnified strains are very low even at the maximum analysis pressure. This is because it is located in a much thicker section of the containment shell than the other penetrations. With 25% corrosion depth, two of the corrosion locations postulated here (at the drywell knuckle and at the wetwell waterline) experience tears at pressures below the failure pressure at any of the locations investigated in the un-degraded containment. Corrosion 25% through the shell at the sand pocket is less critical than tearing at other details of the containment, and does not occur before the time of analysis termination at 1.38 MPa (200psig).

Figure 4.18 shows a plot very similar to that in Figure 4.17, except that the results for the 50% corrosion depth cases are shown in place of the results for the 25% corrosion depth cases. The results for the corrosion through 1 vent line bellows ply are also shown on this plot. The un-corroded detail results are also shown on this plot for comparison purposes, and are exactly the same as those in Figure 4.17. Increasing the corrosion depth to 50% has a significant effect on all of the locations considered. With corrosion 50% through the shell, leakage is now expected to occur at the wetwell waterline before it would occur anywhere in the un-degraded containment. The corroded bellows and drywell knuckle did not completely reach the failure criterion at the time their analysis was terminated, but failure appears imminent, and the results can be reasonably extrapolated to estimate a failure pressure in this case. That analysis terminated early because large strains elsewhere in the model made it difficult to obtain a converged solution.

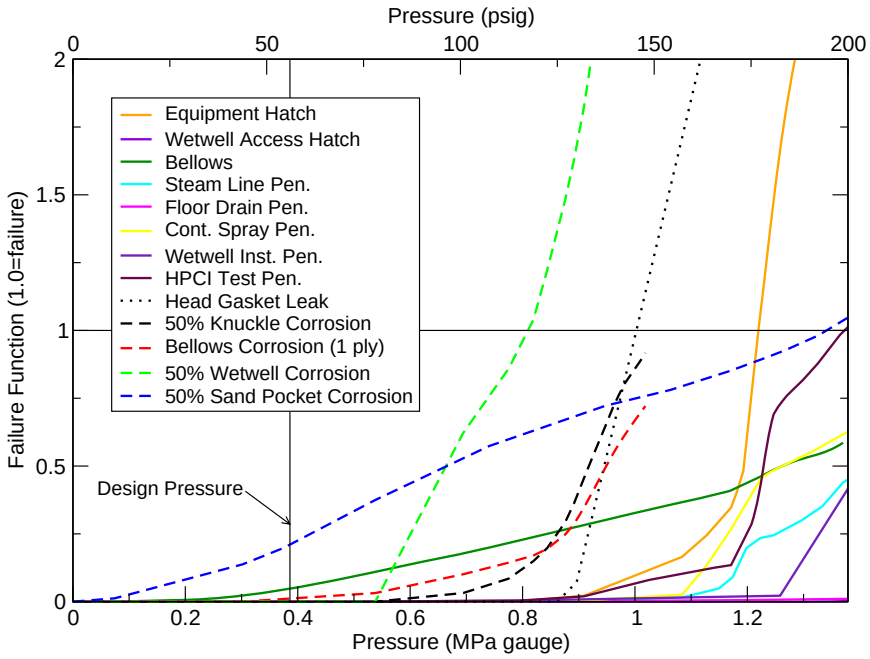

Figure 4.18: Leakage Potential for All Penetration Details and 50% Corrosion Locations (Including 1 Ply Bellows Corrosion)

Table 4.1 provides a summary of the “leak” and “rupture” pressures for the locations checked in the current analyses. This table also provides a listing of the sizes of the features used as an estimate of the crack size for the rupture criterion, as well as the length of the crack that would be required for the containment to rupture given the stress level at the “leak” pressure. Finally, this

table provides a listing of the risk analysis failure modes to which the individual details are assumed to contribute. A listing of the meanings of the abbreviations for these failure modes is provided in

Table 4.2.

Table 4.1: Summary of Locations and Failure Pressures

Location	Leak Pressure MPa (psig)	Rupture Pressure MPa (psig)	Assumed Feature Size m(in)	Crit. Crack Size at Leak m(in)	Risk Model Mode
Equipment Hatch	1.21 (176.9)	1.21 (176.9)	4.57 (180)	0.20 (7.8)	DWL, DWR
Wetwell Access Hatch	†	†	3.05 (120)	†	WWLaW, WWRaW, CWWR
Bellows	†	N/A	N/A	N/A	WWLaW
Steam Line Pen.	†	†	2.90 (114)	†	DWL, DWR
Floor Drain Pen.	†	†	1.02 (40)	†	DWL, DWR
Cont. Spray Pen.	†	†	0.79 (31)	†	DWL, DWR
Wetwell Inst. Pen.	1.56 (225.9)*	1.56 (225.9)*	0.25 (10)	0.09 (3.7)	WWLbW, WWRbW, CWWR
HPCI Test Pen.	1.37 (199.1)	1.37 (199.1)	1.19 (47)	0.05 (2.1)	WWLaW, WWRaW, CWWR
Head Gasket	1.00 (145.4)	1.68 (243.5)	N/A	N/A	DWHL, DWHR
Knuckle Corrosion (25%)	1.18 (170.8)	1.18 (170.8)	2.54 (100)	0.15 (5.8)	DWL, DWR
Knuckle Corrosion (50%)	1.04 (151.0)*	1.04 (151.0)*	2.54 (100)	0.18 (7.2)*	DWL, DWR
Bellows Corrosion	1.12 (162.4)	N/A	N/A	N/A	WWLaW
Wetwell Corrosion (25%)	1.17 (169.6)	1.17 (169.6)	4.32 (170)	0.14 (5.3)	WWLaW, WWRaW
Wetwell Corrosion (50%)	0.809 (117.4)	0.809 (117.4)	4.32 (170)	0.91 (36.0)	WWLaW, WWRaW
Sand Pocket Corrosion (25%)	†	†	2.13 (84)	†	DWL, DWR
Sand Pocket Corrosion (50%)	1.34 (194.5)	1.34 (194.5)	2.13 (84)	1.55 (61.1)	DWL, DWR

*Failure pressure not reached in analysis. Result extrapolated from last analysis steps.
†Failure pressure not reached in analysis. Last step too far from failure point to reasonably extrapolate result.

Table 4.2: Risk Model Failure Mode Abbreviations

Abbreviation	Meaning
DWL	Drywell Leak
DWR	Drywell Rupture
CDWR	Catastrophic Drywell Rupture
DWHL	Drywell Head Leak
DWHR	Drywell Head Rupture
WWLaW	Wetwell Leak above Waterline
WWRaW	Wetwell Rupture above Waterline
WWLbW	Wetwell Leak below Waterline
WWRbW	Wetwell Rupture below Waterline
CWWR	Catastrophic Wetwell Rupture

From the analysis results, it is apparent that in most cases, the assumed crack length, based on the size of the feature where it initiates, is far longer than the crack length required for unstable crack growth at the loading pressure. This means that in most cases, the "leak" and "rupture" pressures are identical. In the best estimate case presented here, there are no instances of the rupture pressure being greater than the leak pressure. In the LHS analyses, however, it is likely that there would be a few cases where a rupture does not form immediately upon tear initiation. As mentioned previously, if a rupture occurs in the drywell, catastrophic rupture is precluded by the presence of the shield wall. In the wetwell, however, a rupture will immediately grow into a catastrophic rupture. In those locations, the pressures for "leak", "rupture", and "catastrophic rupture" are identical in most cases.

It is interesting to note that for most of the penetrations, the critical crack length at the tearing pressure is very small, and clearly below the size of the feature causing the strain localization. For the cases of corrosion, however, the critical crack lengths at the tearing pressure are larger. This is especially true in as the corrosion depth increases, because the tearing pressure is reduced due to the thinning of the shell. If smaller zones of corrosion were assumed, the probability of experiencing leak before rupture would be increased.

4.2 Fragility Analysis of Degraded Steel Mark I Containment

A procedure similar to that used for the reinforced concrete was used to generate fragility curves for the Steel Mark I containment. After the global and local models of this containment were finalized, random variables were chosen and LHS was used to generate a 30 sets of random input parameters to develop fragility curves.

Table 4.3 shows a listing of the random parameters used in this analysis. Random parameters were generated to approximate randomness in properties of the plate steel, bellows steel, and drywell head gasket. In addition, random parameters were used to account for epistemic uncertainty.

Table 4.3: Random Input Parameters

Property	Median	COV/β	Distribution
Plate Steel			
Ultimate Strength (f_u)	682 MPa (98.9 ksi)	0.09	Lognormal
Yield Strength Factor	1.0	0.07	Normal
Elastic Modulus (E_s)	200 GPa (29000 ksi)	0.06	Normal
Uniaxial Failure Strain (ε_{fail})	0.25	0.12	Normal
Fracture Mech. Cutoff *J*	1.0	0.10	Lognormal
Corrosion Depth Uncertainty	1.0	0.10	Normal
Bellows Steel			
Ultimate Strength (f_u)	719 MPa (104.3 ksi)	0.12	Lognormal
Yield Strength Factor	1.0	0.07	Normal
Elastic Modulus (E_s)	200 GPa (29000 ksi)	0.06	Normal
Uniaxial Engineering Failure Strain (ε_{fail})	0.76	0.13	Normal
Drywell Head Gasket			
Temperature Difference	75 °F	0.28	Lognormal
Bolt Preload	445 kN (100 kips)	0.09	Lognormal
Gasket Resiliency	0.38 mm (0.015 in)	0.49	Lognormal
Bolt Yield Strength Factor	1.0	0.07	Normal
Epistemic Uncertainty			
Local 3D Model Strain Factor (f_{FEM-u})	1.0	0.30	Lognormal
Local Shell Model Strain Factor (f_{FEM-u})	1.0	0.35	Lognormal
Corrosion Factor Uncertainty (f_{c-u})	1.0	0.20	Lognormal

Stress/strain curves for the plate and bellows steel were generated in the same manner as was done for steel components of the reinforced concrete containment. Random numbers were generated for the ultimate strength strength, f_u. The yield strength, f_y, is computed by multiplying the ultimate strength by a second parameter, s, which has a mean value of 1.0, and a factor to represent the average ratio of the yield to ultimate strength, denoted as r.

$$f_y = s\,r\,f_u \tag{4.6}$$

For the plate steel, r is 0.53, while for the bellows steel, a value of 0.39 is used for r.

The variability in the parameters describing the randomness in the A516 Gr. 70 plate steel used in the steel containment shell is assumed to be the same as that in the steel liner of the reinforced concrete containment. The parameters describing the bellows steel are taken from the results of a series of coupon tests summarized by Lambert and Parks (1995).

A listing of the 10 failure modes for which conditional probabilities are required by the risk analysis models has been provided in Table 4.2. These modes are comprised of failures of various sizes at four location groupings: the drywell head (DWH), the rest of the drywell (DW),

the wetwell above the waterline (WWaW), and the wetwell below the waterline (WWbW). For the drywell head, failure is assumed to only occur at the gasket. For all of the other location groupings, multiple locations within those groupings were investigated. The raw and fitted fragilities for the locations falling within these groupings are presented below. They are organized by groupings, and the codes for the groupings in which they fall (e.g. DW, WWaW, etc.) are shown in the legends of the plots for each of these locations.

Figure 4.19 shows the fragilities for the leak and rupture modes of the head gasket. As mentioned previously, these were computed from a simple engineering analysis program written specifically for this application rather than from a detailed simulation. Figure 4.20 shows the fragilities for all of the locations within the drywell, and Figure 4.21 shows those for the wetwell both above and below the waterline. The failure locations shown in these plots are all present in the containment in its original condition. As noted in the figure captions, no failures were observed in the floor drain penetration or the wetwell access hatch in the 30 samples that were run. If more samples would have been run, it is possible that failures would have been observed, but these are clearly not governing cases, and will thus have a very negligible effect on the overall results. As a result, these locations are not considered in the computation of the fragility curves.

It should also be noted that in almost all of the locations in the original containment without corrosion, the rupture criterion is always met when the leak criterion is met. This means that the conditional probability of leak given failure at a location is always zero for these cases. The exceptions to this are the drywell head and the bellows failure. The head gasket fails by controlled opening of the pressure unseating gasket rather than tearing, and as mentioned before, it is assumed that a bellows failure can not be large enough to be considered a rupture. In the drywell region, there is a small air gap between the steel drywell shell and the concrete shield building. Because this would preclude a catastrophic rupture, as did the surrogate shield building in the Sandia steel containment test (Luk et. al., 2000), it assumed that a catastrophic rupture cannot occur in the drywell. On the other hand, a rupture in the wetwell shell is assumed to immediately grow to become a catastrophic rupture, because there is nothing to prevent a running crack from stopping.

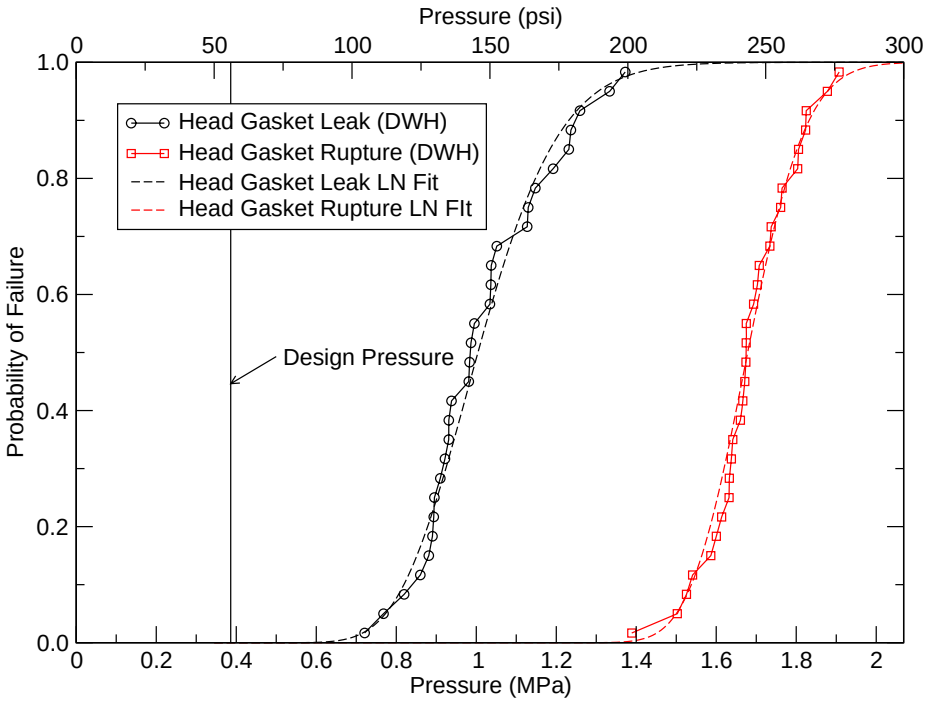

Figure 4.19: Raw and Fitted Fragility Curves for the Drywell Head Region

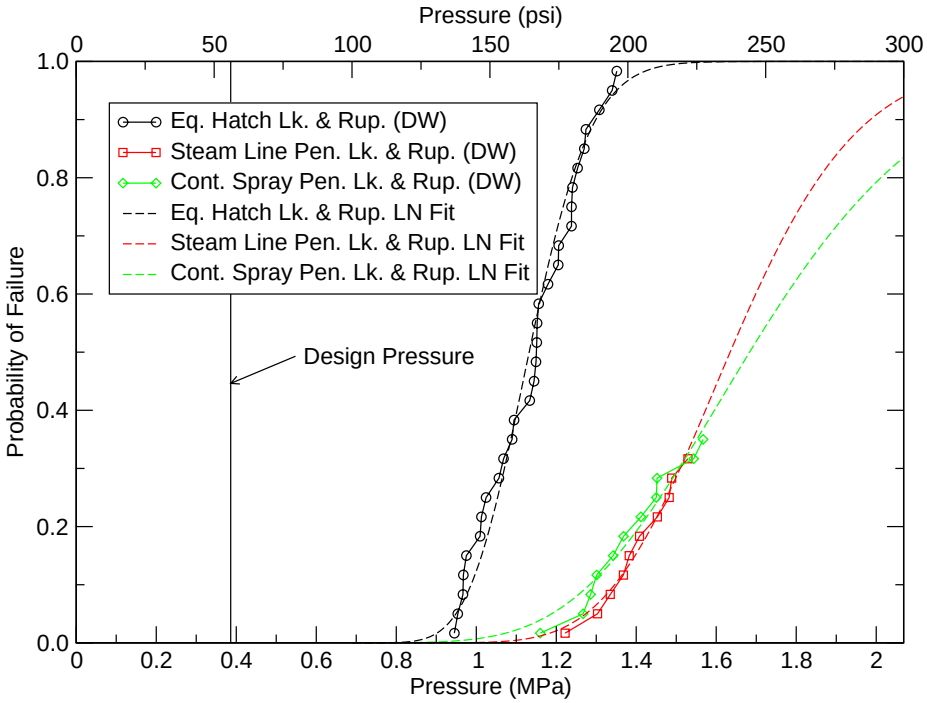

Figure 4.20: Raw and Fitted Fragility Curves for Individual Locations in the Drywell Region (Note: No Observed Failures at Floor Drain Penetration)

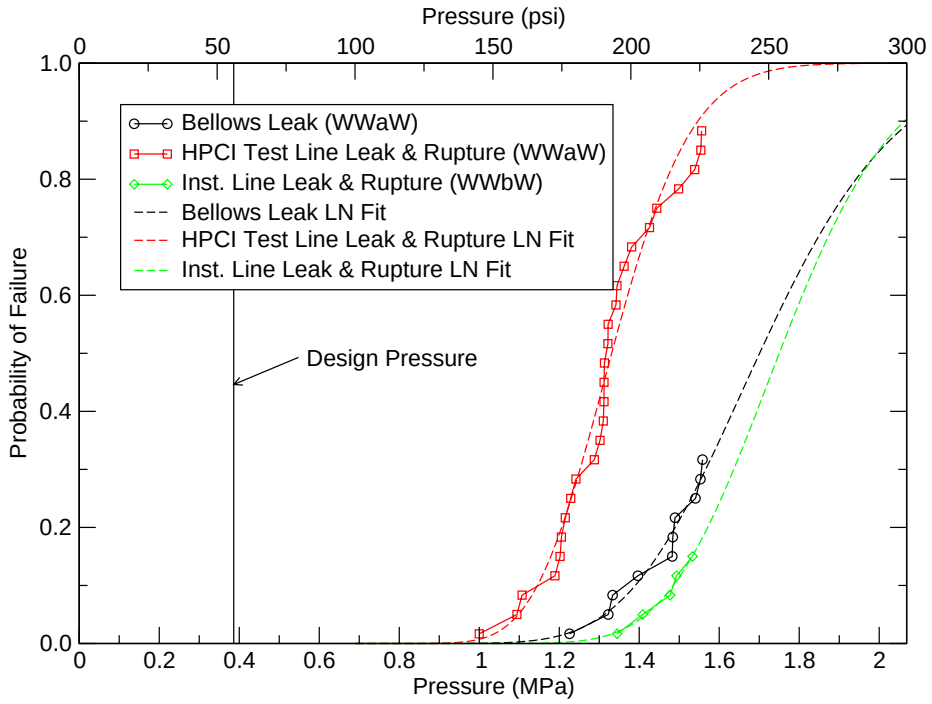

Figure 4.21: Raw and Fitted Fragility Curves for Individual Locations in the Wetwell Region (Note: No Observed Failures at Wetwell Access Hatch)

Figure 4.22 shows the fragilities for failure at the corroded area in the drywell knuckle region for 25% and 50% corrosion depths. The leak and rupture pressures are the same in every case. Figure 4.23 shows similar fragilities for failure in the drywell sand pocket region with 25% and 50% corrosion. This is the only location in this study where the tearing criterion was met before the rupture criterion. A relatively small number of samples failed with 25% corrosion, so the quality of the fitted curves is not as good as in other cases. Finally, Figure 4.24 shows the fragility curves for the postulated corrosion areas within the wetwell above waterline grouping. These include 25% and 50% corrosion at the wetwell waterline and corrosion of one of the vent line bellows plies. As for the un-corroded bellows, a corroded bellows failure is assumed to not constitute a rupture.

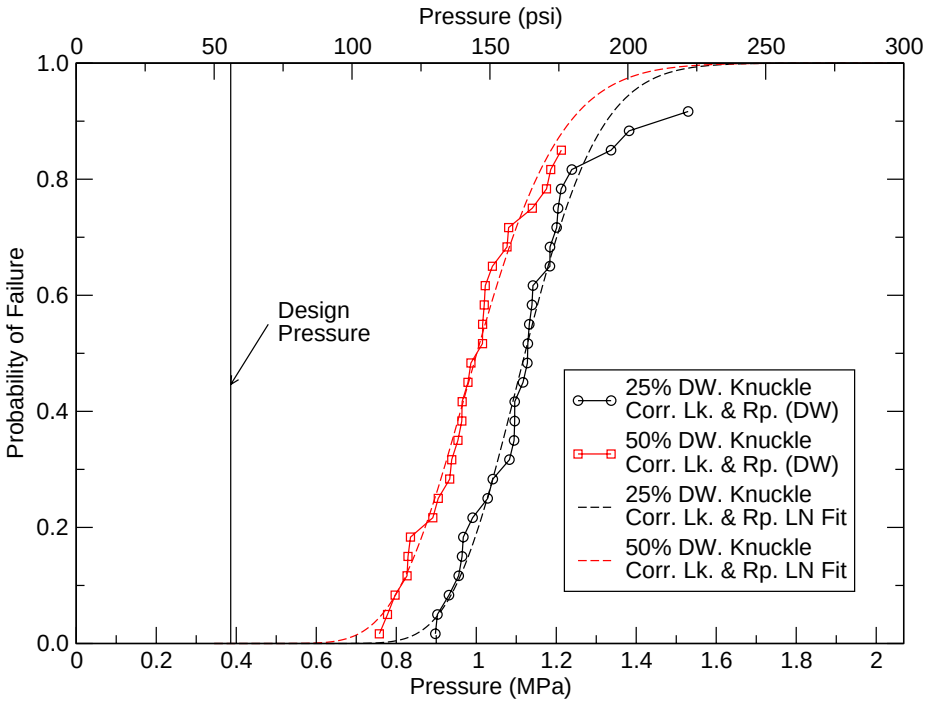

Figure 4.22: Raw and Fitted Fragility Curves for Corrosion Location (25% and 50% depths) in the Drywell Knuckle Region

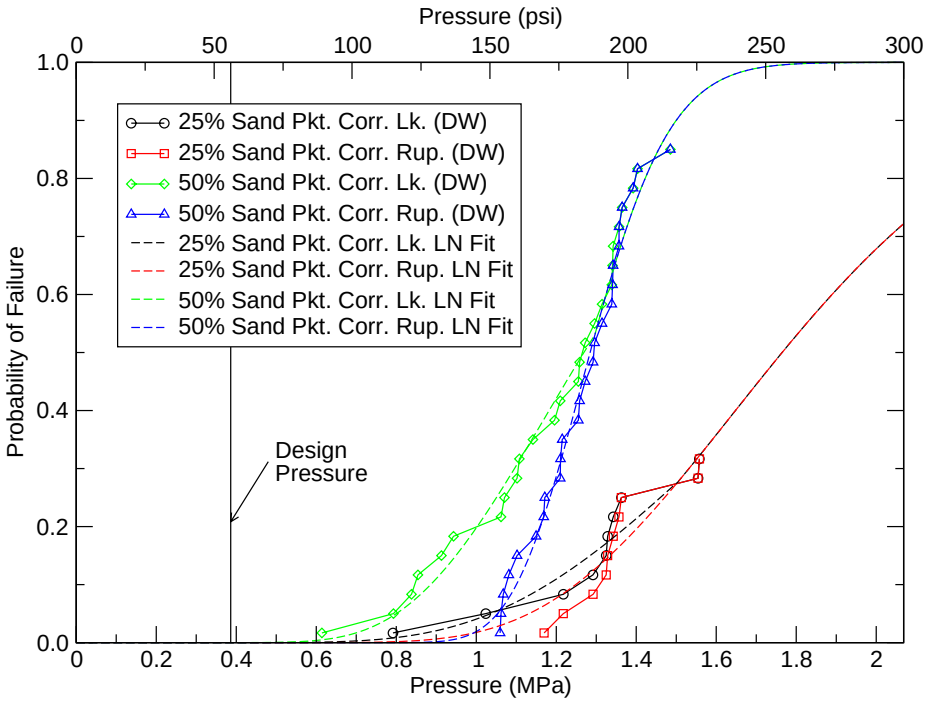

Figure 4.23: Raw and Fitted Fragility Curves for Corrosion Location (25% and 50% depths) in the Drywell Sand Pocket Region

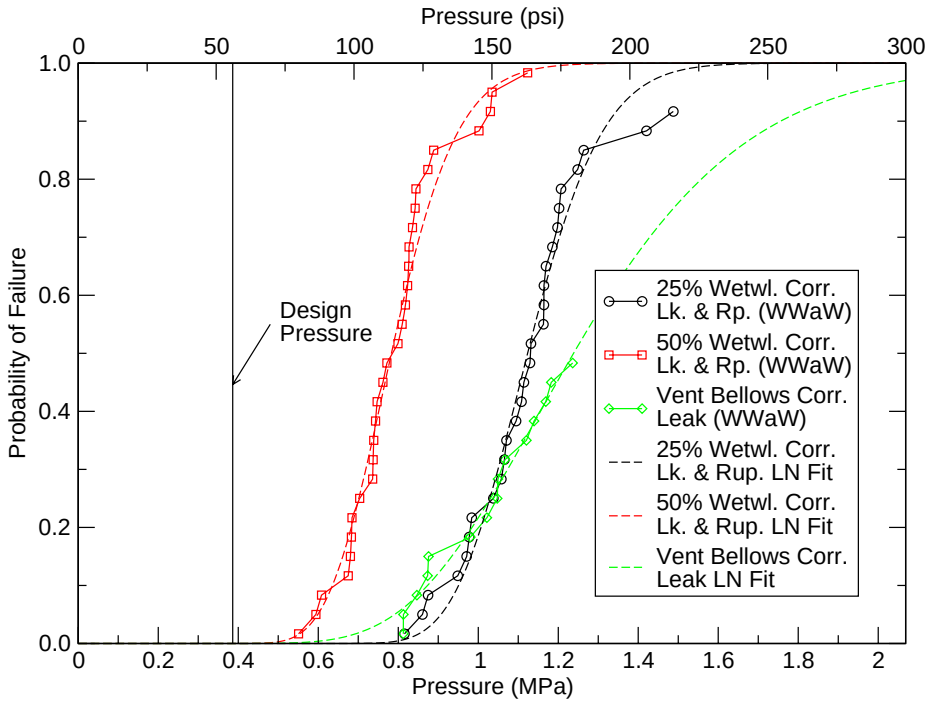

Figure 4.24: Raw and Fitted Fragility Curves for Corrosion Locations at Wetwell Waterline (25% and 50% depths) and Vent Line Bellows (1 Ply Corroded)

Once the parameters for the fitted distributions presented above were computed, the procedure outlined in Chapter 2 was applied to compute overall fragilities and conditional failure probabilities for each of the cases investigated here. Figure 4.25 shows plots of the original containment fragility along with the fragilities of the containment in all of the degraded states considered here. In many of the cases, the presence of degradation did not significantly affect the overall fragility. This is due to the fact that there is already a large number of potential failure locations present in the containment without corrosion. The case that had the most detrimental effect on the overall fragility is that where 50% corrosion was assumed in a large area in the wetwell waterline. The case with 50% corrosion at the drywell knuckle had the second most severe effect, but its effect was much smaller.

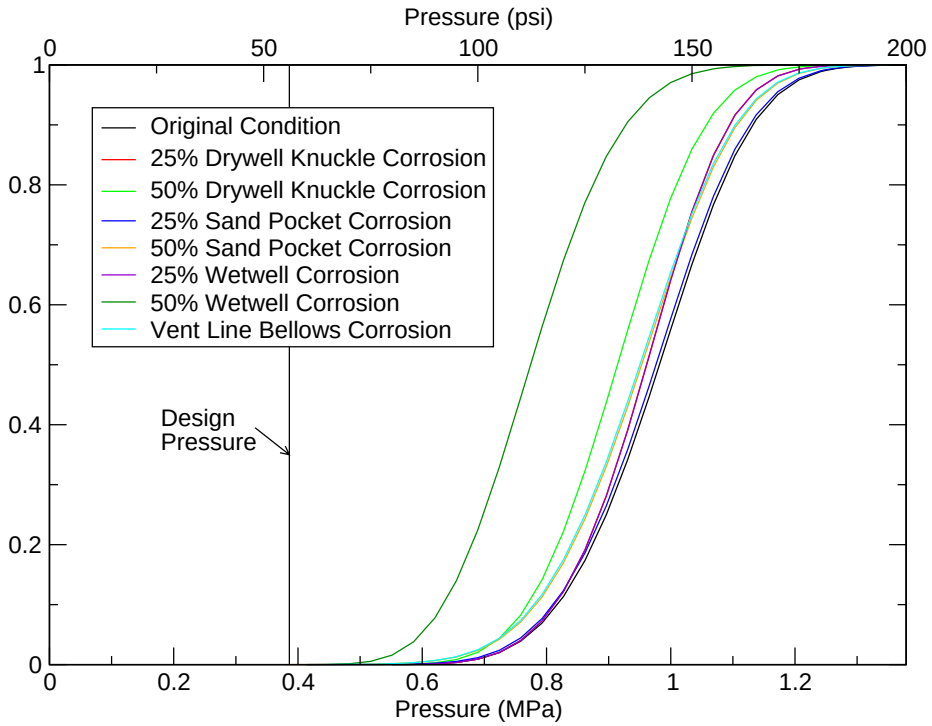

Figure 4.25: Overall Fragilities for Original Condition and All Corroded States Investigated

Figure 4.26 through Figure 4.33 show the conditional probabilities of the failure modes required by the risk analysis for the original containment and for all of the corroded cases. For each case, the overall fragility is shown along with the conditional probabilities. Only the conditional probabilities of those modes that have nonzero probabilities of failure are shown in these plots. This data will be used as input into the risk analysis models.

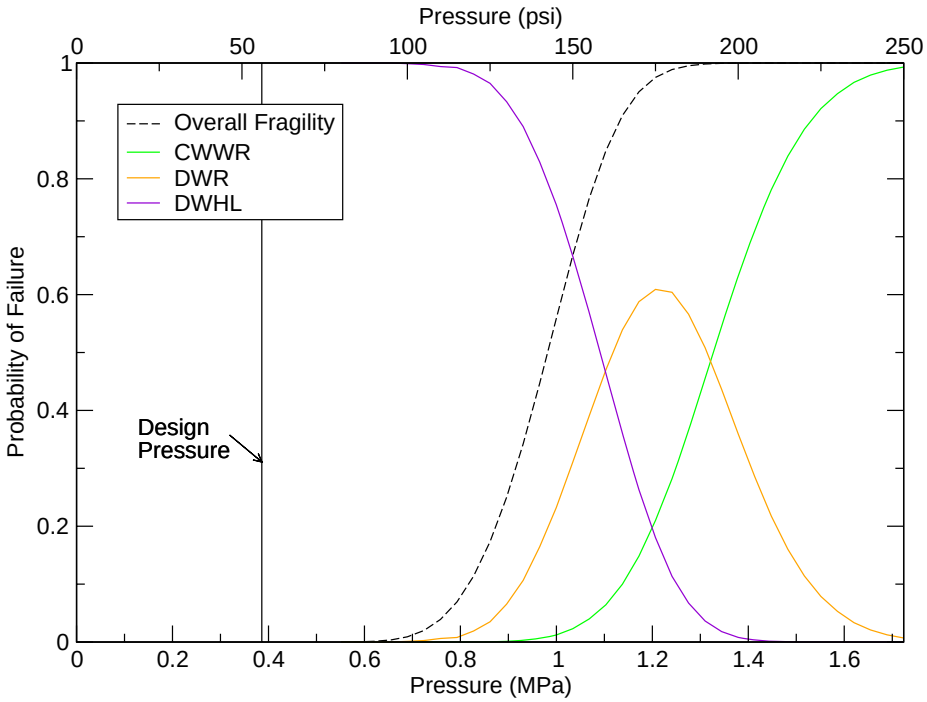

Figure 4.26: Conditional Probabilities of Failure Modes for Original Containment

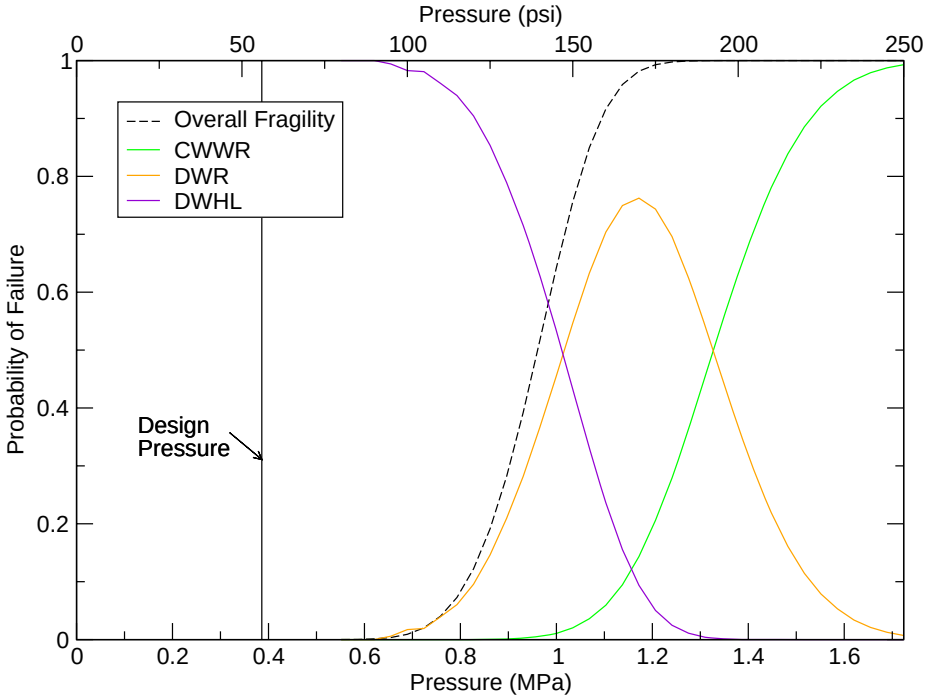

Figure 4.27: Conditional Probabilities of Failure Modes for Containment with 25% Corrosion at Drywell Knuckle

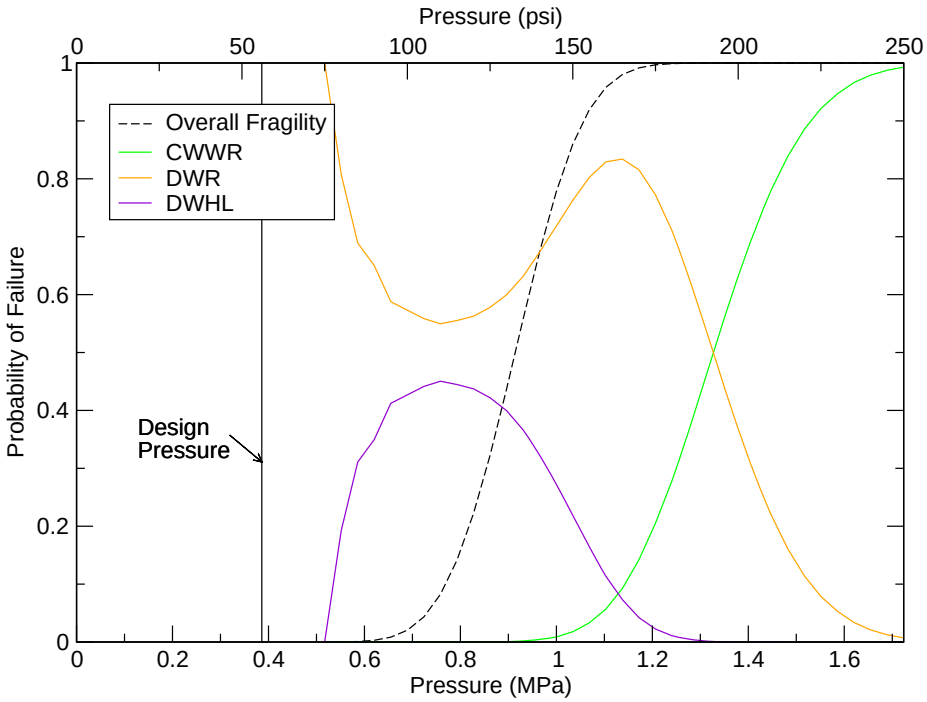

Figure 4.28: Conditional Probabilities of Failure Modes for Containment with 50% Corrosion at Drywell Knuckle

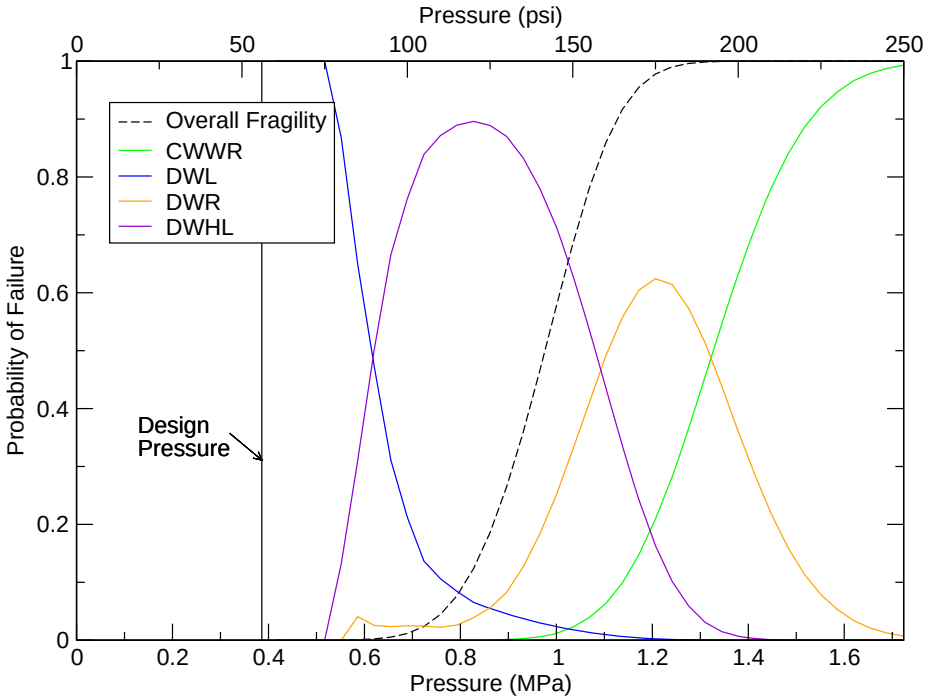

Figure 4.29: Conditional Probabilities of Failure Modes for Containment with 25% Corrosion at Drywell Sand Pocket

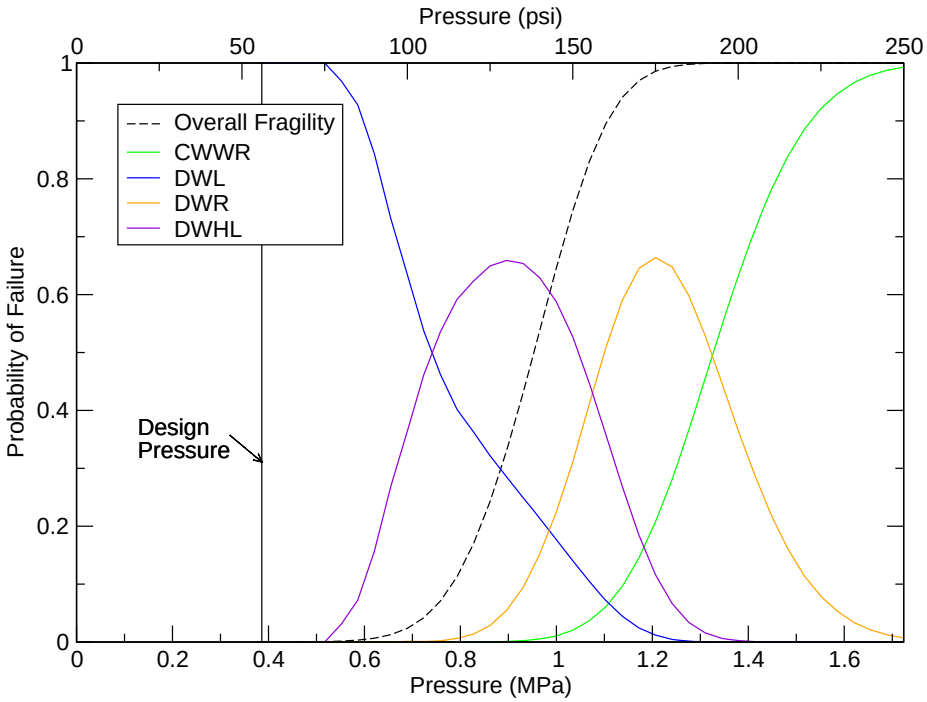

Figure 4.30: Conditional Probabilities of Failure Modes for Containment with 50% Corrosion at Drywell Sand Pocket

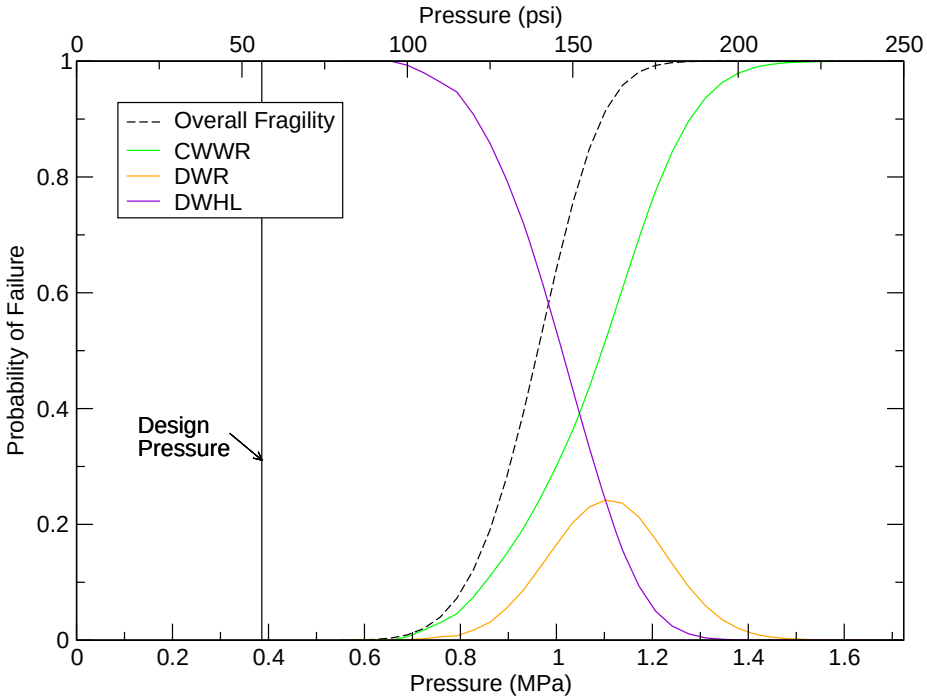

Figure 4.31: Conditional Probabilities of Failure Modes for Containment with 25% Corrosion at Wetwell Water Line

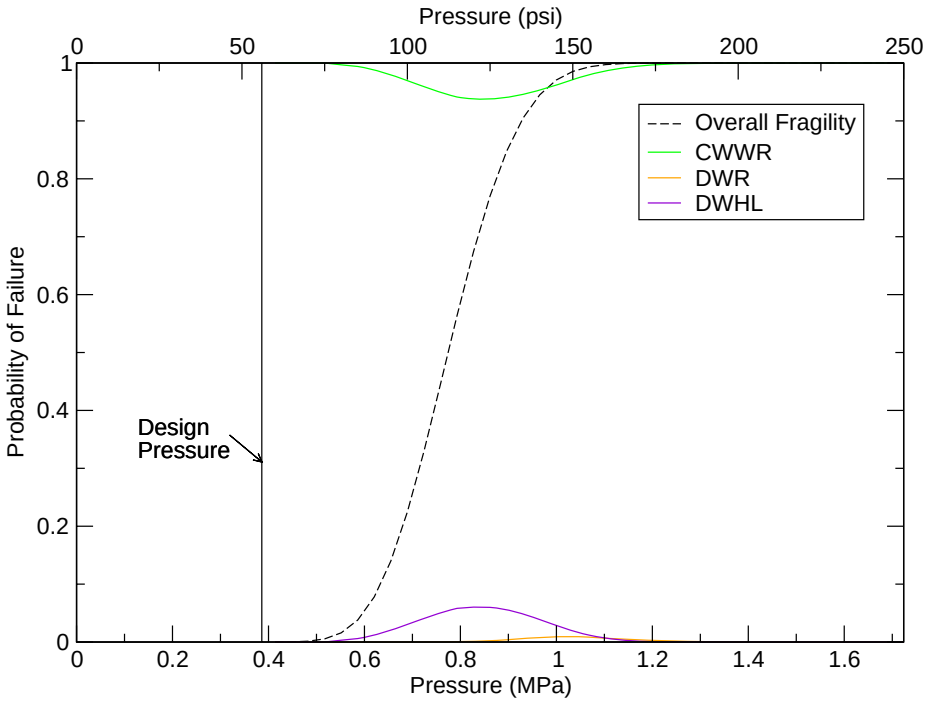

Figure 4.32: Conditional Probabilities of Failure Modes for Containment with 50% Corrosion at Wetwell Water Line

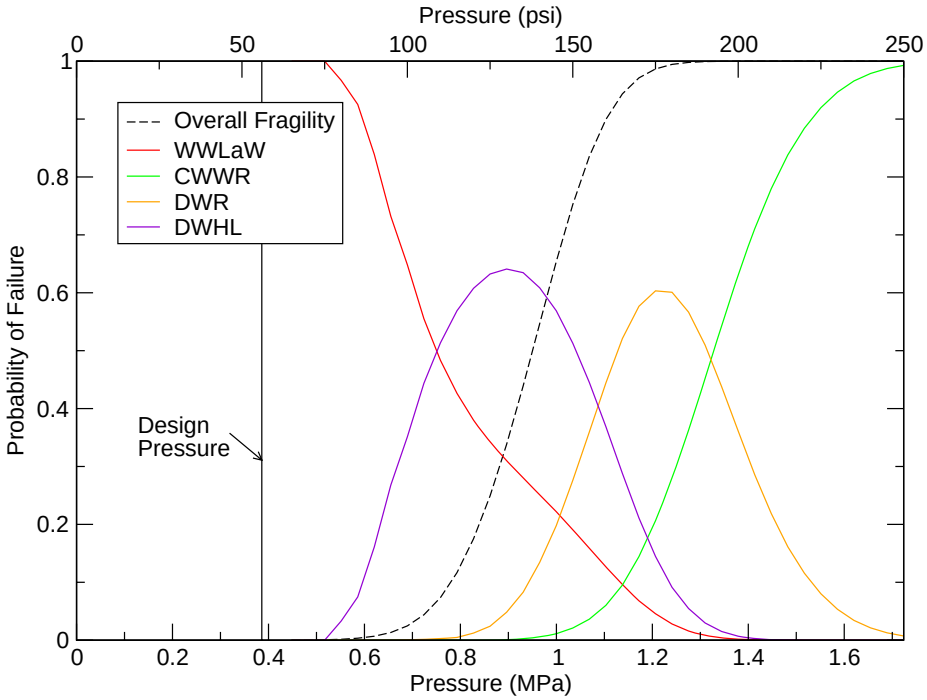

Figure 4.33: Conditional Probabilities of Failure Modes for Containment with Corrosion in One of Vent Line Bellows Plies

4.3 Risk Analysis Results

Table 4.4 shows the CDF values from NUREG-1150. Because the containment response does not affect the CDF for this plant, the results are the same for all of the cases studied.

Table 4.4: Core Damage Frequency (yr^{-1})

Case	Mean	5%	50%	95%
All	4.5E-6	3.5E-7	1.9E-6	1.3E-5

As for the PWR with a reinforced concrete containment evaluated in Chapter 3, it is very important to carefully consider which containment failure modes contribute to the risk metrics being used. Characteristic 5 in the accident progression event tree for this plant tells which mode of failure was experienced by the containment. The answer to this question can be: DWHL, DWL, WWL, DWHR, DWR, drywell melt-through (DWMTH), wetwell venting (WWVENT), wetwell rupture (WWR), or no containment failure (NOCF). There are a number of ways that the risk outcomes could potentially be grouped.

Table 4.5 shows the probabilities of early containment failure conditional on core damage for the reference case (using NUREG-1150 inputs), the un-damaged case using the inputs generated in the current work, and all of the degradation cases investigated. The containment failures are grouped into five categories. All of these categories bin together early containment failures that occur after core damage from the same set of initiating events. The first of these categories, early rupture, groups together all rupture failures (DWHR, DWR, WWR). The second, early drywell leak, groups together all drywell leak failures (DWHL, DWL). The early wetwell leak category is listed separately for reasons that will be explained. It only contains the WWL failures. The early venting category contains the WWVENT failures, and the early melt-through category contains the DWMTH failures.

Table 4.5: Mean Probabilities of Early Containment Failure Conditional on Core Damage

Case:	Early Rupture	Early Drywell Leak	Early Wetwell Leak	Early Venting	Early Melt-through
Un-damaged (Reference)	0.05951	0.0009426	0.002098	0.01771	0.3574
Un-damaged (Current Study)	0.07016	0.002918	0	0.01771	0.3475
Bellow Corrosion	0.07016	0.001067	0.001321	0.01771	0.3475
25% Corrosion at Knuckle	0.07180	0.002820	0	0.01771	0.3459
50% Corrosion at Knuckle	0.07492	0.001125	0	0.01771	0.3443
25% Corrosion at Sand Pocket	0.07082	0.002951	0	0.01771	0.3459
50% Corrosion at Sand Pocket	0.07082	0.002918	0	0.01771	0.3459
25% Corrosion at Wetwell Water Line	0.06131	0.001187	0	0.01771	0.3574
50% Corrosion at Wetwell Water Line	0.05688	0	0	0.01771	0.3639

A very important feature of these results is that there is a very high probability of a melt-through failure. The probability of an early melt-through failure given core damage is roughly 36% for all cases. The probability of a failure in this mode is significantly higher than any of the other types

of failure. The next most significant mode is early rupture, with a probability of about 6-7%, depending on the case, followed by wetwell venting, with a probability of about 2%. All of the other failure modes are relatively insignificant. The summation of all of the mean conditional probabilities for all of the modes listed in Table 4.5 is about 43.8% and changes very little as the various types of degradation are introduced.

This dominance of the melt-through mode of containment failure was noted in NUREG-1150. It stems from the fact that the Mark I containment is relatively small, so that if the core were to melt, it would spread out over a relatively confined area, making it much less likely to cool off before penetrating the containment than it would be in a larger containment.

The wetwell leak failures are in a category separate from the drywell leak failures in Table 4.5 because the outcome is different. Any gasses released from the wetwell will have been scrubbed by passing through the water in the wetwell, and the end outcome is arguably similar to wetwell venting, in which the wetwell is intentionally vented to relieve pressure.

The effects of the various types of containment degradation can be best understood using the categorizations of failure types shown in Table 4.5. In the case of bellows corrosion, the only changes are in the probability of drywell leak and wetwell leak. The drywell leak failure probability decreases, and the wetwell leak probability goes from 0 to .001321. The summation of the probabilities of the two modes of failure is somewhat lower than the original wetwell leak probability. It stands to reason that a weakened bellows would tend to draw failures away from the drywell to the wetwell. Because a release through the vent line bellows would be scrubbed, and the change in risk due to this type of degradation is miniscule compared to the risk of a melt-through, it can be argued that a corroded vent-line bellows ply has a negligible effect on the risk.

The cases where the drywell knuckle is corroded 25% and 50% through the thickness result in an increase in the probability of a drywell rupture, combined with a decrease in the probability of a drywell leak or a drywell melt-through. These effects are more pronounced in the 50% corrosion depth case, and follow the same trends observed in the 25% depth case. These results are intuitive, because corrosion at this location was determined to lead immediately to rupture. Scenarios that would have ended in drywell leakage or melt-through with the original containment have a greater likelihood of ending with drywell rupture with the presence of this type of corrosion.

With the presence of corrosion at the sand pocket, the changes are much less pronounced than those due to those from corrosion at the knuckle. The sand pocket location is much less critical than the drywell knuckle, and even with 50% corrosion depth, failure was likely to occur elsewhere in the containment before occurring at this location.

Corrosion in the wetwell had the greatest influence on the risk of any of the degradation types considered. The results at first seem somewhat counter-intuitive. Wetwell corrosion causes the risk of a rupture (drywell or wetwell) as well as the risk of a drywell leak to drop. At the same time, it causes the risk of a drywell melt-through to increase by roughly the same amount as the decrease in the risk of failure in the other two modes. This appears to be caused by the fact that failure at the corroded zone in the wetwell would result in a catastrophic rupture, and the cooling water in the wetwell would be lost, resulting in a greater likelihood of a drywell melt-through.

To group these failure modes together for the computation of the risk metrics calculated for the other containments, it was decided that early drywell ruptures and drywell melt-through failures would be grouped together for computing LERF. Drywell leakage is used to compute SERF, and

wetwell leakage and venting are excluded from the calculation because the release would be scrubbed in those cases. The total early release frequency is the summation of LERF and SERF. These results are presented in a manner consistent with that used for the other plants considered in this study in the series of tables below. Table 4.6 shows the LERF results, and Table 4.7 shows the probability of large early containment failure conditional on core damage (using the same groupings used for LERF). The change in LERF due to degradation is shown in Table 4.8. Analagous results for SERF, the conditional probability of small early containment failure conditional on core damage, and the change in SERF are shown in Table 4.9, Table 4.10, and Table 4.11, respectively. Finally, TERF, the conditional probability of all containment failures, and the change in TERF are shown in Table 4.12, Table 4.13, and Table 4.14. These total risk tables do not include wetwell leakage or venting, as noted previously.

Table 4.6: Large Early Release Frequency (yr^{-1})

Case	Mean	5%	50%	95%
Un-damaged (Reference)	1.876E-06	8.377E-13	7.335E-07	1.151E-05
Un-damaged (Current Study)	1.880E-06	8.377E-13	7.335E-07	1.268E-05
Bellow Corrosion	1.880E-06	8.377E-13	7.335E-07	1.268E-05
25% Corrosion at Knuckle	1.880E-06	8.377E-13	7.335E-07	1.345E-05
50% Corrosion at Knuckle	1.886E-06	1.779E-12	7.335E-07	1.353E-05
25% Corrosion at Sand Pocket	1.875E-06	8.377E-13	7.335E-07	1.330E-05
50% Corrosion at Sand Pocket	1.875E-06	8.377E-13	7.335E-07	1.330E-05
25% Corrosion at Wetwell Water Line	1.884E-06	8.377E-13	7.335E-07	1.151E-05
50% Corrosion at Wetwell Water Line	1.894E-06	8.377E-13	7.335E-07	1.149E-05

Table 4.7: Probability of Large Early Containment Failure Conditional on Core Damage

Case	Mean	5%	50%	95%
Un-damaged (Reference)	0.4169	2.393E-06	0.3861	0.8851
Un-damaged (Current Study)	0.4177	2.393E-06	0.3861	0.9754
Bellow Corrosion	0.4177	2.393E-06	0.3861	0.9754
25% Corrosion at Knuckle	0.4177	2.393E-06	0.3861	1.0344
50% Corrosion at Knuckle	0.4192	5.082E-06	0.3861	1.0410
25% Corrosion at Sand Pocket	0.4167	2.393E-06	0.3861	1.0230
50% Corrosion at Sand Pocket	0.4167	2.393E-06	0.3861	1.0230
25% Corrosion at Wetwell Water Line	0.4187	2.393E-06	0.3861	0.8857
50% Corrosion at Wetwell Water Line	0.4208	2.393E-06	0.3861	0.8836

Table 4.8: Change in the Large Early Release Frequency (yr^{-1}) due to Degradation

Case	Mean	5%	50%	95%
Bellow Corrosion	0	0	0	0
25% Corrosion at Knuckle	0	0	0	7.672E-07
50% Corrosion at Knuckle	6.639E-09	9.410E-13	0	8.525E-07
25% Corrosion at Sand Pocket	-4.426E-09	0	0	6.180E-07
50% Corrosion at Sand Pocket	-4.426E-09	0	0	6.180E-07
25% Corrosion at Wetwell Water Line	4.426E-09	0	0	-1.166E-06
50% Corrosion at Wetwell Water Line	1.402E-08	0	0	-1.193E-06

Table 4.9: Small Early Release Frequency (yr^{-1})

Case	Mean	5%	50%	95%
Un-damaged (Reference)	4.242E-09	0	0	0
Un-damaged (Current Study)	1.313E-08	0	0	1.287E-07
Bellow Corrosion	4.802E-09	0	0	0
25% Corrosion at Knuckle	1.269E-08	0	0	1.230E-07
50% Corrosion at Knuckle	5.061E-09	0	0	0
25% Corrosion at Sand Pocket	1.328E-08	0	0	1.287E-07
50% Corrosion at Sand Pocket	1.313E-08	0	0	1.287E-07
25% Corrosion at Wetwell Water Line	5.341E-09	0	0	5.733E-08
50% Corrosion at Wetwell Water Line	0	0	0	0

Table 4.10: Probability of Small Early Containment Failure Conditional on Core Damage

Case	Mean	5%	50%	95%
Un-damaged (Reference)	0.0009426	0	0	0
Un-damaged (Current Study)	0.002918	0	0	0.009902
Bellow Corrosion	0.001067	0	0	0
25% Corrosion at Knuckle	0.002820	0	0	0.009459
50% Corrosion at Knuckle	0.001125	0	0	0
25% Corrosion at Sand Pocket	0.002951	0	0	0.009902
50% Corrosion at Sand Pocket	0.002918	0	0	0.009902
25% Corrosion at Wetwell Water Line	0.001187	0	0	0.004410
50% Corrosion at Wetwell Water Line	0	0	0	0

Table 4.11: Change in the Small Early Release Frequency (yr^{-1}) due to Degradation

Case	Mean	5%	50%	95%
Bellow Corrosion	-8.329E-09	0	0	-1.287E-07
25% Corrosion at Knuckle	-4.426E-10	0	0	-5.751E-09
50% Corrosion at Knuckle	-8.070E-09	0	0	-1.287E-07
25% Corrosion at Sand Pocket	1.475E-10	0	0	0
50% Corrosion at Sand Pocket	0	0	0	0
25% Corrosion at Wetwell Water Line	-7.790E-09	0	0	-7.139E-08
50% Corrosion at Wetwell Water Line	-1.313E-08	0	0	-1.287E-07

Table 4.12: Total Early Release Frequency (yr^{-1})

Case	Mean	5%	50%	95%
Un-damaged (Reference)	1.880E-06	8.377E-13	7.335E-07	1.151E-05
Un-damaged (Current Study)	1.893E-06	8.377E-13	7.335E-07	1.281E-05
Bellow Corrosion	1.884E-06	8.377E-13	7.335E-07	1.268E-05
25% Corrosion at Knuckle	1.892E-06	8.377E-13	7.335E-07	1.357E-05
50% Corrosion at Knuckle	1.891E-06	1.779E-12	7.335E-07	1.353E-05
25% Corrosion at Sand Pocket	1.889E-06	8.377E-13	7.335E-07	1.343E-05
50% Corrosion at Sand Pocket	1.888E-06	8.377E-13	7.335E-07	1.343E-05
25% Corrosion at Wetwell Water Line	1.889E-06	8.377E-13	7.335E-07	1.157E-05
50% Corrosion at Wetwell Water Line	1.894E-06	8.377E-13	7.335E-07	1.149E-05

Table 4.13: Probability of Total Early Containment Failure Conditional on Core Damage

Case	Mean	5%	50%	95%
Un-damaged (Reference)	0.4178	2.393E-06	0.3861	0.8851
Un-damaged (Current Study)	0.4206	2.393E-06	0.3861	0.9853
Bellow Corrosion	0.4188	2.393E-06	0.3861	0.9754
25% Corrosion at Knuckle	0.4205	2.393E-06	0.3861	1.0439
50% Corrosion at Knuckle	0.4203	5.082E-06	0.3861	1.0410
25% Corrosion at Sand Pocket	0.4197	2.393E-06	0.3861	1.0329
50% Corrosion at Sand Pocket	0.4196	2.393E-06	0.3861	1.0329
25% Corrosion at Wetwell Water Line	0.4199	2.393E-06	0.3861	0.8901
50% Corrosion at Wetwell Water Line	0.4208	2.393E-06	0.3861	0.8836

Table 4.14: Change in the Total Early Release Frequency (yr^{-1}) due to Degradation

Case	Mean	5%	50%	95%
Bellow Corrosion	-8.329E-09	0	0	-1.287E-07
25% Corrosion at Knuckle	-4.426E-10	0	0	7.615E-07
50% Corrosion at Knuckle	-1.431E-09	9.410E-13	0	7.237E-07
25% Corrosion at Sand Pocket	-4.279E-09	0	0	6.180E-07
50% Corrosion at Sand Pocket	-4.426E-09	0	0	6.180E-07
25% Corrosion at Wetwell Water Line	-3.364E-09	0	0	-1.237E-06
50% Corrosion at Wetwell Water Line	8.852E-10	0	0	-1.322E-06

Even though the conditional probability of containment failure given core damage is quite high for this plant, the LERF is reasonably low, having a value of about 1.88E-6 for all cases. The change in LERF, or any of the other risk metrics, for that matter, is quite low, simply due to the fact that the baseline probability of melt-through given core damage is so high that it dwarfs any changes in the likelihood of rupture failures caused by corrosion.

Comparing the LERF and ΔLERF results with the guidelines of Regulatory Guide 1.174 indicates that any of the degradation cases studied here would be acceptable according to that criterion. This is in large part due to the low value of CDF, which is also well within the bounds of acceptability.

The example plants examined here serves as good case studies indicating that one should be very cautious about simply applying the ΔLERF criterion to evaluate the significance of containment degradation. It is important to closely examine how degradation can increase the likelihood of one failure mode while decreasing the likelihood of another, and evaluate the consequences of these different modes. It cannot be stressed enough that the cases of degradation examined here are extremely limited in scope. There are currently no means of predicting degradation prior to its discovery. Since the location and specific nature of any degradation could dramatically affect the containment capacity and risk, a detailed analysis of that scenario would be required. The specific results reported in this study should in no way be applied to making regulatory decisions on existing plants.

5. Risk Analysis of PWR Ice Condenser Containment

As with the BWR Mark I steel containment, the effects of corrosion are examined for a typical pressurized water reactor (PWR) Ice Condenser steel containment. Figure 5.1 shows a schematic diagram of the PWR Ice Condenser containment. The regions of corrosion are indicated in the locations where moisture is likely to accumulate and weaken the containment. The corroded locations remain consistent with the degraded PWR analyses performed by Cherry and Smith (2001). Corrosion at the basemat and upper floor locations are based on inspections summarized by Shah, et al. (1994). Even though not accessible for inspection, corrosion in the ice basket region is also examined due to the presence of water. All three corroded locations are examined with and without corrosion to determine the effects of degradation. As defined by NUREG/CR-4551, SAND86-1309, Vol. 2, Rev. 1, Part 3, failure in these three locations would bypass the ice condenser. Detailed analysis of the upper containment (region above the ice basket) is also performed where failure is assumed not to bypass the ice condenser.

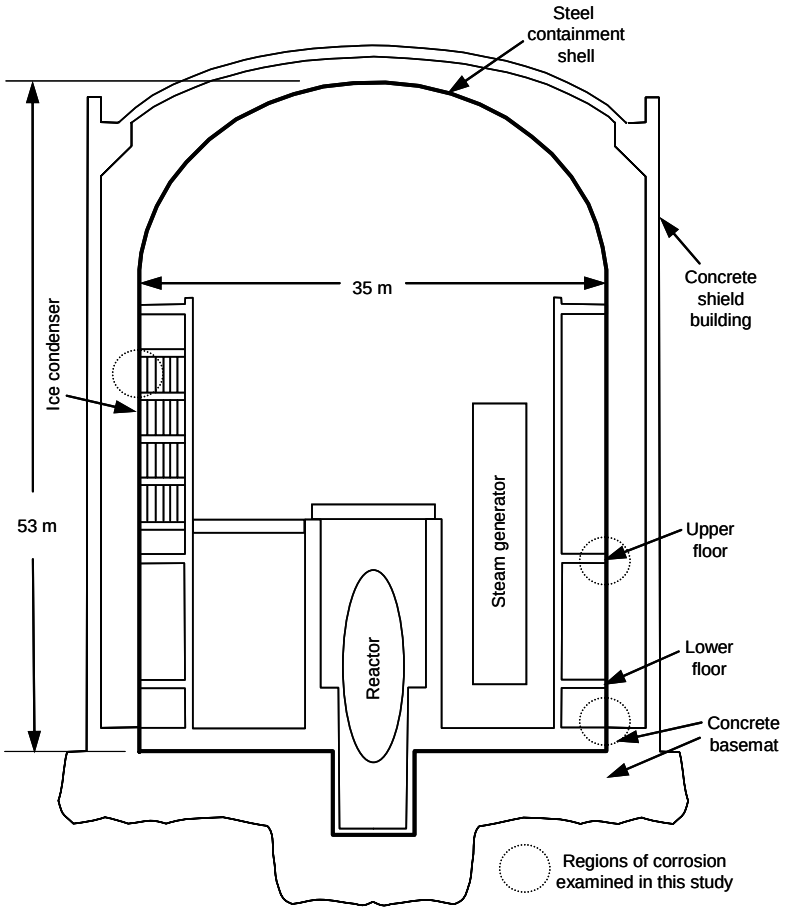

Figure 5.1: Postulated Corrosion in PWR Ice Condenser Steel Shell

5.1 Structural Model of PWR Ice Condenser Containment

Several different finite element models are employed to model the PWR Ice Condenser Containment in its original and corroded states. The global behavior is analyzed with a 3D finite

element model of a 53 degree slice of the containment using shell elements. The 53 degree slice is selected to include the interface between the thickened plate region which contains multiple penetrations and hatches, and the thinner plates which makeup a majority of the containment circumference. The regions of stress and stress concentrations are expected at the thickness transition between plates (Clauss, 1985; Greimann et al., 1987 Cherry and Smith, 2001). In addition to the 53 degree global model, three "submodels" are examined to study the regions of high stress and strain concentration with higher levels of mesh refinement. The effects of corrosion are studied at locations within two of these submodels and at one location within the global model.

The models of the steel PWR Ice Condenser containment use the same baseline material properties as the BWM Mark I steel containment. The material properties are varied in the parametric analysis with parameters generated by LHS.

5.1.1 Global Baseline Containment Model

The 53 degree slice of the global containment in Figure 5.2 resembles closely the model employed by Cherry and Smith. The plate thickness, plate locations, horizontal stiffeners, and vertical stringers remain identical to their model. Due to increases in computational power, the level of mesh refinement has been increased substantially. The global model used by Cherry and Smith contained 10125 four-noded shell elements (S4R ABAQUS elements) and 10335 nodes. The current model includes 24911 shell elements and 25255 nodes. The majority of the additional elements reside in the regions of high stress and strain concentrations or locations of postulated corrosion.

In addition, Cherry and Smith modeled the sections of the anchorage system and anchor bolts. These components are encased in the concrete basemat which was not modeled. Instead, appropriate boundary conditions were applied to bolts and to the shell at the intersection with the top of the concrete basemat. Figure 5.2 shows that the current model of the steel shell extends only to the intersection of the concrete basemat and steel shell. The nodal degrees of freedom are constrained against displacement and rotation along this line of intersection. The anchorage system has been analyzed previously by Fanous et al. (1993) and is not studied here.

Penetrations were not explicitly modeled here since previous work (Miller, 1990; Greimann, et al., 1984) determined that failures will occur in the thin plates near the interface with the thick plate regions (Clauss, 1985; Greimann et al., 1987). Figure 5.3 illustrates the different plate thicknesses for the PWR Ice Condenser containment. Though not explicitly modeled, a significant number of penetrations pass through the thickest plate region (3.81 cm). The plate thickness in the cylinder ranges from 1.27 cm below the springline to 3.18 cm near the basemat. The dome thickness varies from 1.11 cm above the springline to 2.38 cm at the top of the dome. As with the penetrations, the bellows are not explicitly modeled, but leak pressures are estimated using previous experimental and analytical analyses of the bellows (Lambert, et al., 1995; Greimann, et al., 1991).

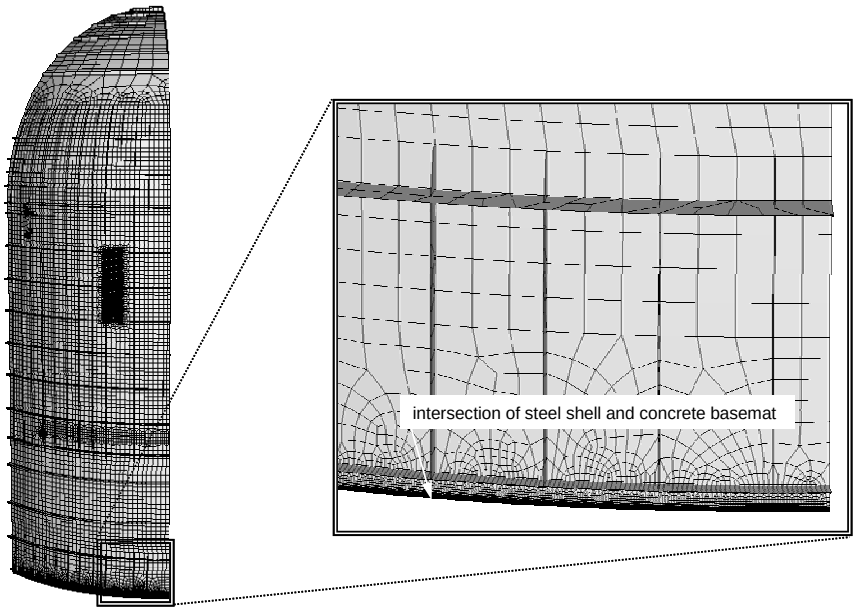

Figure 5.2: Finite Element Mesh of PWR and Detailed View of the Basemat Region

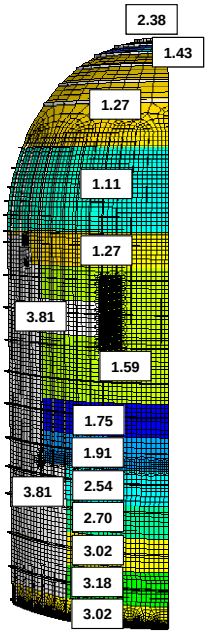

Figure 5.3: Illustration of the Variation in Shell Plate Thickness (cm) for the PWR

5.1.2 Containment Local Models

Figure 5.4 shows the approximate locations of the local regions of concern for the PWR containment. Three of the locations (upper containment, ice basket, and upper floor) highlighted in Figure 5.4 contain regions of strain and stress concentration due to abrupt changes in plate thickness. Each of these regions is analyzed in additional detail using submodels described in this section. The fourth location near the basemat is studied in detail within the global model.

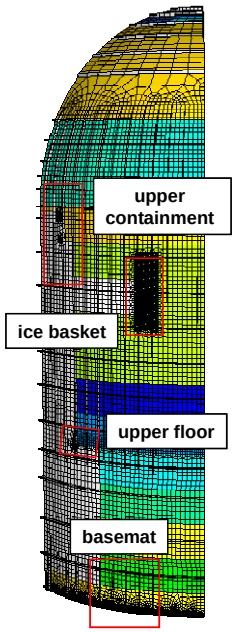

Figure 5.4: Regions of Stress and Strain Concentration for the PWR

5.1.2.1 Basemat Region

Figure 5.5 illustrates the high level of mesh refinement employed near the intersection of the steel shell (3.02 cm plate thickness) and concrete basemat. As described earlier, the nodes along the intersection are constrained against displacement and rotation.

While membrane action is the primary means of load resistance throughout the containment, the strains near the basemat are dominated by bending caused by the outward expansion of the shell. The bending strains are limited since membrane action will eventually resist the increasing loading after the radial displacements become large enough. Cherry and Smith (2000) and Ellingwood and Cherry (1999) increased the strain limit to cause a leak due to bending strains by 50% over the values used for membrane strains. This was introduced to account for the limited nature of the bending strains and since a crack initiated by bending strains at the plate surface would need to propagate through the thickness of the plate prior to leak formation. Cherry and Smith also limited failure to surface (bending) strains above 5%, i.e., no failure was considered possible for bending strains below 5%. This study does not employ the 5% minimum strain but does increase the strain limit for bending strains by 75%. Due to significant bending at the intersection, the mesh was refined in the vertical direction (darkened area at the intersection in Figure 5.5) until obtaining convergence of the maximum plastic strain.

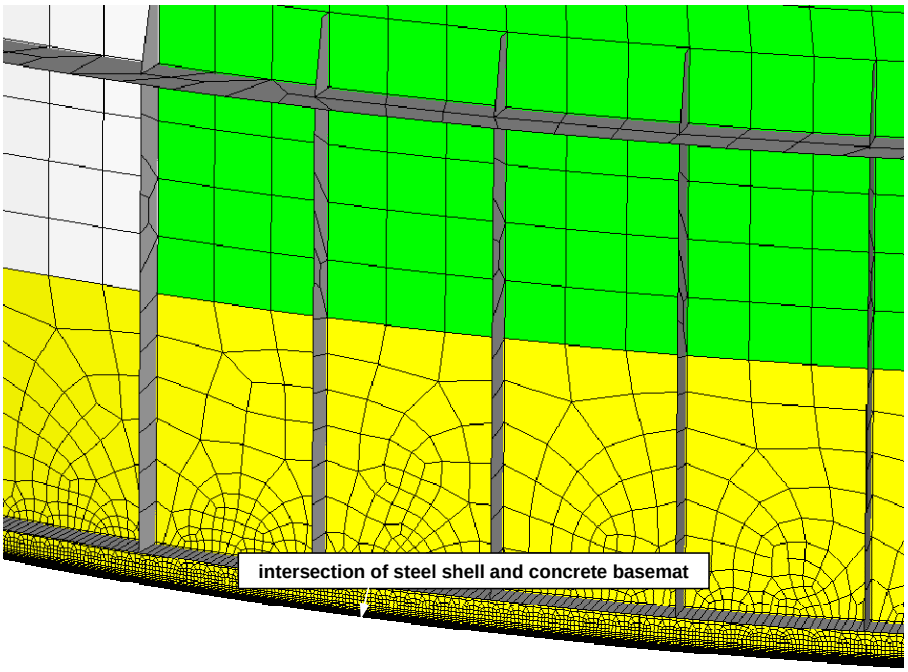

Figure 5.5: Detailed View of the Basemat Region (Intersection of Steel Shell and Concrete Basemat)

5.1.2.2 Ice Basket Region

One region of high strain concentrations occurs at the corners of the thick plate surrounded by thinner material in the region of the ice basket. This region is shown in Figure 5.4 and modeled in additional detail using the submodel illustrated in Figure 5.6. The submodeling capabilities of ABAQUS are employed here to analyze the submodel. ABAQUS applies automatically the corresponding displacements generated from the analysis of the global model to the boundaries of the submodel for each load step. The pressure and temperature histories remain identical to the analysis of the global model.

The thick plate has a thickness of 3.81 cm (1.5 in) and is surrounded by a plate only 1.59 cm (0.625 in) thick. The mismatch in plate thickness leads to significant strain concentrations in the thinner plate near the corners of the thick plate. The thick plate is 290 cm (114 in) wide in the vertical direction. Since shell elements are used here, a region of transition between the two plates was included in the submodel. This region, illustrated in Figure 5.6, follows a slope of 1:4 in transitioning plate thickness from 3.81 cm to 1.59 cm. In addition, the corners of the transition are “rounded” at the interface with the thin plate material. The rounded corners have a radius of 1.27 cm (0.5 in) which is assumed to be a reasonable size for a rounded weld bead. The inclusion of these local details reduces the artificial strain concentrations stemming completely from the finite element representation of the actual containment. The mesh was refined near the corners of the thick plate (darkened areas in Figure 5.6) until obtaining convergence of the maximum plastic strain.

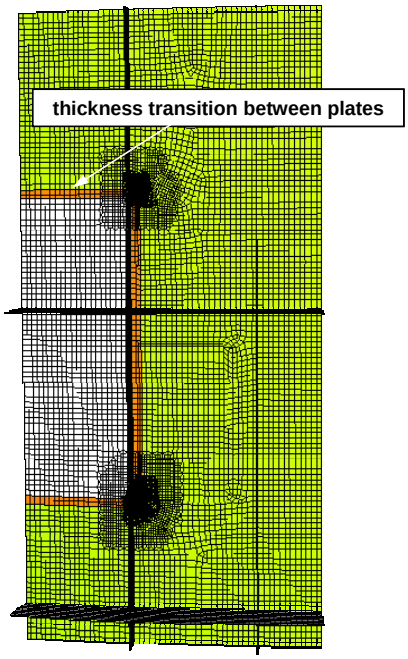

Figure 5.6: Detailed View of the Ice Basket Region Submodel

5.1.2.3 Upper Floor Region

The second submodel includes the shell region at the location of the upper floor at the interface between plates of varying thickness. Figure 5.4 indicates the location of the upper floor submodel shown in Figure 5.7. This specific location contains a thin plate at 1.91 cm (0.75 in) thickness surrounded on two sides by a plate 3.81 cm (1.5 in) thick. The finite element procedures remain identical to those described for the ice basket region submodel. The plate thickness transition follows the 1:4 slope and 1.27 cm (0.5 in) radius for the plate corner. As with the ice basket region submodel, the mesh was refined until obtaining convergence of the maximum plastic strain.

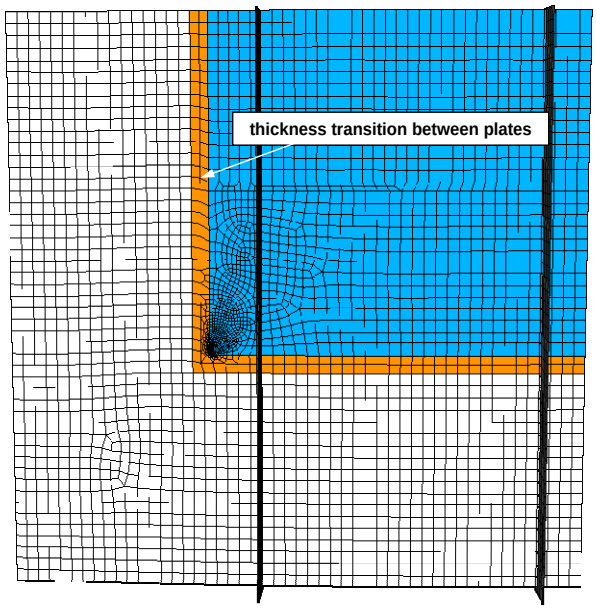

Figure 5.7: Detailed View of the Upper Floor Region Submodel

5.1.2.4 Upper Containment Region

The final submodel created for the analysis of the PWR Ice Condenser containment examines a portion of the upper containment, where the upper containment describes the region above the ice condenser. Failure in this region is assumed not to bypass the ice condenser. Figure 5.8 shows the submodel for the upper containment with the global position outlined in Figure 5.4.

The upper containment submodel contains several plates of varying thickness. The plate at the bottom left of the submodel is the same plate thickness, 3.81 cm (1.5 in), as the thickest plate in the ice basket and upper floor submodels. As described previously, the thick plate contains multiple penetrations for bellows and access hatches. The submodel includes three thinner plates at 1.11 cm (0.4375 in), 1.27 cm (0.5 in), and 1.59 cm (0.625 in), from top to bottom. The springline is located at the bottom of the top plate. Due to the relatively small difference in thickness between the three thinner plates, transition regions were not included. The transitions between the three thin plates and the thick plate are modeled as shown in Figure 5.8. Several locations include rounded corners with the adopted 1.27 cm (0.5 in) radius. As with the previous submodels, the mesh was refined in the regions of strain concentration until obtaining convergence of the maximum plastic strain.

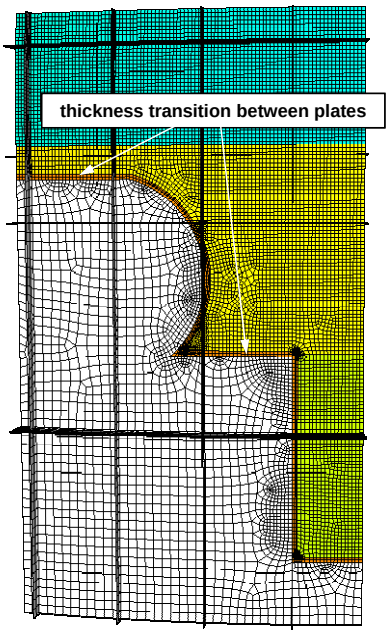

Figure 5.8: Detailed View of the Upper Containment Region Submodel

5.1.3 Corroded Regions

Corrosion is postulated in three locations for the PWR Ice Condenser containment. Figure 5.9 shows the three locations at the basemat, the upper floor, and ice basket region. These locations and their sizes remain similar to the three locations studied by Cherry and Smith. Inspections have observed corrosion in PWR Ice Condenser containments at the basemat and upper floor locations (Shah, et al., 1994). The ice basket region is not accessible for inspection but has a high potential for corrosion due to the presence of water. The finite element meshes are refined in the areas of corrosions, with additional refinement in the regions of strain concentration. Corrosion is introduced into the shell models by reducing the shell thickness in the postulated corroded regions. Two nominal levels of corrosion are assumed for each region, 25% and 50% for the basemat and ice basket regions, and 50% and 65% for the upper floor location.

Due to the relatively large distance between the three corroded regions, the global model is analyzed with corrosion in all three locations. One analysis was performed with 50% corrosion in the basemat region, 50% corrosion at the upper floor region, and 25% at the ice basket region. A second analysis included 25% corrosion at the basemat region, 65% corrosion at the upper floor region, and 50% at the ice basket region. Since the existence of corrosion in one region of the global model has only negligible effects on the strains in the other corroded regions, the solutions for each region can be used independently. This also enables the use of the global models with corrosion in all three locations to supply the boundary conditions for the submodels containing corrosion. Two of the previously described submodels are used to model corrosion in the upper floor and ice basket regions. The global analysis is used to determine the strains at the basemat with corrosion. These corroded regions are described in the following sections.

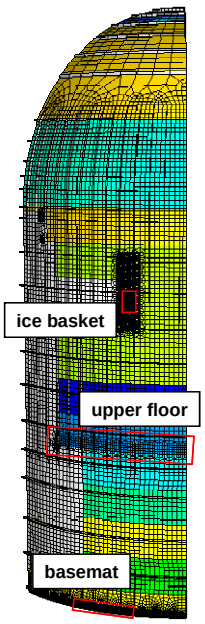

Figure 5.9: Locations of Corrosion Postulated for the PWR

5.1.3.1 Corroded Basemat Region

Figure 5.10 illustrates the postulated corrosion in the basemat region. The corroded region spans 428.5 cm (168.7 in) along the intersection between the containment shell and the concrete basemat. The corrosion extends 10.16 cm (4 in) in the verteical direction, with 3.81 cm (1.5 in) of that length fully corroded. As with the interface between plates of differing thickness in the submodels, a 6.35 cm (2.5 in) transition in thickness is modeled between the uncorroded and corroded plates. Corrosion at 25% and 50% of the original 3.02 cm (1.19 in) thickness reduces the nominal thickness to 2.27 cm (0.894 in) and 1.51 cm (0.594 in), respectively. The model includes a high level of mesh refinement in the corroded region (darkened region in Figure 5.10).

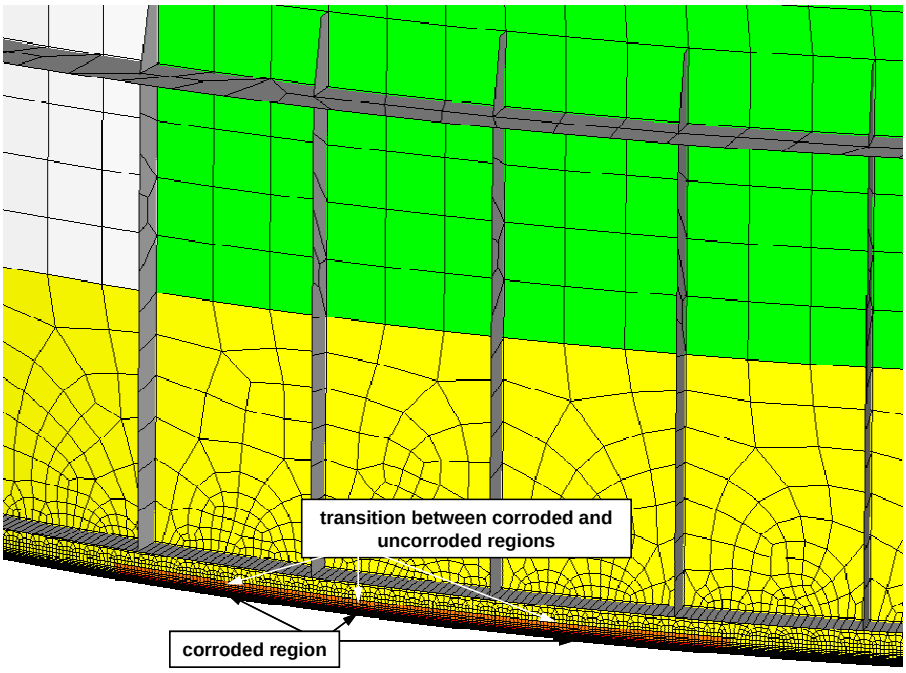

Figure 5.10: Detailed View of the Corroded Basemat Region

5.1.3.2 Corroded Ice Basket Region

Figure 5.11 shows the postulated region of corrosion within the ice submodel. This specific location is not accessible during inspections but is susceptible to corrosion due to the presence of water. The corrosion is placed in the thin plate at the interface with the thicker plate described in the discussion of the ice basket submodel. The corroded region is highlighted in red with the thickness transition in orange. The corrosion extends 12.5 cm (4.9 in) in the horizontal direction and 25.6 cm (10.1 in) in the vertical direction. The two corrosion levels, 25% and 50%, reduce the original 1.59 cm (0.625 in) thickness to 1.19 cm (0.469 in) and 0.79 cm (0.3125 in), respectively. The model includes a high level of mesh refinement in the corroded region with additional refinement in the areas of strain concentration (darkened areas in Figure 5.11).

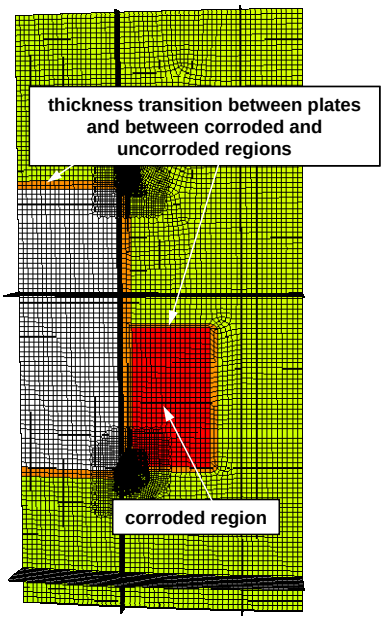

Figure 5.11: Detailed View of the Corroded Ice Basket Region Submodel

5.1.3.3 Corroded Upper Floor Region

Figure 5.12 illustrates the postulated corrosion region within the upper floor submodel. The corroded region was place in the thin plate at the location of the upper floor and is surrounded by a thick plate along the bottom and left sides of the submodel. The postulated corrosion region spans the entire length of the upper floor in the global model, as outlined in Figure 5.9. Here the corroded region only reaches to the edge of the submodel. This does not affect the results for this location since the maximum strains occur in the corner where the thin plate is surrounded by the thicker plate. The corrosion extends 68 cm (27 in) in the vertical direction (typical concrete floor thickness). The two corrosion levels, 50% and 65%, reduce the original 1.91 cm (0.75 in) thickness to 0.953 cm (0.375 in) and 0.667 cm (0.2625 in), respectively. The model includes a high level of mesh refinement in the corroded region with additional refinement in the area of the strain concentration (darkened area in Figure 5.12).

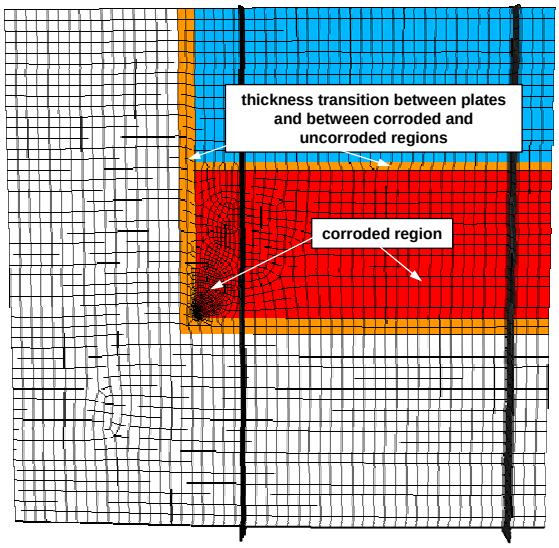

Figure 5.12: Detailed View of the Corroded Upper Floor Region Submodel

5.1.4 Analysis of the Bellows

Previously, a detailed studied and finite element analysis of the bellows in the PWR Ice Condenser containment was performed by Greimann et al. (1991). They determined that the two bellows most likely to leak due to large deformation are located just below the springline in the thick plate region shown in Figure 5.13. These particular bellows supply the containment with glycol and extend approximately 61 cm (24 in) in length with two 15.2 cm (6 in) convolution sections. Greimann et al. concluded that the bellow would remain leak tight until as least 0.427 MPa (62 psi). At this point, the end pipe and bellows wall come into contact with the possibility of the rigid end pipe pushing through the bellow wall.

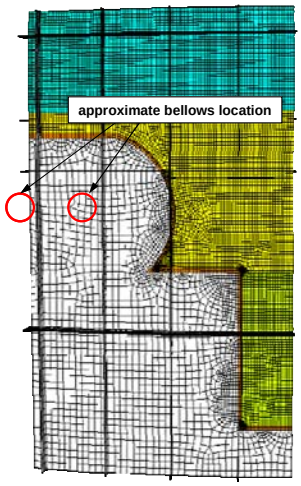

Figure 5.13: Approximate Bellows Location Relative to Upper Containment Submodel

As discussed earlier for the bellow analysis of the BWR containment, typical bellows were tested in an experimental study by Lambert and Parks (1994). The program included nine "like-new" and six corroded bellows of various configurations, test conditions, lateral displacements, and internal loadings. Of the nine like-new bellows, six did not leak even at 100% compression of the convolution. The remaining three bellows leaked prior to 100% compression, but none prior to 86% compression. Since the bellows are not explicitly modeled for the PWR, the results of these experiments are employed to develop a simple failure criterion for determining the point of leak in the critical bellows (location shown in Figure 5.13). Conservatively assuming that the six bellows which did not leak prior to 100% compression, do leak at 100% compression, an average compression of 97% compression is assumed to cause leakage in the bellows. Here, the critical bellow has 30.5 cm (12 in) of convolution. Therefore, leak in the bellow is predicted to occur when the radial (outward) displacement of the containment at the bellow location reaches 97% of 30.5 cm (12 in) (in the average case). The variation (standard deviation) of the data set is used to vary this percentage throughout the 30 LHS samples.

For the six corroded experiments, three leaked prior to any compression due through-thickness corrosion prior to any loading. Of the remaining three bellows, two leaked at 50% and 100% compression, and one did not leak even at 100% compression. Since it can be assumed that bellows with corrosion through the entire thickness of the bellow would be discovered and repaired during inspections, the three bellows which leaked prior to compression where assumed to leak at 50% compression (the next lowest value). As with the like-new procedure, the bellow which did not leak at 100% compression was assumed to leak at 100% compression. Therefore, the corroded bellow is assumed to leak when the compression reaches the average value of 67% of the convolution length (30.5 cm (12 in)). The uncertainty in the percent of compression is reflected in the large variation (standard deviation) employed to generate the LHS samples. Failure in the bellows is limited to leak since rupture is not considered likely to occur (see discussion for bellows in the BWR containment).

5.1.5 Structural Analysis with Best Estimate Properties

As with the BWR containment, a baseline analysis was performed for the PWR Ice Condenser Containment using the median of each LHS input parameters. Figure 5.14 shows the potential for failure vs. pressure for all locations considered in this study. This plot includes results for failures at local details in both original and corroded conditions. For the basemat, upper floor, ice basket, and upper containment, the failure function is defined as the magnified plastic strain divided by the uniaxial failure strain. For the bellows failure, the failure function is defined as the radial displacement at the bellows location divided by the critical compression length (97% of 30.5 cm for no corrosion, and 63% (median value for assumed lognormal distribution) of 30.5 cm for corrosion).

Figure 5.14 shows clearly that corrosion has a significant effect on the failure pressure. In the original condition, failure is predicted to occur at the ice basket local detail, followed by the upper containment, bellow, and upper floor location, respectively. Neither the bending or membrane strains at the uncorroded basemat reach values large enough to initiate failure prior to the finite element analysis convergence limit (pressure at which the analysis failed to converge). The introduction of 50% corrosion to the basemat region does lead to bending failure prior to the end of the analysis. For this median (best estimate) analysis, 25% corrosion was not sufficient to cause failure at the basemat. Failure is obtain in several of the LHS cases with 25% corrosion at the basemat.

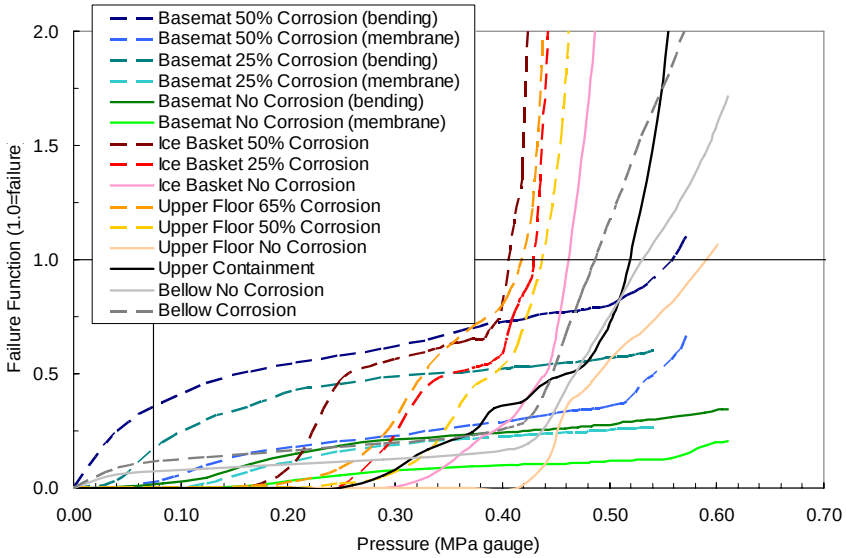

Figure 5.14: PWR Leakage Potential for All Locations and Corrosion Levels

Corrosion at the upper floor and ice basket locations causes a clear reduction in the failure pressure. The differences in failure pressure between 25% and 50% corrosion for the ice basket and 50% and 65% for the upper floor are relatively small compared to the analyses without any corrosion. Lower failure pressure is also seen in the bellow with the introduction of corrosion.

Table 5.1 summarizes the failure pressures at each location and corrosion condition. Even though the failures predicted in Figure 5.14 use the leakage failure criterion, the far field stresses are sufficient to initiate catastrophic rupture immediately after the leak forms in most cases. The catastrophic rupture criterion is based on the *J* integral exceeding the critical *J* at the point of leak initiation. The *J* integral is calculated using the far field stress and an assumed crack length. At the point of leak, the newly formed crack is assumed to immediately grow to the size of a nearby feature, typically the length of the nearest plate edge. The distance between the concrete shield building and the steel containment is assumed to be sufficiently large as to not prevent catastrophic rupture. Therefore, rupture and catastrophic rupture are equivalent for the PWR. In many cases, the far field stresses, assumed to be the driving force for crack growth, are on the order of the yield strength of the material at the point of leak. This further justifies the conclusion that catastrophic rupture will occur immediately after reaching the leakage criterion. This holds for the upper floor, ice basket, and upper containment locations, since none of the 30 LHS analyses showed rupture at higher pressures than leak using the critical *J* integral criterion. Therefore, catastrophic rupture is the only risk mode considered for these locations. Several of the basemat analyses do predict rupture at higher pressures than leak, and can therefore contribute to the leak bypass mode. These cases have leaks occurring at relatively low pressures which do not have sufficient far field stresses to propagate the assumed crack. Finally, the bellows are assumed to leak and not transition to catastrophic rupture. Therefore, a leak in the bellow is assumed to contribute to the leak no bypass mode.

Table 5.1: Summary of Locations and Failure Pressures

Location (Corrosion)	Leak Pressure MPa (psig)	Rupture Pressure MPa (psig)	Feature Size m (in)	Risk Model Mode
Basemat (50% Corrosion)	0.560 (81.2)	0.560 (81.2)	4.285 m (168.7 in)	Bypass - Leak Catastrophic Rupture
Basemat (25% Corrosion)	N/A*	N/A	4.285 m (168.7 in)	Bypass - Leak Catastrophic Rupture
Basemat (No Corrosion)	N/A*	N/A	N/A	Bypass - Leak Catastrophic Rupture
Upper Floor (65% Corrosion)	0.414 (60.2)	0.414 (60.2)	2.896 (114)	Catastrophic Rupture
Upper Floor (50% Corrosion)	0.430 (62.4)	0.430 (62.4)	2.896 (114)	Catastrophic Rupture
Upper Floor (No Corrosion)	0.590 (85.6)	0.590 (85.6)	2.896 (114)	Catastrophic Rupture
Ice Basket (50% Corrosion)	0.406 (58.9)	0.406 (58.9)	2.896 (114)	Catastrophic Rupture
Ice Basket (25% Corrosion)	0.429 (62.2)	0.429 (62.2)	2.896 (114)	Catastrophic Rupture
Ice Basket (No Corrosion)	0.462 (67.0)	0.462 (67.0)	2.896 (114)	Catastrophic Rupture
Upper Containment	0.518 (75.2)	0.518 (75.2)	2.896 (114)	Catastrophic Rupture
Bellows (No Corrosion)	0.530 (76.9)	N/A	N/A	No Bypass - Leak
Bellows (Corrosion)	0.486 (70.5)	N/A	N/A	No Bypass - Leak

*Failure not obtained prior to convergence limit.

5.2 Fragility Analysis of Degraded PWR Ice Condenser Containment

The PWR Ice Condenser Containment was analyzed with 30 sets of random input parameters generated by LHS using the values in Table 5.2. The computation of the yield strength from the yield strength factor for the BWR Mark I containment remains the same for the PWR. Fragility curves were then created using the failure pressures for each of the 30 analyses for each local detail.

Figure 5.15 illustrates the fragility distributions for the locations assumed to cause a bypass of the ice condenser if a leak occurred. The top plot in Figure 5.15 shows the fragility distributions for the basemat with and without corrosion. At low failure probabilities there does exist a small gap between leak and catastrophic rupture. Each fragility distribution was fit with a lognormal distribution and plotted against the raw distributions in Figure 5.15. Since no one distribution fit the leak fragilities, two separate distributions are used to represent the 50% and 25% corrosion cases.

A number of the 30 analysis did not reach failure prior to obtaining the convergence limit for these two levels of corrosion. For these cases, failure pressures were extrapolated based on the last values computed in the analysis. These extrapolated cases were not used in the lognormal fit

leading to poor curve fits at higher pressures, but enables better fits to the low probability failures which are not extrapolated. All five points shown for the basemat case without corrosion were extrapolated and therefore no curve fit is included.

Table 5.2: Random Input Parameters

Property	Median	COV/β	Distribution
Plate Steel			
Ultimate Strength (f_u)	682 MPa (98.9 ksi)	0.09	Lognormal
Yield Strength Factor	1.0	0.07	Normal
Elastic Modulus (E_s)	200 GPa (29000 ksi)	0.06	Normal
Uniaxial Failure Strain (ε_{fail})	0.25	0.12	Normal
Fracture Mech. Cutoff *J*	1.0	0.10	Lognormal
Corrosion Depth Uncertainty	1.0	0.10	Normal
Bellows Leak			
Percent of Convolution Length Compression Required	97%	0.05	Normal
Percent of Convolution Length Compression Required with Corrosion	63%	0.36	Lognormal
Epistemic Uncertainty			
Local Shell Model Strain Factor (f_{FEM-u})	1.0	0.35	Lognormal
Corrosion Factor Uncertainty (f_{c-u})	1.0	0.20	Lognormal

The bottom plot in Figure 5.15 illustrates the fragility curves for the upper floor and ice basket locations. Without corrosion, the ice basket region is by far the most critical region and the likely failure location. Even though the original plate thickness at the upper floor location (1.91 cm) is slightly larger than at the ice basket location (1.59 cm), 50% corrosion is required at the upper floor to produce a similar fragility curve as the ice basket at 25% corrosion. The fragility curves for 65% corrosion at the upper floor and 50% at the ice basket are also similar. As with the leak fragilities for the basemat location, two distributions were required to fit the ice basket fragility with 50% corrosion.

The failures predicted for the upper floor and ice basket lead directly to catastrophic rupture since the far field stresses in the shell are sufficiently large to cause unstable propagation of small leak cracks.

Figure 5.16 shows the fragility curve for the locations assumed not to bypass the ice condenser after developing a leak. Although a leak at the upper containment location would not bypass the ice condenser, the current prediction shows that the upper containment failure proceeds directly to catastrophic rupture (the risk model assumes that all catastrophic ruptures will bypass the ice condenser). No corrosion was considered in this location since the upper containment is located above the ice condenser. Figure 5.15 also includes the fragilities for the bellow assumed most critical. The failure pressures at low probabilities are close to the lower bound pressure of 0.427

MPa determined by Greimann et al. (1991) through finite element analyses. Figure 5.16 also shows the effects of corrosion in the bellows with a slight shift in the fragility.

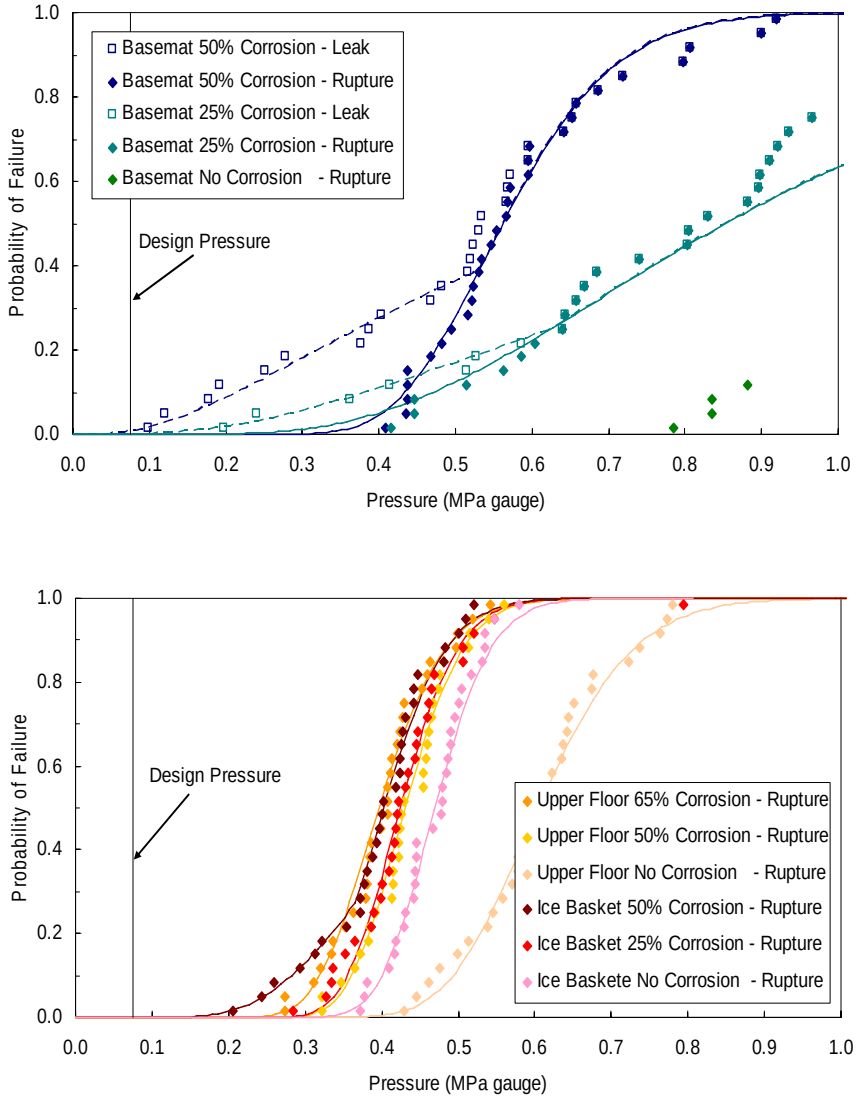

Figure 5.15: Fragility Curves for Locations Contributing to the Bypass Mode: (top) Basemat Location, (bottom) Upper Floor and Ice Basket Locations

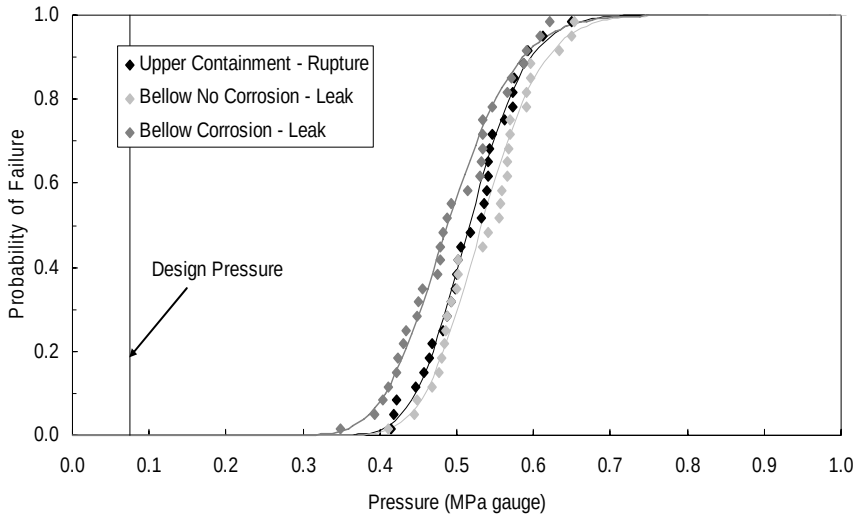

Figure 5.16: Fragility Curves for Locations Contributing to the No Bypass Mode

The fragility curves enable the determination of total cumulative probability of failure distributions. Eight different "conditions" are considered for the PWR Ice Condenser containment: 1) Original (No corrosion at any location), (2) 50% corrosion at the basemat, (3) 25% corrosion at the basemat, (4) 65% corrosion at the upper floor, (5) 50% corrosion at the upper floor, (6) 50% corrosion at the ice basket, (7) 25% corrosion at the ice basket, and (8) corrosion in the bellows. For each condition, no corrosion is present at any location other than the location being considered. Since there are two similar bellows assumed to be equally critical, conditions 1 through 7 include two statistically independent bellows. The corroded bellows condition (8) also considers two statistically independent bellows with both corroded.

Figure 5.17 illustrates the cumulative probability of failure for each of the 8 conditions. Failure is defined at the lowest pressure to cause leak or rupture (these occur simultaneously for most conditions). At low failure probabilities, the pressures exhibit a large level of scatter between the different conditions. This reflects the uncertainty in both material properties and modeling accuracy that are introduced through the LHS method. Failure pressures at higher probabilities show significantly less scatter since catastrophic rupture in a few critical locations dominates the containment behavior (less influence from the corrosion location and level).

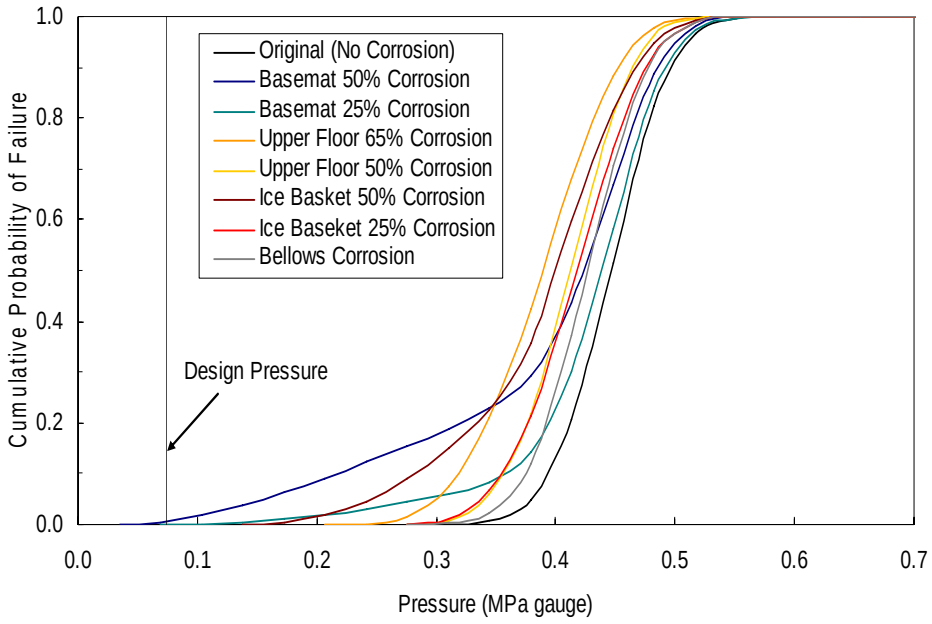

Figure 5.17: Cumulative Probability of Failure for Each Containment Condition

Figure 5.18 through Figure 5.25 show the conditional failure probabilities corresponding to the 8 conditions illustrated in Figure 5.17. The conditional probabilities reflect the probability of a specific mode causing failure, given that a containment failure has occurred.

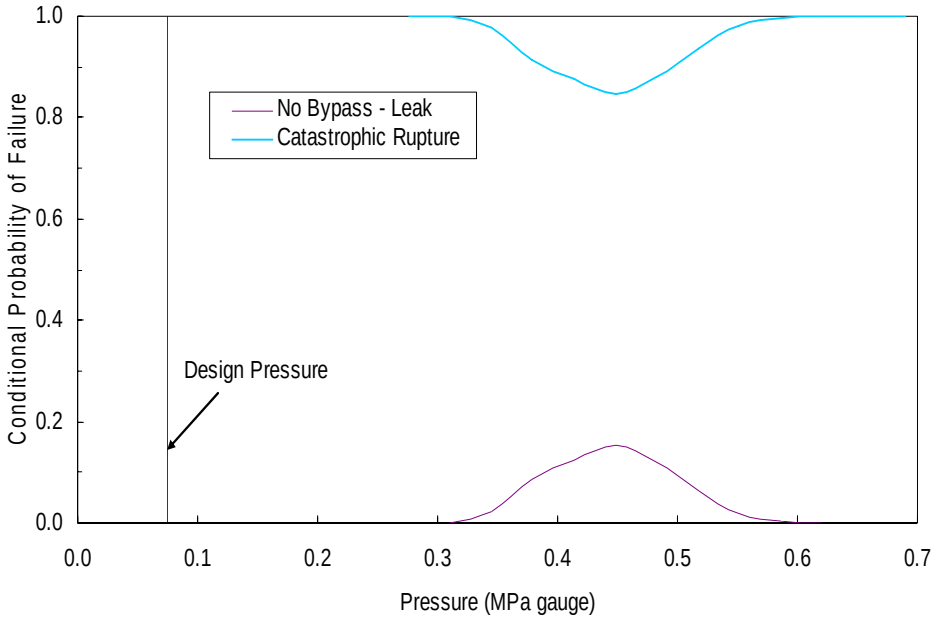

Figure 5.18: Conditional Probabilities for the Original Condition (No Corrosion)

For example, Figure 5.18 shows the conditional probabilities for the containment with no corrosion in any location (original containment state). At low pressures (pressure < 0.32 MPa), the conditional probability of catastrophic rupture is equal to 1. Figure 5.17 indicates that the cumulative probability of failure for the containment without corrosion at pressures lower than approximately 0.34 MPa are close to 0. At these low cumulative failure probabilities near 0, any containment failure that occurs, would occur in the ice basket location which proceeds directly to catastrophic rupture. As the pressure increases, leak in the bellows increases in probability and contributes to the leak no bypass mode. At higher pressures (pressure > 0.6 MPa), the catastrophic rupture conditional probability again reaches 1.

Figure 5.19 and Figure 5.20 contain the conditional probabilities for the two basemat corrosion conditions. For these conditions, leak at the basemat becomes possible at low pressures and contributes to the leak bypass mode.

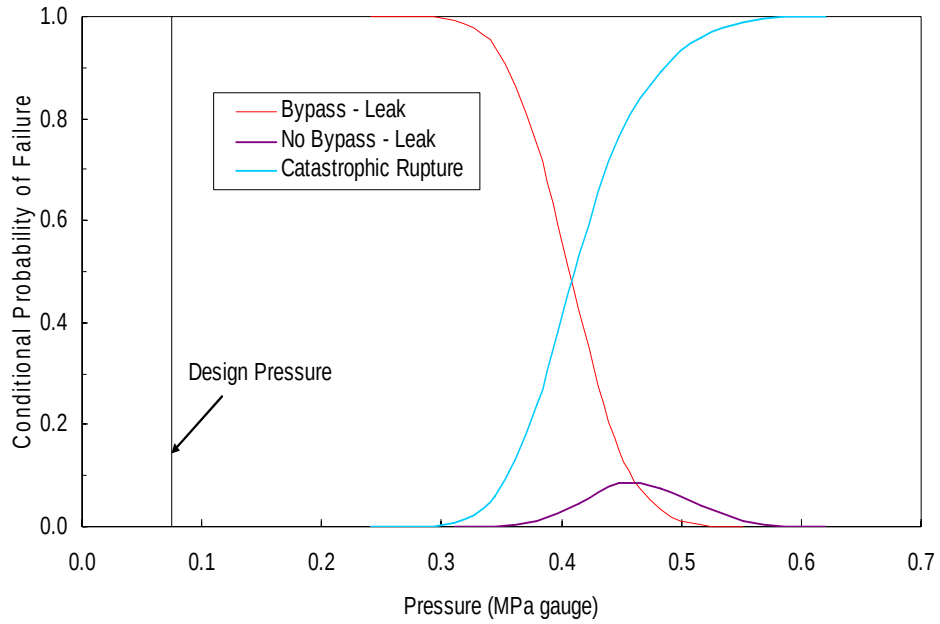

Figure 5.19: Conditional Probabilities for 50% Corrosion at the Basemat

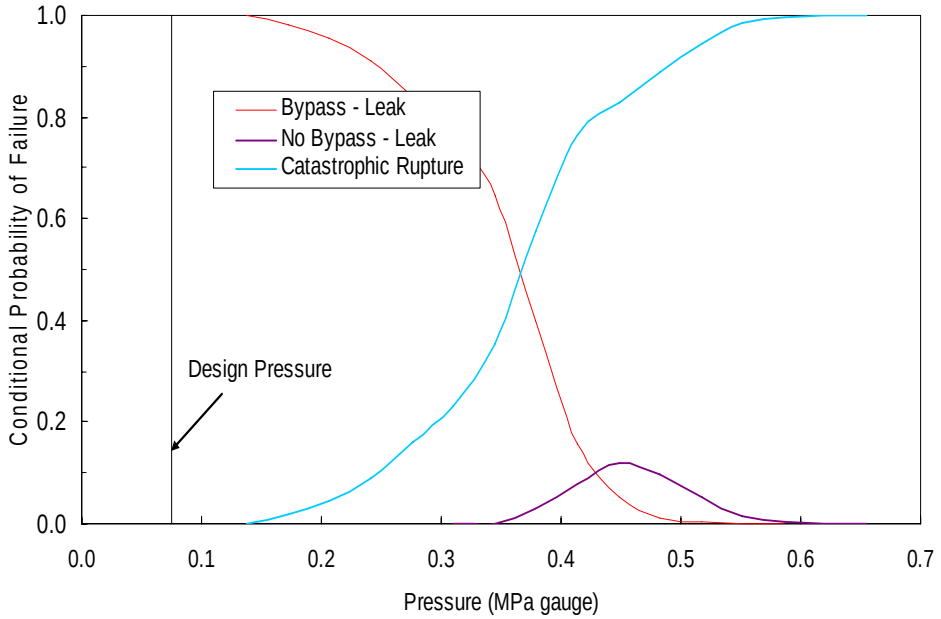

Figure 5.20: Conditional Probabilities for 25% Corrosion at the Basemat

Corrosion in the upper floor and at the ice basket locations leads to conditional probabilities for catastrophic ruptures near 1 at all pressures. Figure 5.21 through Figure 5.24 show that there is a

relatively small conditional probability for the leak no bypass mode due to the bellows in these cases.

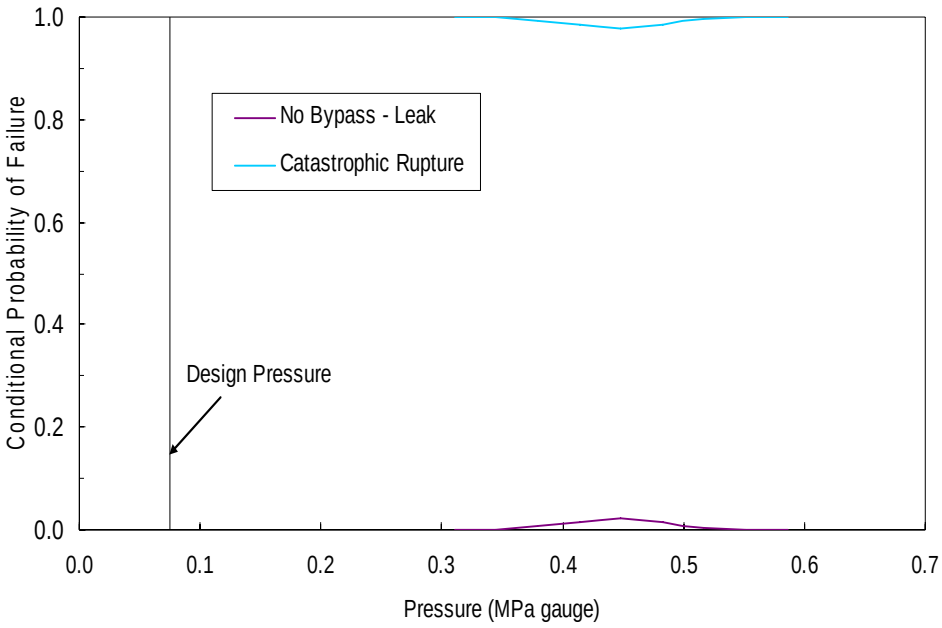

Figure 5.21: Conditional Probabilities for 65% Corrosion at the Upper Floor

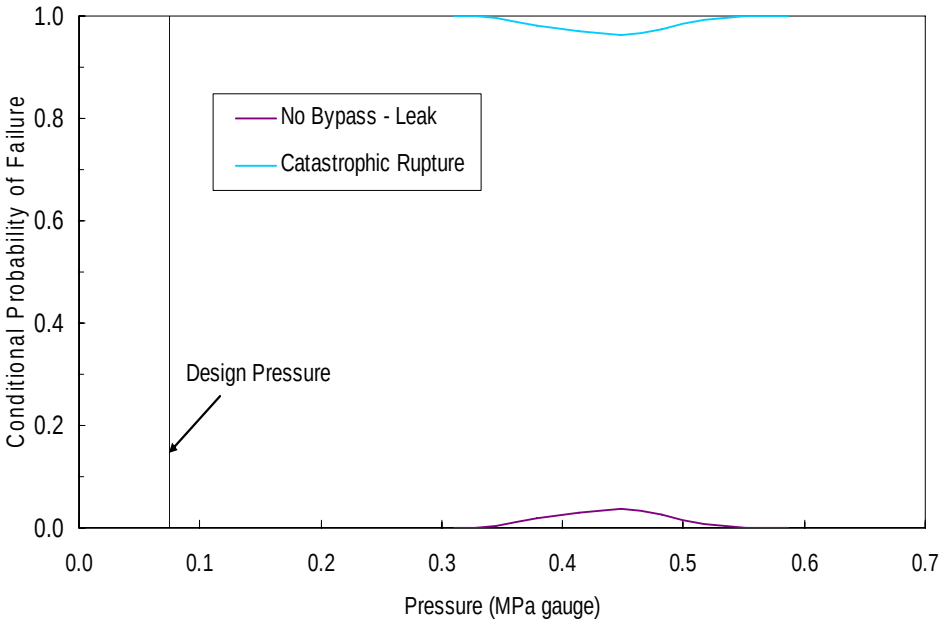

Figure 5.22: Conditional Probabilities for 50% Corrosion at the Upper Floor

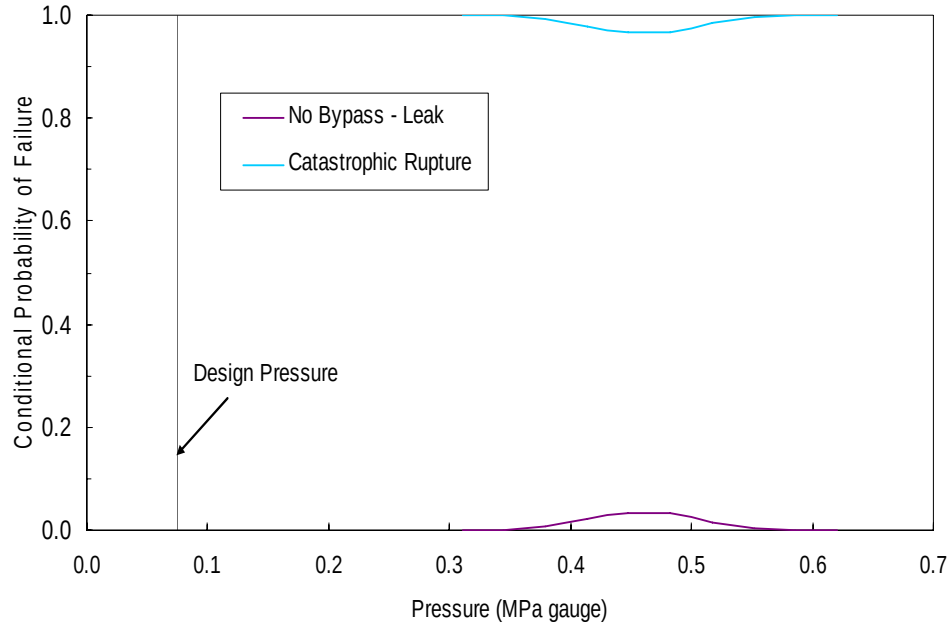

Figure 5.23: Conditional Probabilities for 50% Corrosion at the Ice Basket

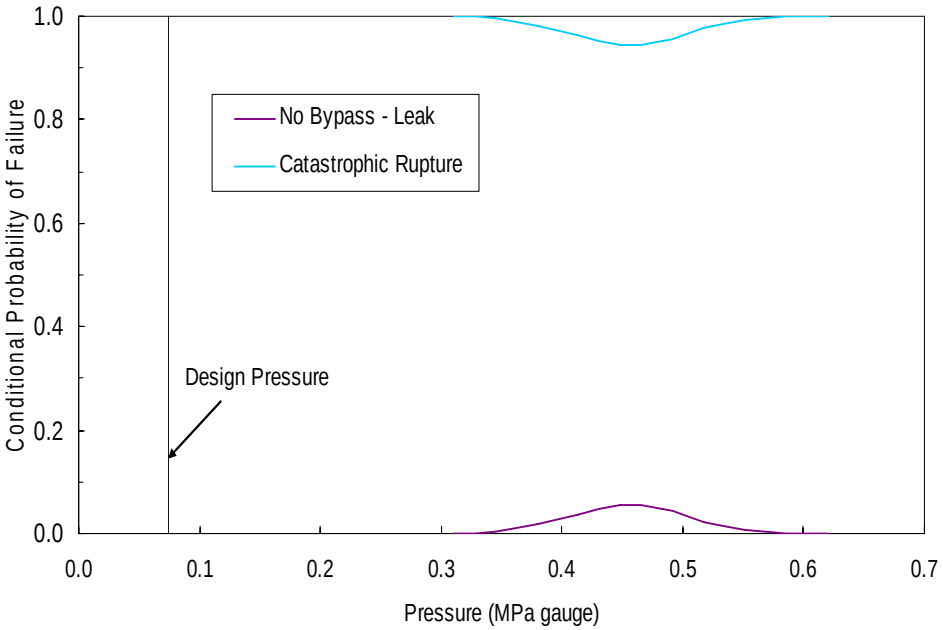

Figure 5.24: Conditional Probabilities for 25% Corrosion at the Ice Basket

Corrosion in the bellows causes the conditional probability of the leak no bypass mode to increase significantly. At low pressures (pressure < 0.3 MPa), catastrophic rupture still dominates, but the cumulative probability of failure is approximately 0 in this range.

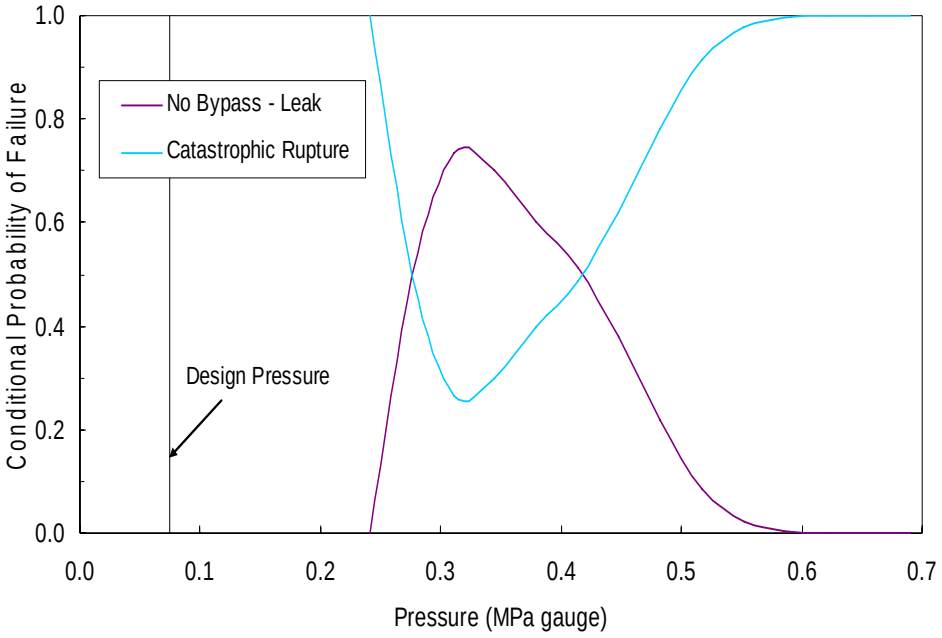

Figure 5.25: Conditional Probabilities for Bellows Corrosion

5.3 Computational Issues Discovered with the NUREG-1150 Ice Condenser PRA Model

While performing the risk analyses with the existing PRA model for the ice condenser containments, several issues were encountered. First, the original conditional failure probabilities were hard-coded into the accident progression event tree (APET) subroutine. Due to the multiple failure modes and locations, an error was determined such that the array which stored the conditional failure probabilities was accessed incorrectly. This led to the wrong conditional failures being accessed and used in the PRA model, i.e., the probability of leak at location 1 was being accessed when rupture at location 2 should have been. It would seem that this resulted from a misinterpretation of how FORTRAN stores three-dimensional arrays. Since the code was modified to read the conditional failure probabilities from an input file, this problem was corrected by altering the input order for the conditional failure probabilities. In addition, numerical problems were discovered with the steel PWR ice condenser conditional failure probabilities. It was determined that non-zero values are required for the conditional failure probability in certain instances. Without finite values, specific accident scenarios do not proceed through the correct path, leading to drastically inaccurate values for LERF. Additional analyses showed that the values used for the conditional failure probability (10^{-6}) did not affect LERF when changed as long as then remained relatively small, but non-zero. These issues were resolved prior to running the PRA analyses.

5.4 Risk Analysis Results

Table 5.3 shows the CDF values from NUREG 1150. Because the containment response does not affect the CDF for this particular plant, the results are the same for all of the cases studied.

Table 5.3: Core Damage Frequency (yr^{-1})

Case	Mean	5%	50%	95%
All	5.7E-5	1.2E-5	3.7E-5	1.8E-4

Table 5.4 shows the LERF results, Table 5.5 shows the probability of large early containment failure conditional on core damage, and Table 5.6 shows the change in LERF relative to the Un-damaged (Current Study) case. The change in LERF is used with Figure 2.2 to assess the acceptability of a given degradation state within the framework of Regulatory Guide 1.174.

Table 5.6 indicates that none of the degraded cases cause an increase of LERF to exceed 10-7. Since LERF does not exceed 5E-5, each of the degraded cases falls within Region III in Figure 2.2. Therefore, each of these cases would be acceptable by Regulatory Guide 1.174.

Table 5.4: Large Early Release Frequency (yr^{-1})

Case	Mean	5%	50%	95%
Un-damaged (Reference)	7.41E-7	0	1.32E-9	1.22E-5
Un-damaged (Current Study)	4.67E-7	0	1.62E-9	1.01E-5
Bellow Corrosion	4.61E-7	0	1.32E-9	1.01E-5
25% Corrosion at Basemat	4.57E-7	0	1.62E-9	1.01E-5
50% Corrosion at Basemat	4.41E-7	0	9.29E-10	1.01E-5
50% Corrosion at Upper Floor	5.14E-7	0	3.89E-9	1.02E-5
65% Corrosion at Upper Floor	5.37E-7	0	6.48E-9	1.02E-5
25% Corrosion at Ice Basket	5.05E-7	0	3.89E-9	1.02E-5
50% Corrosion at Ice Basket	5.57E-7	0	5.55E-09	1.02E-05

Table 5.5: Probability of Large Early Containment Failure Conditional on Core Damage

Case	Mean	5%	50%	95%
Un-damaged (Reference)	1.30E-02	0	1.01E-5	6.75E-02
Un-damaged (Current Study)	8.19E-03	0	4.37E-05	5.61E-02
Bellow Corrosion	8.08E-03	0	3.57E-05	5.61E-02
25% Corrosion at Basemat	8.02E-03	0	4.37E-05	5.62E-02
50% Corrosion at Basemat	7.73E-03	0	2.51E-05	5.62E-02
50% Corrosion at Upper Floor	9.01E-03	0	1.05E-04	5.64E-02
65% Corrosion at Upper Floor	9.42E-03	0	1.75E-04	5.64E-02
25% Corrosion at Ice Basket	8.86E-03	0	1.05E-04	5.64E-02
50% Corrosion at Ice Basket	9.78E-03	0	1.50E-04	5.65E-02

Table 5.6: Change in the Large Early Release Frequency (yr^{-1}) due to Degradation

Case	Mean	5%	50%	95%
Bellow Corrosion	-6.27E-09	0	-2.96E-10	0.00E+00
25% Corrosion at Basemat	-9.69E-09	0	0.00E+00	1.80E-08
50% Corrosion at Basemat	-2.62E-08	0	-6.88E-10	1.80E-08
50% Corrosion at Upper Floor	4.67E-08	0	2.27E-09	5.40E-08
65% Corrosion at Upper Floor	7.01E-08	0	4.86E-09	5.40E-08
25% Corrosion at Ice Basket	3.82E-08	0	2.27E-09	5.40E-08
50% Corrosion at Ice Basket	9.06E-08	0	3.93E-09	7.20E-08

Further examination of the change in LERF for each of the degraded cases shows that LERF actually decreases for three of the degraded cases. Each of these cases, bellows corrosion and the two basemat corrosion cases, has significantly high leak conditional probabilities at lower pressures. The four corrosion cases at the upper floor and ice basket are dominated by catastrophic rupture. This behavior explains the trends in LERF since only ruptures and catastrophic ruptures are included in LERF in the PRA model.

The decrease in LERF is possible for the three leak-dominant cases because leak outcomes are included in the small release frequency (SERF). Table 5.7 through Table 5.9 show the SERF, SERF conditional on core damage, and the change in SERF relative to the Un-damaged (Current Study) case. Table 5.10 through Table 5.12 show the total frequencies (LERF + SERF).

As expected, SERF increases for the leak-dominant cases and decreases for the catastrophic rupture cases. It should be noted that if there were a table similar to

Table 3.4 for SERF, the 50% corrosion at the basemat case would fall within Region II with a ΔSERF of 1.67E-7. A change proposed under the Regulatory Guide 1.174 risk-informed methodology must also satisfy other design goals. It must still maintain defense in depth and acceptable safety margins, and therefore, changes in SERF may need to be addressed.

Table 5.12 illustrates that any form of degradation increases the total release frequency.

Table 5.7: Small Early Release Frequency (yr^{-1})

Case	Mean	5%	50%	95%
Un-damaged (Reference)	1.01E-07	0	4.51E-10	2.09E-06
Un-damaged (Current Study)	1.04E-07	0	4.29E-10	2.09E-06
Bellow Corrosion	1.17E-07	0	5.85E-10	2.79E-06
25% Corrosion at Basemat	1.34E-07	0	5.37E-10	3.28E-06
50% Corrosion at Basemat	2.71E-07	0	1.11E-09	5.44E-06
50% Corrosion at Upper Floor	8.72E-08	0	4.07E-10	1.20E-06
65% Corrosion at Upper Floor	8.72E-08	0	3.92E-10	1.20E-06
25% Corrosion at Ice Basket	8.72E-08	0	4.29E-10	1.20E-06
50% Corrosion at Ice Basket	8.61E-08	0	3.92E-10	1.20E-06

Table 5.8: Probability of Small Early Containment Failure Conditional on Core Damage

Case	Mean	5%	50%	95%
Un-damaged (Reference)	1.78E-03	0	1.22E-05	1.16E-02
Un-damaged (Current Study)	1.82E-03	0	1.16E-05	1.16E-02
Bellow Corrosion	2.05E-03	0	1.58E-05	1.55E-02
25% Corrosion at Basemat	2.35E-03	0	1.45E-05	1.82E-02
50% Corrosion at Basemat	4.75E-03	0	2.99E-05	3.02E-02
50% Corrosion at Upper Floor	1.53E-03	0	1.10E-05	6.66E-03
65% Corrosion at Upper Floor	1.53E-03	0	1.06E-05	6.66E-03
25% Corrosion at Ice Basket	1.53E-03	0	1.16E-05	6.66E-03
50% Corrosion at Ice Basket	1.51E-03	0	1.06E-05	6.66E-03

Table 5.9: Change in the Small Early Release Frequency (yr^{-1}) due to Degradation

Case	Mean	5%	50%	95%
Bellow Corrosion	1.31E-08	0	1.55E-10	7.02E-07
25% Corrosion at Basemat	3.02E-08	0	1.07E-10	1.19E-06
50% Corrosion at Basemat	1.67E-07	0	6.77E-10	3.35E-06
50% Corrosion at Upper Floor	-1.65E-08	0	-2.22E-11	-8.89E-07
65% Corrosion at Upper Floor	-1.65E-08	0	-3.70E-11	-8.89E-07
25% Corrosion at Ice Basket	-1.65E-08	0	0.00E+00	-8.89E-07
50% Corrosion at Ice Basket	-1.77E-08	0	-3.70E-11	-8.89E-07

Table 5.10: Total Early Release Frequency (yr^{-1})

Case	Mean	5%	50%	95%
Un-damaged (Reference)	8.42E-07	0	8.25E-10	1.42E-05
Un-damaged (Current Study)	5.71E-07	0	2.05E-09	1.22E-05
Bellow Corrosion	5.77E-07	0	1.91E-09	1.29E-05
25% Corrosion at Basemat	5.91E-07	0	2.15E-09	1.34E-05
50% Corrosion at Basemat	7.11E-07	0	2.04E-09	1.56E-05
50% Corrosion at Upper Floor	6.01E-07	0	4.29E-09	1.14E-05
65% Corrosion at Upper Floor	6.24E-07	0	6.87E-09	1.14E-05
25% Corrosion at Ice Basket	5.92E-07	0	4.31E-09	1.14E-05
50% Corrosion at Ice Basket	6.44E-07	0	5.94E-09	1.14E-05

Table 5.11: Probability of Total Early Containment Failure Conditional on Core Damage

Case	Mean	5%	50%	95%
Un-damaged (Reference)	1.48E-02	0	2.23E-05	7.91E-02
Un-damaged (Current Study)	1.00E-02	0	5.53E-05	6.77E-02
Bellow Corrosion	1.01E-02	0	5.15E-05	7.16E-02
25% Corrosion at Basemat	1.04E-02	0	5.82E-05	7.44E-02
50% Corrosion at Basemat	1.25E-02	0	5.50E-05	8.64E-02
50% Corrosion at Upper Floor	1.05E-02	0	1.16E-04	6.31E-02
65% Corrosion at Upper Floor	1.10E-02	0	1.86E-04	6.31E-02
25% Corrosion at Ice Basket	1.04E-02	0	1.17E-04	6.31E-02
50% Corrosion at Ice Basket	1.13E-02	0	1.61E-04	6.32E-02

Table 5.12: Change in the Total Early Release Frequency (yr^{-1}) due to Degradation

Case	Mean	5%	50%	95%
Bellow Corrosion	6.84E-09	0	-1.41E-10	7.02E-07
25% Corrosion at Basemat	2.05E-08	0	1.07E-10	1.21E-06
50% Corrosion at Basemat	1.41E-07	0	-1.11E-11	3.37E-06
50% Corrosion at Upper Floor	3.02E-08	0	2.25E-09	-8.35E-07
65% Corrosion at Upper Floor	5.36E-08	0	4.82E-09	-8.35E-07
25% Corrosion at Ice Basket	2.17E-08	0	2.27E-09	-8.35E-07
50% Corrosion at Ice Basket	7.30E-08	0	3.90E-09	-8.17E-07

The example plants examined here serves as good case studies indicating that one should be very cautious about simply applying the ΔLERF criterion to evaluate the significance of containment degradation. It is important to closely examine how degradation can increase the likelihood of one failure mode while decreasing the likelihood of another, and evaluate the consequences of these different modes. It cannot be stressed enough that the cases of degradation examined here are extremely limited in scope. There are currently no means of predicting degradation prior to its discovery. Since the location and specific nature of any degradation could dramatically affect the containment capacity and risk, a detailed analysis of that scenario would be required. The specific results reported in this study should in no way be applied to making regulatory decisions on existing plants.

6. Risk Analysis of PWR Plant with Prestressed Concrete Containment

The final containment investigated in this study is a prestressed concrete containment vessel at a PWR nuclear power plant. As for the other three plants investigated in this study, a risk model was developed for this plant in the NUREG-1150 study. The original intent was to develop containment fragility curves for this containment and integrate those into the NUREG-1150 risk model for this plant, as was done for the other three cases. As this study progressed, however, it became evident that for a number of reasons, it would not be possible to use the original risk model for this plant.

Because of the large effort involved in developing a risk model for a plant from the ground up, it was decided to pursue an alternative route to perform a representative risk analysis of a PWR plant with a prestressed concrete containment. It was observed that the representative prestressed concrete containment has a volume roughly 30% greater than that of the reinforced concrete containment studied in Chapter 3, but that the design pressures of these two containments are very similar, 0.324 MPa (47 psi) for the prestressed concrete containment, and 0.310 MPa (45 psi) for the reinforced concrete containment. The greater volume of the prestressed concrete containment is due to the fact that it houses a 4-loop PWR reactor, while the reinforced concrete containment houses a smaller, 3-loop PWR reactor. The increased amount of steam produced in a loss of coolant accident (LOCA) in the 4-loop system requires a larger containment volume to resist that load while keeping the design pressure roughly constant.

Because the reinforced concrete and prestressed concrete containments have approximately the same design pressure, it is reasonable to use the structural models of the prestressed concrete containment together with the risk model for the plant with the reinforced concrete containment. If a prestressed concrete containment were chosen in the original design of the 3-loop PWR plant instead of the reinforced concrete containment that was acutally built, it would exhibit roughly the same structural response as is seen in the prestressed containment in the 4-loop PWR plant.

The actual structural dimensions (wall thickenss, amount of prestressing and reinforcing steel, etc.) are somewhat larger in the containment with a larger volume because the forces are larger as a result of the increased volume. However, if two containments of differing size are built to the same design codes and design pressure, they will experience leak, rupture, and catastrophic rupture failures at approximately the same pressures. This was a key premise of the series of scaled containment model tests conducted at Sandia National Laboratories.

The risk assessment of the PWR plant with a prestressed concrete containment studied here should be viewed as a study of the plant investigated in Chapter 3, but with an alternative design scenario where a prestressed concrete containment was chosen in place of a reinforced concrete containment. This is clearly not an analysis of an actual plant, but that is not the intention of this study. The goal is to demonstrate the risk significance of various types of degradation that might be observed at typical U.S. nuclear power plants.

The analysis of the prestressed concrete containment assesses the effects of corrosion in the liner as well as degradation of the prestressing tendons. The effects of corrosion in the liner wall are investigated near the wall-basemat juncture and at the mid-height of the containment. Two cases

of tendon degradation at the mid-height are also examined. Figure 6.1 shows these degradation locations on a schematic diagram of the containment building.

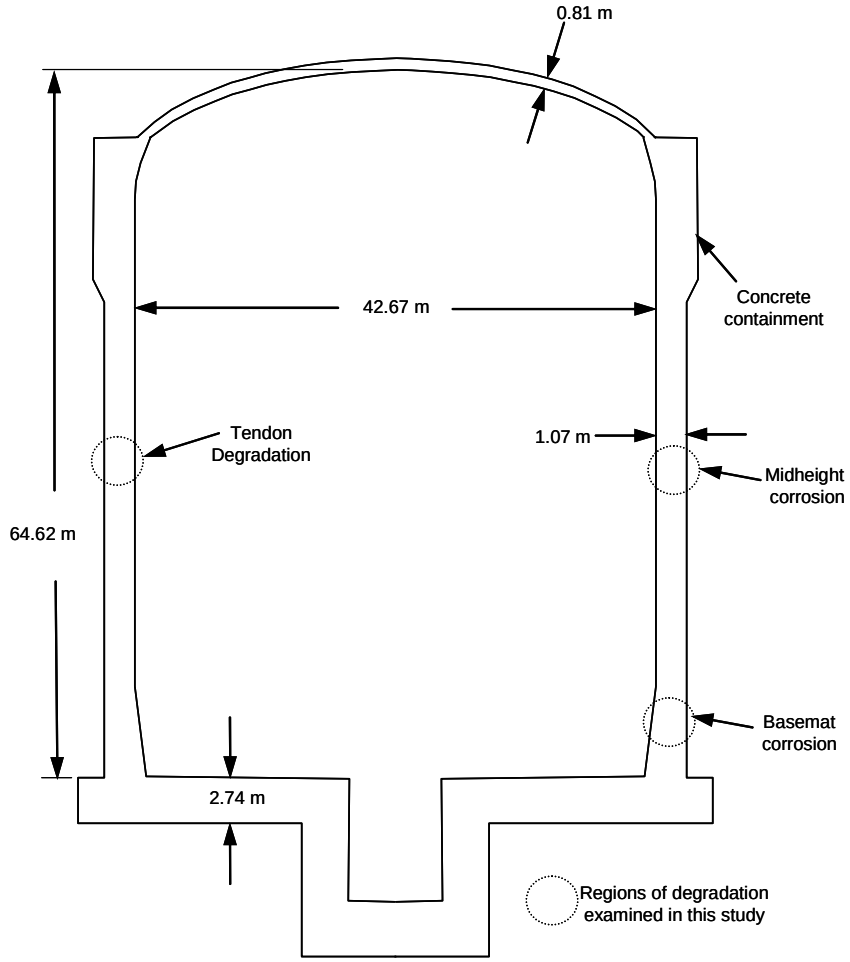

Figure 6.1: Postulated Degradation in Prestressed Concrete Containment

The corrosion locations were chosen because they are regions of potentially high liner strains, where corrosion has been observed in similar containments, or potential regions of corrosion. It should be re-emphasized that although the dimensions and other properties of the containment vessel were taken from the drawings of an actual plant, the corrosion assumed for this study is not representative of actual corrosion observed at that plant.

6.1 Structural Model of Prestressed Concrete Containment

Experimental evidence from a pressurization test of a 1:4 scale model of a prestressed concrete containment vessel with a steel liner (Hessheimer et al, 2003) indicates that this type of containment tends to resist pressures well beyond its design pressure. In the 1:4 scale model test, the containment exhibited limited structural damage on a global scale up to 3.3 times the design pressure. At that point, the leak rate exceeded the capacity of the pressurization system. An inspection of the liner revealed 26 discrete tears, nearly all located at fabrication defects. The onset of linear tearing and leakage occurred at a pressure 2.5 times the design pressure with an average hoop strain of 0.18%. After applying a leak-resistant coating to the liner and

repressurizing the containment with water and nitrogen gas, the containment resisted a pressure approximately 3.6 times the design pressure. At this point, the containment catastrophically ruptured at the mid-height of the cylinder. The initial average hoop strain at peak pressure was 1.02% and increased to 1.65% just prior to rupture.

The procedure used in this study to analyze the prestressed containment is very similar to that used by Cherry and Smith (2001). In that study, an axisymmetric model of the containment structure was developed to find the global strains. This model included the effects of the liner, the concrete, the reinforcing steel, and tendons. The global strains were then used as boundary conditions for refined 2-D liner submodels with corrosion damage and a 3-D hatch submodel. An area of the liner with a reduced thickness modeled corrosion damage. A strain criterion was used to determine the point when tearing occurred. Factors were used in the failure criterion to account for the multi-axial stress state, the level of model refinement, and the level of refinement in the analytical model.

A second study by Smith (2001) reexamined the prestressed containment including degradation of the prestressing tendons. The analysis used a 30º wedge segment of the containment, rather than the axisymmetric model employed in the first study. Seventeen different tendon degradation scenarios were considered including losses in prestressing and tendon cross-sectional area (due to corrosion). Degradation of both the vertical and horizontal tendons was considered. The same strain criterion was used to determine the point of tearing in the liner.

The approach of this study closely follows the work done by Cherry and Smith (2001) and Smith (2001), with a few notable exceptions. The global 3-D 30º wedge model of the containment has essentially remained unchanged. Local 2-D models are also used to model the corroded regions in the liner. However, the finite element meshes of the corroded areas have been modified to more realistically model the shape of a corroded region. In the meshes used by Cherry and Smith, the corroded regions were rectangular in shape, which resulted in stress concentrations at the corners of those regions. The edges of the corroded regions have been rounded, and the transition between the corroded and non-corroded areas has been made more gradual. In addition, the 3-D model of the hatch used in the previous work was not analyzed here. Strain concentrations caused by penetrations are taken into account with strain magnification factors similar to those used in the reinforced concrete containment analysis.

The work of Cherry and Smith (2001) Smith (2001) was primarily focused on finding the failure pressure of degraded containments. For the purposes of this study, it is important to not only characterize the strength of degraded containments, but to find the difference between the containment in its original and degraded conditions for the purposes of computing the change in risk. For this reason, an additional effort has been made to account for the effects of local penetrations, which are important contributors to early failure in the un-degraded model. In addition, failure criteria are established for leak, rupture, and catastrophic rupture, whereas the previous studies only considered leak in their failure estimates.

6.1.1 3-D Global Models

As mentioned previously, the global behavior of the containment is modeled with essentially the same 3-D 30º wedge finite element model used by Smith (2001). The 3-D finite element mesh of the containment is shown in Figure 6.2(a).

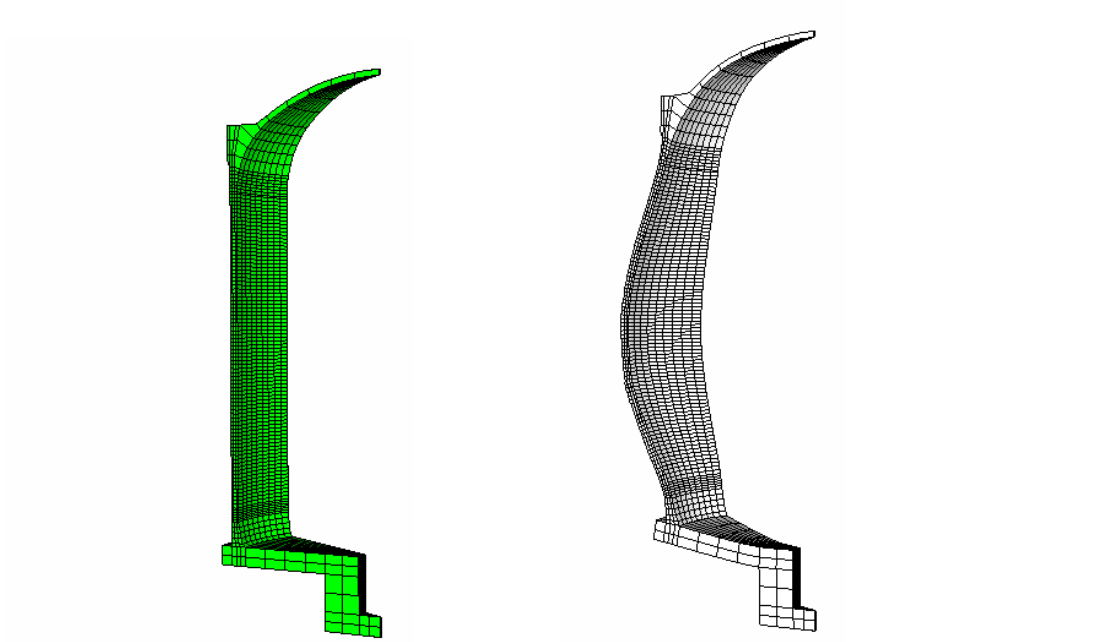

(a) Original Mesh (b) Deformed at 1.08 MPa (157 psi)

Figure 6.2: 3-D Wedge Finite Element Model of Prestressed Containment

The concrete is modeled using the ANACAP-U (ANATECH, 1997) constitutive model, which is linked with the ABAQUS program. 20-node bricks are used to model the concrete components. Nonlinear behavior of the concrete is modeled with a stress-strain law evaluated at element integration points, so the effects of cracking and crushing are "smeared out" over an element. When a tensile strain criterion, which takes multi-axial stress states into account, is met at an integration point, a fixed smeared crack is initiated and softening occurs. A hardening-softening model accounts for the nonlinear behavior of concrete in compression.

Reinforcing bars are modeled by embedding them within the concrete elements with the ABAQUS `*REBAR` command. A uniaxial model accounts for hardening in the reinforcing steel. The hoop and dome tendons are also modeled using reinforcing bars, while the vertical tendons are modeled with truss elements. The liner is modeled with 3-D, 8-node shell elements directly attached to the concrete elements on the inside face of the containment. Nonlinear behavior of the steel in the shell is modeled using a steel plasticity model. Nonlinear spring elements are used to approximate the contact conditions between the containment and the soil below. The spring elements have a high elastic stiffness in compression, and have no strength in tension.

The containment model is subjected to a monotonically increasing internal pressure loading. An increasing temperature is applied to the containment in conjunction with the pressure loading. Initially, the internal surface (liner) of the containment has a temperature of 21^{o} Celsius (70^{o} Fahrenheit). This increases to a maximum of 180^{o} Celsius (356^{o} Fahrenheit) at a pressure of 1.0 MPa (145 psi). Since concrete cracking and reinforcing bar yielding dissipate the liner strains, the thermal loads do not have a significant effect. Because the analysis is performed using load control, it reaches a point where small increases in the pressure result in very large deformations. At this point, the analysis cannot continue because obtaining a converged solution becomes too difficult. This generally occurs when the pressure load is around 1.1 MPa (160 psi) for this model, but varies depending on the input parameters.

Figure 6.2(b) shows the deformed shape of the 3-D model for a typical case near the end of the analysis. Deformations have been magnified by a factor of 5 in this figure. It is evident from the figure that hoop strains are very large near the mid-height of the containment. There are also large bending deformations in the wall-basemat junction.

6.1.2 Local Models with Liner Corrosion

In the analysis of this containment, the strain magnification factors described in Section 2.4.2.1 are used to approximate strain concentrations in the liner at discontinuities, while detailed 2-D finite element models are used to model regions of hypothetical corrosion. To determine the relative significance of corrosion in different locations, two cases of liner corrosion are assumed: at the mid-height of the containment, and in the wall just above the junction with the basemat.

In both cases, corrosion is evaluated at two depths of penetration : 50% and 65% of the liner thickness. The finite element models for both cases are identical, with the corrosion assumed to have occurred over a region 14 cm (5.5 in) wide and 7.3 cm (2.9 in) high. The finite element mesh of this region is shown in Figure 6.4. Figure 6.3 illustrates the full mesh, which covers a 95.3 cm (37.5 in) by 261 cm (105 in) region. At the boundaries of the mesh, the average length of an element edge is 50 mm (2 in), while in the corroded area, the mesh is refined considerably and the average element length is approximately 2.54 mm (0.1 in).

Displacements are extracted from the 3-D global analyses and used as boundary conditions for the submodels. Symmetry conditions are set on the right side of the submodel, and displacements imposed on the top, bottom, and left side. Displacements are also imposed at the location of L-section steel anchors running in the vertical direction. These L-sections are modeled in the 2-D mesh with beam elements.

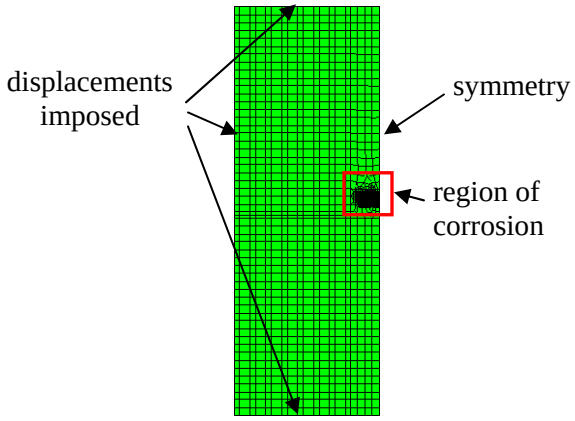

Figure 6.3: Submodel Finite Element Mesh

In both of these cases, a 2.54 cm (1 in) layer of elements surrounding the fully corroded region is used to make a more gradual transition from the un-damaged area to the corrosion zone. In that layer of elements, the corrosion is assumed to penetrate 25% and 32.5% of the wall thickness for the 50% and 65% corrosion cases, respectively. In these models, the steel is modeled using a plasticity model.

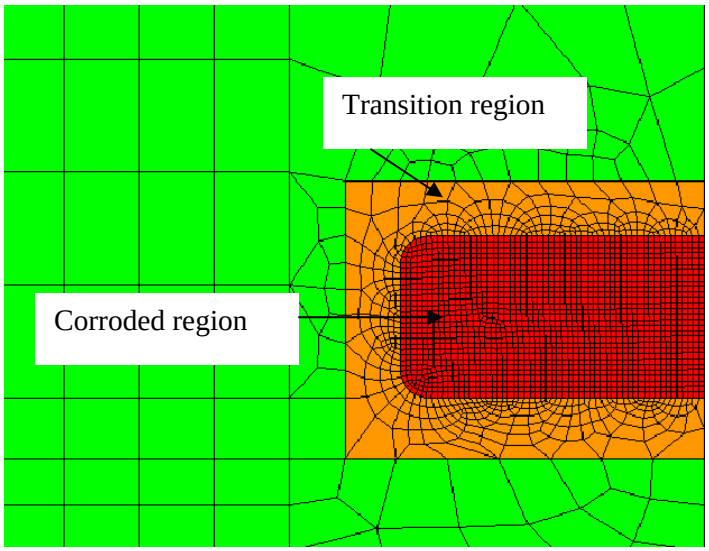

Figure 6.4: Corroded Region in Submodel Finite Element Mesh

The results from the local models are post-processed to determine the point at which tearing (leak), rupture, and catastrophic rupture occurs. For leak, the effective plastic strains are multiplied by factors to account for the effects of the multiaxial stress state, corrosion, gauge length, and modeling uncertainty, as described in Section 2.4.1.1.

6.1.3 Degraded Tendon Analyses

In addition to examining the effects of corrosion in the liner, two cases of tendon degradation are studied here. Smith (2001) examined 17 different tendon degradation cases. Here, two of these cases are studied within the risk assessment framework. The first degraded case reduces the area of 20% of the hoop tendons grouped at the midheight of the cylinder by 50%. It is assumed that the area could have been reduced by general corrosion, pitting, stress corrosion cracking, or hydrogen embrittlement (Smith, 2001). The second case reduces the prestressing force in the same 20% of tendons at the midheight by 50%. Lower than expected levels of prestressing have been observed in existing plants (Ashar et al., 1994) possibly due to improper calibration of the jacks during initial post-tensioning, higher than expected prestressing losses, and failures in quality control. The 3-D global model was modified to introduce these two cases of tendon degradation.

6.1.4 Structural Analysis with Best Estimate Properties

The primary focus of the structural analysis in this study is to develop fragility curves to interface with the risk model. However, it is instructive to study the results of a baseline analysis that uses the median values of the input parameters that are randomly generated for the LHS analyses.

Six potential liner failure modes are considered: failure at the four locations of geometric discontinuities for which magnification factors are used (see Section 2.4.2.1), failure at a corroded region at the wall midheight, and failure at a corroded region on the wall near the basemat. In addition, two cases of tendon degradation are examined with failures determined at the four locations of geometric discontinuities. To investigate the potential for failure (leak) at all of these locations, the 3-D global model is analyzed, and results are extracted for use as displacement boundary conditions for the two 2-D local corrosion models. The two local corrosion models are run with 50% and 65% corrosion and post-processed to find the most critical value of $\bar{\varepsilon}_p$ at every loading step using the steel leak criterion (see Section 2.4.1.1). A separate post-processing tool is applied to the results of the 3-D models to apply appropriate magnification factors to find $\bar{\varepsilon}_p$ for the four selected discontinuity locations at every loading increment. The uniaxial plastic failure strain, ε_{fail}, was assumed to be 25% for these analyses. The gauge length factor was assumed to be 4.0 for the local corrosion models in this baseline analysis.

Figure 6.5 shows the plot of the ratio of $\bar{\varepsilon}_p$ to ε_{fail} (0.25) for the 4 discontinuities and 2 liner corrosion locations as a function of internal pressure for the baseline analysis (no tendon degradation). A horizontal line has been drawn at 1.0 to show the failure criterion. It is evident that the failure condition is met first at the wall-basemat junction, and that the discontinuity at the springline appears to be the least critical location. From this analysis, it appears that a containment without any degradation would leak at 0.744 MPa (107.8 psi) at the wall-basemat junction. If the postulated corrosion were present at the basemat, it would fail at that location at an internal pressure of 0.904 MPa (131.1 psi) and 0.892 MPa (129.4 psi) for 50% and 65% corrosion, respectively. Leakage near the corroded midheight location does not occur until 1.070 MPa (155.3 psi) and 1.030 MPa (149.4 psi) for 50% and 65% corrosion, respectively. Leakage occurs at the wall-basemat junction prior to leak in the corroded basemat location. Table 6.1 summarizes the leak pressures for each location.

Although Cherry and Smith (2001) assumed somewhat different corrosion patterns, it is useful to compare their failure pressures with those obtained in this study. For their best estimate model of

the containment, they found that the un-damaged containment failed at 0.99 MPa (143 psi). Here, we predict failure at the wall-basemat junction at 0.744 MPa (107.8 psi). A possible reason for the lower capacity in the current study is the use of the magnification factors (see Section 2.4.2.1) to determine failure at the discontinuities within global model. The magnification factors enable the use of global models that do not include detailed modeling of discontinuities. The analysis by Cherry and Smith did not use the magnification factor technique, but used the strains from a coarsely meshed axisymmetric model to determine failure.

With corrosion 50% through the wall, Cherry and Smith (2001) found that the containment failed at 0.93 MPa (135 psi) when the corrosion was at the mid-height and 0.92 MPa (134 psi) with corrosion at the basemat. The failure pressures for the un-damaged model and midheight corrosion obtained in the current study are somewhat higher than those found by Cherry and Smith. This may be due to the fact that Cherry and Smith obtained the boundary conditions for their submodel from an axisymmetric global model. Cherry and Smith also assumed a slightly different corrosion shape and location. These are possible reasons for the higher capacity of the corroded midheight area found in the current study.

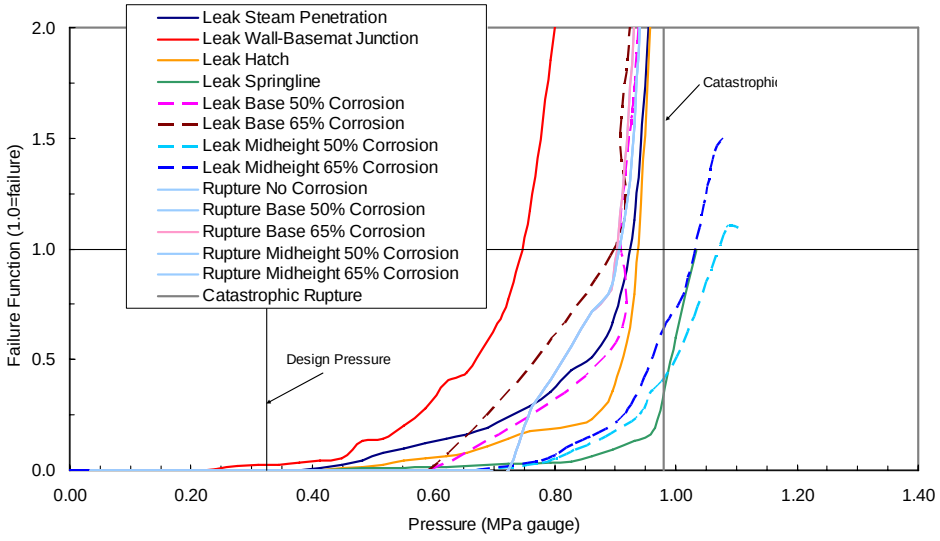

Figure 6.5: Failure Potential at Liner Corrosion and Discontinuity Locations

Figure 6.5 and Table 6.1 also include failure curves and pressures for five rupture cases: the original containment with no corrosion, 50% corrosion at the basemat, 65% corrosion at the basemat, 50% corrosion at the midheight, and 65% corrosion at the midheight. The procedure in Section 2.4.2.2 is used to compute the ratio of the total rupture area, A_{total}, to the rupture area limit of 0.028 m2 (0.3 ft2), as a function of pressure. The four features, steam penetration, wall-basemat junction, hatch, and springline, are each assumed to contain four cracks (n_i) each after the leak criterion has been reached. The choice of four cracks at each location is somewhat arbitrary, though based on the upper limit of the number of tears observed in the 1:6 scale reinforced concrete containment testing at Sandia National Laboratories (Horschel, 1992). The number of cracks at each location could have been introduced as a random variable, but due to the approximate nature of the rupture estimate employed here, a random variable with a large

uncertainty is imposed on the total rupture area. One crack is assumed at the basemat and midheight locations for cases considering corrosion.

For the two midheight and two basemat corroded cases, leak occurs only slightly before the overall rupture failure, if not after. This has only a negligible effect on the total rupture area, since only one crack is assumed to initiate at the corroded locations. Therefore, the rupture curves for the original case with no corrosion and the two midheight corrosion cases and 50% basemat corrosion case share the same curve. The 65% basemat corrosion case increase diverges slightly from the other rupture cases, but only after failure. Obviously, assuming more than one corroded location for each case will increase the rupture area and lower the rupture pressure. Variation in the total area assumed to cause rupture (0.028 m^2 or 0.3 ft^2) will also affect the rupture pressure. As mentioned previously, a large uncertainty is imposed on the total rupture area to account for the approximate nature of the rupture criterion.

Finally, Figure 6.5 and Table 6.1 include the simple estimate for catastrophic rupture described in Section 2.4.2.3. It is clear from the failure pressures that catastrophic rupture will occur prior to a leak failure at many of the discontinuities and small regions of corrosion.

Table 6.1: Summary of Locations and Failure Pressures without Tendon Degradation

Location	Failure Pressure MPa (psig)
Leak Steam Penetration	0.921 (133.6)
Leak Wall-Basemat Junction	0.744 (107.8)
Leak Hatch	0.935 (135.7)
Leak Springline	1.035 (150.1)
Leak Base 50% Corrosion	0.904 (131.1)
Leak Base 65% Corrosion	0.892 (129.4)
Leak Midheight 50% Corrosion	1.070 (155.3)
Leak Midheight 65% Corrosion	1.030 (149.4)
Rupture No Corrosion	0.904 (131.1)
Rupture Base 50% Corrosion	0.900 (130.6)
Rupture Base 65% Corrosion	0.900 (130.6)
Rupture Midheight 50% Corrosion	0.904 (131.1)
Rupture Midheight 65% Corrosion	0.904 (131.1)
Catastrophic Rupture	0.980 (142.1)

Figure 6.6 and Table 6.2 show the failure functions and pressures for the case with 50% area loss of 20% of the midheight tendons. With the exception of leak at the springline, a failure mode which did not occur during the analysis, all of the discontinuities failed at lower pressures than in the undegraded tendon case. The pressures at the steam and hatch penetrations were most effected since they reside closest to the midheight of the containment. The rupture pressure also decreases significantly. Most significant is the reduction in the catastrophic rupture pressure which is now predicted to occur prior to leak or rupture in any location. This is due to the 50% reduction in the area of the tendons when computing the catastrophic rupture pressure.

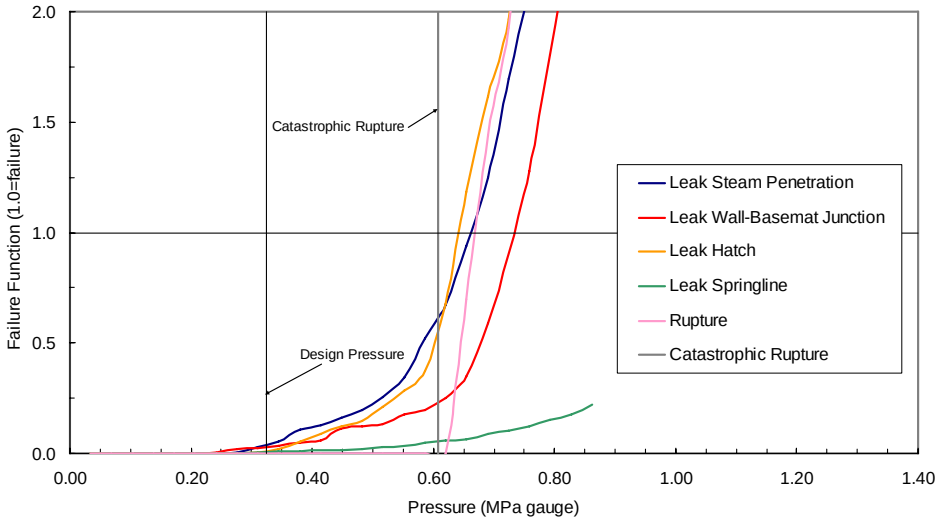

Figure 6.6: Failure Potential at Discontinuity Locations for 50% Area Degradation in the Midheight Tendons

Table 6.2: Summary of Locations and Failure Pressures with 50% Area Reduction of the Midheight Tendons

Location	Failure Pressure MPa (psig)
Leak Steam Penetration	0.662 (96.0)
Leak Wall-Basemat Junction	0.733 (106.3)
Leak Hatch	0.642 (93.2)
Leak Springline	No failure during analysis
Rupture	0.669 (97.0)
Catastrophic Rupture	0.608 (88.2)

Figure 6.7 and Table 6.3 show the failure functions and pressures for the case with 50% loss of the prestressing for 20% of the midheight tendons. All of the discontinuities failured at lower pressures than in the undegraded tendon case, but in general not as low as the 50% area reduction case. The pressures at the steam and hatch penetrations were most affected since they reside closest to the midheight of the containment. The catastrophic rupture pressure remains the same as the undegraded tendon case since the level of prestressing in not factored into the catastrophic rupture criterion.

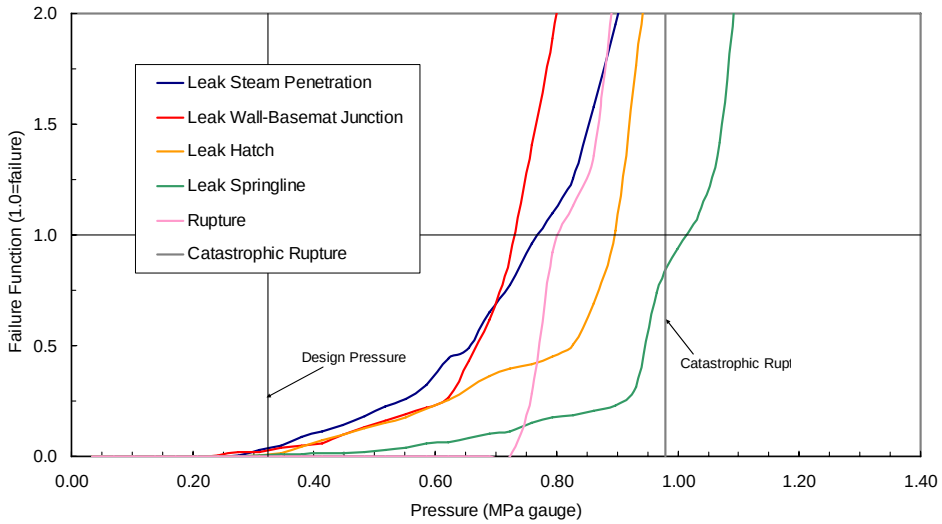

Figure 6.7: Failure Potential at Discontinuity Locations for 50% Loss of Prestressing of the Midheight Tendons

Table 6.3: Summary of Locations and Failure Pressures with 50% Prestressing Reduction of the Midheight Tendons

Location	Failure Pressure MPa (psig)
Leak Steam Penetration	0.768 (111.4)
Leak Wall-Basemat Junction	0.731 (106.0)
Leak Hatch	0.894 (129.7)
Leak Springline	1.013 (146.9)
Rupture	0.806 (116.9)
Catastrophic Rupture	0.980 (142.1)

6.2 Fragility Analysis of Degraded Prestressed Concrete Containment

The principal goal of the current study is to integrate structural analyses of degraded containments with risk analysis models to understand the significance of the degradation from a risk-informed perspective. Fragility curves of containments under pressurization with and without degradation serve as the interface between the structural and risk analyses. As explained in Section 2.5, Latin Hypercube Sampling is used in this study to generate sets of random variables to be used as input to the structural finite element analyses. For this containment, 23 input parameters were selected as random variables, and 30 samples of those parameters were taken for analysis.

Of the 23 input parameters, 18 describe the inherent randomness, or aleatory uncertainty, in the basic properties of concrete, reinforcing bars, and liner steel. The remaining 5 parameters describe epistemic uncertainty, or uncertainty in the ability to characterize the failure pressure. Several of the random input parameters are correlated with others. For concrete, the tensile

strength, f'_t, and modulus of elasticity, E_c, are correlated with the cylinder compressive strength, f'_c. Likewise, there is correlation between the yield strength and ultimate strength of steel.

Whenever possible, statistical test data was used as the basis for the probability distributions in this study. When such data was unavailable, engineering judgment was used to provide reasonable estimates of uncertainty. Based on as-built material properties from Butler and Fugelso (1982), the elastic modulus of concrete in the containment is related to the compressive strength as:

$$E_c = c_1 \, 70000\sqrt{f'_c} \tag{6.1}$$

where c_1 is a random variable with a median of 1.0 and a coefficient of variation of 0.077. From Mirza et al. (1979), f'_t in the containment is computed as:

$$f'_t = c_2 \, 8.3\sqrt{f'_c} \tag{6.2}$$

where c_2 has a median of 1.0 and a coefficient of variation of 0.196. Units of psi are used in both of these equations. Under average control conditions, Mirza et al. suggest that a coefficient of variation (COV) of 0.15 can be assumed for f'_c.

The concrete in the base slab varies from the concrete in the containment. The relationship between the elastic modulus and tensile strengths with the compressive strength follow as,

$$E_c = c_1 \, 65000\sqrt{f'_c} \tag{6.3}$$

from Butler and Fugelso (1982) with a coefficient of variation of 0.077, and

$$f'_t = c_2 \, 8.3\sqrt{f'_c} \tag{6.4}$$

from Mirza et al. (1979) with a coefficient of variation of 0.196.

The prestressed containment investigated in this study has reinforcing bars and prestressed steel tendons. For both materials, the elastic modulus, E_s is assumed to be independent of the yield strength, f_y, and the ultimate strength, f_u. Correlation is induced between f_y and f_u in a manner similar to that for concrete:

$$f_y = s \; r \; f_u \tag{6.5}$$

where s is a random variable with a median of 1.0. The variable r is the ratio of the yield stress to the ultimate stress, and differs depending on the type of steel. For the reinforcing bars, a value of 0.63 was assumed for r (Weatherby, 1988). For tendons, this value was set at 0.875 (Weatherby, 1988), and for the liner steel, a value of 0.535 was used.

Additional uncertainties include the variation in the corrosion depth. This is applied to the corroded thickness of the submodels of the liner and to the two degraded tendon cases. For the 50% reduced area tendons, the corrosion depth uncertiainty is multiplied by 50% of the normal tendon area for the hoop tendons at the midheight thoughout the 30 analyses. For the 50% loss in prestressing, the corrosion depth uncertainty is multiplied by the normal prestressing values for the hoop tendons at the midheight of the containment thoughout the 30 analyses. The normal prestressing levels for the tendons are 970 MPa for the hoop tendons, 1014 MPa for the meridonal tendons, and 981 MPa for the dome tendons. Even for the undegraded tendon cases, each of the prestressing levels is multiplied by a prestressing uncertainty with a median of 1.0 and a COV of 0.03.

Five separate variables are used to describe the epistemic uncertainty. Variable describes the uncertainty inherent in predicting the global strains, the local strains from the 2-D submodels with corrosion, the strain magnification in the presence of corrosion, the calculation of the rupture area, and the simple estimate for catastrophic rupture.

Each of these variables has a median value of 1.0. A COV of 0.3 was assumed for the global strain prediction variable, f_{FEM-u}. The magnification factors for the liner discontinuities for the prestressed containment (Figure 2.10) are simply multiplied by the uncertainty factor in Equation 2.9. Failures at the these discontinuities are determined from the undegraded containment analyses and for both of the degraded tendon cases.

The COV of the local model uncertainty factor, f_{FEM-u}, was set to 0.35 because it was felt that there is more uncertainty in the local models than in the global models. For the local detailed models, Equation 2.1 is used to compute the magnified strains. Since the local models contain corrosion, the corrosion factor, f_c, equals 2 and is multiplied by an uncertainty factor, f_{c-u}, with a COV of 0.20.

The final two epistemic factors account for the uncertainty in the rupture area, f_{rupt-u}, and catastrophic rupture pressure, f_{cat-u}. Since the calculation of the rupture area in Equation 2.12 contains several approximations, a large COV is employed, equal to 0.40. The simple method used here to compute the catastrophic rupture pressure (Equation 2.13) should provide a reasonable estimate, enabling the use of a low COV of 0.10. This uncertainty is in addition to the variation in the ultimate strengths random variables used in Equation 2.13.

Table 6.4 shows all of the random input parameters. This table shows the median values of the parameters, a measure of the variation assumed for the parameter, and the type of distribution. For variables with normal distributions, the COV is used as the measure of variation, while β is used for variables represented with a lognormal distribution.

A total of 30 sets of these input parameters were generated based on analyses using the specified distribution functions. Once the analyses were run, the 30 leak pressures were used to develop fragility curves for each of the four locations of linear discontinuity. Figure 6.8 shows the fragility curves based on the sorted analyses values and associated lognormal curve fits for the case with no tendon degradation. The fragility curves represent the leak pressure for the four discontinuity locations. Figure 6.9 shows the fragility curves for leak at the two corroded locations, basemat and midheight, at the two levels of corrosion, 50% and 65%. These plots indicate that increasing the level of corrosion from 50% to 65% of the liner thickness has only a minimal effect.

Table 6.4: Random Input Parameters

Property	Median	COV/β	Distribution
Concrete (Containment)			
Compressive Strength (f'_c)	45.0 MPa (6.529 ksi)	0.15	Lognormal
Elastic Modulus factor (c_1)	1.0	0.077	Normal
Tensile Strength factor (c_2)	1.0	0.196	Normal
Concrete (Base Region)			
Compressive Strength (f'_c)	40.4 MPa (5.861 ksi)	0.15	Lognormal
Elastic Modulus factor (c_1)	1.0	0.077	Normal
Tensile Strength factor (c_2)	1.0	0.196	Normal
Reinforcing Steel			
Ultimate Strength (f_u)	721.2 MPa (104.6 ksi)	0.09	Lognormal
Yield Strength Factor (s)	1.0	0.07	Normal
Elastic Modulus (E_s)	200 Gpa (29000 ksi)	0.06	Normal
Liner Steel			
Ultimate Strength (f_u)	576.8 MPa (83.66 ksi)	0.09	Lognormal
Yield Strength Factor (s)	1.0	0.07	Normal
Elastic Modulus (E_s)	200 GPa (29000 ksi)	0.06	Normal
Uniaxial Failure Strain (ε_{fail})	0.25	0.12	Normal
Corrosion Depth Uncertainty (also used for tendon degradation)	1.0	0.10	Normal
Tendon Steel			
Ultimate Strength (f_u)	1649 MPa (239.1 ksi)	0.09	Lognormal
Yield Strength Factor (s)	1.0	0.07	Normal
Elastic Modulus (E_s)	200 Gpa (29000 ksi)	0.06	Normal
Tendon Prestressing Factor	1.0	0.03	Normal
Epistemic Uncertainty			
Axisymmetric Model Strain Factor Uncertainty (f_{FEM-u})	1.0	0.30	Lognormal
Sub-model Strain Factor Uncertainty (f_{FEM-u})	1.0	0.35	Lognormal
Corrosion Factor Uncertainty (f_{c-u})	1.0	0.20	Lognormal
Leak Area for Rupture Uncertainty	1.0	0.40	Lognormal
Catastrophic Rupture Uncertainty	1.0	0.10	Lognormal

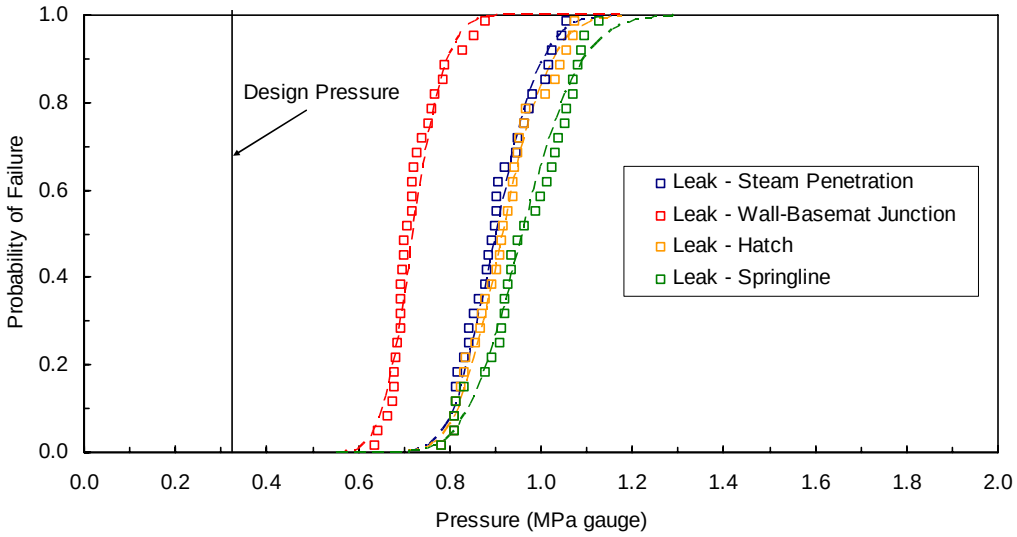

Figure 6.8: Fragility Curves for Leak at Discontinuity Locations

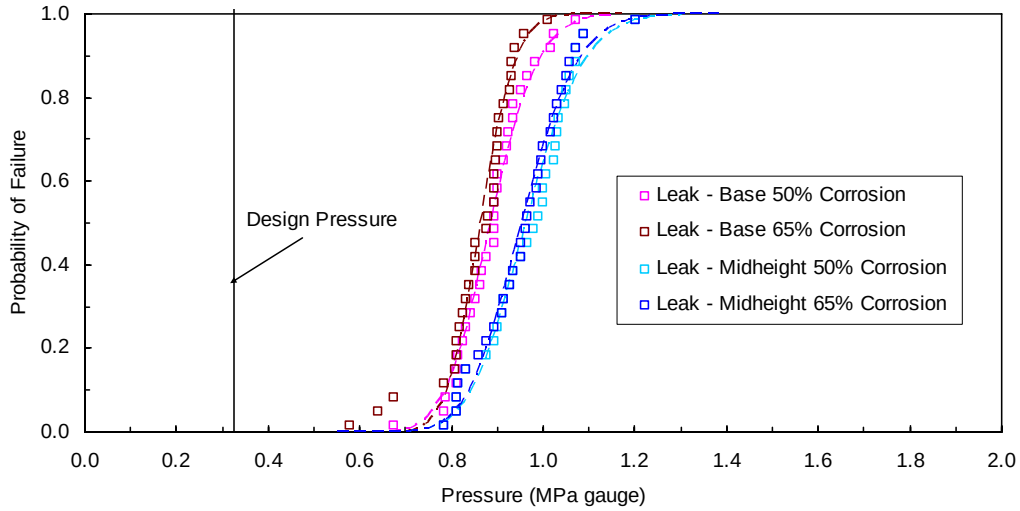

Figure 6.9: Fragility Curves for Leak at Corroded Locations

As discussed previously, the rupture threshold is assumed to be reached when the total crack opening caused by initiated leaks, exceeds 0.028 m^2 (0.3 ft^2). Figure 6.10 shows the rupture fragility curves for the five cases examined in this study. Since no significant change in pressure occurs for the both corroded midheight and the 50% basemat cases, the curves for these cases remain identical. The crack opening near the basemat with 65% corrosion are large enough to cause a slight decrease in rupture pressure. Figure 6.10 also illustrates the fragility curve for catastrophic rupture. Since the criteria for catastrophic rupture is not affected by the corrosion in the liner, the catastrophic rupture fragility remains the same for each of the 4 corroded cases as well as the undegraded case.

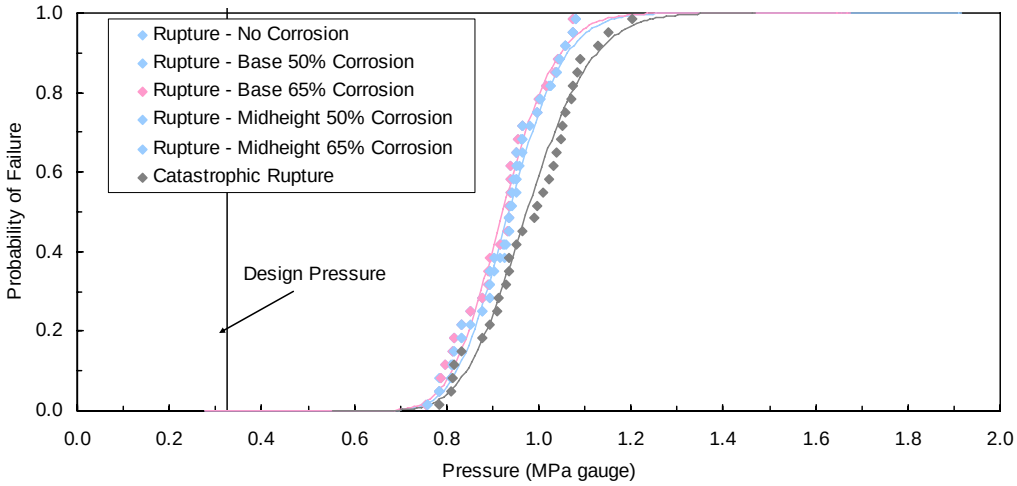

Figure 6.10: Fragility Curves for Rupture and Catastrophic Rupture

Figure 6.11 illustrates the fragility curves for leak at the 4 discontinuity locations, rupture, and catastrophic rupture for the case with 50% area degradation in the midheight tendons. Catastrophic rupture occurs at approximately the same pressure as the leak locations and rupture. This is due to the leak and rupture pressures being set to the catastrophic rupture pressure if it is smaller than the computed leak or rupture pressure.

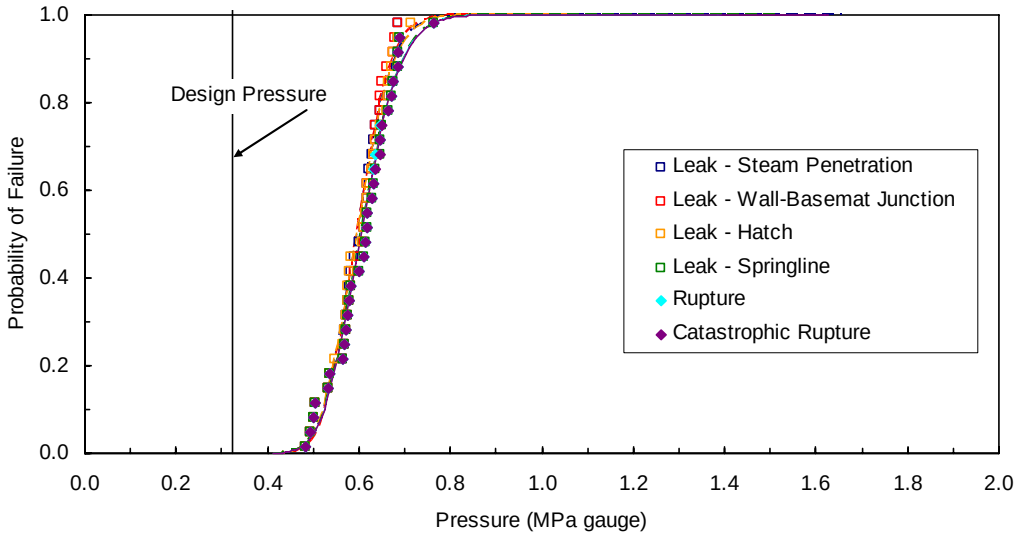

Figure 6.11: Fragility Curves for 50% Area Reduction in Midheight Tendons

Figure 6.12 shows the fragility curves for leak at the 4 discontinuity locations, rupture, and catastrophic rupture for the case with 50% prestressing loss in the midheight tendons. Due to the shape of the distribution for leak and the wall-basemat junction, the lognormal curve fits required one curve fit for high probabilities and one curve fit for low probabilities.

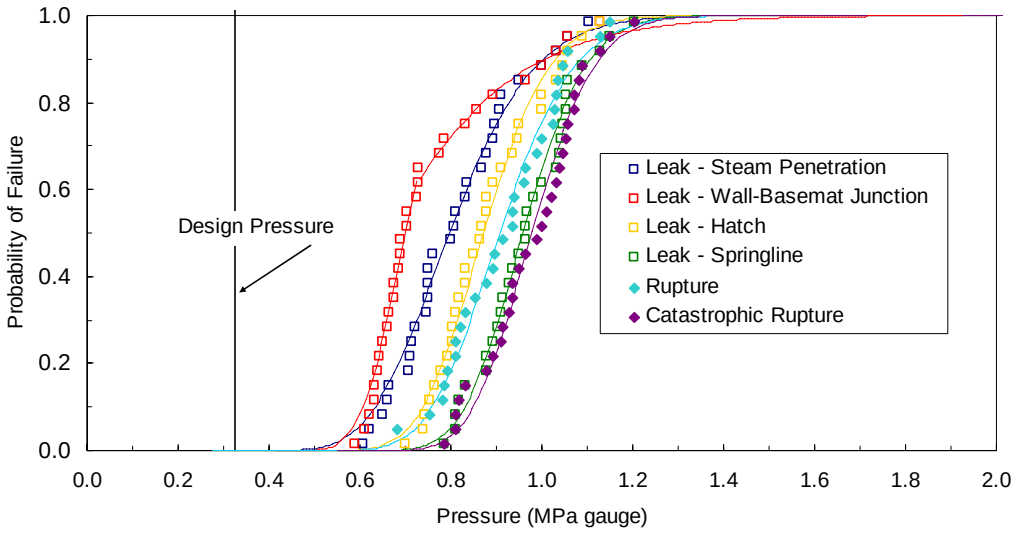

Figure 6.12: Fragility Curves for 50% Prestressing Loss for the Midheight Tendons

The leak fragilites for the four discontinuity locations were used to develop a cumulative probability of failure curve for the original, uncorroded, containment. Figure 6.13 shows the cumulative probability of failure (leak) curves obtained in the current study for the containment with corrosion degradation at the midheight and at the base, tendon degradation, and the fragility of the containment in its original condition. The drop in capacity due to corrosion at the midheight and basemat is negligible, while the shifts due to tendon degradation prove more significant.

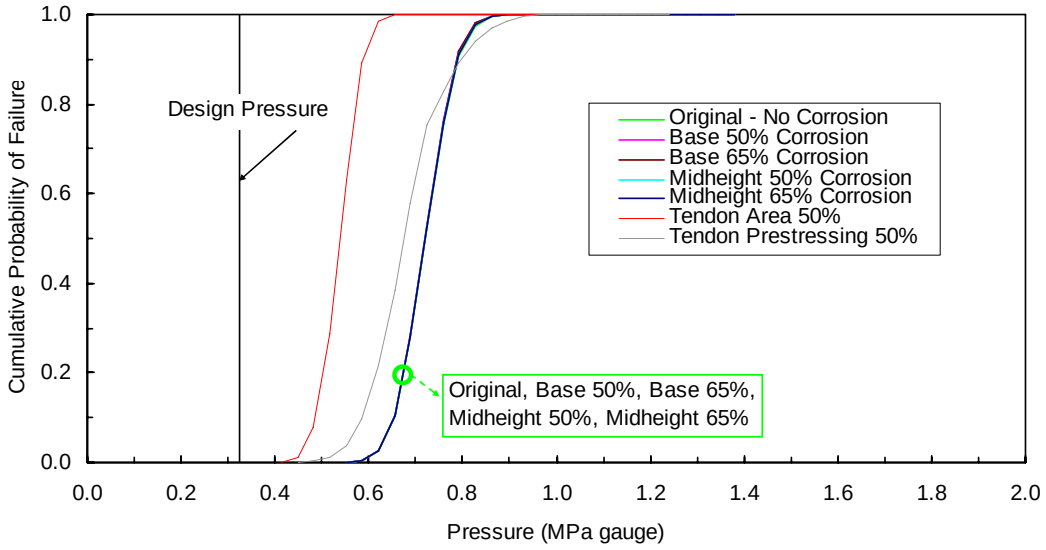

Figure 6.13: Cumulative Probability of Failure Curves for Original and Degraded Prestressed Containment

The conditional probability of failure curves were computed for each of the seven cases and shown in Figure 6.14Figure 6.20. Since the rupture and catastrophic curves are relatively constant throughout the liner corrosion cases, the conditional probability distributions are extremely similar. At low pressures ($P < 0.70$ MPa), the probability of leak is equal to 1.0 with the rupture and catastrophic rupture probabilities at 0.0. With increasing pressure, the rupture and the catastrophic rupture conditional probabilities begin to rise. The leak probability decreases quickly as the rupture probabilities increase. The rupture curve peaks at approximately 1.0 MPa. At this point, both the leak and rupture curves decrease gradually to probabilities of 0.0 and the catastrophic curve increase to a probability of 1.0 at approximately 1.4 MPa.

Figure 6.19 shows the conditional probabilities for the 50% tendon area degradation case. These curve are significantly different that the undegraded and liner corrosion curves. For one, there is essentially no rupture probability, and the leak and catastrophic rupture curves are shifted to the left (lower pressures). Figure 6.20 illustrates the 50% loss in tendon prestressing case. These conditional probabilities are similar to the undegraded and liner corrosion curves, but with a slightly larger peak rupture probability which occurs at a slightly lower pressure.

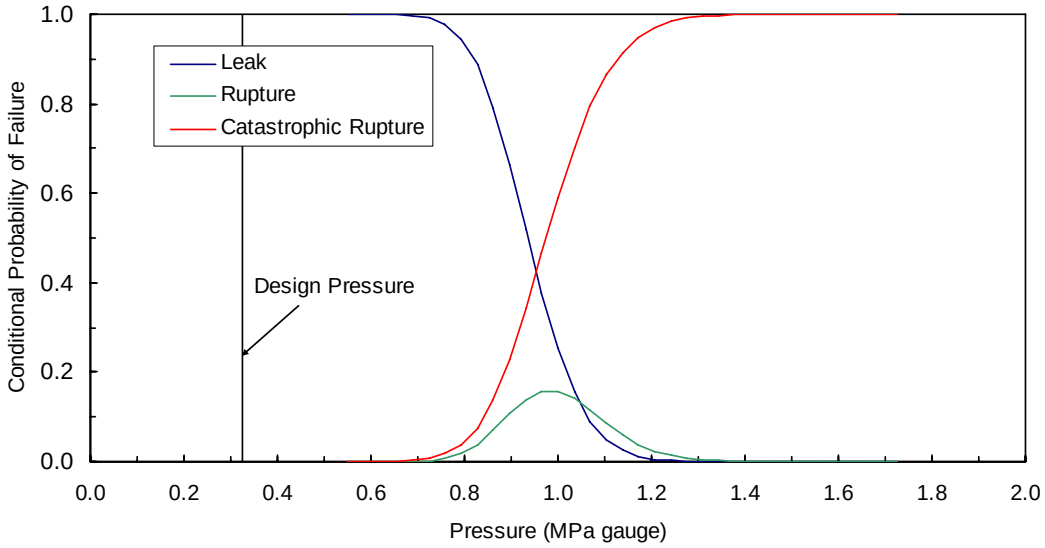

Figure 6.14: Conditional Probability of Failure for Original Containment (No Corrosion)

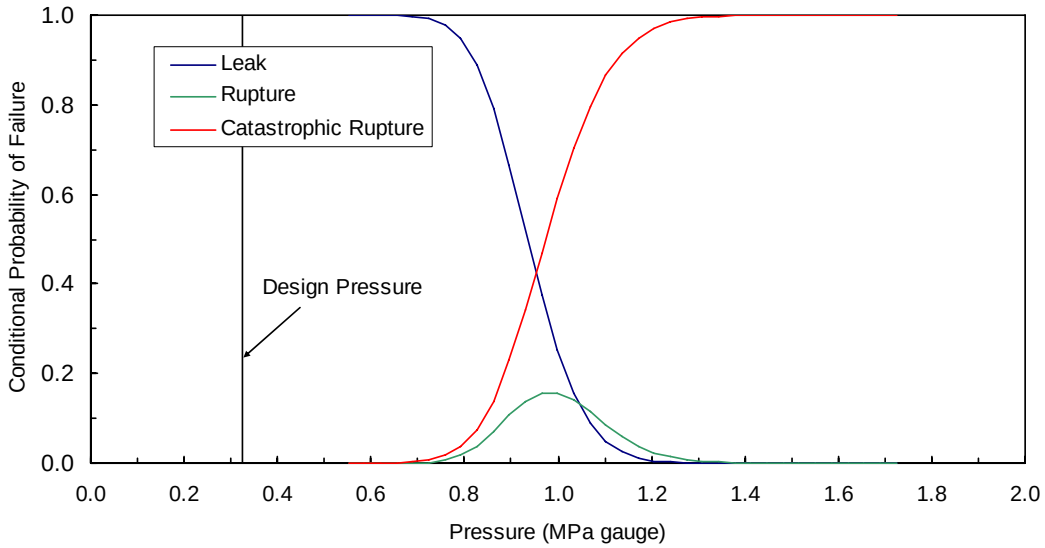

Figure 6.15: Conditional Probability of Failure for 50% Corrosion at Basemat

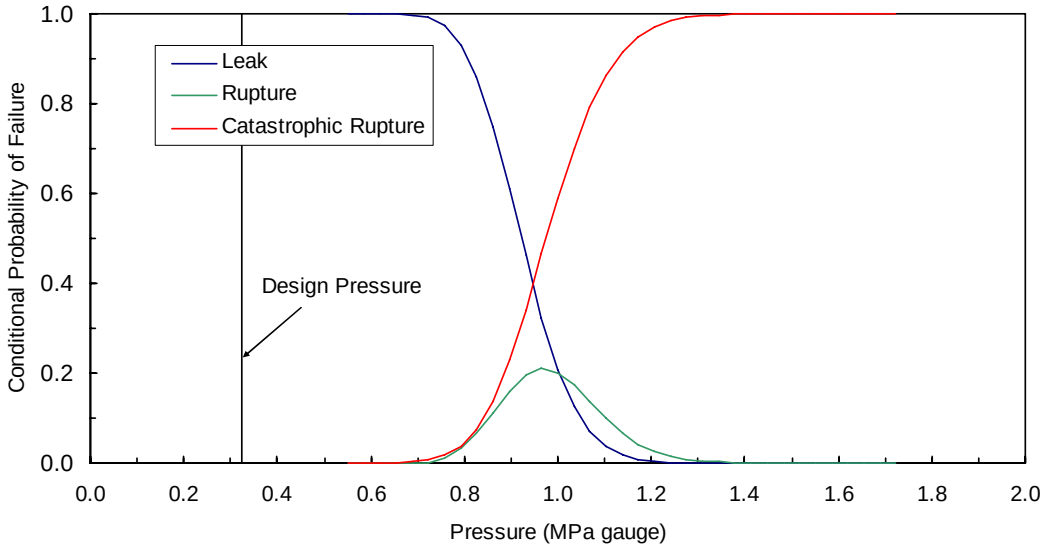

Figure 6.16: Conditional Probability of Failure for 65% Corrosion at Basemat

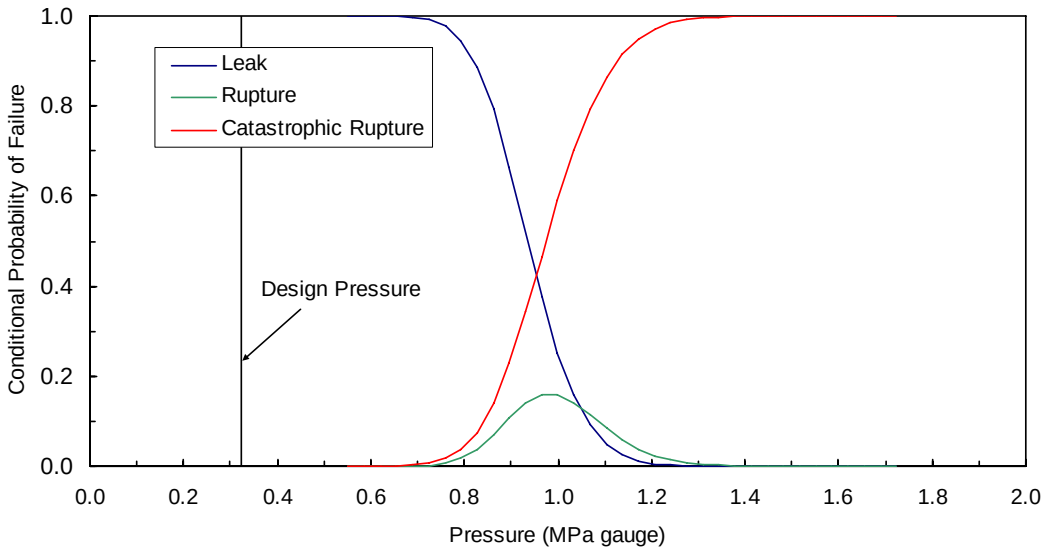

Figure 6.17: Conditional Probability of Failure for 50% Corrosion at Midheight

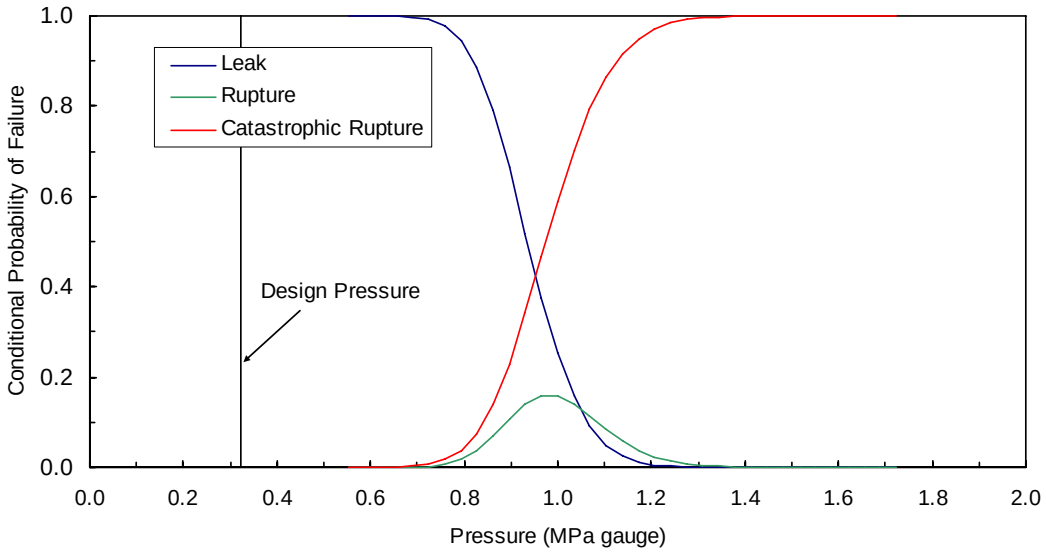

Figure 6.18: Conditional Probability of Failure for 65% Corrosion at Midheight

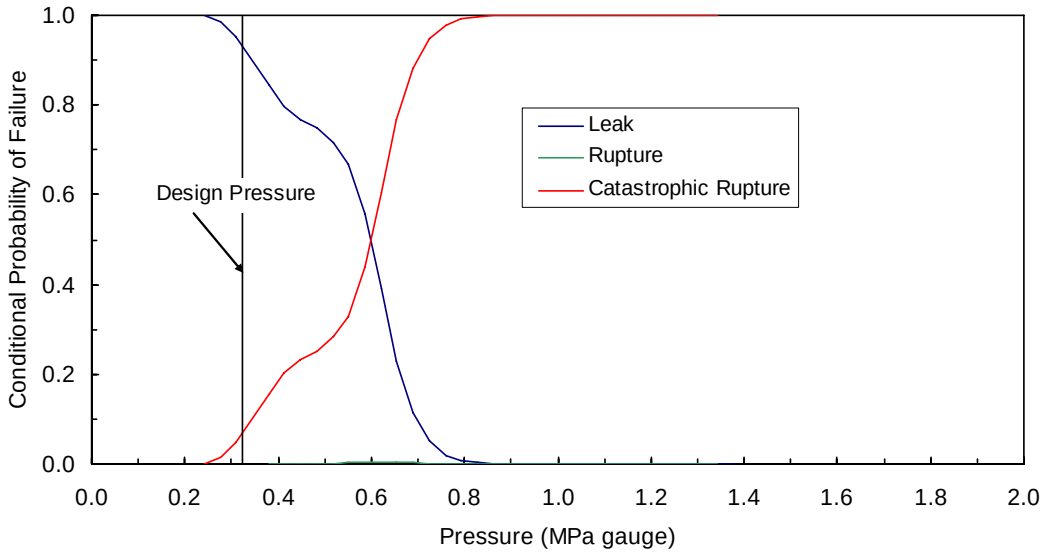

Figure 6.19: Conditional Probability of Failure for 50% Area Reduction of the Midheight Tendons

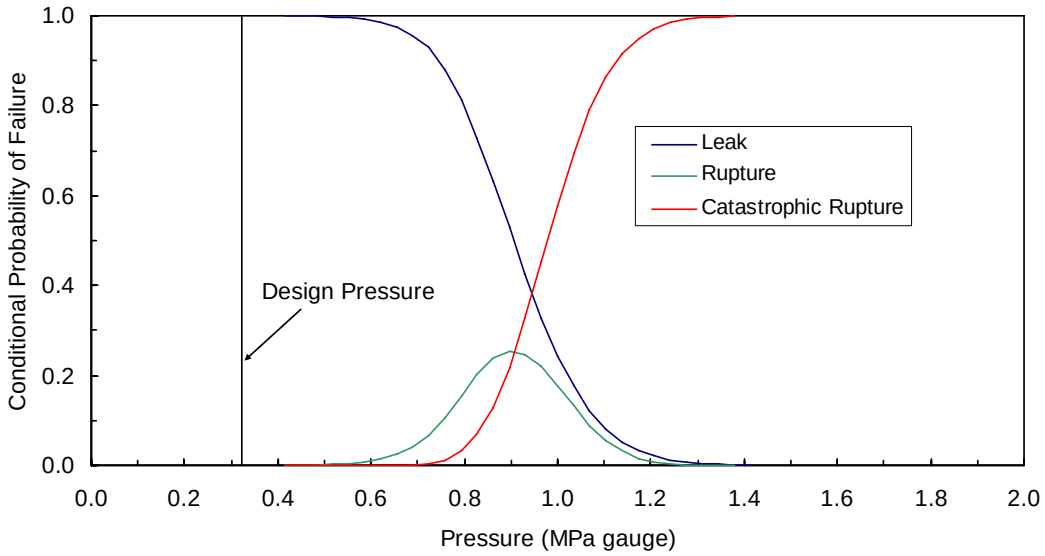

Figure 6.20: Conditional Probability of Failure for 50% Loss of Prestressing for the Midheight Tendons

6.3 Risk Analysis Results

Table 6.5 shows the CDF results from NUREG 1150 for the reinforced concrete containment analyzed in Section 3. As explained at the beginning of this chapter, because the risk model for the prestressed containment was not available, the risk model for the PWR plant with a reinforced concrete containment described in Chapter 3 is used instead. The two containments have roughly the same design pressure, so this can be viewed as an assessment of the plant in Chapter 3, but with a hypothetical prestressed concrete containment design option. Because the containment response does not affect the CDF for the plant for the reinforced concrete containment, the results are the same for all of the cases studied.

Table 6.5: Core Damage Frequency (yr^{-1})

Case	Mean	5%	50%	95%
All	4.1E-5	6.8E-6	2.3E-5	1.3E-4

Table 6.6 shows the LERF results obtained from the current study, Table 6.7 shows the probability of large early containment failure conditional on core damage, and Table 6.8 shows the change in LERF relative to the un-damaged state due to degradation for the degradation types and extents evaluated here.

Table 6.6: Large Early Release Frequency (yr^{-1})

Case	Mean	5%	50%	95%
Un-damaged (Current Study)	1.50E-7	0	1.98E-10	2.23E-6
50% Corrosion near basemat	1.41E-7	0	1.83E-10	2.04E-6
50% Corrosion at midheight	1.41E-7	0	1.83E-10	2.04E-6
65% Corrosion near basemat	1.41E-7	0	1.83E-10	2.04E-6
65% Corrosion at midheight	1.41E-7	0	1.83E-10	2.04E-6
50% Tendon Area Reduction	6.97E-7	0	1.81E-9	1.45E-5
50% Tendon Prestressing Loss	1.51E-7	0	2.03E-10	2.23E-6

Table 6.7: Probability of Large Early Containment Failure Conditional on Core Damage

Case	Mean	5%	50%	95%
Un-damaged (Current Study)	0.0037	0	8.61E-6	0.0171
50% Corrosion near basemat	0.0034	0	7.94E-6	0.0157
50% Corrosion at midheight	0.0034	0	7.94E-6	0.0157
65% Corrosion near basemat	0.0034	0	7.94E-6	0.0157
65% Corrosion at midheight	0.0034	0	7.94E-6	0.0157
50% Tendon Area Reduction	0.0170	0	7.86E-5	0.1110
50% Tendon Prestressing Loss	0.0037	0	8.84E-6	0.0171

Table 6.8: Change in the Large Early Release Frequency (yr^{-1}) due to Degradation

Case	Mean	5%	50%	95%
50% Corrosion near basemat	-8.79E-9	0	-1.54E-11	-1.86E-7
50% Corrosion at midheight	-8.79E-9	0	-1.54E-11	-1.86E-7
65% Corrosion near basemat	-8.79E-9	0	-1.54E-11	-1.86E-7
65% Corrosion at midheight	-8.79E-9	0	-1.54E-11	-1.86E-7
50% Tendon Area Reduction	5.47E-7	0	1.61E-9	1.22E-5
50% Tendon Prestressing Loss	1.17E-9	0	5.26E-12	0

The key risk criteria for acceptance of a proposed plant change in Regulatory Guide 1.174 (USNRC, 2001) are the baseline values of CDF and LERF, and the changes in those values due to the proposed modification, denoted as ΔCDF and ΔLERF. The acceptance criteria must be met for both the pairs of ΔCDF and CDF and of ΔLERF and LERF. Because CDF is unaffected by the containment properties in this particular plant, ΔCDF is 0, so the effects of the change clearly fall within Region III for the CDF acceptance criteria, which can be seen in Figure 2.1. In Region III, it is not actually necessary to compute the baseline CDF, although for these analyses, the mean CDF was computed, and has a value of 4.1E-5, which is clearly acceptable.

For both the lower bound and best estimate fragility curves, there is a reduction in LERF relative to the un-damaged containment in the case where corrosion exists near the basemat or the midheight. Because LERF is reduced by the increases in leak (leak is included in SERF, not LERF) in these particular case, ΔLERF is negative, so the effects of the change are assumed to fall within Region III for the LERF acceptance criteria, which can be seen in Figure 2.2. Therefore, the corrosion cases investigated in this study would be permissible modifications from a risk standpoint by Regulatory Guide 1.174.

The two degraded tendon cases increase the probability of catastrophic rupture, which is included in LERF. The slight increase in LERF for the 50% reduction in tendon prestressing case falls within the acceptable Region III. The increase in LERF for the 50% tendon area reduction case is sufficient to reach Region II in Figure 2.2. This indicates that increased scrutiny would be required, but the change would still be acceptable from the standpoint of the risk metrics.

There are other criteria for acceptance that also must be met. A change proposed under that risk-informed methodology must also satisfy other design goals. It must still maintain defense in depth and acceptable safety margins.

The small early release frequency (SERF) is included in Table 6.9 for comparison. The probability of small early containment failure conditional of core damage is also shown in Table 6.10. The sum of the large and small release frequencies and conditional are shown in Table 6.12 and Table 6.13.

Table 6.9: Small Early Release Frequency (yr^{-1})

Case	Mean	5%	50%	95%
Un-damaged (Current Study)	1.96E-7	1.58E-10	8.77E-10	4.53E-6
50% Corrosion near basemat	2.04E-7	1.58E-10	8.77E-10	5.07E-6
50% Corrosion at midheight	2.04E-7	1.58E-10	8.77E-10	5.07E-6
65% Corrosion near basemat	2.07E-7	1.58E-10	8.81E-10	5.07E-6
65% Corrosion at midheight	2.04E-7	1.58E-10	8.77E-10	5.07E-6
50% Tendon Area Reduction	2.26E-7	1.33E-10	8.25E-10	3.70E-6
50% Tendon Prestressing Loss	2.78E-7	1.58E-10	8.84E-10	6.30E-6

Table 6.10: Probability of Small Early Containment Failure Conditional on Core Damage

Case	Mean	5%	50%	95%
Un-damaged (Current Study)	0.00477	2.33E-5	3.81E-5	0.0349
50% Corrosion near basemat	0.00499	2.33E-5	3.81E-5	0.0390
50% Corrosion at midheight	0.00499	2.33E-5	3.81E-5	0.0390
65% Corrosion near basemat	0.00506	2.33E-5	3.83E-5	0.0390
65% Corrosion at midheight	0.00499	2.33E-5	3.81E-5	0.0390
50% Tendon Area Reduction	0.00551	1.96E-5	3.59E-5	0.0284
50% Tendon Prestressing Loss	0.00679	2.33E-5	3.84E-5	0.0484

Table 6.11: Change in the Small Early Release Frequency (yr^{-1}) due to Degradation

Case	Mean	5%	50%	95%
50% Corrosion near basemat	8.79E-9	0	0	5.39E-7
50% Corrosion at midheight	8.79E-9	0	0	5.39E-7
65% Corrosion near basemat	1.17E-8	0	3.29E-12	5.39E-7
65% Corrosion at midheight	8.79E-9	0	0	5.39E-7
50% Tendon Area Reduction	3.05E-8	0	-5.26E-11	-8.36E-7
50% Tendon Prestressing Loss	8.26E-8	0	6.57E-12	1.76E-6

Table 6.12: Total Early Release Frequency (yr^{-1})

Case	Mean	5%	50%	95%
Un-damaged (Current Study)	3.46E-7	1.58E-10	1.08E-9	6.76E-6
50% Corrosion near basemat	3.46E-7	1.58E-10	1.06E-9	7.11E-6
50% Corrosion at midheight	3.46E-7	1.58E-10	1.06E-9	7.11E-6
65% Corrosion near basemat	3.49E-7	1.58E-10	1.06E-9	7.11E-6
65% Corrosion at midheight	3.46E-7	1.58E-10	1.06E-9	7.11E-6
50% Tendon Area Reduction	9.23E-7	1.33E-10	2.63E-9	1.82E-5
50% Tendon Prestressing Loss	4.29E-7	1.58E-10	1.09E-9	8.52E-6

Table 6.13: Probability of Total Early Containment Failure Conditional on Core Damage

Case	Mean	5%	50%	95%
Un-damaged (Current Study)	0.00843	2.33E-5	4.68E-5	0.0520
50% Corrosion near basemat	0.00843	2.33E-5	4.61E-5	0.0547
50% Corrosion at midheight	0.00843	2.33E-5	4.61E-5	0.0547
65% Corrosion near basemat	0.00850	2.33E-5	4.62E-5	0.0547
65% Corrosion at midheight	0.00843	2.33E-5	4.61E-5	0.0547
50% Tendon Area Reduction	0.02250	1.96E-5	1.14E-4	0.1400
50% Tendon Prestressing Loss	0.01050	2.33E-5	4.73E-5	0.0656

Table 6.14: Change in the Total Early Release Frequency (yr^{-1}) due to Degradation

Case	Mean	5%	50%	95%
50% Corrosion near basemat	0	0	-1.54E-11	3.53E-7
50% Corrosion at midheight	0	0	-1.54E-11	3.53E-7
65% Corrosion near basemat	2.93E-9	0	-1.22E-11	3.53E-7
65% Corrosion at midheight	0	0	-1.54E-11	3.53E-7
50% Tendon Area Reduction	5.78E-7	-2.53E-11	-1.56E-9	1.14E-5
50% Tendon Prestressing Loss	8.38E-8	0	1.18E-11	1.76E-6

The example plants examined here serves as good case studies indicating that one should be very cautious about simply applying the ΔLERF criterion to evaluate the significance of containment degradation. It is important to closely examine how degradation can increase the likelihood of one failure mode while decreasing the likelihood of another, and evaluate the consequences of these different modes. It cannot be stressed enough that the cases of degradation examined here are extremely limited in scope. There are currently no means of predicting degradation prior to its discovery. Since the location and specific nature of any degradation could dramatically affect the containment capacity and risk, a detailed analysis of that scenario would be required. The specific results reported in this study should in no way be applied to making regulatory decisions on existing plants.

7. Use of Regulatory Guide 1.174 and PRA Models in Assessing Containment Degradation

7.1 Use of Regulatory Guide 1.174 Methodology Assessment

Regulatory Guide 1.174 outlines the application of probabilistic risk assessment (PRA) techniques to make risk-informed decisions regarding changes to a nuclear power plant's licensing basis. The five principles to guide a risk-informed licensing basis change are outlined:

1) "The proposed change meets the current regulations unless it is explicitly related to a requested exemption or rule change, i.e., a "specific exemption" under 10 CFR 50.12 or a "petition for rulemaking" under 10 CFR 2.802."
2) "The proposed change is consistent with the defense-in-depth philosophy."
3) "The proposed change maintains sufficient safety margins."
4) "When proposed changes result in an increase in core damage frequency (CDF) or risk, the increases should be small and consistent with the intent of the Commission's Safety Goal Policy Statement. " (USNRC, 1986)
5) "The impact of the proposed change should be monitored using performance measurement strategies."

As mentioned in the fourth principle above, if a change results in an increase in risk, the increase in risk must be small and fall within certain acceptance guidelines. In Regulatory Guide 1.174, core damage frequency and large early release frequency (LERF) have been designated as criteria for determining the acceptance of a proposed change. If a proposed change in the licensing basis results in an increase in either the CDF or LERF, the change is only deemed acceptable if the baseline values of CDF and LERF, as well as the change in those values due to the proposed change, fall within certain bounds. Though we are not concerned with changes in CDF, many accident scenarios could affect CDF. For example, damage to the reactor vessel, feedwater or steam piping and supports due to the collapse of the bridge crane or other large section of material could increase CDF. This would have additional effects on LERF that are not considered in this study. Here, we assume that CDF is not affected due to containment degradation, and therefore, we are only concerned with LERF. For this reason, among others, this report should not be used for plant specific assessments.

The acceptance criteria for a proposed licensing basis change are shown graphically in terms of LERF in Figure 2.2. This space is divided into three regions. In the area denoted as Region I, the risk of the proposed change is deemed too high to be acceptable, and the change is not permitted. In Region II, the risk increase is considered small, and the change is permitted. In Region III, the risk increase is considered very small, and the change is permitted. A proposed change must meet the acceptance guidelines for LERF to be deemed acceptable. If a change is deemed acceptable, the cumulative impact of other plant changes on the risk over time must be monitored.

This study was successful in demonstrating a methodology to determine the change in LERF due to containment degradation when the overall pressure capacity, or probability of catastrophic rupture, of the containment was affected. The increase in risk due to the degradation has been clearly illustrated. Although, several cases of degradation have been shown to not affect LERF, and even decrease LERF in some scenarios. This could lead to the misleading conclusion that degradation may be beneficial from a risk standpoint. This is obviously not acceptable and shows

that changes in LERF may not be the appropriate criteria to be applied in assessing containment degradation.

The approach defined in Regulatory Guide 1.174 for risk-informed decision-making is not intended to relieve the duty of licensees to do things that they view as undesirable simply because those things can be demonstrated to have a minimal impact on the risk. If a proposal results in a risk increase, there must be clearly demonstrated benefits that outweigh the risk. If degradation is shown to not affect risk (or decrease risk), additional scrutiny should be placed on the selected risk parameter to determine if it is sufficient to base a regulatory decision upon.

Several cases of degradation explored in this study decrease the capacity of the containment to resist internal pressure with little or no leaking prior to catastrophic failure. This could lead to a release of radiation to the outside of the containment earlier than would have been the case had the containment been in its original, un-degraded state. This could be in violation of maintaining sufficient safety margins in the third principle above. Safety factors comparing the ratio of the pressure capacity at 50% failure probability to the design pressure exceeds 2 for the 4 un-degraded containments examined here. This ratio falls considerably below 2 for several cases of degradation. A required safety margin should be determined for future implantation of this methodology.

Additional structural performance criteria may also be essential to assessing the acceptability of any modification, including degradation. In design codes, structures are typically required to satisfy appropriate safety factors, but also meet deflection criteria under those loads. Specifically, nuclear containments have multiple penetrations, and may be in contact with other structure, etc. Increased displacements due to degradation may cause failures not predicted in this study. Issues related to other performance criterion could potentially be more significant to the increase in risk than explored here. This could affect several of the principles above.

Arguably, the most important performance metric of a containment vessel undergoing pressurization is its leak rate at a given pressure. For every type of containment vessel, there exists a limiting pressure beyond which the structure can no longer be pressurized. This structural capacity limit pressure is also an important performance characteristic, although it can be of secondary importance simply because it is often far in excess of the pressure at which the containment first begins to leak, especially for reinforced and prestressed concrete containment vessels. The leak rate was not determined here due to the complexities in its prediction, though SERF was determined for each case of degradation. The current Regulatory Guide 1.174 does not consider SERF directly. It could be argued that large increases in SERF are of significant importance and would not be acceptable in a license basis change per the above principles.

In severe accident scenarios when the containment is subjected to pressures significantly higher than the design pressure, translating structural response metrics such as strain and displacement into crack initiation and propagation can be quite difficult, and dependent on the containment design. Further research is needed to fully implement this methodology for several reasons. The failure criterion used to predict crack initiation continues to be an open research topic. In addition, the prediction of the propagation of the crack in a large scale 3D structure with a multiaxial stress state is also an open area of research. The use of simple uniaxial tensile failure strains to predict failure in three-dimensional finite element models with varying element sizes remains an area of uncertainty. The division between leak, rupture, and catastrophic rupture are definitions based on computation convenience. These were employed in large to remain consistent with the NUREG-1150 PRA models. As far as the fragility analysis, the effect of multiple penetrations also needs to be explored.

Overall, this methodology shows considerable promise in assessing the effects of degradation in nuclear containments. Several items require further study, including the quantification of limits on SERF and TERF, reductions in the safety factor, increases in the deformation, and the criterion used to predict crack initiation and propagation among others.

7.2 Limitations of PRA Models for Assessing the Effects of Containment Degradation

The following description of the issues concerning the use of PRA models in the assessment of containment performance was provided by Mark Leonard of Dycoda. These insights are based on a review of the work performed in this study and the methods employed within the NUREG-1150 PRA models (Leonard, 2006).

> The common practice in Level 2 and Level 3 PRA is to define discrete outcomes (i.e., 'bins' or groups) to various aspects of physical behavior. This is a practical necessity of PRA due to the enormous range of scenarios and conditions being considered in a single, integrated assessment or plant response to core damage accidents. This simplification of actual plant behavior can restrict the ability of the PRA to discern subtle changes in risk metrics. In the case of the NUREG-1150 PRAs, the containment structural response to a particular severe accident scenario must be categorized as resulting in one of four possible outcomes: 'no failure', 'leakage', 'rupture' or 'catastrophic rupture.' Combinations of these discrete outcomes representing changes as the accident progresses in time are difficult to capture with high fidelity in a PRA. For example, containment leak rate during a severe accident is likely to be a continuously changing parameter. The structure would initially leak at (or below) the design basis leak rate, increase with time as containment internal pressure increases and then increase more rapidly when an induced failure (e.g., crack) grows in size. Later in time, gross structural failure(s) might occur at entirely different locations as different competing failure mechanisms become important. The PRA analyst is challenged to fit this continuously changing containment leak rate into one of the discrete outcomes with the PRA logic models.
>
> A second simplification inherent to PRA models concerns time. It is well known that the time of "containment failure" has a first-order effect on radionuclide releases to the environment. However, time itself is also discretized in PRA models. That is, the central logic model of a PRA (e.g., the Accident Progression Event Tree, or APET, in NUREG-1150) is typically divided into two or more time periods. The time at which a particular event occurs along an actual severe accident timeline is assigned to one of these time periods. In the NUREG-1150 APETs, for example, an event can occur 'very early' (i.e., before the onset of core damage), 'early' (after the onset of core damage but before reactor vessel lower head failure), or 'late' (long after the time of reactor vessel failure). The time at which major changes in containment leakage occur must be fit into this discrete representation of the accident time line in the same way that changes in the magnitude of containment leakage are treated.
>
> The loss of information caused by these simplifications is generally acknowledged as being small and acceptable for the purposes of risk assessment. That is, frequency of scenarios treated by a slight exaggeration in the size (or time) of containment leakage in one scenario is balanced by the frequency of cases in which the leak rate is understated. Similarly, these simplifications are often judged as a minor limitation in the fidelity of the Level 2/3 risk

models for measuring the risk importance of changes to underlying parameters – such as the containment fragility curve(s) examined in this study. In this context, small calculated changes in LERF are properly interpreted as meaning the effect of a proposed change to the fragility curve(s) is within the modeling uncertainty of the PRA model itself.

However, for this conclusion to be valid the fundamental structure of the Level 2 PRA models must faithfully represent contemporary understanding of containment performance. It is not clear that this is the case in the NUREG-1150 models, or in many other contemporary Level 2 PRAs for that matter. The coarse discretization of containment leak rate (or area) in PRA models is qualitatively consistent with the physical behavior expected in free-standing steel containments, but not concrete containments. Differences in the radiological source term using the simplified, discrete outcome approach in the NUREG-1150 models versus a more realistic, continuous containment response model have not been characterized deterministically. Therefore, the quantitative conclusions drawn from this study should be tempered by some concern that the criteria used to define conditions leading to a large, early release in the NUREG-1150 models may not be accurate or complete.

This discussion of the limitations of PRA models in assessing containment performance should be considered when interpreting the results of this study. Even with these limitations, it is important to note that this study does provide a useful methodology and general information on the effects of degradation in nuclear containments.

8. Summary and Conclusions

8.1 Program Overview

This study couples detailed structural analyses of degradation in 4 typical nuclear containments with an existing series of Probabilistic Risk Assessment (PRA) models for each containment. The 4 containments include two concrete containments, 1) a Pressurized Water Reactor (PWR) with a large, dry reinforced concrete containment, and 2) a PWR with a large, dry prestressed concrete containment, and two steel containments, 1) a Boiling Water Reactor (BWR) with a Mark I steel containment, and 2) a PWR with a steel ice condenser containment. The majority of the degradation examined focuses on local corrosion of the steel liners in concrete containments and the steel shells in steel containments.

Multiple finite element analyses of each containment within a Latin Hypercube Simulation (LHS) framework enable the development of fragility curves for each containment under specific degradation scenarios. The LHS framework introduces material property, construction, modeling, and knowledge uncertainties into the deterministic structural analyses to produce the fragility curves required in the coupling with the PRA model.

The fragility curves produced initially represent failures at one specific location and mode (leak, rupture, etc) within a given containment. Fragility curves for various possible failure locations are combined to determine cumulative probabilities of failure fragility curves and their conditional failure probabilities with respect to leak, rupture, and catastrophic rupture. The introduction of these curves into the existing PRA models produces values for the Large Early Release Frequency (LERF) under each case of degradation. Finally, we assess the application of Regulatory Guide 1.174 to containment degradation using computed changes in LERF and other risk metrics.

While actual plants are being used as examples in this study, it should be emphasized that the analyses in this report are not intended to represent the actual condition of the plants. The information concerning the plant systems and structures used in the analyses is not current, and current operating conditions likely differ considerably from those assumed in the analyses. Most important, degradation is assumed only to demonstrate an analytical methodology, and does not represent actual degradation that has been observed at any of the plants. Any similarity between the degradation assumed in this study and that observed in the plants used for these demonstrations is purely coincidental. For these reasons along with the assumptions required to conduct these analyses, the specific results of these analyses should not be used as a basis for regulatory decisions.

8.2 Effects of Degradation on the Fragility, LERF, and other Risk Metrics

The results of the fragility and PRA analyses for each plant with various forms of degradation can be summarized easily due to the observed consistent trends. With magnitudes depending on the depth and location, liner/shell corrosion significantly reduces the capacity of a given containment. Only the 50% corrosion at the basemat case for the steel PWR ice condenser containment shows leak possible near the design pressure at even low probabilities. Other degradation cases throughout the containments studies here show shifts in the fragility curves, but not approaching

the design pressure even at low probabilities. It should be noted that the leaks predicted here are based on geometrically idealized models. Even in regions of corrosion, the area is thinned uniformly. In these cases, a definitive leak initiation is computed with an assumed criterion. Experiments (Hessheimer, 2003) have shown (especially for concrete containments) that leaks (though small) can occur at very low pressures near the design pressure and that the leak rate is a continuous function of internal pressure (see Figure 2.3). These small leak rates at low pressures often initiate at local details throughout the containment. The modeling of these local details would require a model of significantly higher fidelity than the models created in this study. Even though these early leaks are typically small compared to the leak initiations predicted in this study, this should be considered when interpreting the results of this study.

This study adopted a step function failure progression to remain consistent with the NUREG-1150 PRA models. From these PRA model results, liner/shell degradation causes a small increase in LERF in cases where catastrophic rupture dominates the failure mode. Containment failure proceeds directly from leak to catastrophic rupture with little or no gap between the failure modes. This is observed in the steel shell containments where sufficient energy exists within the pressurized containment to propagate a crack after the initiation of a leak. Of the catastrophic rupture dominated cases examined here with corrosion in the steel shell of a steel containment, all remain within Region III of Figure 2.2.

Concrete containments also show increases in LERF with degradation when the overall capacity is affected by the degradation. The two cases of tendon degradation of the prestressed concrete containment show increases in LERF. The largest increase occurs when 50% of the area is reduced for the midheight hoop tendons. The degradation of the tendons leads to a significant probability of catastrophic rupture at low pressures. Here, LERF increases enough to enter Region II of Figure 2.2.

Other cases actually show LERF remaining constant or even experiencing a reduction with degradation. These cases were encountered when leak was the dominant failure mode at low pressures. Specifically, these cases occurred in the basemat and bellows corrosion cases for the steel PWR ice condenser and the two concrete containments with liner corrosion. The large bending field at the base of the ice condenser containment causes leaks at low pressures prior to catastrophic rupture. The concrete containment liners tear at relatively low pressures compared to the overall capacity of the concrete vessel.

Since LERF was found to decrease in some cases where leaks dominates and would cause a release, the Small Early Release Frequency (SERF) was included in the PRA results for each containment. When leak dominates the failure, SERF increases and leads to the observed decrease in LERF. In these cases, the leak site acts as a “vent” at low pressures, slowly releasing material with the possibility of preventing or delaying a catastrophic rupture. In these scenarios, the consequences of small early releases must be examined prior to the determination of acceptability.

Since SERF decreases for the cases where catastrophic rupture dominates, the total early release frequency (TERF = LERF + SERF) was computed for each containment at each degradation case. TERF was included to illustrate that the total frequency increases or remains constant when introducing degradation regardless of the dominant failure mode.

If limits were placed on the increase in SERF or TERF that were analogous to those for LERF in Figure 2.2, Region II would be reached for several additional degradation cases in this study. In addition, the PRA models used here do not directly compute LERF or SERF. The binning

process is performed during the post-processing of the PRA results. It is at this point where the results from the event tree analysis are placed into LERF, SERF, and other "bins" depending on the failure mode (e.g. leak, rupture, etc). This study places leak failures into the SERF bin, and ruptures and catastrophic ruptures into the LERF bin. This was done assuming that a leak would not depressurize the containment in less than two hours (NUREG-1150 definition).

Obviously, this study has examined several simple cases of containment degradation. The specific results presented here should not be applied to any existing plant since actual degradation may be considerable more severe or widespread than examined here. This study also uses many assumptions for material properties and some of the procedures (e.g. failure criteria) are still the subject of research. This study was conducted to demonstrate a methodology of applying a risk-informed assessment to structural degradation. This methodology could be applied to specific degradation found in an existing plant, but significant care should be taken in selecting the failure criteria, modeling assumptions, risk metrics, and the implementation of the containment behavior in the PRA models or other risk analyses, among others.

9. References

ANATECH, 1997, "ANACAP-U User's Manual, Version 2.5" ANATECH Corp., San Diego, CA.

Anderson, T.L., 1995, *Fracture Mechanics: Fundamentals and Applications* –2nd ed., CRC Press, Boca Raton, FL.

Ang, A.H-S. and Tang, W.H., 1975, *Probability Concepts in Engineering Planning and Design, Volume 1-Basic Principles*, Wiley.

Ashar, H., Naus, D., and Tan, C.P., 1994, "Prestressed Concrete in U.S. Nuclear Power Plants (Part I)." Concrete International, May 1994, 30-34.

Breeding, R.J., F.T. Harper, T.D. Brown, J.J. Gregory, A.C. Payne, E.D. Gorham, W. Murfin, and C.N. Amos, 1992, "Evaluation of Severe Accident Risks: Quantification of Major Input Parameters." NUREG/CR-4551, SAND86-1309, Vol. 2, Rev. 1, Part 3, Sandia National Laboratories, Albuquerque, NM.

Breeding, R.J., J.C. Helton, W.B. Murfin, and L.N. Smith, 1990, "Evaluation of Severe Accident Risks: Surry Unit 1." NUREG/CR-4551, SAND86-1309, Vol. 3, Sandia National Laboratories, Albuquerque, NM.

Butler, T.A., and Fugelso, L.E, 1982, "Response of the Zion and Indian Point Containment Building to Severe Accident Pressures." NUREG/CR-2569, LA-9301-MS, Los Alamos, NM, Los Alamos National Laboratory.

Castro, J.C., R.A. Dameron, R.S. Dunham, and Y.R. Rashid, 1993, "A Probabilistic Approach for Predicting Concrete Containment Leakage." EPRI Report TR-102176, T1, ANATECH Corp., San Diego, CA.

Cherry, J.L., J.M. Clauss, M. Pilch, J.J. Gregory, and J.A. Smith, 2001, "Aging Management and Performance of Stainless Steel Bellows in Nuclear Power Plants." NUREG/CR-6726, SAND2001-1147P, Sandia National Laboratories, Albuquerque, NM.

Cherry, J.L. and J.A. Smith, 2001, "Capacity of Steel and Concrete Containment Vessels with Corrosion Damage." NUREG/CR-6706, SAND2000-1735, Sandia National Laboratories, Albuquerque, NM.

Clauss, D.B., 1985, "Comparison of Analytical Predictions and Experimental Results for a 1:8-Scale Steel Containment Model Pressurized to Failure." NUREG/CR-4209, SAND85-0679, Sandia National Laboratories, Albuquerque, NM.

Clauss, D.B., 1985, "Pretest Predictions for the Response of a 1:8-Scale Steel LWR Containment Building Model to Static Overpressurization." NUREG/CR-4913, SAND85-0891, Sandia National Laboratories, Albuquerque, NM.

Clauss, D.B., 1987, "Round-Robin Pretest Analyses of a 1:6 scale Reinforced Concrete Containment Model Subject to Static Internal Pressurization." NUREG/CR-4913, SAND87-0891, Sandia National Laboratories, Albuquerque, NM.

Dameron, R.A., Rashid, Y.R., and H.T. Tang, 1995, "Leak area and leakage prediction for probabilistic risk assessment of concrete containments under severe core conditions." *Nuclear Engineering and Design*, 156, 173-179.

Dameron, R.A., L. Zhang, Y.R. Rashid, and M.S. Vargas, 2000, "Pretest Analysis of a 1:4-Scale Prestressed Concrete Containment Vessel Model." NUREG/CR-6685, SAND2000-2093, Sandia National Laboratories, Albuquerque, NM.

Eldred, M.S., A.A. Giunta, B.G. van Bloeman Waanders, S.F. Wojtkiewicz Jr., W.E. Hart, and M.P. Alleva, 2002, "DAKOTA, A Multilevel Parallel Object-Oriented Framework for Design Optimization, Parameter, Estimation, Uncertainty Quantification, and Sensitivity Analysis. Version 3.0 Users Manual." SAND2001-3796, Sandia National Laboratories, Albuquerque, NM.

Ellingwood, B. R. and J.L. Cherry, 1999, "Fragility Modeling of Aging Containment Metallic Pressure Boundaries." NUREG/CR-6631, ORNL/SUB/99-SP638V, Oak Ridge National Laboratories, Oak Ridge, TN.

Gregory, J.J., W.B. Murfin, S.J. Higgins, R.J. Breeding, J.C. Helton, and A.W. Shiver, 1990, "Evaluation of Severe Accident Risks: Sequoyah, Unit 1." NUREG/CR-4551, SAND86-1309, Vol. 5, Sandia National Laboratories, Albuquerque, NM.

Greimann, L., F. Fanous, and D. Bluhm, 1984, "Final Report, Containment Analysis Techniques, A State-of-the-Art Summary." NUREG/CR-3653, Ames Laboratory, IA.

Greimann, L., F. Fanous, J. Rogers, and D. Bluhm, 1987, "An Evaluation of the Effects of Design Details on the Capacity of LWR Steel Containment Buildings." NUREG/CR-4870, SAND87-7066.

Greimann, L., W. Wassef, F. Fanous, and D. Bluhm, 1991, "Analysis of Bellows Expansion Joints in the Sequoyah Containment." NUREG/CR-5561, SAND90-7020, Institute for Physical Research and Technology, Iowa State University, Ames, IA.

Hancock, J.W. and A.C. Mackenzie 1976, "On the Mechanisms of Ductile Failure in High-Strength Steels Subjected to Multi-Axial Stress States," *Journal of Mechanics and Physics of Solids*, 24, 147-169.

Hibbit, Karlsson and Sorenson, 2002, "ABAQUS/Standard User's Manual, Version 6.3," Hibbit, Karlsson and Sorenson, Inc, Pawtucket, RI.

Hessheimer, M.F., E.W. Klamerus, L.D. Lambert, G.S. Rightley, and R.A. Dameron, 2003, "Overpressurization Test of a 1:4-Scale Prestressed Concrete Containment Vessel Model." NUREG/CR-6810, SAND2003-0840P, Sandia National Laboratories, Albuquerque, NM.

Horschel, D.S., 1992, "Experimental Results From Pressure Testing a 1:6-Scale Nuclear Power Plant Containment." NUREG/CR-5121, SAND88-0906, Sandia National Laboratories, Albuquerque, NM.

International Standard Problem No. 48 Containment Capacity, Synthesis Report, Prepared by Sandia National Laboratories, Nuclear Safety NEA/CSNI/R(2005)/Vol.1, August 2005.

Lam, P.S. and R.L. Sindelar, 2000, "Flaw Stability in Mild Steel Tanks in the Upper-Shelf Ductile Range – Part II: *J*-Integral-Based Fracture Analysis." *Journal of Pressure Vessel Technology*, ASME, 122, 169-173. *Figure 1 of this reference has been reproduced within Figure 2.7 of this NUREG/CR with permission from ASME (Copyright 2000).*

Lambert, L.D. and M.B. Parks, 1995, "Experimental Results from Containment Piping Bellows Subjected to Severe Accident Conditions." NUREG/CR-6154, SAND94-1711, Vol. 1&2, Sandia National Laboratories, Albuquerque, NM.

Luk, V.K., M.F. Hessheimer, G.S. Rightley, L.D. Lambert, and E.W. Klamerus, 2000, "Design, Instrumentation, and Testing of a Steel Containment Vessel Model." NUREG/CR-5679, SAND 98-2701, Sandia National Laboratories, Albuquerque, NM 87185.

McKay, M.D., R.J. Beckman, and W.J. Conover, 1979, "A Comparison of Three Methods for Selecting Values of Input Variables in the Analysis of Output from a Computer Code." *Technometrics*, 21(2),239-245.

Miller, J.D., 1990, "Analysis of Shell-Rupture Failure Due to Hypothetical Elevated-Temperature Pressurization of the Sequoyah Unit I Steel Containment Building." NUREG/CR-5405, SAND89-1650, Sandia National Laboratories, Albuquerque, NM.

Mirza, S.A., M. Hatzinikolas, and J.G. MacGregor, 1979, "Statistical Descriptions of Strength of Concrete." *Journal of the Structural Division*, ASCE, 105 (6),1021-1037.

Papaspyropoulus, V., C. Marschall, and M. Landow, "Predictions of J-R Curves with Large Crack Growth from Small Specimen Data." NUREG/CR-4575, BMI-2137, Battelle's Columbus Division, Columbus, OH.

Rots, J. G., and J. Blaauwendraad, 1989, "Crack models for concrete: discrete or smeared? Fixed, multidirectional or rotating?" Heron, 34(1), Delft University of Technology, The Netherlands.

Shah, V.N., S.K. Smith, U.P. Sinha, 1994, "Insights for Aging Management of Light Water Reactor Components." NUREG/CR-5314, EGG-2562, Vol. 5, Idaho National Engineering Laboratory, Idaho Falls, ID.

Shih, C.F., and J.W. Hutchinson, 1976, "Fully Plastic Solutions and Large Scale Yielding Estimates for Plane Stress Crack Problems." *Journal of Engineering Materials and Technology*, ASME, 98, 289-295.

Sindelar, R.L., P.S. Lam, G.R. Caskey, Jr., and L.Y. Woo, 2000, "Flaw Stability in Mild Steel Tanks in the Upper-Shelf Ductile Range – Part I: Mechanical Properties." *Journal of Pressure Vessel Technology*, ASME, 122, 169-173.

Smith, J.A., 2001, "Capacity of Prestressed Concrete Containment Vessels with Prestressing Loss." SAND2001-1762, Sandia National Laboratories, Albuquerque, NM.

Takenaka, M., T. Omotani, T. Yamashita, and K. Tsukimori, 1989, "Surface Crack Propagation and Stability of Through-Wall Crack of Bellows." *Pressure Vessels and Piping Division Publication*, ASME, 168, 159-171.

Tang, H.T., R.A. Dameron, and Y.R. Rashid, 1995, "Probabilistic Evaluation of Concrete Containment Capacity for Beyond Design Basis Internal Pressures," *Nuclear Engineering and Design*, 157, 455-467. *Figures 6-9 and 11-14 of this reference have been reproduced within Figures 2.9 and 2.10 of this NUREG/CR with permission from Elsevier (Copyright 1995).*

Tronskar, J.P., M.A. Mannan, and M.O. Lai, 2003, "Correlation Between Quasi-Static and Dynamic Crack Resistance Curves," *Engineering Fracture Mechanics*, 70, 1527-1542.

United States Nuclear Regulatory Commission, 1986, "Safety Goals for the Operations of Nuclear Power Plants; Policy Statement," *Federal Register*, Vol. 51, p. 30028 (51 FR 30028), August 4, 1986.

United States Nuclear Regulatory Commission, 1990, "Severe Accident Risks: An Assessment for Five U.S. Nuclear Power Plants," NUREG-1150.

United States Nuclear Regulatory Commission, 1995, "Use of Probabilistic Risk Assessment Methods in Nuclear Activities: Final Policy Statement," *Federal Register*, Vol. 60, p. 42622, (60 FR 42622), August 16, 1995.

United States Nuclear Regulatory Commission, 2001, "An Approach for Using Probabilistic Risk Assessment in Risk-Informed Decisions on Plant-Specific Changes to the Licensing Basis." Regulatory Guide 1.174 (Draft Regulatory Guide DG-1110).

Weatherby, J.R., 1988, "Structural Assessments of the Surry and Zion Reactor Containments Buildings for NUREG-1150," memorandum to R.J. Breeding, Sandia National Laboratories, Albuquerque, NM.